THE UNIVERSITY OF CHICAGO

A LOADLOCK PLATFORM FOR NEXT-GENERATION QUANTUM OPTICS EXPERIMENTS

A DISSERTATION SUBMITTED TO
THE FACULTY OF THE DIVISION OF THE PHYSICAL SCIENCES
IN CANDIDACY FOR THE DEGREE OF
DOCTOR OF PHILOSOPHY

DEPARTMENT OF PHYSICS

BY
CHUAN YIN

CHICAGO, ILLINOIS
GRADUATION DATE

For those who want to know.

TABLE OF CONTENTS

LIST OF FIGURES

LIST OF TABLES

ACKNOWLEDGMENTS

Throughout my PhD journey, I had the incredible opportunity to build an atomic-molecular-optical (AMO) system from the ground up, witness its first use, and fully immerse myself in the research process. This journey was anything but solitary, and I am profoundly grateful to everyone who supported me along the way, helping to shape my experience and guiding me through my scientific journey involving The Divine Beast.

I must begin with my thesis advisor, **Jonathon Simon**, for taking a chance on me when I joined the lab. Jon's advice—"focus on science", "people are just being people", and "success is about making good decisions"—are deceptively simple yet deeply impactful tenets that have guided me throughout my PhD. Jon's first-principles, no-nonsense, JUST DO IT approach to problem-solving, characterized by his preference for under-the-hood tinkering, was both inspiring and instructive. I appreciate Jon for recommending the movie The Matrix and deeply admire his unique ability to apply Principal Component Analysis (PCA) to seemingly intractable scientific, technical, and interpersonal many-body problems, tackling them with remarkable determination and grace. His scientific vision, infectious enthusiasm, and keen observational skills motivated me to persevere through the challenges of constructing a new apparatus, navigating unfamiliar territories, and managing the logistical hurdles. Jon's high standards for professionalism, accountability, and efficacy pushed me to improve continuously. Through him, I learned the art of asking precise questions, telling clear stories, and delivering compelling presentations. Jon's unwavering belief in the intellectual capabilities of his students empowered me to aspire to greatness—like my role models Donna Strickland, Hedy Lamarr, and Lynn Hill—by committing to continuous self-improvement. Although it may not be wise for me to fully emulate Jon's masterful skills in salesmanship, showmanship, and leadership, I am sincerely grateful for his guidance, sarcastic humor, and unwavering support. I will always cherish our professional relationship.

I am deeply grateful to my thesis committee members–Young-Kee Kim, Cheng Chin,

Aashish Clerk, and David Schuster, as well as the faculty in the department–Peter Littlewood and Zosia Krusberg. Your insightful feedback, constructive criticism, and thoughtful suggestions have been invaluable in guiding me through some of the most challenging aspects of this work. Thank you for your mentorship, encouragement, and unwavering commitment to my success.

I am also deeply thankful to my undergraduate advisor, **Robert Rosner**, who epitomizes the idea that those who excel in science do so because they truly love it. Bob inspired me to work hard without counting the hours, demonstrated the power of kindness, and taught me the value of friendship and community. From Bob, I learned that admitting "I don't know" is far more respected in science than pretending otherwise, and that fostering trust and credibility is essential. His guidance helped me understand that there are no hard problems, only hard days, and that knowing when to take breaks is crucial. Bob also emphasized that if one cannot teach or explain something well, one probably does not fully understand it. I will always remember not to laugh at certain phrases, but to laugh at everything else, especially at myself.

Over the past five years, I have greatly benefited from the (at times) gentle guidance and support within the Simon Lab, and I have built meaningful relationships along the way. I am particularly grateful to:

Henry Ando, my longest collaborator and an absolute pleasure to work with, to whom I owe an immense debt of gratitude. Henry is a naturally gifted scientist, possessing traits that many would imagine a great scientist should possess—intelligence, inquisitiveness, creativity, and a remarkable sense of humor. Henry's focus on creating high-quality solutions that stand the test of time was instrumental in building The Loadlock Experiment. His dedication, from vacuum assembly to wrapping bias coils, crafting acousto-optic modulator (AOM) drivers, and constructing bench-top electronics, was vital, especially given the physically demanding and mentally taxing nature of the work. On a personal level, Henry exemplifies the value of

teamwork. He always gives others the benefit of the doubt, treats everyone with fairness and kindness, and is exceptional at deescalating conflicts and fostering mutual understanding. His approach allows both parties to move forward with a solution in mind and a lesson learned. I will miss our lab sessions, our workout sessions, and the many experiences we shared. Henry, you will be a great addition to any team, and I wish you all the best.

I would like to extend my deepest gratitude to **Matt Jaffe**, whose influence on my journey as a graduate student has been profound. Matt is not only an exceptional scientist but also a natural leader, a skilled Frisbee player, and one of the most positive, genuine, and collaborative individuals I have had the privilege of knowing. His ability to multitask, synthesize information, and see the bigger picture is truly remarkable. Despite being a postdoc on a different experiment, Matt consistently offered invaluable support to The Loadlock Experiment, helping to build it up from the ground. He generously shared his expertise, teaching me essential experimental skills, introducing me to a wealth of scientific literature, and providing countless practical tips and tricks. Matt's mentoring extended beyond the lab, offering advice and solutions that were both practical and unconventional, yet always effective. Matt has a unique talent for creating a non-judgmental space where creativity and innovation can thrive. His informal speaking style, combined with a strong sense of integrity, fostered an environment where academic discourse flourished, and interpersonal relationships were built on trust and mutual respect. He helped me realize that no problem is too complex, no question too trivial, and no challenge too daunting to overcome. For all these reasons and more, I am incredibly grateful to Matt. His guidance and support have not only shaped my research but also uplifted me personally, allowing me to navigate the challenges of graduate school with confidence and determination. Thank you, Matt, for everything, and I wish you all the best in your future endeavors.

Lavanya Taneja has been an exceptional colleague and a valued friend throughout my time on this project. Beyond her evident scientific intelligence, Lavanya possesses remark-

able emotional intelligence, resourcefulness, and a genuine kindness that is both rare and admirable. Her thoughtful and insightful questions often brought clarity and calm to even the most challenging situations, whether it involved complex experimental setups or the stress of academic life. Her ability to approach problems holistically, with transparency and honesty, has been inspiring. As a teacher and mentor, Lavanya exemplifies curiosity, patience, humility, and an appreciation for diversity. She fosters an environment where difficult questions are welcomed, and meaningful dialogue is encouraged. I am grateful for her willingness to engage in constructive debates, her reminders of what truly matters, and her unwavering support throughout this journey.

Mark Stone provided invaluable guidance on the fundamentals of experimental AMO physics, sharing his expertise in optics, electronics, and mechanical engineering with me when I was still a junior graduate student, working on an independent project. His mentorship extended beyond just teaching practical tips and tricks that only hands-on experience can offer; he also imparted a comprehensive understanding of the big picture and instilled a resilient problem-solving mentality. The long days of rigorous work were always made brighter by Mark's subtle and dark humor, for which I am deeply grateful.

Claire Baum has played a crucial role in fostering a positive and supportive lab culture. From organizing video game nights and hosting New Year's lab dinner parties, to playing Hanabi during lunch breaks and promoting lab safety, Claire consistently prioritizes the health and well-being of everyone in the lab. Her efforts have greatly contributed to creating a collaborative and enjoyable work environment.

Ash Kumar is the first postdoc on The Loadlock Experiment. His skills as a cold atom scientist are unparalleled, and his ability to assess and prioritize efforts in complex scientific environments has been incredibly educational. I admire his work ethic, tenacity, and adaptability. Ash, your guidance has helped me sharpen my questions, seek answers independently, and maintain confidence. I am grateful for your support, and I wish you

continued success in your scientific journey.

Danial Shadmany and **Anna Soper**, who joined the Loadlock Experiment recently, have both made invaluable contributions to the project already. I wish them both continued success in their scientific careers and eagerly look forward to seeing where the future of the experiment leads.

Lukas Palm, a true polymath and remarkable conversationalist, brought a stabilizing presence to the lab. Lukas's technical expertise, ability to make sound decisions, and collaborative spirit were invaluable. His sensitivity to safety and security concerns and his willingness to share knowledge and experiences made him an exceptional colleague. Lukas, I will greatly miss our discussions including those involving cooking recipes, and your calming influence in the lab.

I would like to express my heartfelt gratitude to my **close friends** for being an incredible source of support and encouragement throughout this journey. Your companionship, laughter, and understanding made the challenging times bearable and the good times even better. Whether it was offering a listening ear, sharing a meal, being there when I needed it most, or joining in on climbing expeditions, running competitions, biking adventures, sailing sessions, folding origami, visiting jazz clubs, or comedy rehearsals, each moment of your friendship has been invaluable. I am truly fortunate to have you all in my life and cannot thank you enough for the joy you've brought into these years.

Finally, I extend my deepest gratitude to my loving partner, **Saul**, and my supportive **parents**. Saul, you have shown me that mixed martial arts (MMA) and experimental physics are not so different after all. Your unwavering confidence, exceptional patience, and boundless kindness have been my source of strength, guiding me through the tunnel and helping me emerge as a better person. Life has thrown so many dark clouds our way, but your steadfast positivity has always been my silver lining. Mom, your example of strength, intelligence, and professionalism has been my guiding light. You've taught me the value of

hard work and the importance of effort over outcome. Dad, your dedication to our family and your remarkable athleticism have been a constant inspiration throughout this journey. I hope this work, along with my future endeavors, makes all of you proud as we embark on a new chapter in life together.

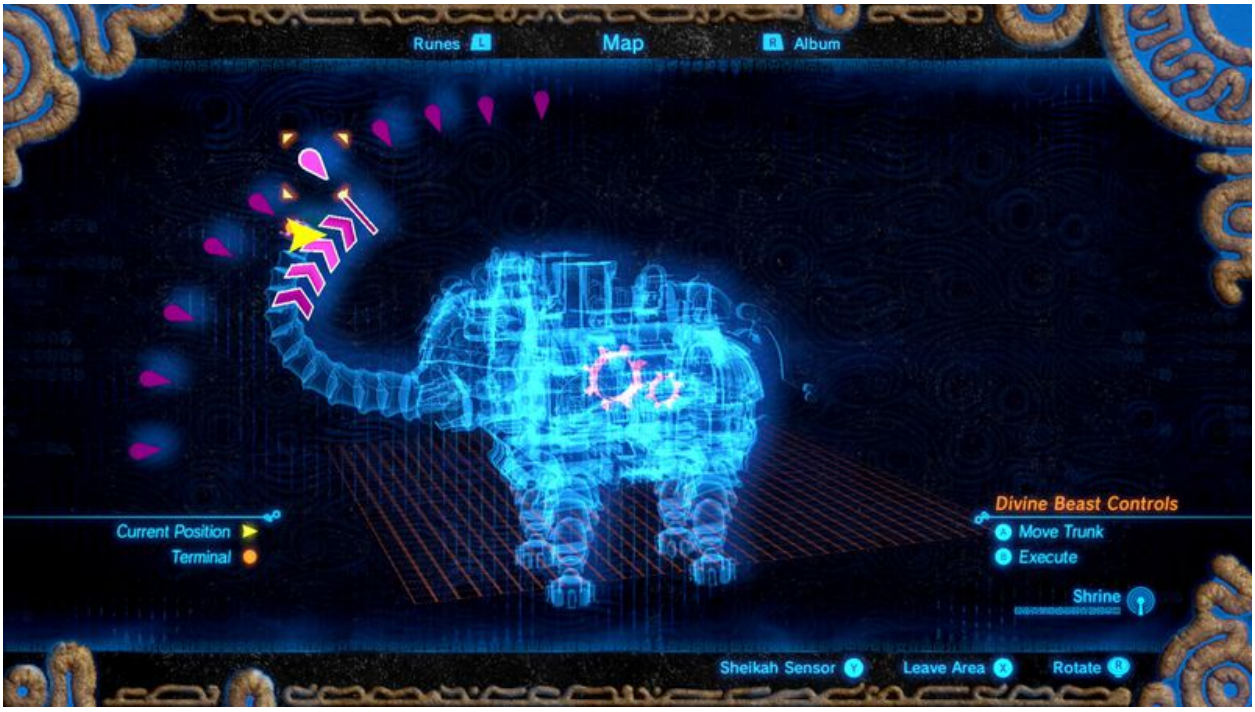

Figure 1: Spoiler alert: Vah Ruta, from The Legend of Zelda: Breath of the Wild. The Divine Beast.

CHAPTER 1

OVERVIEW OF THE THESIS

This PhD thesis presents the design, development, and implementation of a loadlock platform tailored for next-generation quantum optics experiments. Quantum optics, a field at the forefront of both fundamental research and technological innovation, relies heavily on precise control over light-matter interactions. To advance this field, the thesis provides a comprehensive exploration of the theoretical and experimental foundations of quantum optics, followed by a detailed examination of the loadlock platform's role in enhancing experimental capabilities. The thesis is structured into several key parts:

Part I: Theory of Classical Optics. This part of the thesis provides a comprehensive exploration of classical optics, starting with the fundamental principles of ray optics (Chp. 2). The concept of paraxial rays is introduced (Sec. 2.1), which simplifies the analysis of optical systems by assuming small angles of incidence. This is followed by the ABCD matrix formalism (Sec. 2.2), which offers a powerful tool for analyzing the propagation of light through a sequence of optical elements. The study then progresses to Gaussian beams (Chp. 3), where the paraxial wave equation is derived (Sec. 3.1) as the foundation for understanding Gaussian beam propagation. The properties of Gaussian beams are studied (Sec. 3.2), highlighting their importance in optical systems. The ABCD law is revisited (Sec. 3.3), specifically applied to Gaussian beams, bridging the gap between ray optics and wave optics. The part concludes with an in-depth analysis of Fabry-Perot cavities (Chp. 4), covering key aspects such as the resonance condition (Sec. 4.1), finesse (Sec. 4.2), and cavity transmission (Sec. 4.3). The stability of optical resonators is discussed (Sec. 4.4), followed by an examination of Gaussian modes (Sec. 4.5) and Hermite-Gaussian modes (Sec. 4.6), which are critical for understanding the behavior of light within these cavities.

Part II: Theory of Atom Optics. This part shifts focus to the interaction between atoms and light, a central theme in atom optics. It begins with a detailed analysis of the

two-level atom (Chp. 5), which serves as a model for understanding atom–field interactions. The fundamental interaction between atoms and electromagnetic fields is explored (Sec. 5.1), leading to phenomena such as Rabi flopping (Sec. 5.2), which is crucial for understanding coherent dynamics in atom optics. The concept of dressed states is introduced (Sec. 5.3), providing deeper insight into the energy structure of atoms in the presence of light fields. The theoretical foundation laid in Chp. 5 is then extended to specific forces in atom optics (Chp. 6). The dipole force (Sec. 6.1) and the radiation pressure (Sec. 6.2), two key concepts of atom cooling and trapping, are both explored. Practical applications of these theoretical concepts are explored (Chp. 7), where examples such as dipole traps (Sec. 7.1), magneto-optical traps (MOTs) (Sec. 7.2), and saturation absorption spectroscopy (Sec. 7.3) are presented. These examples illustrate the real-world applications of atom optics theory, demonstrating how light can be used to control and manipulate atomic systems.

Part III: Theory of Quantum Optics. This part of the thesis delves into the quantum mechanical aspects of light-matter interactions, particularly within the framework of cavity quantum electrodynamics (cQED) (Chp. 8). The Jaynes–Cummings model is a cornerstone of cQED (Sec. 8.1), providing a quantum description of the interaction between a single atom and a single mode of the electromagnetic field. Various modifications to this model are discussed (Sec. 8.2), accommodating more complex physical situations and extending the applicability of cQED theory. The Purcell effect (Sec. 8.3), is another crucial concept, illustrating how the spontaneous emission rate of an atom can be significantly enhanced by the presence of a resonant cavity. The study of spontaneous emission continues (Chp. 9), beginning with Fermi's golden rule (Sec. 9.1), which governs the transition rates in quantum systems. The density of states (Sec. 9.2) is discussed, a concept that plays a pivotal role in determining the emission characteristics of quantum systems. Finally, a detailed analysis of the spontaneous emission rate (Sec. 9.3) is presented, tying together the quantum mechanical principles that govern light emission in these systems. This part of the thesis integrates the

classical and atom optics foundations established in the earlier parts, offering a cohesive understanding of quantum optics and its applications in modern physics.

Part IV: Experimental Quantum Optics. This part focuses on the practical realization of advanced quantum optics experiments, with an emphasis on innovative techniques and setups. It begins with two feasibility assessment projects I undertook during my first year, which, despite yielding results that fell short of our expectations, provided critical insights and laid the groundwork for the design of high-NA and confocal cavities. The first project involves a detailed exploration of methods to suppress spontaneous emission using a high-NA cavity (Chp. 10), addressing a key challenge in quantum optics. The second project investigates the enhancement of Rydberg coupling using a confocal cavity (Chp. 11), examining how this configuration can strengthen interactions between Rydberg atoms, an essential component in quantum information processing. Both chapters discuss the experimental design, setup, and outcomes, highlighting both the potential and limitations in achieving the scientific objectives.

The centerpiece of this part is the development of a loadlock platform designed for next-generation quantum optics experiments (Chp. 12). The chapter begins with an overview of the research landscape involving cavities in vacuum and introduces the challenges of integrating and testing exotic cavity geometries with cold atoms (Sec. 12.1), which underscores the need for a loadlock apparatus to optimize turnaround time for cold atom cavity QED experiments. The innovative loadlock technique is then introduced (Sec. 12.2), detailing how it enables efficient loading and unloading of samples while maintaining vacuum integrity. This is followed by a high-level description of the ultra-high vacuum (UHV) system and its components (Sec. 12.3). The assembly and integration of the entire UHV system with the loadlock are outlined (Sec. 12.4), including a step-by-step account of assembling the bare UHV system (Sec. 12.5), and its operation and maintenance (Sec. 12.6). Finally, the performance of the UHV system with the loadlock is evaluated (Sec. 12.7), focusing on its stability

and suitability for quantum optics experiments.

The thesis then delves into critical components, such as the cavity carrier, feedthrough, and translator (Chp. 13). The design and components of the cavity carrier is described (Sec. 13.2), followed by the assembly and integration of the translator with the cavity carrier (Sec. 13.3). The feedthrough system's design is covered (Sec. 13.4), followed by its integration into the UHV system (Sec. 13.5), and an assessment of the system's stability (Sec. 13.6).

The magneto-optical trap (MOT) setup is then discussed (Chp. 14). The chapter starts with the in-vacuum MOT design (Sec. 14.2) and the integration of the science chamber with this setup (Sec. 14.3). The generation of cooling beams using outside-vacuum optics (Sec. 14.4) and the use of outside-vacuum bias magnetic coils for field correction (Sec. 14.5) are then described. The optimization and electronics control of the MOT system are then detailed (Sec. 14.6), including the laser lockbox, fast laser feedback, and coil driver. The characterization of the atom source is presented (Sec. 14.7), which serves as a benchmark that the MOT system operates successfully.

The final chapter in this part (Chp. 15) introduces the concept of an atomic conveyor belt, a novel mechanism for transporting atoms within the experimental setup. The design and construction of this conveyor belt is covered (Sec. 15.2), followed by its physical implementation within the broader experimental framework (Sec. 15.3). The performance and characterization of the atomic conveyor belt are discussed (Sec. 15.4), highlighting its effectiveness in manipulating atomic positions with precision.

Appendices. This part provides supplementary materials, including mechanical drawings and technical specifications that support the experimental work described in the thesis.

This thesis not only advances the technical infrastructure for quantum optics experiments but also contributes to the broader understanding of light-matter interactions, paving the way for new discoveries and applications in the field.

Part I

Theory of Classical Optics

CHAPTER 2

RAY OPTICS

Ray optics, also known as **geometrical optics**, is the simplest theory of optics. The fundamental assumption behind ray optics is that light travels in the form of rays. This theory simplifies the understanding of how light interacts with objects and materials. In most situations—where the wavelength of light is much smaller than the objects involved—ray optics describes the behavior of light accurately. In other situations—where the wave-like behavior of light manifests itself more strongly, and therefore would be better described by the theory of **wave optics**—ray optics still provides good intuitions for the more complex behavior of optical waves [1].

We assume that the optical media the optical rays propagate in are lossless, and can be completely characterized by their **index of refraction** n. The effect of the refractive index is that it changes the speed of light to c_0/n, where c_0 is the vacuum speed of light. For most media existed in nature, n is strictly greater than 1.

The fundamental principle of ray optics is the **Fermat's Principle**, also referred to as the "Principle of Least Time", which states that optical rays traverse paths that minimize the **optical path length functional** l, such that the variation of l is zero:

$$\delta l = 0 \tag{2.1}$$

And the **optical path length** is defined as:

$$l[\boldsymbol{r}] := \int_0^d n(\boldsymbol{r})\, ds \tag{2.2}$$

where $\boldsymbol{r}(s)$ is a path inside an optical medium parameterized by the variable s, between two endpoints corresponding to $\boldsymbol{r}(0)$ and $\boldsymbol{r}(d)$.

By applying Fermat's principle under the proper mathematical framework, the **calculus**

of variations, we arrive at the following familiar results:

1. In a **Homogeneous Medium**, light travels in a straight line.

2. At a **plane mirror**, light bounces off the mirror such that the incident angle θ_i and the reflective angle θ_r are equal,

$$\theta_i = \theta_r \tag{2.3}$$

   which is the **Law of Reflection**.

3. At a **planar interface** between two optical media of different indices of refraction n_1 and n_2,

$$n_1 \sin\theta_1 = n_2 \sin\theta_2 \tag{2.4}$$

   which is the **Snell's Law**. If $n_1 > n_2$, there is a critical angle θ_c given by

$$\frac{n_1}{n_2} \sin\theta_c = 1 \tag{2.5}$$

   such that if $\theta_1 > \theta_c$ there is no transmitted ray, causing **total internal reflection**.

4. A **Spherical Mirror** focuses rays from an object at the center back to itself.

5. An **Elliptical Mirror** images an object at a **focus** A to the other focus A'.

6. A **Parabolic Mirror** collimates all rays starting at the focus A to be outgoing parallel rays. And reversely, it focuses all incoming parallel rays orthogonal to the directrix to the focus A.

2.1 Paraxial Rays

In the ray optics paradigm, a ray can be specified *completely* by a vector containing the displacement y from, and the direction θ relative to the **optical axis**—the reference axis

for optical propagation. If both the displacement y and the angle θ are small, the angle θ is approximately equivalent to the slope y' of the ray:

$$\begin{bmatrix} y \\ \theta \end{bmatrix} \approx \begin{bmatrix} y \\ y' \end{bmatrix} \tag{2.6}$$

We can regard an optical system as a *transformation* of ray vectors, from input vector (y_1, y_1') to output vector (y_2, y_2'), via a function $\boldsymbol{f}$ that characterizes the optical system,

$$\begin{bmatrix} y_2 \\ y_2' \end{bmatrix} = \boldsymbol{f} \begin{bmatrix} y_1 \\ y_1' \end{bmatrix} \tag{2.7}$$

Assume that y and y' are small, then we can Taylor-expand the function to lowest order in y_1 and y_1':

$$y_2 = f_1(y_1, y_1') = \left.\frac{\partial f_1}{\partial y_1}\right|_{y_1=y_1'=0} y_1 + \left.\frac{\partial f_1}{\partial y_1'}\right|_{y_1=y_1'=0} y_1' + \mathcal{O}(2) \tag{2.8}$$

$$y_2' = f_1(y_1, y_1') = \left.\frac{\partial f_2}{\partial y_1}\right|_{y_1=y_1'=0} y_1 + \left.\frac{\partial f_2}{\partial y_1'}\right|_{y_1=y_1'=0} y_1' + \mathcal{O}(2) \tag{2.9}$$

where $\mathcal{O}(2)$ represents all higher-order terms in y_1, y_1'.

In the **paraxial approximation**, we will ignore the quadratic terms and above, and model the optical system using only linear transformations. The transformation function can be collected as a matrix of derivatives, called the **transfer matrix**, that represents the optical system in the paraxial approximation, as detailed in the following section. The higher order corrections are treated in **aberration theory**.

2.2 ABCD Matrix

The general *linear* transformation of a two-dimensional ray in the paraxial approximation is a 2×2 matrix,

$$\begin{bmatrix} y_2 \\ y_2' \end{bmatrix} = \begin{bmatrix} A & B \\ C & D \end{bmatrix} \begin{bmatrix} y_1 \\ y_1' \end{bmatrix} \tag{2.10}$$

The matrix representing the optical system is called the "**ABCD matrix**". Below are a few fundamental matrices that can be derived from first principles.

1. **Free-Space Propagation**. The free-space propagation matrix is given by

$$\mathbf{M} = \begin{bmatrix} 1 & d \\ 0 & 1 \end{bmatrix} \tag{2.11}$$

   where d is the distance of propagation.

2. **Thin Lens**. The ABCD matrix for a thin lens is given by

$$\mathbf{M} = \begin{bmatrix} 1 & 0 \\ -\frac{1}{f} & 1 \end{bmatrix} \tag{2.12}$$

   where f is the focal length, and $f > 0$ for a convex lens, $f < 0$ for a concave lens.

3. **Plane Mirror**. The ABCD matrix for a plane mirror is given by

$$\mathbf{M} = \begin{bmatrix} 1 & 0 \\ 0 & 1 \end{bmatrix} \tag{2.13}$$

4. **Spherical Mirror**. The ABCD matrix for a spherical mirror is given by

$$\mathbf{M} = \begin{bmatrix} 1 & 0 \\ \frac{2}{R} & 1 \end{bmatrix} \tag{2.14}$$

where R is the radius of the spherical mirror. Note that in the paraxial approximation, a spherical mirror is equivalent to a thin lens with a focal length $f = -R/2$.

5. Planar Refractive Interface. The ABCD matrix for a planar refractive interface is given by

$$\mathbf{M} = \begin{bmatrix} 1 & 0 \\ 0 & n_1/n_2 \end{bmatrix} \tag{2.15}$$

where the ray travels from a medium with index of refraction n_1 to that of n_2.

6. Spherical Refractive Interface. The ABCD matrix for a thin lens is given by

$$\mathbf{M} = \begin{bmatrix} 1 & 0 \\ -\frac{n_2 - n_1}{n_2 R} & \frac{n_1}{n_2} \end{bmatrix} \tag{2.16}$$

where the ray travels from a medium with index of refraction n_1, through a refractive interface with radius R, into another medium with index of refraction n_2.

A *composite* optical system consists of more basic optical elements. The transfer matrix of a composite system is the *product* of individual transfer matrices,

$$\mathbf{M_{composite}} = \mathbf{M_n M_{n-1} ... M_2 M_1} \tag{2.17}$$

where $\mathbf{M}_1$ acts first on the input ray first.

CHAPTER 3

GAUSSIAN BEAMS

A Gaussian beam is the simplest model of a directed beam that satisfies Maxwell's equations. Simpler waves exist, such as the plane wave of the form, or spherical wave of the form, albeit trivial and somewhat unrealistic. The Gaussian beams are seen commonly in lasers or the outputs of spherical resonators.

3.1 Paraxial Wave Equation

A paraxial wave is a simplified version of a general wave. For a paraxial wave, the curves normal to the wave fronts are paraxial, and the wave itself stays close to the optical axis z. So, we can rewrite the scalar electric field as,

$$E(\mathbf{r}) = \psi(\mathbf{r})e^{ikz} \tag{3.1}$$

where ψ is the **envelope** and $\exp(ikz)$ is the **carrier wave**.

Plugging it into the wave equation, $(\nabla^2 + k^2)E = 0$, where $\nabla^2 = \frac{\partial^2}{\partial x^2} + \frac{\partial^2}{\partial y^2} + \frac{\partial^2}{\partial z^2}$, have,

$$\left(\nabla_T^2 + i2k\frac{\partial}{\partial z} + \frac{\partial^2}{\partial z^2}\right)\psi = 0 \tag{3.2}$$

where $\nabla_T^2 = \frac{\partial^2}{\partial x^2} + \frac{\partial^2}{\partial y^2}$ is the **transverse Laplacian**.

We can make a **slowly varying envelope approximation** if ψ varies slowly on the scale of λ, in which case $\partial\psi/\partial z \ll \psi/\lambda \sim k\psi$, and $\partial^2\psi/\partial z^2 \ll k\ \partial\psi/\partial z$, so we can drop the second order term and get the following **paraxial wave equation**:

$$\left(\nabla_T^2 + i2k\frac{\partial}{\partial z}\right)\psi = 0 \tag{3.3}$$

3.2 Gaussian Beams

The Gaussian beam satisfies the paraxial wave equation, and takes the form of,

$$E(\mathbf{r}) = E_0(\mathbf{r})\frac{w_0}{w(z)}\exp\left[-\frac{r^2}{w^2(z)}\right]\exp\left[ikz - i\tan^{-1}\left(\frac{z}{z_R}\right)\right]\exp\left[ik\frac{r^2}{2R(z)}\right] \tag{3.4}$$

which is the **Gaussian**, or $\mathbf{TEM}_{0,0}$ beam, where the transverse radial position is $r = \sqrt{x^2+y^2}$. The **beam waist parameter** w_0 is,

$$w_0 := \sqrt{\frac{\lambda z_R}{\pi}} \tag{3.5}$$

The **Rayleigh range** z_R is,

$$z_R = \frac{\pi w_0}{\lambda} \tag{3.6}$$

The **beam waist** $w(z)$ along the optical axis is,

$$w(z) := w_0\sqrt{1+\left(\frac{z}{z_R}\right)^2} \tag{3.7}$$

Evidently, the beam waist $w(z)$ forms a parabolic curve in z, achieving its minimum value w_0 at the focus at $z = 0$. Further dividing into two regimes, the near field and the far field, separated by the Rayleigh range z_R, we have

$$\begin{aligned} w(z) &\sim w_0 && \text{for } |z| \ll z_R \\ w(z) &\sim (w_0/z_R)z && \text{for } |z| \gg z_R \end{aligned} \tag{3.8}$$

In the far field, the beam propagates in a cone of half angle θ_0, where $\tan\theta_0 := w_0/z_R$. So, in the paraxial regime, the **far-field divergence half-angle** is,

$$\theta_0 \sim \frac{w_0}{z_R} = \frac{\lambda}{\pi w_0} \tag{3.9}$$

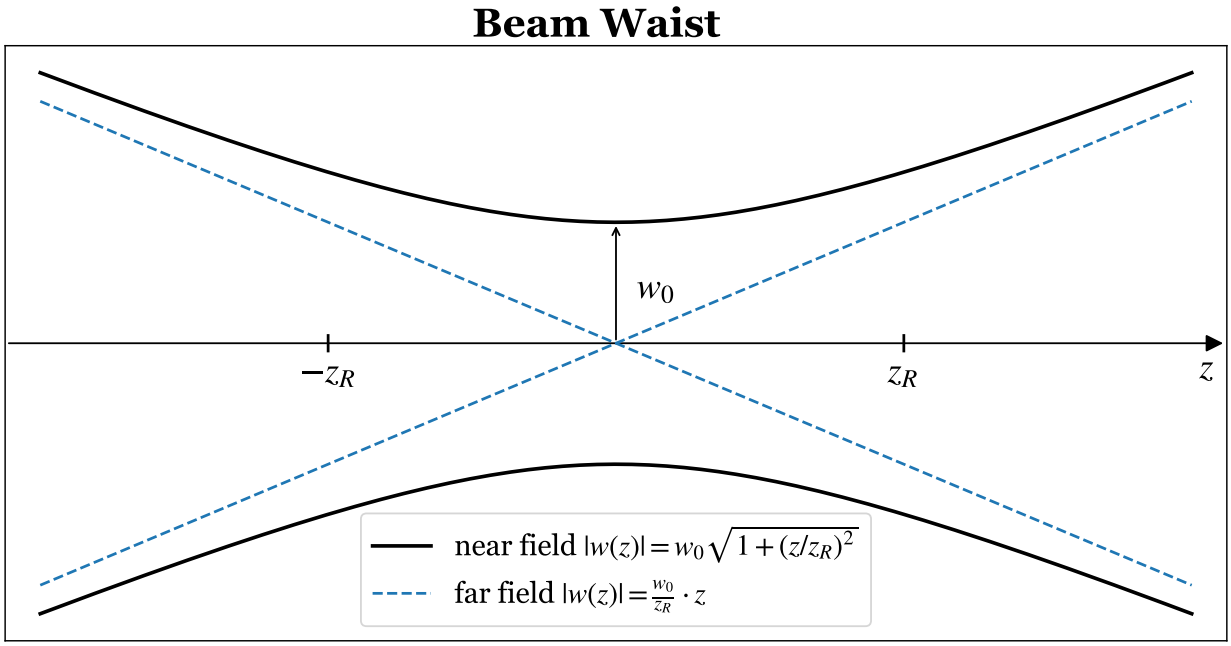

Figure 3.1: Beam waist as a function of propagation distance, in near-field exact form and far-field approximation.

The wave front **radius of curvature** is,

$$R(z) := z\left[1+\left(\frac{z}{z_R}\right)^2\right] \tag{3.10}$$

Breaking down the Gaussian beam solution term-by-term,

$$E(\mathbf{r}) = E_0(\mathbf{r})\frac{w_0}{w(z)}\exp\left[-\frac{r^2}{w^2(z)}\right] \times \exp\left[ikz - i\tan^{-1}\left(\frac{z}{z_R}\right)\right] \times \exp\left[ik\frac{r^2}{2R(z)}\right] \tag{3.11}$$

- The **amplitude factor**, $E_0(\mathbf{r})\frac{w_0}{w(z)}\exp\left[-\frac{r^2}{w^2(z)}\right]$, describes the intensity profile of the Gaussian beam, whereas the other two oscillating factors make no contribution on this front. The **intensity profile** of a Gaussian beam $I(r,z)$ is therefore

$$I(r,z) = I_0\left[\frac{w_0}{w(z)}\right]^2\exp\left[-\frac{2r^2}{w^2(z)}\right] \tag{3.12}$$

  which scales as the inverse square of the beam waist, and the profile in the radial direction follows a Gaussian function. Incidentally, we define the beam waist as the "$1/e^2$ radius" of the beam. The **total power** of the Gaussian beam is given by integrating the intensity over the transverse plane at any z,

$$P = \int_0^\infty I(r,z)2\pi r\,dr = \frac{I_0}{2}(\pi w_0^2) \tag{3.13}$$

  And we can rewrite the intensity profile as

$$I(r,z) = \frac{2P}{\pi w^2(z)}\exp\left[-\frac{2r^2}{w^2(z)}\right] \tag{3.14}$$

  For example, a circle of radius $R = w(z)$ contains $(e^2-1)/e^2$ fraction of the total power of a Gaussian beam.

- The **longitudinal phase factor**, $\exp\left[ikz - i\tan^{-1}\left(\frac{z}{z_R}\right)\right]$, includes the phase of a plane wave in the first term ikr, and the **Guoy phase shift** in the second term

$i \tan^{-1}\left(\frac{z}{z_R}\right)$. It represents a phase retardation relative to the plane wave, as in the generic case of focusing-beam-type solutions to the wave equation.

- The **radial phase factor**, $\exp\left[ik\frac{r^2}{2R(z)}\right]$, where $R(z) := z\left[1+\left(\frac{z}{z_R}\right)^2\right]$, represents how the radius of curvature changes with z for a Gaussian beam. Compare the phase of a Gaussian wave $\exp\left[ikz + ik\frac{r^2}{2R(z)}\right]$ without the Guoy phase shift, to the phase of a spherical wave $\exp[ikR]$, where $R = |\mathbf{r}| = \sqrt{r^2+z^2}$. In the paraxial regime $r \ll z$, have

$$\begin{aligned}
\text{phase}_{\text{spherical}} &= \exp[ikR] \\
&= \exp\left[ik\sqrt{r^2+z^2}\right] \\
&= \exp\left[ik|z|\sqrt{1+\frac{r^2}{z^2}}\right] \\
&\approx \exp\left[ik|z|\left(1+\frac{r^2}{2z^2}\right)\right] \\
&= \exp\left[ik|z| + ik\frac{r^2}{2|z|}\right] \\
&\approx \exp\left[ik|z| + ik\frac{r^2}{2R}\right] = \text{phase}_{\text{Gaussian}}
\end{aligned} \tag{3.15}$$

Furthermore, examining at the near field and the far field,

$$R(z) \sim \frac{z_R}{z} \qquad \text{for } |z| \ll z_R \tag{3.16}$$

$$R(z) \sim z \qquad \text{for } |z| \gg z_R \tag{3.17}$$

the Gaussian beam approaches a spherical wave in the far field.

3.3 ABCD Law

The ABCD Law is a simple method for propagating Gaussian beams, related to the *geometric optics* ABCD matrix for the optical system. Define a **complex q parameter** for a Gaussian beam by

$$q(z) := z - iz_R \tag{3.18}$$

Since q specifies both the spot size and the radius of curvature at a given location z, q completely specifies the Gaussian beam geometry. The inverse of q is computed to be

$$\frac{1}{q(z)} = \frac{1}{R(z)} + \frac{i\lambda}{\pi w^2(z)} \tag{3.19}$$

where $w_0 = \sqrt{\lambda z_R/\pi}$, $w(z) = w_0\sqrt{1+(z/z_R)^2}$, and $R(z) = z\left[1+(z/z_R)^2\right]$. The Gaussian beam can be rewritten in a simplified form,

$$E(\mathbf{r}) = E_0\frac{q_0}{q(z)}\exp\left[\frac{ikr^2}{2q(z)}\right]\exp(ikz) \tag{3.20}$$

Let q_1 and q_2 be the q parameters before and after an optical system specified by the geometrical optics ABCD matrix, respectively, then the **ABCD Law** is,

$$q_2 = \frac{Aq_1 + B}{Cq_1 + D} \tag{3.21}$$

CHAPTER 4

FABRY-PEROT CAVITIES

A **Fabry-Perot cavity** is a resonator consisting of two mirrors. The wave nature of light leads to interference between the incoming wave and the waves resonating within the cavity, resulting in a range of intriguing optical phenomena.

4.1 Resonance Condition

In a planar Fabry-Perot cavity of length d with ideal reflecting mirrors, a plane wave can only exist in the cavity if it returns to exactly the same phase after one round trip, leading to constructively interference with itself. This implies that,

$$2kd = 2\pi m \tag{4.1}$$

The allowed stationary waves, or **modes**, of the cavity must have wave numbers that satisfy

$$k_m = \frac{\pi m}{d} \tag{4.2}$$

Equivalently, the wavelength and frequencies must satisfy

$$\lambda_m = \frac{2d}{m}; \quad \nu_m = \frac{cm}{2d}; \quad \omega_m = \frac{\pi cm}{d} \tag{4.3}$$

The **free spectral range (FSR)** is the frequency spacing between allowed modes:

$$\text{FSR} := \nu_{m+1} - \nu_m = \frac{c}{2d} = \frac{c_0}{2nd} \tag{4.4}$$

where n is the index of refraction of the medium filling the cavity.

4.2 Finesse

However, a real cavity is imperfect and "leaky", with some loss of light on each round trip that dampens the amplitude of the electric field within the cavity. This loss can result from mirror transmission, aperture limitations due to finite-sized mirrors, scattering, heating, and other factors. Consequently, the resonances broaden, similar to a driven mechanical oscillator.

Suppose the amplitude of the wave is reduced by r after one round trip,

$$E_{n+1}^{(+)} = re^{i2kd} E_n^{(+)} \tag{4.5}$$

The total wave inside the cavity comprises the initial wave transmitted through the first mirror $E_0^{(+)}$, and all subsequent waves reflected off the two cavity mirrors. The phase change of a plane wave after one round trip is $\Delta\phi = 2kd$. Summing up all these contributions,

$$E^{(+)} = E_0^{(+)} + E_1^{(+)} + E_2^{(+)} + \cdots = E_0^{(+)} \left[1 + re^{i2kd} + (re^{i2kd})^2 + \cdots\right] = \frac{E_0^{(+)}}{1 - re^{i2kd}} \tag{4.6}$$

The total intensity inside the cavity is therefore

$$\begin{aligned} I &= \frac{I_0}{|1 - re^{i2kd}|^2} \\ &= \frac{I_0}{\left(1 - re^{i2kd}\right)\left(1 - re^{-i2kd}\right)} \\ &= \frac{I_0}{1 + r^2 - 2r\cos(2kd)} \\ &= \frac{I_0}{(1-r)^2 + 4r\sin^2(kd)} \end{aligned} \tag{4.7}$$

where $I_0 = \frac{1}{2}\epsilon_0 |E^{(+)}|^2 c$ is the initial intensity inside the cavity before any round trip is made. The maximum intensity is identified to be

$$I_{\max} := \frac{I_0}{(1-r)^2}. \tag{4.8}$$

Define **finesse** as a parameter that characterizes the loss of the cavity,

$$\mathcal{F} := \frac{\pi\sqrt{r}}{1-r}, \tag{4.9}$$

then we can rewrite the resonator intensity to be

$$I = \frac{I_{\max}}{1 + \left(\frac{2\mathcal{F}}{\pi}\right)^2 \sin^2(kd)} = \frac{I_{\max}}{1 + \left(\frac{2\mathcal{F}}{\pi}\right)^2 \sin^2\left(\frac{\pi\nu}{\mathrm{FSR}}\right)}. \tag{4.10}$$

To calculate the full width at half maximum (FWHM) of the resonances, we identify the frequencies where the intensity drops to $I_{\max}/2$. This corresponds to the denominator of Eq. 4.10 being equal to 2, i.e.

$$\left(\frac{2\mathcal{F}}{\pi}\right)^2 \sin^2\left(\frac{\pi\nu}{\mathrm{FSR}}\right) = 1 \tag{4.11}$$

$$\nu = \pm\frac{\mathrm{FSR}}{\pi} \sin^{-1}\left(\frac{\pi}{2\mathcal{F}}\right) \tag{4.12}$$

In the limit of large finesse, where the resonances are well resolved, the small angle approximation applies. Thus, the full width at half maximum of the resonance can be expressed as:

$$\delta\nu_{\mathrm{FWHM}} = \frac{\mathrm{FSR}}{\mathcal{F}} \tag{4.13}$$

4.3 Cavity Transmission

How does a Fabry-Perot cavity allow nearly all laser power to transmit through a nearly perfectly reflecting mirror by placing a second mirror at the right distance behind it? The answer lies in interference.

Suppose a Fabry-Perot cavity is made of a mirror (M_1) on the left and a mirror (M_2) on the right. Our previous discussion only concerned the light intensity inside the cavity,

whether it is the initial intensity I_0, or the total circulating intensity I. Now, denote the input intensity incident to the cavity as I_{in}, and the output intensity emitted from the cavity as I_{out}. Denote the field reflection and transmission coefficients for the two mirrors to be r_1, t_1 for M_1 and r_2, t_2 for M_2, respectively.

The output (transmitted) intensity is related to the intra-cavity intensity by

$$I_{\text{out}} = |t_2|^2 I, \tag{4.14}$$

and the input (incident) intensity is related to the initial intensity by

$$I_0 = |t_1|^2 I_{\text{in}}. \tag{4.15}$$

Thus, we can define the **cavity intensity transmission coefficient** T_{cav} by

$$T_{\text{cav}} := \frac{I_{\text{out}}}{I_{\text{in}}} = |t_1 t_2|^2 \frac{I}{I_0} = \frac{T_{\text{cav,max}}}{1 + \left(\frac{2\mathcal{F}}{\pi}\right)^2 \sin^2\left(\frac{\pi\nu}{\text{FSR}}\right)}, \tag{4.16}$$

where

$$T_{\text{cav,max}} := \frac{|t_1 t_2|^2}{(1 - r_1 r_2)^2}. \tag{4.17}$$

For a symmetrical cavity with identical mirrors, $r_1 = r_2 = r$ and $t_1 = t_2 = t$, then the maximum cavity transmission becomes

$$T_{\text{cav,max}} = \frac{|t^2|^2}{(1 - r^2)^2} = 1 \tag{4.18}$$

where the last equality comes from identifying $r^2 + t^2 = 1$ for a given mirror. In other words, a resonant symmetrical Fabry-Perot cavity transmits all the input light, independent of the transmission of each mirror.

4.4 Resonator Stability

To see whether a cavity is stable, is equivalent in asking if the resonator is able to confine the ray. Consider the ray after n round trips in the cavity,

$$\begin{bmatrix} y_n \\ y'_n \end{bmatrix} = \begin{bmatrix} A & B \\ C & D \end{bmatrix}^n \begin{bmatrix} y_0 \\ y'_0 \end{bmatrix} \tag{4.19}$$

In general, the characteristic polynomial for a 2×2 matrix can be written as,

$$\lambda^2 - \mathrm{Tr}(\mathbf{M})\lambda + \det(\mathbf{M}) = 0 \tag{4.20}$$

Since the matrix describes one round trip, the input and output are exactly at the same place, we also have,

$$\det(\mathbf{M}) = 1 \tag{4.21}$$

The eigenvalues of $\mathbf{M}$ are solutions of this polynomial, given by

$$\lambda_\pm = \beta \pm \sqrt{\beta^2 - 1} \tag{4.22}$$

where $\beta = \mathrm{Tr}(\mathbf{M})/2 = (A + D)/2$, and $\det(\mathbf{M}) = \lambda_+\lambda_-$. The eigenvectors of $\mathbf{M}$ satisfies

$$\mathbf{M} \begin{bmatrix} y_\pm \\ y'_\pm \end{bmatrix} = \lambda_\pm \begin{bmatrix} y_\pm \\ y'_\pm \end{bmatrix} \tag{4.23}$$

We can rewrite the initial condition vector in the basis of eigenvectors,

$$\begin{bmatrix} y_0 \\ y'_0 \end{bmatrix} = \alpha_+ \begin{bmatrix} y_+ \\ y'_+ \end{bmatrix} + \alpha_- \begin{bmatrix} y_- \\ y'_- \end{bmatrix} \tag{4.24}$$

So, after n passes in the cavity,

$$\begin{bmatrix} y_n \\ y'_n \end{bmatrix} = \mathbf{M}^n \begin{bmatrix} y_0 \\ y'_0 \end{bmatrix} = \alpha_+ \lambda_+^n \begin{bmatrix} y_+ \\ y'_+ \end{bmatrix} + \alpha_- \lambda_-^n \begin{bmatrix} y_- \\ y'_- \end{bmatrix} \tag{4.25}$$

Consider only the position y_n, have

$$y_n = (\alpha_+ y_+)\lambda_+^n + (\alpha_- y_-)\lambda_-^n \tag{4.26}$$

There are two distinct possibilities: either $|\beta| \leq 1$ or $|\beta| > 1$. First consider the case where $|\beta| > 1$, then according to Eq. 4.22, the eigenvectors $\lambda_\pm$ are real, in fact $|\lambda_+| > 1$ and $|\lambda_-| < 1$. So according to the solution Eq. 4.26, the first term of y_n is exponentially growing, and the second term of y_n is exponentially damping, therefore altogether $y_n \sim \lambda_+^n$ which is not bounded by above. This is the **unstable case**.

Now consider the case where $|\beta| \leq 1$, then according to Eq. 4.22, the eigenvectors $\lambda_\pm$ are complex,

$$\lambda_\pm = \beta \pm i\sqrt{1-\beta^2} \tag{4.27}$$

Furthermore, both eigenvalues have unit modulus,

$$|\lambda_\pm|^2 = \left(\beta \pm i\sqrt{1-\beta^2}\right)\left(\beta \mp i\sqrt{1-\beta^2}\right) = \beta^2 + (1-\beta^2) = 1 \tag{4.28}$$

Define $\phi = \cos^{-1}\beta$, have $\beta = \cos\phi$, $\sqrt{1-\beta^2} = \sin\phi$, and $\lambda_\pm = \exp(\pm i\phi)$, $\lambda_\pm^n = \exp(\pm in\phi)$, thus,

$$y_n = (\alpha_+ y_+)e^{in\phi} + (\alpha_- y_-)e^{-in\phi} = y_{\max}\sin(n\phi + \phi_0) \tag{4.29}$$

for some constants $y_{\max}$ and ϕ_0. This is the **stable case**.

Thus, the **stability condition** for the ray to be bounded by the resonator in the long

term is simply $|\beta| \leq 1$, or equivalently,

$$|\mathrm{Tr}(\mathbf{M})| := |A + D| \leq 2 \tag{4.30}$$

To analyze the stability condition more explicitly, consider a resonator composed of two concave spherical mirrors of spherical curvature R_1 and R_2 separated by a distance d. This is equivalent to a thin lens system with focal lengths $f_1 = |R_1/2|$ and $f_2 = |R_2/2|$. The cavity round-trip matrix is the product of two free propagation and two mirror reflections,

$$\begin{aligned}\mathbf{M} = \begin{bmatrix} A & B \\ C & D \end{bmatrix} &= \begin{bmatrix} 1 & 0 \\ -\frac{1}{f_1} & 1 \end{bmatrix} \begin{bmatrix} 1 & d \\ 0 & 1 \end{bmatrix} \begin{bmatrix} 1 & 0 \\ -\frac{1}{f_2} & 1 \end{bmatrix} \begin{bmatrix} 1 & d \\ 0 & 1 \end{bmatrix} \\ &= \begin{bmatrix} 1 - \frac{d}{f_2} & d\left(2 - \frac{d}{f_2}\right) \\ -\frac{1}{f_1} - \frac{1}{f_2} + \frac{d}{f_1 f_2} & \left(1 - \frac{d}{f_1}\right)\left(1 - \frac{d}{f_2}\right) - \frac{d}{f_1} \end{bmatrix}\end{aligned} \tag{4.31}$$

According to Eq. 4.30,

$$0 \leq \frac{A + D + 2}{4} \leq 1 \tag{4.32}$$

Plugging in expressions from Eq. 4.31,

$$0 \leq \left(1 - \frac{d}{2f_1}\right)\left(1 - \frac{d}{2f_2}\right) \leq 1 \tag{4.33}$$

The **stability parameters** g_1, g_2 are conventionally defined as,

$$g_{1,2} := \left(1 - \frac{d}{2f_{1,2}}\right) = \left(1 + \frac{d}{R_{1,2}}\right) \tag{4.34}$$

and the stability condition can be rewritten as,

$$0 \leq g_1 g_2 \leq 1 \tag{4.35}$$

Below are some of the most important types of resonators, and their stability parameters, illustrated in Fig. 4.1.

1. **Planar resonator**. $R_1 = R_2 = \infty$. $g_1 = g_2 = 1$.

2. **Confocal resonator**. The foci of the two spherical concave mirrors overlap, and the geometric center of each mirror is on the surface of the other one. $R_1 = R_2 = -d$. $g_1 = g_2 = 0$.

3. **Concentric resonator**. The geometric centers of the two spherical concave mirrors overlap at the middle of the spacing. $R_1 = R_2 = -d/2$. $g_1 = g_2 = -1$.

4. **Confocal-planar resonator**. $R_1 = -d, R_2 = \infty$. $g_1 = 0, g_2 = 1$.

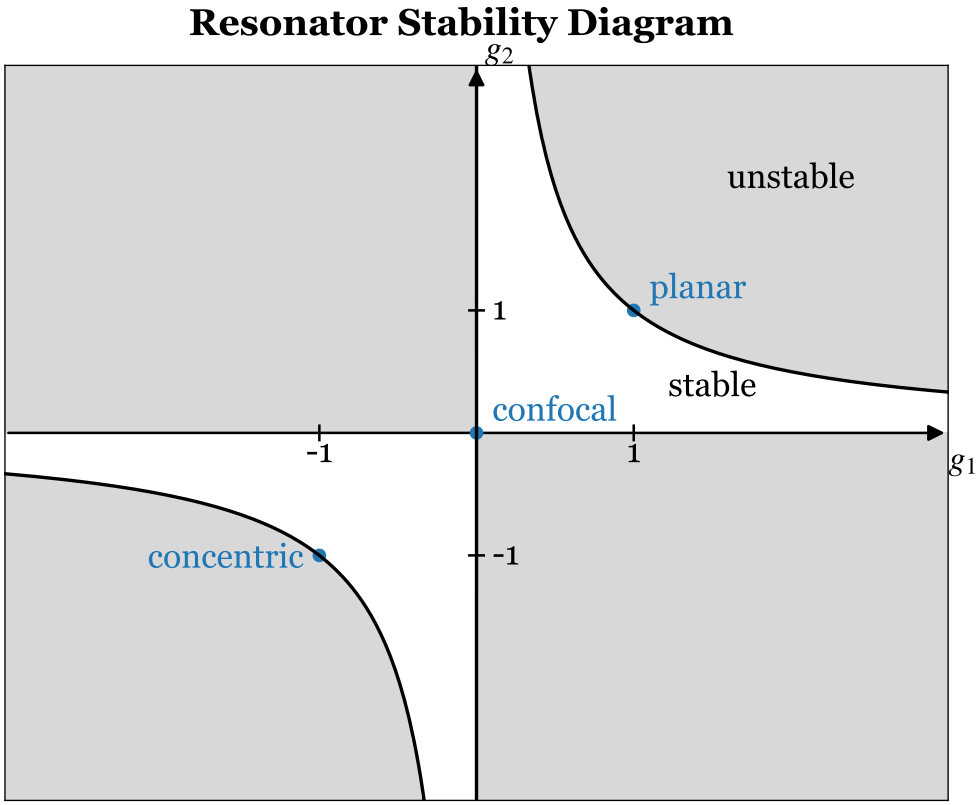

Figure 4.1: Beam stability diagram.

For a symmetrical cavity, the mirror curvatures are equal, and $g_1 = g_2 = g$. The focus occurs at the center of the cavity. The corresponding beam waist at the focus, and the beam waists at the mirrors (Eq. 4.41) can be rewritten as:

$$w_0^2 = \frac{\lambda d}{2\pi}\sqrt{\frac{1+g}{1-g}}$$
$$w_1^2 = w_2^2 = \frac{\lambda d}{\pi}\sqrt{\frac{1}{1-g^2}} \tag{4.36}$$

The dependence of beam waists on g, as it varies from -1 (concentric) to +1 (planar), is plotted in Fig. 4.2.

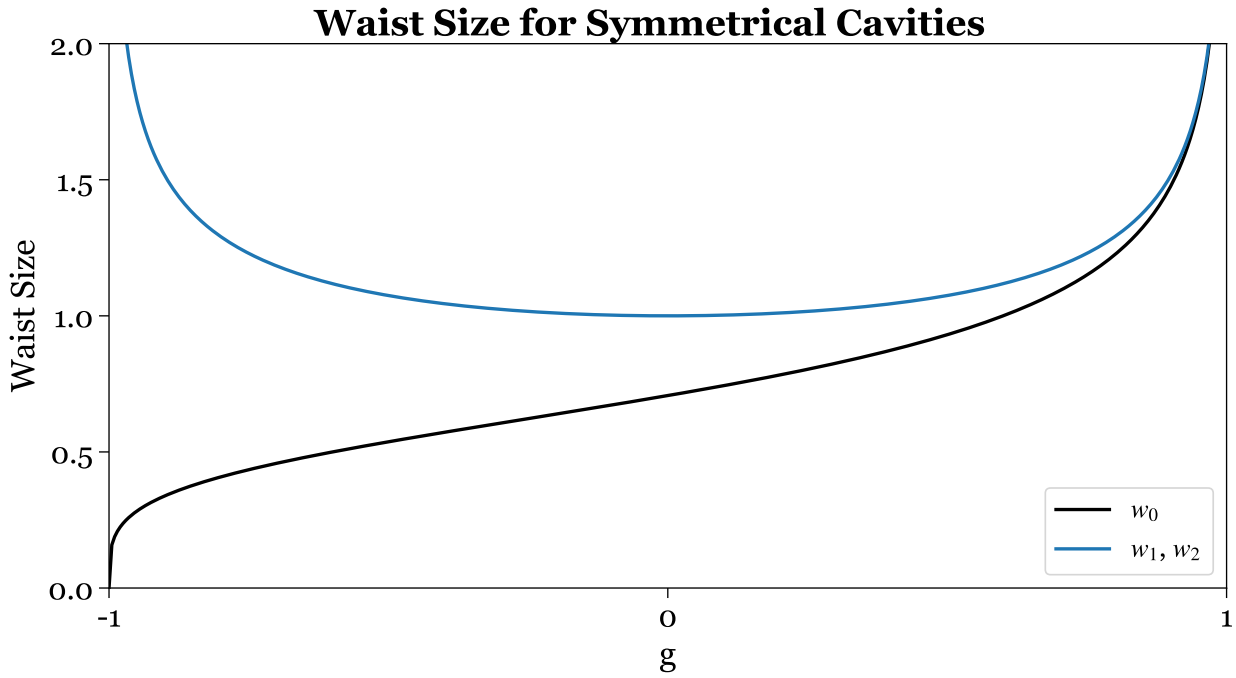

Figure 4.2: Beam waist w_0, as well as the beam waists w_1, w_2 at the mirror locations, as functions of g, for symmetrical cavities.

For a confocal cavity, the foci of the two mirrors overlap at the center of the cavity, and the geometric center of each mirror is not on the surface of the other one. With $R_1 = R_2 = -d$, $g_1 = g_2 = 0$, we have $w_1 = w_2 = \sqrt{2}w_0$. In fact, it can be shown that the confocal cavity has the smallest average waist size along its length compared to any other stable cavity.

Additionally, $z_R = d/2$, meaning each mirror is at a distance z_R from the focus. Tilting either mirror still leaves the center of curvature located on the other mirror's surface, merely displacing the optical axis of the cavity by a small amount. The confocal cavity is thus advantageous for optical designs where misalignment needs to be tolerated or leveraged, as we will see in later parts of this thesis.

4.5 Gaussian Modes

As dictated by Maxwell's equations, the electric field must vanish at the mirror boundaries. For a cavity composed of spherical mirrors, this requirement implies that the supported waves must have spherical wavefronts, making Gaussian beams a natural choice for cavity modes.

Consider a cavity consisting of mirror M_1 on the left with curvature R_1 and mirror M_2 on the right with curvature R_2, separated by a distance d. A Gaussian mode is supported within the cavity. Let w_0 be the minimum waist size of the Gaussian beam at $z = 0$, and let w_1 and w_2 be the waist sizes at the two mirrors located at z_1 and z_2, respectively. Since the curvature of the Gaussian beam must match with the curvature of the mirrors, following Eq. 3.10, we have

$$\begin{aligned} R(z_1) &= R_1 \\ R(z_2) &= -R_2 \end{aligned} \tag{4.37}$$

where the negative sign arises from a discrepancy between the ray-optics convention of radius of curvature and the Gaussian-beam convention of wavefront curvature. In the ray-optics convention, the radius of curvature is positive for a concave lens and a convex mirror, and vice versa. In contrast, in the Gaussian-beam convention, the wavefront curvature is positive to the right of the beam waist and negative to the left. So far, we have not made any

assumptions regarding the concavity of the two mirrors.

Solving the following system of equations

$$\begin{aligned} z_1\left[1+\left(\frac{z_1}{z_R}\right)^2\right] &= R_1 \\ z_2\left[1+\left(\frac{z_2}{z_R}\right)^2\right] &= -R_2 \\ z_2 - z_1 &= d \end{aligned} \tag{4.38}$$

for unknowns z_R, z_1, z_2, we arrive at the following solutions:

$$\begin{aligned} z_1 &= -\frac{d(R_2+d)}{R_1+R_2+2d} \\ z_2 &= \frac{d(R_1+d)}{R_1+R_2+2d} \\ z_R^2 &= -\frac{d(R_1+d)(R_2+d)(R_1+R_2+d)}{(R_1+R_2+2d)^2} \end{aligned} \tag{4.39}$$

For a symmetrical concave cavity, the mirror curvatures are equal $R_1 = R_2 = -R$ where $R > 0$. Then the above equations are simplified to:

$$\begin{aligned} z_1 &= -\frac{d}{2} \\ z_2 &= \frac{d}{2} \\ z_R^2 &= \frac{d}{2}\sqrt{\frac{2R}{d}-1} \end{aligned} \tag{4.40}$$

Using Eq. 3.5 to relate the beam waist parameter w_0 to the Rayleigh range w_R, and using the beam propagation formula (Eq. 3.7) to relate the beam waists at the mirrors w_1, w_2 to

beam waist parameter w_0, we arrive at

$$w_0^2 = \frac{\lambda d}{2\pi}\sqrt{\frac{2R}{d} - 1}$$
$$w_1^2 = w_2^2 = \frac{\lambda d}{\pi}\sqrt{\frac{1}{\left(\frac{d}{R}\right)\left(2 - \frac{d}{R}\right)}} \tag{4.41}$$

4.5.1 Resonance Frequencies

The total phase of a Gaussian beam, as given by Eq. 3.4, comprises two components: the phase associated with wavefront curvature and the longitudinal phase. Having previously examined phase matching with the mirror radius of curvature, we now focus on the longitudinal phase, which determines the resonance frequencies of the cavity.

$$\phi(r, z) = kz - \tan^{-1}\left(\frac{z}{z_R}\right) + k\frac{r^2}{2R(z)} \tag{4.42}$$

Consider the on-axis Guoy phase $\phi(0, z)$,

$$\phi(0, z) = kz - \tan^{-1}\left(\frac{z}{z_R}\right) \tag{4.43}$$

Suppose in a cavity of length d, the minimum waist size w_0 occurs at $z = 0$, and the waist sizes at the two mirrors located at z_1, z_2 are w_1, w_2, respectively. The round-trip phase can be expressed as

$$\phi_{\text{rt}} = 2[\phi(0, z_2) - \phi(0, z_1)] = 2k(z_2 - z_1) - 2\left[\tan^{-1}\left(\frac{z_2}{z_R}\right) - \tan^{-1}\left(\frac{z_1}{z_R}\right)\right] \tag{4.44}$$

For the field within the cavity to build up through constructive interference, the total phase accumulated over a round trip must satisfy $\phi_{\text{rt}} = 2\pi q$, where q is an integer. Using the

relations that $\nu_q = 2\pi k_q/c$ and $\text{FSR} = c/2d$, the **resonance frequencies** are

$$\nu_q = \text{FSR}\left\{q + \frac{1}{\pi}\left[\tan^{-1}\left(\frac{z_2}{z_R}\right) - \tan^{-1}\left(\frac{z_1}{z_R}\right)\right]\right\} \tag{4.45}$$

Plugging in expressions of z_1, z_2 and z_R in Eq. 4.39, the expression can be simplified to:

$$\nu_q = \text{FSR}\left(q + \frac{1}{\pi}\cos^{-1}\sqrt{g_1 g_2}\right) \tag{4.46}$$

4.6 Hermite-Gaussian Modes

If axial symmetry is not assumed, a complete set of properly normalized high-order solutions to the paraxial equation can be obtained, namely the **Hermite-Gaussian modes**, also known as **TEM$_{l,m}$ modes**. These beams are mathematically equivalent to the eigenfunctions of the quantum harmonic oscillator, forming a complete set. Consequently, any beam can be represented as a linear combination of Hermite-Gaussian modes.

The general form of the Hermite-Gaussian mode can be written in terms of a simple Gaussian beam, with key differences including the presence of Hermite polynomials $H_n(z)$, a normalization factor ensuring convergence and consistent total beam power for any combination of l and m, and a factor of $(1 + l + m)$ in the Guoy phase.

Hermite polynomials are n-degree polynomials with n zeros on the real axis. For example, $H_0(z) = 1$, $H_1(z) = 2z$, $H_2(z) = 2(2z^2 - 1)$, just to name a few. The explicit formula for the Hermite polynomial is

$$H_n(z) = (-1)^n e^{z^2}\frac{d^n}{dz^n}e^{-z^2} \tag{4.47}$$

For $l = m = 0$, the Hermite-Gaussian beam reduces to the Gaussian beam, also known as the TEM$_{0,0}$ beam. The intensity pattern of TEM$_{l,m}$ modes features l dark bands across the x-direction and m dark bands across the y-direction, or a grid of $(l + 1)$ bright spots in

the x-direction and $(m+1)$ in the y-direction.

$$E_{l,m}^{(+)}(\mathbf{r}) = E_0^{(+)} \frac{w_0}{w(z)} \sqrt{\frac{1}{2^{l+m} l! m!}} H_l\left[\frac{\sqrt{2}\,x}{w(z)}\right] H_m\left[\frac{\sqrt{2}\,y}{w(z)}\right] \times \exp\left[-\frac{r^2}{w^2(z)}\right] \exp\left[ikz - i(1+l+m)\tan^{-1}\left(\frac{z}{z_R}\right)\right] \exp\left[ik\frac{r^2}{2R(z)}\right] \tag{4.48}$$

Using the complex q parameter as before, the field in one transverse direction can also be expressed as follows:

$$E_l^{(+)}(x,z) = E_0^{(+)} \left(\frac{2}{\pi}\right)^{1/4} \sqrt{\frac{1}{2^l l! w_0}} \sqrt{\frac{q_0}{q(z)}} \left[\frac{q_0}{q_0^*}\frac{q^*(z)}{q(z)}\right]^{l/2} H_l\left(\frac{\sqrt{2}x}{w(z)}\right) \exp\left[-i\frac{kx^2}{2q(z)}\right] \tag{4.49}$$

The two expressions are equivalent and can be converted into one another using Euler's formula $e^{i\theta} = \cos\theta + i\sin\theta$, and identifying $\tan\theta = z/z_R$.

When considering higher-order modes, the effective beam waist at the waist (i.e., at $z = 0$) is modified by the mode numbers l and m:

$$w_{\text{eff}} = w_0\sqrt{1+l+m} \tag{4.50}$$

Hermite-Gaussian beams maintain their intensity patterns during propagation, similar to Gaussian beams, and exhibit the same far-field divergence characteristics. Higher-order modes are wider for the same w_0. Hermite-Gaussian beams also adhere to the same transformation rules, including the ABCD law. The beam intensity profile of the lowest few Hermite-Gaussian modes is plotted in Fig. 4.3, and an example higher-order mode of $l = 100$ is plotted in Fig. 4.4. The beam width as a function of mode number are plotted in Fig. 4.5.

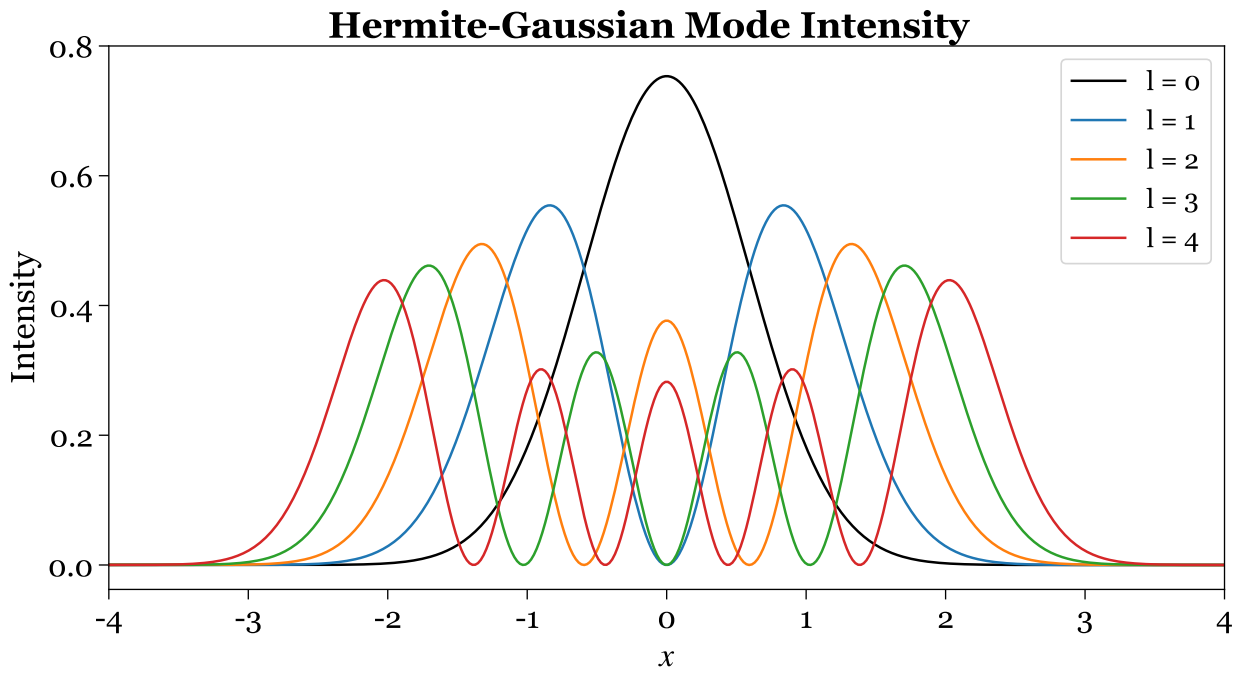

Figure 4.3: Hermite-Gaussian mode intensity as a function of transverse location, for the lowest order modes.

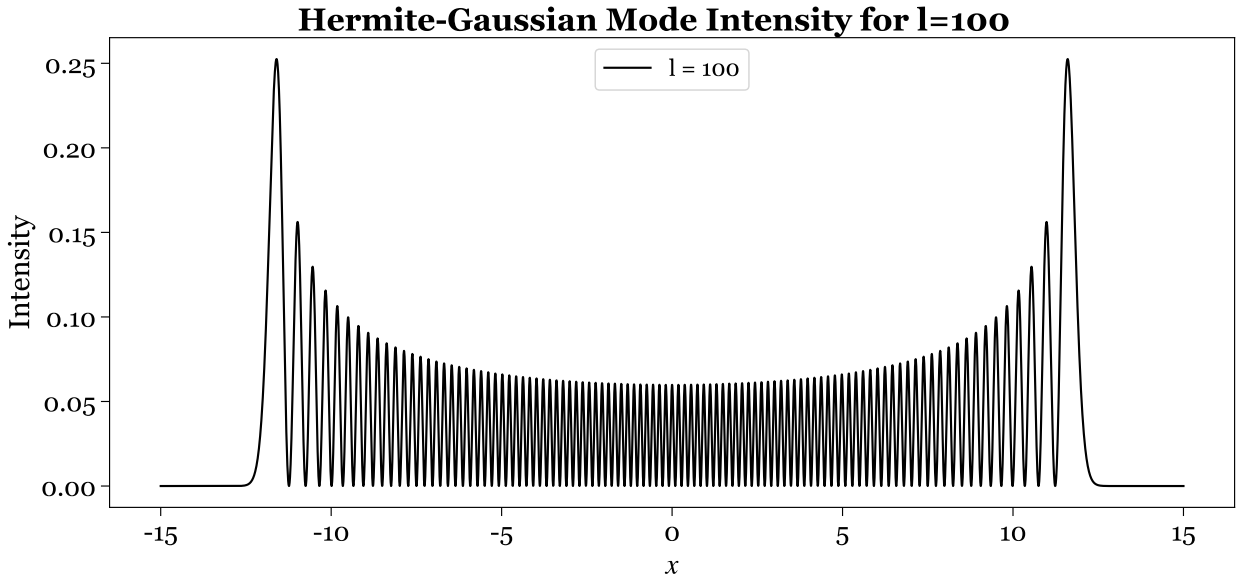

Figure 4.4: Hermite-Gaussian mode intensity as a function of transverse location, for mode $l = 100$.

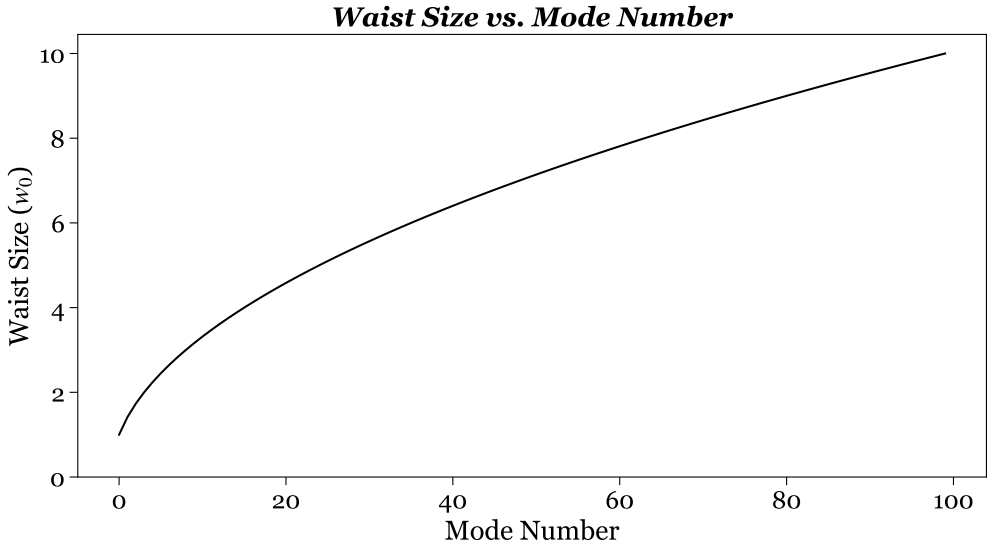

Figure 4.5: Effective waist size as a function of mode number for Hermite-Gaussian modes.

4.6.1 Resonance Frequencies

The total phase of a higher-order Hermite-Gaussian mode, is similar to that of a Gaussian mode, with an extra factor in front of the Guoy term. The on-axis Guoy phase $\phi_{l,m}(0,z)$ is given by

$$\phi_{l,m}(0,z) = kz - (1+l+m)\tan^{-1}\left(\frac{z}{z_R}\right) \tag{4.51}$$

The resonance frequencies are given by

$$\nu_{l,m,q} = (\text{FSR})\left(q + \frac{1}{\pi}(1+l+m)\cos^{-1}\sqrt{g_1 g_2}\right) \tag{4.52}$$

As shown above, the cavity modes must be labeled by three indices. The terminology distinguishes between longitudinal and transverse modes. Modes corresponding to different q values are the **longitudinal modes**, which are structurally similar to plane-wave resonances. Modes corresponding to different l and m values are the **transverse modes**, characterized by different transverse intensity patterns. Due to the axial symmetry of the resonator, there are several degeneracies among these modes. For example, $lm = 01$ mode is degenerate with

$lm = 10$ mode, and $lm = 02, 11, 20$ modes are all degenerate with each other. The transverse mode frequencies for near-planar, confocal, and near-concentric cavities are plotted in Fig. 4.6.

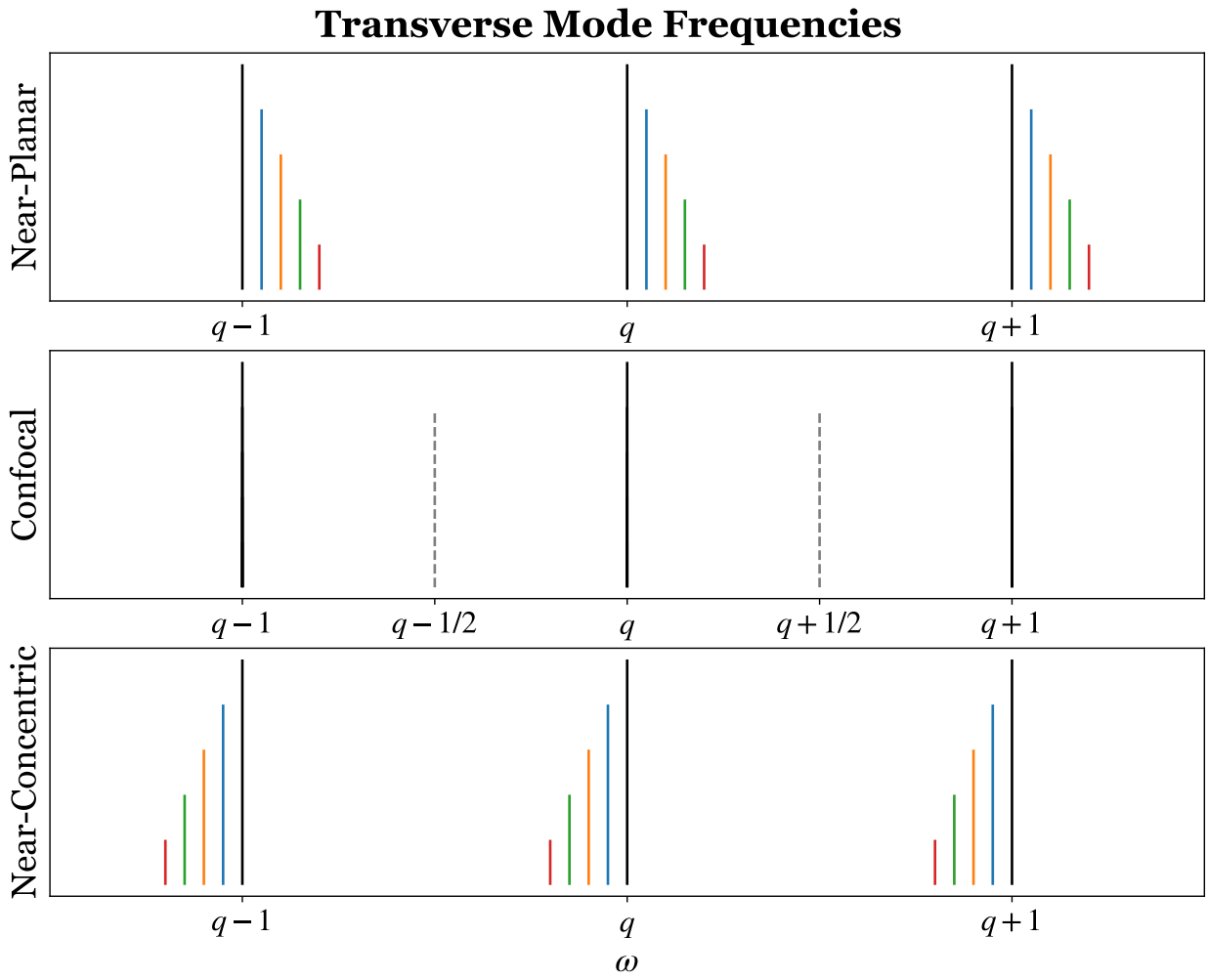

Figure 4.6: Transverse mode frequencies for different cavity types, e.g. near-planar, confocal, and near-concentric cavities. The longitudinal modes are indexed by q, and the transverse modes are color-coded, with the relative intensities indicated by their heights.

For a confocal cavity, $g_1 = g_2 = 0$, and therefore $g_1 g_2 = 0$ and $\cos^{-1}\sqrt{g_1 g_2} = \pi/2$. Then, the expression for resonance frequencies in Eq. 4.52 becomes much simpler:

$$\nu_{l,m,q\ \text{(confocal)}} = (\text{FSR})\left(q + \frac{1}{2}(1 + l + m)\right) \tag{4.53}$$

Alternatively, we can define an effective index s such that

$$\nu_{s\ (\text{confocal})} = (\text{FSR}_{\text{confocal}}) \cdot s \tag{4.54}$$

where $s = 2q + 1 + l + m$ is a positive integer, and

$$\text{FSR}_{\text{confocal}} := \frac{\text{FSR}}{2} = \frac{c}{4d} \tag{4.55}$$

is the effective free spectral range for the confocal cavity. This results in a spectrum similar to a planar cavity but with an effective length of $2d$. The confocal cavity's trajectory involves 4 passes per round trip, effectively doubling its length compared to a planar cavity, causing off-axis modes to travel twice as far before repeating. Therefore, the modes of confocal cavities fall into two frequency resonance series based on whether s is even or odd, as shown in the middle panel of Fig. 4.6.

This analysis holds only if several transverse modes are excited by the input source. If only the $lm = 00$ mode is present, the free spectral range reverts to its original value, FSR, instead of $\text{FSR}_{\text{confocal}}$. As we will discuss in later experimental chapters, to achieve confocality, the input beam to a confocal cavity is typically slightly misaligned so the cavity is operating in the "ring mode". When the input beam is adjusted to populate only the $lm = 00$ mode, all even modes become degenerate and overlap, while all odd modes become degenerate and disappear, restoring the original free spectral range. However, in ring mode, the finesse changes because the line width remains the same while the free spectral range is halved, resulting in $\mathcal{F}_{\text{confocal}} = \mathcal{F}/2$.

Part II

Theory of Atom Optics

CHAPTER 5

TWO-LEVEL ATOM

The interaction of a two-level atom with a classical field is a fundamental model in quantum optics. This model treats the atom quantum mechanically, accounting for quantum coherence between the two levels. Quantum coherence, a fundamental property of a quantum system in a superposition of states, ensures that there are well-defined relative phases between the different states in the superposition [2].

5.1 Atom–Field Interaction

The electric field $E(t)$ generated by a monochromatic laser with angular frequency ω can be described as:

$$\mathbf{E}(t) = \hat{\varepsilon} E_0 \cos(\omega t) \tag{5.1}$$

where E_0 is the amplitude of the electric field and ϕ is the phase. We can decompose the electric field $E(t)$ into its positive- and negative-rotating components using the trigonometric identity:

$$\cos(\omega t) = \frac{1}{2}\left(e^{i\omega t} + e^{-i\omega t}\right) \tag{5.2}$$

Thus, the electric field $E(t)$ can be written as:

$$\mathbf{E}(t) = \hat{\varepsilon}\frac{E_0}{2}\left(e^{i\omega t} + e^{-i\omega t}\right) := \mathbf{E}_0^{(+)} e^{-i\omega t} + \mathbf{E}_0^{(-)} e^{i\omega t} \tag{5.3}$$

In reality, an atom has infinitely many bound states, so the two-level approximation ($|g\rangle$ for the ground state and $|e\rangle$ for the excited state) simplifies the analysis. The resonant frequency is ω_0, and the **detuning** of the laser field from this resonance is $\Delta = \omega - \omega_0$. This approximation is valid for near-resonant interactions, where $\Delta \ll \omega_0$, making transitions to other levels negligible.

The **total Hamiltonian** for the two-level system in the presence of the classical field, taking into account the quantum coherence between the two levels, can then be written as:

$$H = H_{\mathrm{A}} + H_{\mathrm{AF}} \tag{5.4}$$

where H_{A} is the unperturbed Hamiltonian of the two-level atom and H_{AF} represents the atom-field interaction which accounts for the quantum coherence.

Given the application of the **dipole approximation**, we neglect the spatial variation of the field and consider only its value at the location of the atom. This approximation is justified because the optical wavelengths involved (several hundred nanometers) are much larger than the atomic scale (angstroms). Under the dipole approximation, the **atom-field interaction Hamiltonian** can be expressed as:

$$H_{\mathrm{AF}} = -\mathbf{d} \cdot \mathbf{E} \tag{5.5}$$

where $\mathbf{d}$ is the atomic dipole operator given in terms of the atomic electron position $\mathbf{r}_e$ and the electron charge e as:

$$\mathbf{d} = -e\mathbf{r}_e \tag{5.6}$$

The **atomic Hamiltonian** is

$$H_{\mathrm{A}} = \hbar\omega_0 \left|e\right\rangle \left\langle e\right| \tag{5.7}$$

By using a parity argument when evaluating the wave function integral for the position operator, we find that $\langle a|\mathbf{r}_e|b\rangle = 0$. Consequently, the diagonal matrix elements of the dipole operator $\mathbf{d}$ must vanish:

$$\langle g|\mathbf{d}|g\rangle = \langle e|\mathbf{d}|e\rangle = 0 \tag{5.8}$$

However, the off-diagonal elements $\langle g|\mathbf{d}|e\rangle$ can be non-zero if the states $|g\rangle$ and $|e\rangle$ have

opposite parity. Therefore, the dipole operator $\mathbf{d}$ can be written as:

$$\mathbf{d} = \langle g|\mathbf{d}|e\rangle(\sigma + \sigma^\dagger) \tag{5.9}$$

where $\sigma := |g\rangle\langle e|$ is the **atomic lowering operator**, and $\sigma^\dagger = |e\rangle\langle g|$ is the atomic raising operator. The total atom-field Hamiltonian is then:

$$H = H_{\mathrm{A}} + H_{\mathrm{AF}} = \hbar\omega_0\sigma^\dagger\sigma - \langle g|\mathbf{d}|e\rangle \cdot \mathbf{E}(\sigma + \sigma^\dagger) \tag{5.10}$$

We can similarly decompose the dipole operator into positive- and negative-rotating parts: $\mathbf{d} = \langle g|\mathbf{d}|e\rangle(\sigma + \sigma^\dagger) = \mathbf{d}^{(+)} + \mathbf{d}^{(-)}$, where $\mathbf{d}^{(+)} \sim \sigma$ and $\mathbf{d}^{(-)} \sim \sigma^\dagger$. This is because σ a time dependence of $e^{-i\omega_0 t}$. Including the same decomposition of the field, the atom-field Hamiltonian shows that the rapidly oscillating terms with a time dependence of $e^{-i(\omega_0+\omega)t}$ can be neglected using the **rotating-wave approximation** (RWA, to be distinguished from rotating-frame approximation which will be discussed later), focusing on the slowly varying terms. The RWA is valid under the condition that the detuning is much smaller than the optical frequency, $|\omega - \omega_0| \ll \omega + \omega_0$.

The atom–field interaction Hamiltonian in the RWA is:

$$\begin{aligned} H_{AF} &= -\mathbf{d}^{(+)} \cdot \mathbf{E}^{(-)} - \mathbf{d}^{(-)} \cdot \mathbf{E}^{(+)} \\ &= -\langle g|\hat{\varepsilon} \cdot \mathbf{d}|e\rangle \left(E_0^{(+)} e^{-i\omega t} + E_0^{(-)} e^{i\omega t}\right) \\ &= \frac{\hbar\Omega}{2}\left(\sigma^\dagger e^{-i\omega t} + \sigma e^{i\omega t}\right) \end{aligned} \tag{5.11}$$

where we defined the **Rabi frequency** as

$$\Omega := -\frac{2\langle \mathrm{g}|\hat{\varepsilon} \cdot \mathbf{d}|\mathrm{e}\rangle E_0^{(+)}}{\hbar} = -\frac{\langle \mathrm{g}|\hat{\varepsilon} \cdot \mathbf{d}|\mathrm{e}\rangle E_0}{\hbar} \tag{5.12}$$

Thus far, we can express the total Hamiltonian of a two-level atom in a classical light field in matrix form, in the basis $|g\rangle$ and $|e\rangle$, in units of $\hbar$:

$$H = \begin{bmatrix} 0 & \Omega e^{i\omega t}/2 \\ \Omega e^{-i\omega t}/2 & \omega_0 \end{bmatrix} \tag{5.13}$$

The **atomic state evolution** is governed by the Schrödinger equation:

$$i\hbar\partial_t|\psi\rangle = H|\psi\rangle \tag{5.14}$$

We express the atomic state as $|\psi\rangle = c_{\mathrm{g}}|g\rangle + c_{\mathrm{e}}|e\rangle$, where c_{g} and c_{e} account for the time dependence of the state. Plugging in the atomic Hamiltonian H_A (Eq. 5.7) and the interaction Hamiltonian H_{AF} (Eq. 5.11), the Schrödinger equation becomes:

$$\partial_t c_{\mathrm{g}}|g\rangle + \partial_t c_{\mathrm{e}}|e\rangle = -i\omega_0 c_{\mathrm{e}}|e\rangle - i\frac{\Omega}{2}e^{i\omega t}c_{\mathrm{e}}|g\rangle - i\frac{\Omega}{2}e^{-i\omega t}c_{\mathrm{g}}|e\rangle \tag{5.15}$$

By projecting with $\langle g|$ and $\langle e|$, we obtain the coupled differential equations for the atomic evolution:

$$\begin{aligned} \partial_t c_{\mathrm{g}} &= -i\frac{\Omega}{2}c_{\mathrm{e}}e^{i\omega t} \\ \partial_t c_{\mathrm{e}} &= -i\omega_0 c_{\mathrm{e}} - i\frac{\Omega}{2}c_{\mathrm{g}}e^{-i\omega t} \end{aligned} \tag{5.16}$$

We now proceed with another method to simplify the equations of motion, known as the **rotating-frame transformation**. At resonance, the oscillatory terms can be eliminated by transforming to a corotating frame, leading to a slowly varying excited-state amplitude

$$\tilde{c}_{\mathrm{e}} := c_{\mathrm{e}}e^{i\omega t}. \tag{5.17}$$

The equations of motion can then be expressed as:

$$\begin{aligned}\partial_t c_{\mathrm{g}} &= -i\frac{\Omega}{2}\tilde{c}_{\mathrm{e}} \\ \partial_t \tilde{c}_{\mathrm{e}} &= i\Delta\tilde{c}_{\mathrm{e}} - i\frac{\Omega}{2}c_{\mathrm{g}}\end{aligned} \tag{5.18}$$

The rotating frame approximation is equivalent to having an atomic Hamiltonian of

$$\tilde{H}_{\mathrm{A}} = -\hbar\Delta \left|e\right\rangle \left\langle e\right| \tag{5.19}$$

and an interaction Hamiltonian H_{AF} (Eq. 5.11) of

$$\begin{aligned}H_{AF} &= -\mathbf{d}^{(+)} \cdot \mathbf{E}^{(-)} - \mathbf{d}^{(-)} \cdot \mathbf{E}^{(+)} \\ &= \frac{\hbar\Omega}{2}\left(\sigma^{\dagger} + \sigma\right)\end{aligned} \tag{5.20}$$

where the the eigenvalues or eigenvectors for the two systems are the same.

Finally, we can express the total Hamiltonian in matrix form in the basis $|g\rangle$ and $|e\rangle$ and in units of $\hbar$ as:

$$H = \begin{bmatrix} 0 & \Omega/2 \\ \Omega/2 & -\Delta \end{bmatrix} \tag{5.21}$$

5.2 Rabi Flopping

We proceed with solving the equations of motion (Eq. 5.18) to gain insight for temporal evolution, in the following two limits: resonance- and near-resonance interaction.

5.2.1 Resonance

At resonance, $\Delta = 0$, the coupled equations reduce to:

$$\begin{aligned} \partial_t c_{\mathrm{g}} &= -i\frac{\Omega}{2}\tilde{c}_{\mathrm{e}} \\ \partial_t \tilde{c}_{\mathrm{e}} &= -i\frac{\Omega}{2}c_{\mathrm{g}} \end{aligned} \tag{5.22}$$

Decoupling these by differentiation and substitution yields:

$$\begin{aligned} \partial_t^2 c_{\mathrm{g}} &= -\left(\frac{\Omega}{2}\right)^2 c_{\mathrm{g}} \\ \partial_t^2 \tilde{c}_{\mathrm{e}} &= -\left(\frac{\Omega}{2}\right)^2 \tilde{c}_{\mathrm{e}} \end{aligned} \tag{5.23}$$

indicating a harmonic oscillator with frequency $\Omega/2$. The general solution for the two amplitudes in terms of the initial conditions $c_{\mathrm{g}}(0)$ and $\tilde{c}_{\mathrm{e}}(0)$ are:

$$\begin{aligned} c_{\mathrm{g}}(t) &= c_{\mathrm{g}}(0)\cos\left(\frac{1}{2}\Omega t\right) - i\tilde{c}_{\mathrm{e}}(0)\sin\left(\frac{1}{2}\Omega t\right) \\ \tilde{c}_{\mathrm{e}}(t) &= \tilde{c}_{\mathrm{e}}(0)\cos\left(\frac{1}{2}\Omega t\right) - ic_{\mathrm{g}}(0)\sin\left(\frac{1}{2}\Omega t\right) \end{aligned} \tag{5.24}$$

If an atom is initially in the ground state, then $c_{\mathrm{g}}(0) = 1$ and $\tilde{c}_{\mathrm{e}}(0) = 0$. The general solution (Eq. 5.24) then becomes

$$\begin{aligned} c_{\mathrm{g}}(t) &= \cos\left(\frac{1}{2}\Omega t\right) \\ \tilde{c}_{\mathrm{e}}(t) &= -i\sin\left(\frac{1}{2}\Omega t\right) \end{aligned} \tag{5.25}$$

The populations of the ground and excited states are:

$$P_g(t) = |c_{\mathrm{g}}(t)|^2 = \cos^2\left(\frac{\Omega}{2}t\right) = \frac{1}{2}(1+\cos\Omega t)$$
$$P_e(t) = |c_{\tilde{e}}(t)|^2 = \sin^2\left(\frac{\Omega}{2}t\right) = \frac{1}{2}(1-\cos\Omega t) \tag{5.26}$$

which is plotted in Fig. 5.1. These population oscillations between the ground and excited states at the angular frequency Ω are known as **Rabi flopping**.

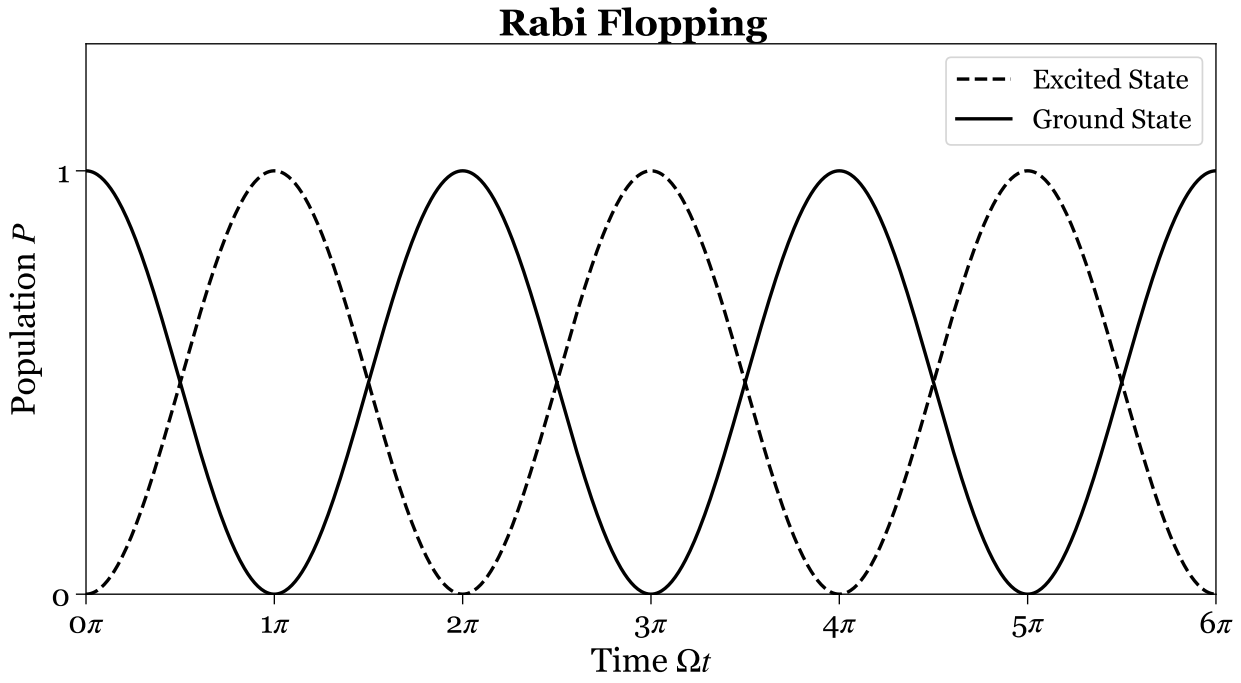

Figure 5.1: Illustration of Rabi flopping. At resonance, the populations of the ground and excited states oscillate at an angular frequency of Ω, the Rabi frequency.

5.2.2 Near-Resonance

Near resonance, again decoupling the equations of motion by differentiation and substitution yields:

$$\begin{aligned}\left(\partial_t^2 - i\Delta\partial_t + \frac{\Omega^2}{4}\right) c_{\mathrm{g}} &= 0 \\ \left(\partial_t^2 - i\Delta\partial_t + \frac{\Omega^2}{4}\right) \tilde{c}_{\mathrm{e}} &= 0\end{aligned} \tag{5.27}$$

or

$$\begin{aligned}\left(\partial_t - i\frac{\Delta}{2} + i\frac{\tilde{\Omega}}{2}\right)\left(\partial_t - i\frac{\Delta}{2} - i\frac{\tilde{\Omega}}{2}\right) c_{\mathrm{g}} &= 0 \\ \left(\partial_t - i\frac{\Delta}{2} + i\frac{\tilde{\Omega}}{2}\right)\left(\partial_t - i\frac{\Delta}{2} - i\frac{\tilde{\Omega}}{2}\right) \tilde{c}_{\mathrm{e}} &= 0\end{aligned} \tag{5.28}$$

where $\tilde{\Omega}$ is the **generalized Rabi frequency**

$$\tilde{\Omega} := \sqrt{\Omega^2 + \Delta^2} \tag{5.29}$$

The general solution for the two amplitudes in terms of the initial conditions $c_{\mathrm{g}}(0)$ and $\tilde{c}_{\mathrm{e}}(0)$ are:

$$c_{\mathrm{g}}(t) = e^{i\Delta t/2}\left[c_{\mathrm{g}}(0)\cos\left(\frac{1}{2}\tilde{\Omega}t\right) - \frac{i}{\tilde{\Omega}}\left[\Delta c_{\mathrm{g}}(0) + \Omega c_{\mathrm{e}}(0)\right]\sin\left(\frac{1}{2}\tilde{\Omega}t\right)\right] \tag{5.30}$$

$$\tilde{c}_{\mathrm{e}}(t) = e^{i\Delta t/2}\left[\tilde{c}_{\mathrm{e}}(0)\cos\left(\frac{1}{2}\tilde{\Omega}t\right) + \frac{i}{\tilde{\Omega}}\left[\Delta\tilde{c}_{\mathrm{e}}(0) - \Omega c_{\mathrm{g}}(0)\right]\sin\left(\frac{1}{2}\tilde{\Omega}t\right)\right] \tag{5.31}$$

Rabi oscillations now occur at an amplitude of $\sqrt{\Omega^2/(\Omega^2+\Delta^2)}$ and a frequency of $\sqrt{\Omega^2+\Delta^2}/2$. If an atom is initially in the ground state, then $c_{\mathrm{g}}(0) = 1$ and $\tilde{c}_{\mathrm{e}}(0) = 0$. The general solution

(Eq. 5.31) then becomes

$$c_{\mathrm{g}}(t) = e^{i\Delta t/2}\left[\cos\left(\frac{1}{2}\tilde{\Omega}t\right) - i\frac{\Delta}{\tilde{\Omega}}\sin\left(\frac{1}{2}\tilde{\Omega}t\right)\right]$$
$$\tilde{c}_{\mathrm{e}}(t) = -ie^{i\Delta t/2}\frac{\Omega}{\tilde{\Omega}}\sin\left(\frac{1}{2}\tilde{\Omega}t\right) \tag{5.32}$$

The populations of the ground and excited states are:

$$P_e(t) = |c_{\tilde{e}}(t)|^2 = \sin^2\left(\frac{\Omega}{2}t\right) = \frac{1}{2}(1-\cos\Omega t)$$
$$P_g(t) = 1 - P_e(t) \tag{5.33}$$

which is plotted in Fig. 5.2.

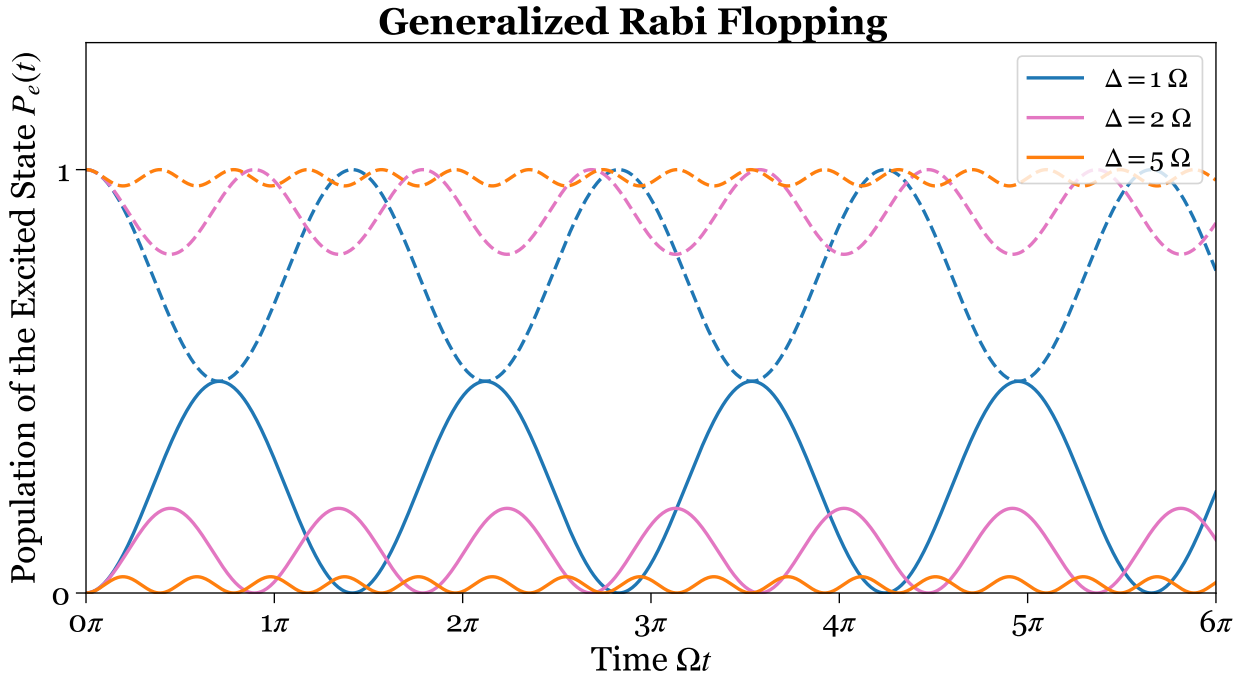

Figure 5.2: Illustration of Rabi flopping with detuning as in the general case. Rabi oscillations occur at a reduced amplitude of $\sqrt{\Omega^2/(\Omega^2+\Delta^2)}$ and a frequency of $\sqrt{\Omega^2+\Delta^2}/2$.

5.3 Dressed States

When an interaction Hamiltonian is included, the previous eigenstates $|g\rangle$ and $|g\rangle$ are no longer eigenstates of the new system. Diagonalizing the rotating-frame Hamiltonian, where $\Delta = \omega - \omega_0$ is the detuning of the laser field from the atomic resonance,

$$H = \begin{bmatrix} 0 & \Omega/2 \\ \Omega/2 & -\Delta \end{bmatrix} \tag{5.34}$$

the eigenvalues are

$$E_{\pm} = -\frac{\Delta}{2} \pm \frac{\hbar\tilde{\Omega}}{2} = \frac{-\Delta \pm \sqrt{\Omega^2 + \Delta^2}}{2} \tag{5.35}$$

with eigenvectors

$$\begin{aligned} |+\rangle &= \sin\theta\,|\mathrm{g}\rangle + \cos\theta\,|\mathrm{e}\rangle \\ |-\rangle &= \cos\theta\,|\mathrm{g}\rangle - \sin\theta\,|\mathrm{e}\rangle \end{aligned} \tag{5.36}$$

where θ is the **Stückelberg angle** defined as

$$\tan 2\theta = -\frac{\Omega}{\Delta} \quad \left(0 \leq \theta < \frac{\pi}{2}\right) \tag{5.37}$$

Alternatively, the eigenvectors can be written as

$$|\pm\rangle = \begin{bmatrix} \Delta \pm \sqrt{\Omega^2 + \Delta^2} \\ \Omega \end{bmatrix} \tag{5.38}$$

These are the **dressed states** of the atom.

Energies of the ground and excited states are plotted against laser detuning in the absence and in the presence of light-atom interactions. In the uncoupled case, the bare states have

energies 0 and $-\hbar\Delta$, crossing when $\Delta = 0$. However, coupling lifts the degeneracy, creating a hyperbolic **avoided crossing**, as shown in Fig.5.3. This phenomenon mixes the states near resonance and shifts their energies, resulting in **ac Stark shifts** or **Lamb shifts**.

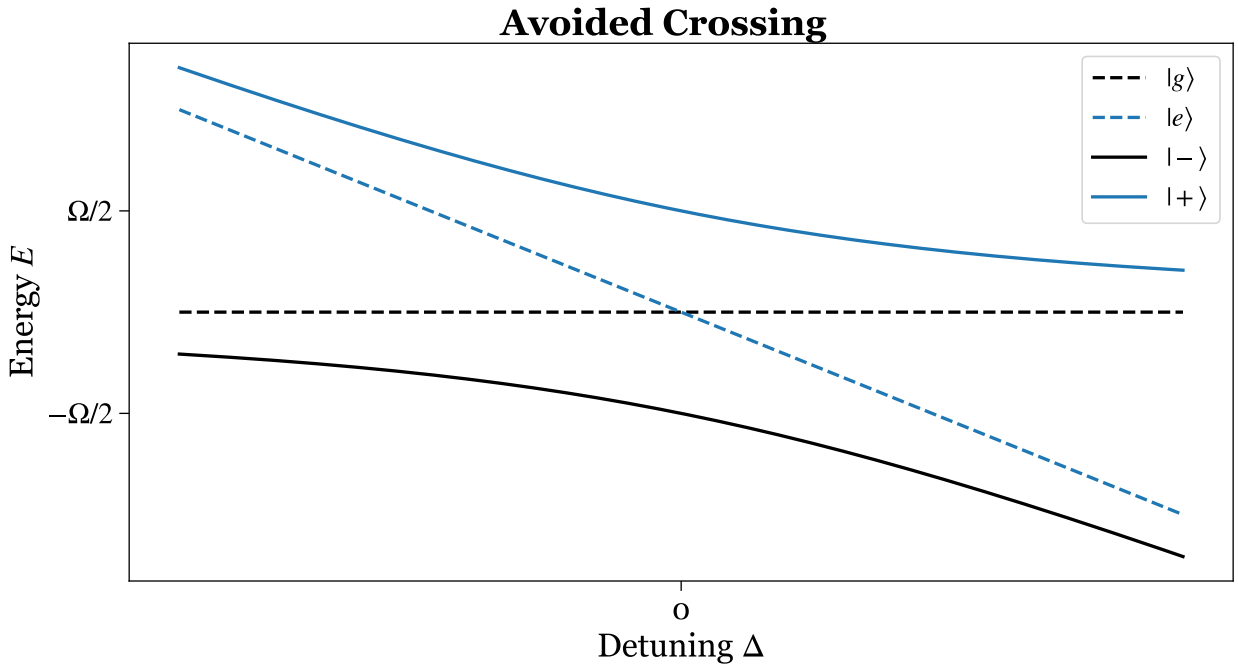

Figure 5.3: Illustration of the avoided crossing: In the presence of coupling between light and atoms, the energy levels of the dressed states are altered, lifting the degeneracy of the bare states at zero detuning.

In the limit of resonance interaction $\Delta = 0$, the eigenvalues reduce to

$$E_{\pm} = \pm\frac{\Omega}{2} \tag{5.39}$$

and the eigenvectors reduce to

$$|\pm\rangle = \frac{1}{\sqrt{2}}\begin{bmatrix} \pm 1 \\ 1 \end{bmatrix} \tag{5.40}$$

In the limit of far detuning $\Delta \gg |\Omega|$, the eigenvalues reduce to

$$E_{+} = -\Delta - \frac{\Omega^2}{4\Delta} \qquad E_{-} = \frac{\Omega^2}{4\Delta} \tag{5.41}$$

and the eigenvectors reduce to

$$|+\rangle = \frac{1}{\sqrt{2}} \begin{bmatrix} \Omega/2\Delta \\ 1 \end{bmatrix} \qquad |-\rangle = \frac{1}{\sqrt{2}} \begin{bmatrix} 1 \\ -\Omega/2\Delta \end{bmatrix} \tag{5.42}$$

which gives rise to the dipole force.

CHAPTER 6

ATOM OPTICS: THEORY

We will describe the interaction between light and atoms using models of increasing complexity. All models are wrong, some are useful, as they say. The point, however, is less on arriving at a perfectly accurate model as it does not realistically exist (move on), but more on working with a sufficiently intricate model which can produce useful results with high predictability. Indeed, we shall see that on multiple occasions, a simpler, more classical model, can yield similar results to a more sophisticated, or more quantum, model.

An atom can be modeled in the following ways, to start with. At its Spherical Cow form, an atom is as simple a point with defined position and velocity. In Dalton's Atomic Theory, atoms are indivisible small particles that are constituents of some chemical element, neither created or destroyed, and that all atoms of the same chemical element are the same, whereas atoms of different chemical elements are different. In Thomson's Plum Pudding Model, an atom is a uniform, positively charged sphere with negatively charged electrons embedded within, just like plums in a pudding. In the Bohr Model, an atom contains a positively charged nucleus at the center of the atom, and electrons orbiting the nucleus in circular orbits with quantized energy levels—an electron can jump between energy levels by absorbing or emitting a photon whose frequency matches the energy difference between the two levels. In the Wave Mechanical Model, developed by Heisenberg, de Broglie, and Schrödinger, The Uncertainty Principle was taken into account, stating that position and velocity of an electron cannot be simultaneously known to infinite accuracy.

In the field of **atom optics**, which deals with optics involving matter (de Broglie) waves, we focus on how to trap and cool atoms using laser light through the classical Lorentz model of the atom. There are two main types of mechanical forces exerted by light on atoms. The first is the dipole force, which is associated with the potential energy of the induced dipole in the electric field, will be described in Sec. 6.1. The second is radiation pressure, which

results from the absorption and re-emission of incident light, will be described in Sec. 6.2.

6.1 Dipole Force

6.1.1 Dipole Potential

A dipole trap or far-off resonance trap (FORT) is a device used to trap atoms by the dipole force. First realized by [3], later observed by [4], the dipole trap has become a standard experimental routine to confine atomic ensembles in the trapping regime. Given an atom with polarizability α, an external field $\mathbf{E}$, an induced dipole $\mathbf{d} = \alpha\mathbf{E}$, the dipole potential is

$$V_{\text{dipole}} = -\frac{\mathbf{d}\cdot\mathbf{E}}{2} = -\frac{dE}{2} \tag{6.1}$$

It is convenient to define an intensity scale known as the saturation intensity. For an atom with resonant frequency ω_0, resonant cross section σ_0, and damping rate Γ, the **saturation intensity** is

$$I_{\text{sat}} := \frac{\hbar\omega_0\Gamma}{2\sigma_0} \tag{6.2}$$

In particular, for ^{87}Rb on the D_2 transition (780 nm), the saturation intensity is $I_{\text{sat}} = 1.67$ mW/cm^2. Taking into account of all transitions and incorporating the saturation intensity, the dipole potential is rewritten to be

$$V_{\text{dipole}} = -\sum_j \frac{\hbar\omega_{j0}\Gamma_j^2}{4}\frac{\omega_{j0}^2-\omega^2}{(\omega_{j0}^2-\omega^2)^2+\Gamma_j^2\omega^2}\frac{I(\mathbf{r})}{I_{\text{sat},j}} \tag{6.3}$$

In the far-off resonance regime, this expression can be simplified

$$V_{\text{dipole}} = \sum_j \frac{\hbar\Gamma_j^2}{8}\left(\frac{1}{\omega-\omega_{j0}}-\frac{1}{\omega+\omega_{j0}}\right)\frac{I(\mathbf{r})}{I_{\text{sat},j}} \tag{6.4}$$

The first term represents the Stark shift due to the atomic resonances. The second term

is weaker in comparison, and accounts for partially of the Bloch–Siegert shift, the Lamb shift, and the Casimir–Polder effect. If one resonance is dominant, as in the case of the laser being tune far away from resonance, but much closer to one resonance than all the others, the **dipole potential** is

$$V_{\text{dipole}} = \frac{\hbar\Gamma^2}{8\Delta}\frac{I(\mathbf{r})}{I_{\text{sat}}} \tag{6.5}$$

6.1.2 Photon Scattering Rate

When photons scatter off atoms, momentum is being transferred. The **total radiated power** in terms of the polarizability is

$$P_{\text{rad}} = \frac{\omega^4|\alpha(\omega)|^2}{6\pi\epsilon_0^2 c^4} I \tag{6.6}$$

The photon scattering rate is the radiated power divided by the photon energy $\hbar\omega$

$$\Gamma_{\text{sc}} = \frac{P_{\text{rad}}}{\hbar\omega} = \left| \sum_j \frac{\omega^{3/2}}{\sqrt{2\omega_{j0}}} \frac{\Gamma_j^{3/2}}{\omega_{j0}^2 - \omega^2 - i\Gamma_j\omega} \sqrt{\frac{I}{I_{\text{sat},j}}} \right|^2 \tag{6.7}$$

If the system is dominated by a single resonance, such as in the near-detuning regime, the photon scattering rate is

$$\Gamma_{\text{sc}} = \frac{\eta_0}{\hbar}\frac{\omega^2}{\omega_0^2}\text{Im}[\alpha] I(\mathbf{r}) \tag{6.8}$$

Close to a single resonance, the scattering rate is

$$\Gamma_{\text{sc}} = \frac{(\Gamma/2)^3}{\Delta^2 + (\Gamma/2)^2}\frac{I}{I_{\text{sat}}} \tag{6.9}$$

If the system is far away from the dominant resonance ($|\Delta| \gg \Gamma$), but still close enough for

the resonance to dominate, the **photon scattering rate** is

$$\Gamma_{\text{sc}} \approx \frac{\Gamma^3}{8\Delta^2}\frac{I}{I_{\text{sat}}} = \frac{\Gamma}{\hbar\Delta}V_{\text{dipole}} \tag{6.10}$$

In designing an optical dipole trap, we must consider two crucial competing factors. The dipole potential V_{dipole}, as described in Eq. 6.5, represents the trapping force. The photon scattering rate R_{sc}, as described in Eq. 6.10, represents heating of the atoms. Fortunately, the scaling of these two factors works in our favor, leading to the possibility of realizing an optical dipole trap.

6.2 Radiation Pressure

Next, we will examine the forces resulting from the absorption and reemission of incident light. Each photon carries a momentum of $\hbar k$. Therefore, the photon scattering rate (Eq. 6.10) determines the rate of momentum transfer, resulting in a radiation pressure force given by

$$F_{\text{rad}} = \hbar k R_{\text{sc}} \tag{6.11}$$

Close to a single resonance, using the scattering rate from Eq. 6.9, the **force due to radiation pressure** is then

$$\mathbf{F}_{\text{rad}} = \frac{\hbar\mathbf{k}_0(\Gamma/2)^3}{\Delta^2 + (\Gamma/2)^2}\frac{I}{I_{\text{sat}}} \tag{6.12}$$

The **recoil velocity** v_r, defined as the velocity corresponding to one photon recoil momentum $\hbar k$, is computed to be

$$v_r = \frac{\hbar k}{m}. \tag{6.13}$$

CHAPTER 7

ATOM OPTICS: EXAMPLES

7.1 Dipole Trap

7.1.1 Trap Depth

Recall from Sec. 5.3 that the interaction between light and two-level atoms modifies the bare states to dressed states, shifting the ground- and excited-state energies. In the case of a red-detuned laser, it creates an attractive potential for the atoms since $E_- < 0$; conversely, a blue-detuned laser forms a repulsive potential. The square of the Rabi frequency is proportional to the laser intensity. Fig. 7.1 illustrates the dipole trap potential as a function of atomic position relative to the laser beam waist.

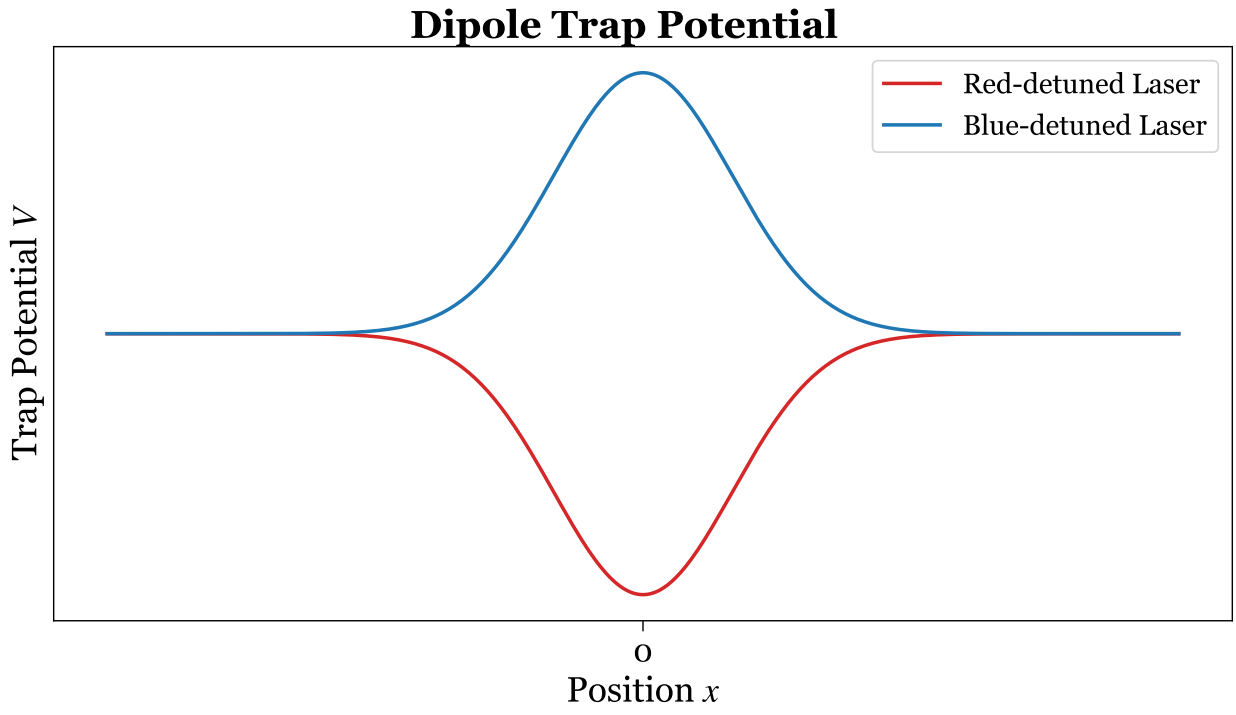

Figure 7.1: Illustration of dipole trap potential: attractive when the laser is red-detuned from the atomic transition and repulsive when blue-detuned.

We perform a quick calculation of the dipole trap discussed later. The dipole trap is

composed of two counter-propagating beams, each with a power of 120 mW and a wavelength of 785 nm. Each beam is focused at the center of the transport path to a waist of 120 μm. Then, the detuning of the laser beam is:

$$\Delta = \frac{c}{785\text{nm}} - \frac{c}{780\text{nm}} = -2.448 \times 10^{12}\,\text{Hz} \tag{7.1}$$

The intensity I of each laser beams at the focus is:

$$I = \frac{2P}{\pi w_0^2} = \frac{2 \times 120 \times 10^{-3}\,\text{W}}{\pi \left(120 \times 10^{-6}\,\text{m}\right)^2} \approx 5.31 \times 10^6\,\text{W/m}^2 \tag{7.2}$$

The electric field amplitude E_0 of each laser beam can be calculated using the formula:

$$E_0 = \sqrt{\frac{2P}{\epsilon_0 c A}} = \sqrt{\frac{2 \times 120 \times 10^{-3}}{8.854 \times 10^{-12} \times 3 \times 10^8 \times 4.52 \times 10^{-8}}} \approx 1.414 \times 10^5\,\text{V/m} \tag{7.3}$$

The Rabi frequency Ω can be calculated using the formula, where $d_{\text{eg}} = 3.584 \times 10^{-29}\,\text{C} \cdot \text{m}$ is the dipole moment of the ^{87}Rb D_2 line:

$$\Omega = \frac{d_{\text{eg}} E_0}{\hbar} = \frac{3.584 \times 10^{-29} \times 1.414 \times 10^5}{1.054 \times 10^{-34}} \approx 4.81 \times 10^{10}\,\text{rad/s} \approx 7.66 \times 10^9\,\text{Hz} \tag{7.4}$$

The dipole potential U includes contributions from the Stark shifts (as described in Eq. 5.35) of both beams, and is given by:

$$V_{\text{dipole}} = 4 \times \frac{\Omega^2}{4\Delta} = \frac{\Omega^2}{\Delta} = \frac{5.87 \times 10^{19}}{-2.45 \times 10^{12}} \approx -2.39 \times 10^7\,\text{Hz} \approx 2\pi \times 6\ \text{MHz}$$

The slight discrepancy in the last step can be resolved through a more careful treatment of the atomic states by considering a more comprehensive set of dipole moments.

7.1.2 Scattering Rate

The scattering rate can be calculated using Eq. 6.9 in the far-detuned limit $\Delta >> \Gamma$:

$$\Gamma_{\text{sc}} \approx \frac{\Gamma}{\hbar\Delta} V_{\text{dipole}} = \frac{2\pi \times 6 \text{ MHz}}{2.448 \times 10^{12} \text{ Hz}} 2\pi \times 6 \text{ MHz} \approx 580 \text{ Hz} \tag{7.5}$$

7.1.3 Trap Frequency

The trap oscillation frequency can be calculated by modeling the dipole trap as a classical harmonic oscillator in both axial and transverse directions:

$$H = \frac{p^2}{2m} + \frac{1}{2}m\omega_x^2 x^2 + \frac{1}{2}m\omega_y^2 y^2 + \frac{1}{2}m\omega_z^2 z^2 \tag{7.6}$$

For the transverse directions,

$$\frac{2V_{\text{dipole}}x^2}{\omega_0^2} \approx \frac{1}{2}m\omega_x^2 x^2 \tag{7.7}$$

$$\omega_x = \sqrt{\frac{4V_{\text{dipole}}}{m\omega_0^2}} \tag{7.8}$$

For the axial direction,

$$\frac{V_{\text{dipole}}k^2 z^2}{2} \approx \frac{1}{2}m\omega_z^2 z^2 \tag{7.9}$$

$$\omega_z = \sqrt{\frac{V_{\text{dipole}}k^2}{m}} \approx 110 \text{ kHz} \tag{7.10}$$

7.2 Magneto-Optical Trap (MOT)

A magneto-optical trap (MOT) is a device used to cool and trap neutral atoms to very low temperatures using laser cooling and magnetic trapping. First demonstrated by [5], the MOT has become a standard experimental routine to produce atomic ensembles in the micro kelvin regime.

Creating a MOT is akin to crafting cotton candy. One heats up the flavored sugar (salty Rb atoms), liquefying the particles (atoms in the dispensers) to fill the bowl. Slower atoms condense around the stick, forming a sweet (salty) cloud of actual molasses (optical molasses). To make the salty Rb cotton candy more appetizing to the scientific community, please visit the amusement park below with no surcharge.

7.2.1 Laser Cooling

As discussed above (Eq. 6.12), the force due to radiation pressure is

$$\mathbf{F}_{\text{rad}} = \frac{\hbar \mathbf{k}_0 (\Gamma/2)^3}{\Delta^2 + (\Gamma/2)^2} \frac{I}{I_{\text{sat}}} \tag{7.11}$$

The mechanism of using the radiation-pressure force to cool atoms is the following. Consider an atom moving with velocity v, exposed to identical but counter-propagating laser fields along the velocity axis. The **radiation-pressure force** on the atom due to the two fields is, depicted in Fig. 7.2,

$$F_{\text{rad}} = \hbar k (\Gamma/2)^3 \left(\frac{1}{\Delta_1^2 + (\Gamma/2)^2} - \frac{1}{\Delta_2^2 + (\Gamma/2)^2} \right) \frac{I}{I_{\text{sat}}} \tag{7.12}$$

For small velocity $v \ll \max(|\Delta|, \Gamma)/k$, we can expand the lowest order in v to obtain the damping force

$$F_{\text{rad}} = \frac{\hbar k^2 \Gamma^3}{2} \frac{\Delta}{[\Delta^2 + (\Gamma/2)^2]^2} \frac{I}{I_{\text{sat}}} v \tag{7.13}$$

For red-detuning $\Delta < 0$, this force leads to overdamped motion for trapped atoms, and this light configuration is called **optical molasses**.

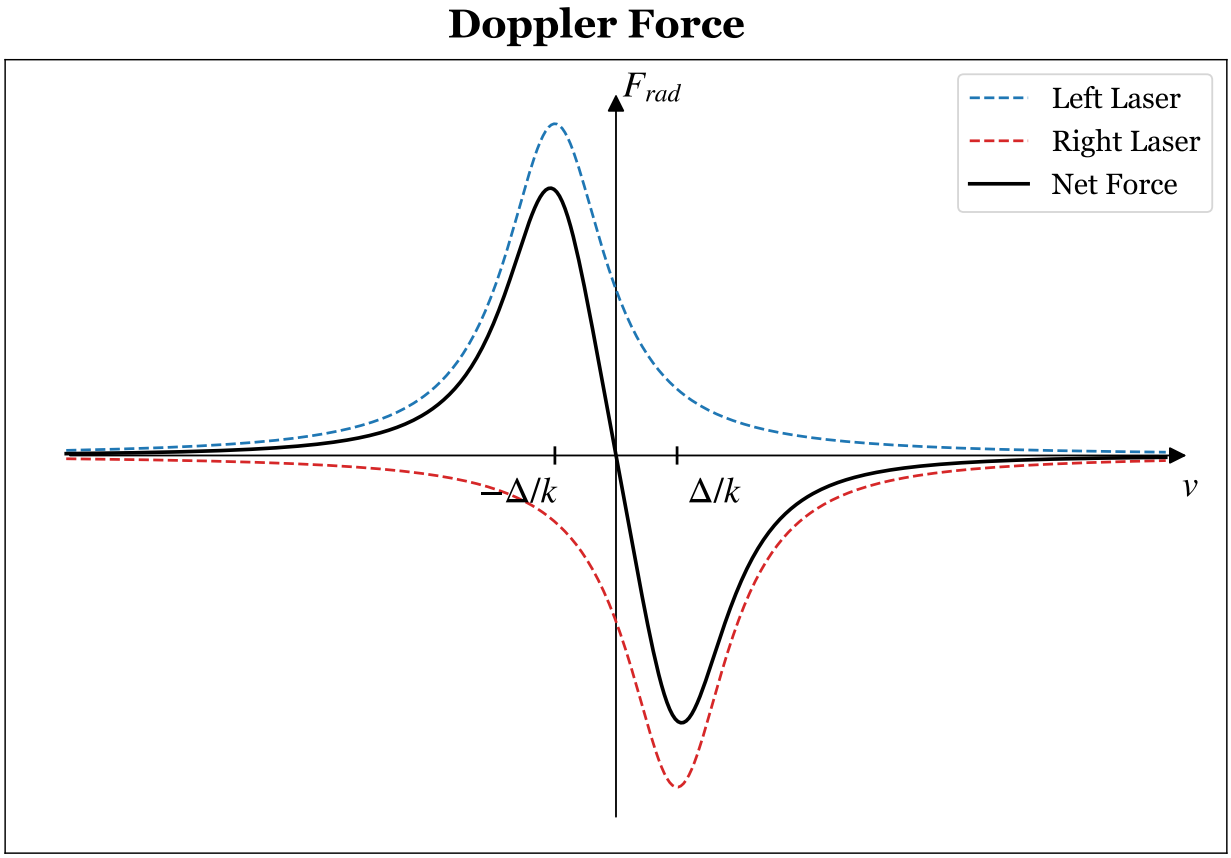

Figure 7.2: Doppler force due to counter-propagating lasers.

7.2.2 Limitations and Challenges

While naively it might seem like the atomic velocity may be damped away completely, this is not the case in reality, as we have only thus far considered the average cooling force. The fluctuations of the cooling force, however, sets a lower temperature limit known as the Doppler limit. By examining the variance of the velocity distribution in steady state, and invoking a thermodynamics argument, we can see that the temperature is minimized for the detuning $\Delta = -\Gamma/2$, arriving at the **Doppler temperature** T_D

$$k_{\mathrm{B}} T_{\mathrm{D}} = \frac{\hbar \Gamma}{2} \tag{7.14}$$

This temperature is the theoretical limit for Doppler cooling, which for ^{87}Rb at 780 nm is $T_D = 146\mu$K.

7.2.3 Polarization gradient cooling (PGC)

Sub-Doppler cooling, first observed by [6], subsequently by [7], allows atoms to be cooled below the Doppler limit. The theoretical treatment of this phenomenon is provided by [8].

7.3 Saturation Absorption Spectroscopy

Saturated Absorption Spectroscopy (SAS) is a technique used to obtain high-resolution spectra of atoms by eliminating Doppler broadening effects. This method involves using two counter-propagating laser beams: a strong **pump beam** and a weaker **probe beam**, both of which directed through the same sample of atoms.

The pump beam, which is tuned to a specific frequency, passes through the sample, causing saturation of the absorption transition for atoms that are stationary or moving slowly relative to the beam direction. These atoms or molecules become less likely to absorb additional photons due to depletion of ground-state atoms.

Simultaneously, the probe beam, which is weaker, also passes through the sample. It can be absorbed by atoms that have not been saturated by the pump beam.

When the pump and probe beams interact with atoms moving at the same velocity (thus experiencing the same Doppler shift), the absorption of the probe beam decreases because those atoms or molecules are already saturated by the pump beam. This results in a dip in the absorption signal of the probe beam, known as a Lamb dip, which appears at the frequency corresponding to the exact transition of the stationary or slow-moving atoms. For counter-propagating pump and probe beams, this happens for stationary or slow-moving atoms.

By scanning the frequency of the pump beam and recording the absorption of the probe

beam, a high-resolution spectrum is obtained. The sharp features in this spectrum correspond to the natural linewidth of the atomic transitions, free from Doppler broadening effects.

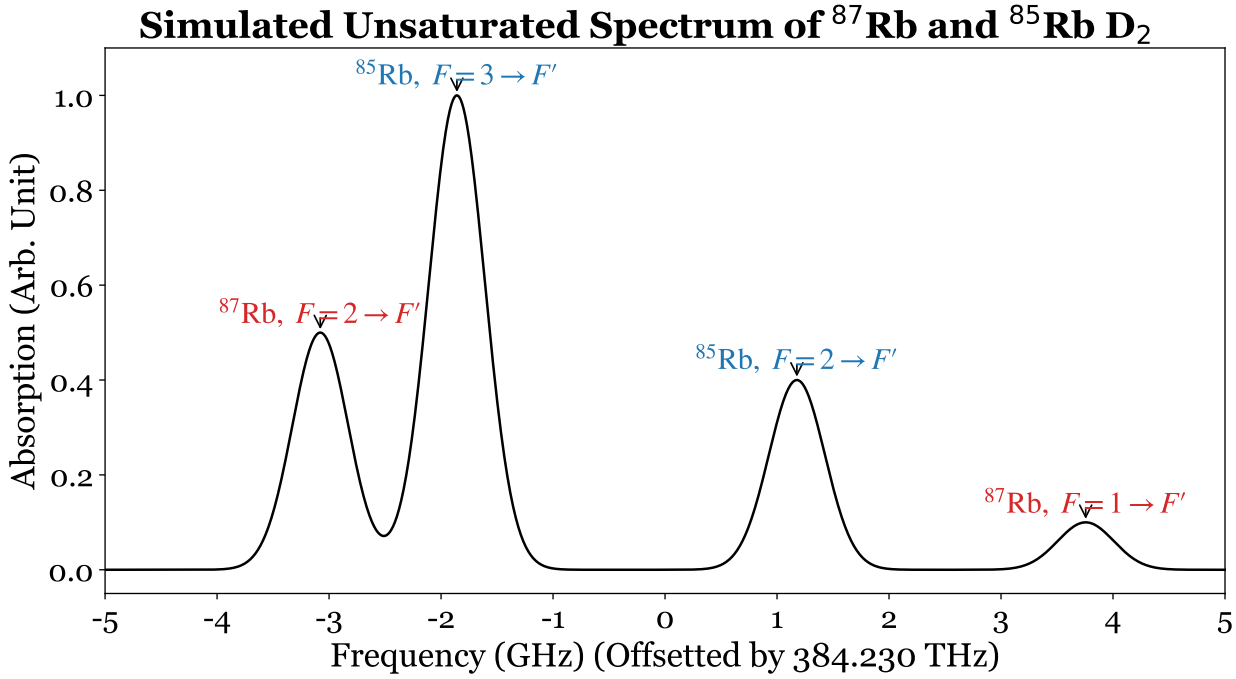

Figure 7.3: Simulated unsaturated spectrum of ^{87}Rb and ^{85}Rb with Doppler broadened resonance peaks. The D2 lines for the elements are displayed, where the ^{87}Rb lines are spaced 6.8 GHz apart, and the ^{85}Rb lines are spaced 3.0 GHz apart. Absorption intensity is in arbitrary units, and relative heights are for illustration purposes only.

Part III

Theory of Quantum Optics

CHAPTER 8

CAVITY QUANTUM ELECTRODYNAMICS (CQED)

8.1 The Jaynes–Cummings Model

Having explored a model in which a two-level atom interacts with a classical field, we now turn to a quantum-mechanical treatment of the light field. The Jaynes–Cummings model serves as a fundamental quantum framework for describing the interaction between a two-level atom and a single mode of the electromagnetic field.

The uncoupled Hamiltonian for a two-level atom and a single optical cavity mode is given by:

$$H_{\mathrm{A}} + H_{\mathrm{F}} = \hbar\omega_0 |e\rangle\langle e| + \hbar\omega \left(a^\dagger a + \frac{1}{2} \right) \tag{8.1}$$

where ω_0 is the atomic transition frequency and ω is the cavity resonance frequency.

The dipole interaction Hamiltonian is:

$$H_{\mathrm{AF}} = -\mathbf{d} \cdot \mathbf{E} \tag{8.2}$$

with the atomic dipole operator defined as:

$$\mathbf{d} := \mathbf{d}_{\mathrm{ge}} (\sigma + \sigma^\dagger) \tag{8.3}$$

Let $f(r)$ be the normalized spatial mode profile. We can define a **cavity QED coupling constant** that sets the energy scale for the atom-field coupling:

$$g(\mathbf{r}) = -\sqrt{\frac{\omega}{2\epsilon_0 \hbar}} \mathbf{d}_{ge} \cdot f(\mathbf{r}) \tag{8.4}$$

The interaction Hamiltonian becomes, n the rotating-wave approximation (RWA):

$$H_{AF} = \hbar g(\sigma^\dagger a + \sigma a^\dagger) \tag{8.5}$$

The **total Hamiltonian**, neglecting vacuum field energy and any loss channel, and assuming the atom is fixed, is given by:

$$H = H_A + H_F + H_{AF} = \hbar\omega_0\sigma^\dagger\sigma + \hbar\omega a^\dagger a + \hbar g(\sigma^\dagger a + \sigma a^\dagger) \tag{8.6}$$

This is the **Jaynes–Cummings model** [9], which describes the dynamics of a two-level atom interacting with a single near-resonant cavity mode, without any dissipation.

8.2 Modifications to the Model

A few modifications can be made to the Jaynes–Cummings model to better reflect reality. The inclusion of atomic spontaneous emission and cavity decay alters the dynamics described by the master equation in the semi-classical treatment. The interaction of the atom with other modes, especially those outside the cavity, results in atomic spontaneous emission, represented by the free-space decay rate Γ. Additionally, the cavity's intensity diminishes due to transmission and mirror losses, which are characterized by the cavity decay rate κ.

These effects can be incorporated into the master equation as follows:

$$\frac{\partial\rho}{\partial t} = -i[H,\rho] + \Gamma D[\sigma]\rho + \kappa D[a]\rho \tag{8.7}$$

by attaching the **Lindblad superoperator** defined as:

$$D[\sigma]\rho = \sigma\rho\sigma^\dagger - \frac{1}{2}\left(\sigma^\dagger\sigma\rho + \rho\sigma^\dagger\sigma\right) \tag{8.8}$$

$$D[a]\rho = a\rho a^\dagger - \frac{1}{2}\left(a^\dagger a\rho + \rho a^\dagger a\right) \tag{8.9}$$

This model exhibits the same dynamics as a classical damped oscillator.

Equivalently, to include the atomic spontaneous emission, we can modify the Hamiltonian from Eq. 5.34 to be:

$$H = \begin{bmatrix} 0 & \Omega/2 \\ \Omega/2 & -\Delta + i\Gamma/2 \end{bmatrix} \tag{8.10}$$

In the limit of a weak drive, as $\Omega \to 0$, the eigenvalue for the ground state is given by:

$$E_- = \frac{\Omega^2}{4\Delta} + \frac{1}{2}i\frac{(\Omega/2)^2}{\Delta^2 + (\Gamma/2)^2}\Gamma \tag{8.11}$$

with the associated eigenvector:

$$|-\rangle = \begin{bmatrix} 1 \\ \frac{\Omega/2}{-\Delta - i\Gamma/2} \end{bmatrix} \tag{8.12}$$

Define the **scattering rate** Γ_{sc} as

$$\Gamma_{\text{sc}} = \frac{(\Omega/2)^2}{\Delta^2 + (\Gamma/2)^2}\Gamma \tag{8.13}$$

In the far-detuning limit, the scattering rate reduces to

$$\Gamma_{\text{sc}} \approx \frac{1}{2}\frac{\Omega^2}{\Delta^2}\Gamma \tag{8.14}$$

In the on-resonance limit, the scattering rate reduces to

$$\Gamma_{\text{sc}} \approx \frac{1}{4}\frac{\Omega^2}{\Gamma} \tag{8.15}$$

For the Jaynes–Cummings model to accurately reflect true dynamics, the system must operate in the **strong coupling regime**, where $g \gg \kappa, \Gamma$. In this regime, dissipation is

slow, and atomic emission primarily occurs into the cavity mode.

8.3 Purcell Effect

The Purcell effect ([10] [11]) describes the enhancement or suppression of the spontaneous emission rate of an atom due to its interaction with a resonant cavity. **Purcell enhancement** is more familiar to the quantum optics community, which refers to the increase in the spontaneous emission rate of an atom when placed inside a resonant cavity that modifies the local density of optical states. **Purcell suppression** is a similar concept, which involves reducing the spontaneous emission rate by engineering an off-resonant optical environment around the atom.

Both effects can be quantified using the **Purcell factor** F_P, which depends on the quality factor and mode volume of the cavity. Purcell factor is the ratio of the modified spontaneous emission rate to the natural emission rate. It depends on the quality factor (Q) of the cavity and the mode volume (V) as follows:

$$F_P = \frac{3}{4\pi^2}\left(\frac{\lambda}{n}\right)^3 \frac{Q}{V} \tag{8.16}$$

Various techniques can be employed to achieve a high Purcell factor. High-Q cavities, constructed from materials and structures that minimize energy loss, can attain a high quality factor Q. Additionally, cavities with small mode volumes can enhance V, further improving the Purcell factor.

High-NA cavities can capture spontaneous emission light over a wider angle. By tuning the cavity sufficiently far from the atomic resonance, these cavities have the potential to significantly alter the spontaneous emission rate.

CHAPTER 9

SPONTANEOUS EMISSION

For spontaneous emission, the rate is derived using Fermi's Golden Rule. This involves calculating the interaction Hamiltonian, determining the matrix element for the transition, and evaluating the final density of states.

9.1 Fermi's Golden Rule

Fermi's golden rule is used to calculate the transition rate between quantum states due to a perturbation. The transition rate $\Gamma_{\mathrm{i}\to\mathcal{F}}$ from an initial state $|i\rangle$ to a final state $|f\rangle$ due to an perturbation H_{int} is given by:

$$\Gamma_{\mathrm{i}\to\mathrm{f}} = \frac{2\pi}{\hbar}|\langle \mathrm{i}|H_{\mathrm{int}}|\mathrm{f}\rangle|^2\rho(E_{\mathrm{f}}) \tag{9.1}$$

where $\rho(E_{\mathrm{f}})$ is the density of final states at the energy E_{f}.

For an atom interacting with the electromagnetic field, the interaction Hamiltonian can be written as:

$$H_{\mathrm{int}} = -\mathbf{d}\cdot\mathbf{E} \tag{9.2}$$

where $\mathbf{d}$ is the electric dipole moment of the atom and $\mathbf{E}$ is the electric field of the emitted photon.

Assuming the electric field is in the form of a plane wave $\mathbf{E} = \mathbf{E_0}e^{i\mathbf{k}\cdot\mathbf{r}}$, the matrix element becomes:

$$\langle i|H_{\mathrm{int}}|f\rangle = -\langle i|\mathbf{d}\cdot\mathbf{E}|f\rangle = -\mathbf{d}\cdot\mathbf{E_0} \tag{9.3}$$

The electric field amplitude $\mathbf{E_0}$ of a single photon in a volume V is:

$$|\mathbf{E_0}|^2 = \frac{\hbar\omega}{2\epsilon_0 V} \tag{9.4}$$

9.2 Density of States

9.2.1 Photons in a Vacuum

We derive the density of states for photons in a vacuum, which describes the number of available photon states per unit volume per unit energy interval.

Consider photons confined in a cubic volume $V = L^3$ with side length L. The boundary conditions impose that the wavevector components k_x, k_y, k_z are quantized:

$$k_i = \frac{2\pi n_i}{L}, \quad \text{for} \quad i = x, y, z \tag{9.5}$$

where n_i are integers.

The set of all states with energy less than E corresponds to the set of all states in k-space within a radius of $k = E/\hbar c$ from $k = 0$. The number of states is the volume of a sphere with this radius divided by $(2\pi)^3/V$ and then multiply by 2 to account for the two independent polarizations:

$$n(E) = 2\frac{4\pi k^3}{3}\frac{V}{(2\pi)^3} = \frac{E^3 V}{3\pi^2(\hbar c)^3} \tag{9.6}$$

The density of states is:

$$\rho(E) = \frac{dn}{dE} = \frac{E^2 V}{\pi^2(\hbar c)^3} \tag{9.7}$$

Since the photon energy E is related to its frequency ω by $E = \hbar\omega$, we can also express the **density of states** for photons in a vacuum in terms of ω:

$$\rho(\omega) = \frac{\omega^2}{\pi^2 \hbar c^3} \tag{9.8}$$

9.2.2 Photons in an Optical Cavity

The density of states in an optical cavity differs from that in free space due to the boundary conditions imposed by the cavity. These boundary conditions lead to discrete modes rather

than a continuous spectrum.

Consider a simple Fabry-Pérot cavity with length L. The boundary conditions require that the electromagnetic field has nodes or antinodes at the cavity mirrors, leading to quantized wavevectors. For a one-dimensional cavity, the wavevector k is quantized as:

$$k_n = \frac{n\pi}{L}, \quad n = 1, 2, 3, \ldots \tag{9.9}$$

with the corresponding resonant frequency ω_n given by:

$$\omega_n = ck \tag{9.10}$$

The density of states for photons in an optical cavity in terms of ω is thus:

$$\rho(\omega) = \delta(\omega - \omega_n) \tag{9.11}$$

9.3 Spontaneous Emission Rate

Substituting the matrix element and the density of states for photons in a vacuum into Fermi's golden rule, we have:

$$\Gamma_{\mathrm{i}\to\mathrm{f}} = \frac{2\pi}{\hbar}|\mathbf{d}\cdot\mathbf{E_0}|^2\frac{V\omega^2}{\pi^2c^3} = \frac{2\pi}{\hbar}\left(\mathbf{d}\cdot\sqrt{\frac{\hbar\omega}{2\epsilon_0 V}}\right)^2\frac{V\omega^2}{\pi^2c^3} = \frac{\omega^3|\mathbf{d}|^2}{3\pi\epsilon_0\hbar c^3} \tag{9.12}$$

Redefining the absolute value of the dipole moment for the transition as d_{ge}, we get the **spontaneous emission rate** into a vacuum:

$$\Gamma_{\mathrm{i}\to\mathrm{f}} = \frac{\omega^3 d_{\mathrm{ge}}^2}{3\pi\epsilon_0\hbar c^3} \tag{9.13}$$

For the Rubidium D2 line, $\lambda = 780\,\mathrm{nm}$, $d_{\mathrm{ge}} \approx 3.58 \times 10^{-29}\,\mathrm{C\ m}$:

$$\Gamma_{\mathrm{i}\to\mathrm{f}} = \left(\frac{2\pi}{\lambda}\right)^3 \frac{d_{\mathrm{ge}}^2}{3\pi\epsilon_0\hbar} \tag{9.14}$$

$$= \left(\frac{2\pi}{780\,\mathrm{nm}}\right)^3 \frac{(3.58 \times 10^{-29}\,\mathrm{C\ m})^2}{3\pi \times 8.85 \times 10^{-12}\,\mathrm{C}^2/(\mathrm{N\ m}^2) \times 1.055 \times 10^{-34}\,\mathrm{J\ s}} \tag{9.15}$$

$$\approx 2\pi \times 6\,\mathrm{MHz} \tag{9.16}$$

Part IV

Experimental Quantum Optics

CHAPTER 10

SUPPRESSING SPONTANEOUS EMISSION WITH A HIGH-NA CAVITY

10.1 Introduction

Atomic spontaneous emission is a fundamental quantum mechanical process where an excited atom spontaneously releases a photon and transitions to a lower energy state. Unlike stimulated emission, which is driven by an external field as in lasers, spontaneous emission occurs without external influence and is governed by Fermi's Golden Rule (Eq. 9.1). According to this rule, the decay rate of spontaneous emission is the product of the interaction Hamiltonian between the atom and the light field, and the density of photon states. For photons decaying into free space, the density of states leads to a well-known expression for the decay rate (Eq. 9.13) .

However, spontaneous emission is often undesirable in quantum systems due to its detrimental effects. It introduces decoherence, causing a loss of quantum information, which is critical for high-fidelity quantum computing. In optical cavities, spontaneous emission can result in unwanted photon loss, reducing the efficiency of quantum devices. Two significant studies have explored the disadvantages of spontaneous emission, particularly in the context of quantum Rabi oscillation and atom-cavity microscopy [12, 13].

Control over spontaneous emission is therefore a central goal in quantum optics. One well-known approach involves the use of photonic crystals, which create photonic bandgaps– ranges of frequencies where light cannot propagate. When light emitters are embedded within these crystals, spontaneous emission is suppressed if the emission frequency falls within the photonic bandgap, effectively inhibiting the emission. Additionally, introducing defects in photonic crystals forms photonic nanocavities with high quality factors and small mode volumes, enabling significant modification of spontaneous emission rates (Purcell effect) and

strong coupling, as demonstrated in studies involving semiconductor quantum dots in inverse opal photonic crystals [14, 15].

Our proposed approach also seeks to engineer the final density of states to suppress spontaneous emission. In free space, the final photon states form a continuum, supporting all frequencies, making the spontaneous emission decay rate constant. However, if the atom is enclosed in a cavity, the spontaneous emission rate can be dramatically altered. When the cavity is on-resonance, the spontaneous emission rate along the cavity axis is enhanced, whereas the rate away from the cavity axis is suppressed, by a factor known as the Purcell factor or cooperativity, which is crucial for efficient quantum information exchange between the atom and the cavity field. When the cavity is off-resonant, the behavior changes significantly.

To suppress the spontaneous emission rate, we propose enclosing the atom in a sufficiently detuned off-resonance cavity, which can significantly alter the final density of states [16]. This suppression is maximized by the numerical aperture (NA) of the cavity, expressed in solid angle, divided by the spontaneous emission rate in free space:

$$F = 1 - \frac{\mathrm{NA}}{4\pi} \tag{10.1}$$

where F is the suppression factor. Specifically, designing an off-resonant cavity with a high numerical aperture using localized quarter-wave phase coatings can suppress spontaneous emission in all directions while enhancing emission along the cavity axis. This approach aims to mitigate the loss of quantum information to spontaneous emission and improve the cooperativity of the system, thereby enhancing the computational power of quantum computers.

While high-NA cavities offer significant advantages, they also present several practical challenges. Theoretical limitations arise due to the breakdown of the paraxial approximation in high NA systems. The paraxial approximation assumes that light rays are close and

nearly parallel to the optical axis, which simplifies the analysis. However, at high NA, this approximation no longer holds, leading to more complex diffraction effects and potentially limiting the accuracy of theoretical models used for designing these cavities [17].

On the experimental front, surface fabrication imperfections can have a considerable impact on the performance of high-NA cavities [18]. Any deviations or irregularities in the surface of the mirrors or other components can disrupt the precise alignment required for optimal cavity performance. Such imperfections can lead to losses in cavity efficiency and affect the quality of the light confinement. Addressing these challenges involves meticulous fabrication processes and rigorous quality control to ensure that the practical implementation aligns with theoretical expectations and achieves the desired results.

10.2 Experimental Methods

The high-NA cavity design summarized in Tab. 10.2 and illustrated in Fig. 10.1 features a compact configuration with a cavity length d of 4 mm and mirrors that each have a radius of curvature (ROC) of 10 mm. The mirrors, with a diameter of 7.75 mm, are designed to accommodate a beam waist parameter w_0 of 31.5 μm. The cavity's free spectral range (FSR) is 37.5 GHz, and the Rayleigh range z_R is 4.0 mm.

The setup for testing the high-NA cavity is summarized in Fig. 10.2. Light is focused using a 100 mm focal length achromatic doublet lens (Thorlabs, PN: AC254-100-B) and a 6.2 mm aspheric lens for fiber coupling (Thorlabs, PN: C171TMD-B). A 50:50 non-polarizing beamsplitter cube (Thorlabs, PN: BS011) divides the light path. The setup also includes a camera and a photodiode (Thorlabs, PN: PDA100A) for alignment and detection, ensuring optimal performance of the system. The setup includes two mirrors that control the angle and position of the incident beam. The mirror closer to the cavity primarily adjusts the angle, while the mirror further from the cavity mainly adjusts the transverse position. In this experiment, we predominantly utilize the outer mirror to offset the beam.

The beam waist parameter w_0, according to Eq. 4.41, is calculated from

$$w_0 = \sqrt{\frac{\lambda d}{2\pi}\sqrt{\frac{2R}{d} - 1}} = \sqrt{\frac{780 \text{ nm} \times 4 \text{ mm}}{2\pi} \times \sqrt{4}} = 31.5 \ \mu\text{m} \tag{10.2}$$

The highest mode number N achievable within this geometric setup occurs when the edge of the mode touches the rim of the mirror. By definition, this represents the maximum confinement of the beam within the cavity dimensions, allowing the system to have a theoretically possible highest mode number N of

$$N = \left(\frac{w_0}{\lambda n}\right)^2 = \left(\frac{31.5 \ \mu\text{m}}{780 \text{ nm} \times 1.4537}\right)^2 = 772 \tag{10.3}$$

The numerical aperture (NA) of the cavity is defined to be

$$NA = n \sin\theta \tag{10.4}$$

where θ is the largest angle subtend in the cavity. The NA can be estimated using the diffraction formula applied to the smallest observable feature. This approach allows us to quantify the NA based on the system's ability to focus light and resolve fine details within the optical cavity. Let x be the size of the smallest observed feature, $n = 1.4537$ be the index of refraction of the substrate, then according to the diffraction formula,

$$x \sin\theta = n\lambda \tag{10.5}$$

$$\theta = \arcsin\left(\frac{\lambda n}{w_0}\sqrt{N}\right) \tag{10.6}$$

High-NA Cavity	Supplier	PN	Qty
Cavity Mirror: fused silica pl-concave, diameter Φ=7.75 mm, ROC = 10 mm, AR coated, reflectivity R=99.9%	Layertec	obsolete	2
Lens: f = 100.0 mm, Φ =1" Achromatic Doublet, ARC: 650 - 1050 nm	Thorlabs	AC254-100-B	1
Asphere: for fiber coupling, $f = 6.2$ mm	Thorlabs	C171TMD-B	1
Beam Splitter: 50:50 Non-Polarizing Beamsplitter Cube	Thorlabs	BS011	1
Photodiode	Thorlabs	PDA100A	1

Table 10.1: Breakdown of high-NA cavity setup components.

High-NA Cavity	Symbol	Detail
Cavity Length	d	4 mm
Radius of Curvature	ROC	10 mm
Mirror Diameter	Φ	7.75 mm
Free Spectral Range	FSR	37.5 GHz
Waist Size	w_0	31.5 μm
Rayleigh Range	z_R	4.0 mm
Highest Mode Number	N	278
Highest NA	NA	0.67 rad
Finesse	$\mathcal{F}$	3140 (expected)

Table 10.2: Summary of the high-NA cavity setup.

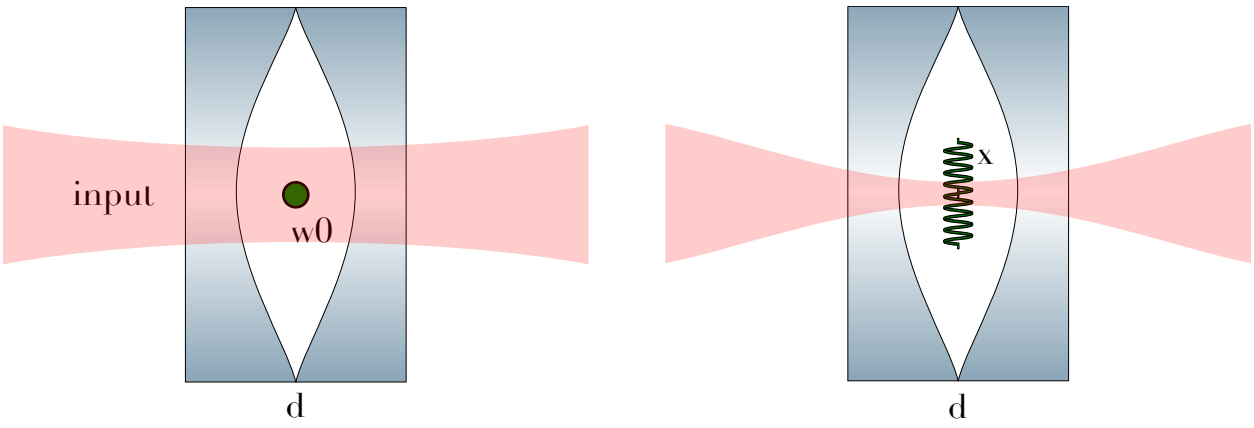

Figure 10.1: Schematic of the high-NA cavity design. The cavity consists of two mirrors with a radius of curvature (ROC) of 10 mm, positioned 4 mm apart, forming the cavity length (d). The mirrors have a diameter of 7.75 mm, accommodating a waist size (w_0) of 31.5 μm. Left, The beam waist parameter is shown when the cavity is in TEM_{00} mode. Right, the cavity excites a higher-order mode N with a minimum diffraction feature of size x.

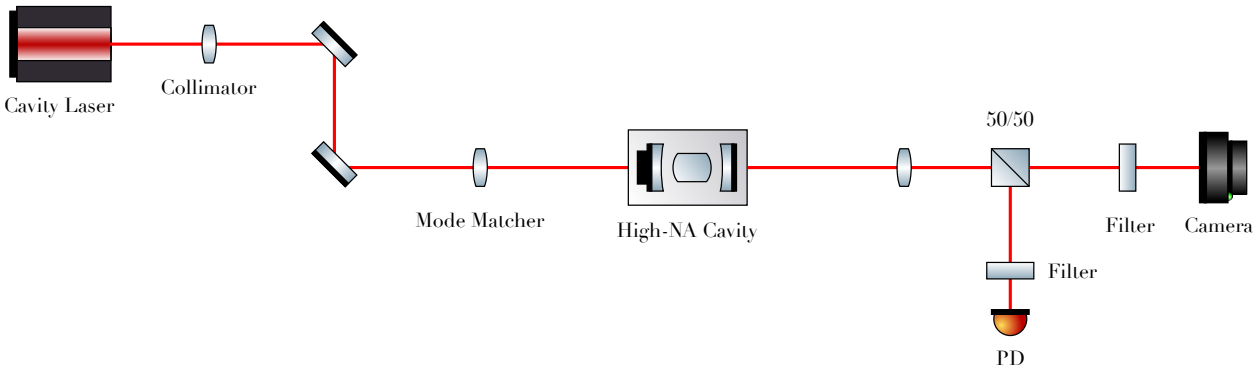

Figure 10.2: Schematic of the High-NA Cavity Setup: The cavity laser beam is collimated and mode-matched to the high-NA cavity. Initially coupled to the 00 mode, the input beam is laterally displaced to excite higher-order modes. The resulting output from the cavity is monitored using both a camera and a photodiode.

10.3 Results and Discussion

Camera images of the cavity output are captured (Fig. 10.3), revealing fringes along the axis of the offset as the mode number increases. Following image processing, we slice the mode along the axis to extract a 1D intensity profile, and employ a peak-finding software to count the number of fringes, which allows us to deduce the mode number (Fig. 10.4). As anticipated from the behavior of Hermite-Gaussian modes (Sec. 4.6), the mode size increases with mode number as $\sqrt{N}$ and the fringe size decreases with mode number as $1/\sqrt{N}$. Moreover, a threshold offset appears to exist beyond which the quality of the mode deteriorates significantly; at this point, the mode becomes uneven, exhibiting bending and splitting.

The design achieves a highest mode number N of 278. The smallest feature observed is

$$x = \frac{\sqrt{N} w_0}{N} = \frac{31.5\ \mu\text{m}}{278} = 1.89\ \mu\text{m} \tag{10.7}$$

This corresponds to a numerical aperture half angle θ of

$$\theta = \arcsin\left(\frac{\lambda n}{w_0}\sqrt{N}\right) = \arcsin\left(\frac{780\text{ nm} \times 1.4537}{31.5\ \mu\text{m}}\sqrt{278}\right) = 0.67\text{ rad} = 38.57^\circ \tag{10.8}$$

The solid angle Ω subtended by both forward and backward direction is:

$$\Omega = 4\pi(1 - \cos\theta) = 4\pi(0.2167) \approx 4\pi \times 0.2167 \approx 2.723\text{ steradians} \tag{10.9}$$

Since we only block 22% of the spontaneous emission angle, this setup is insufficient for enhancing cooperativity. To put this into perspective, achieving 99% suppression of spontaneous emission—comparable to the performance of medium-finesse mirrors—would require a half-angle of 82 degrees.

Access to higher-order modes may be constrained by several factors. One significant issue could be the strain on the mirrors along an axis, which might impede our ability to

efficiently couple to Hermite-Gaussian (HG) modes. Additionally, the non-normal incidence on the mirror coatings results in large AOI, particularly given the small diffraction features involved, which can dramatically reduce reflectivity. We reverse-engineered the mirror coating modeling function provided by the supplier, transforming the reflectivity data from an AOI of 0 degrees to an AOI of 10 degrees, and then extrapolated the reflectivity at an AOI of 40 degrees (Fig. 10.5). The results indicate that the reflectivity at this angle would be significantly low at our wavelength of interest. Furthermore, the presence of spherical aberration, due to the mirrors not being perfectly parabolic, adds complexity to the coupling efficiency.

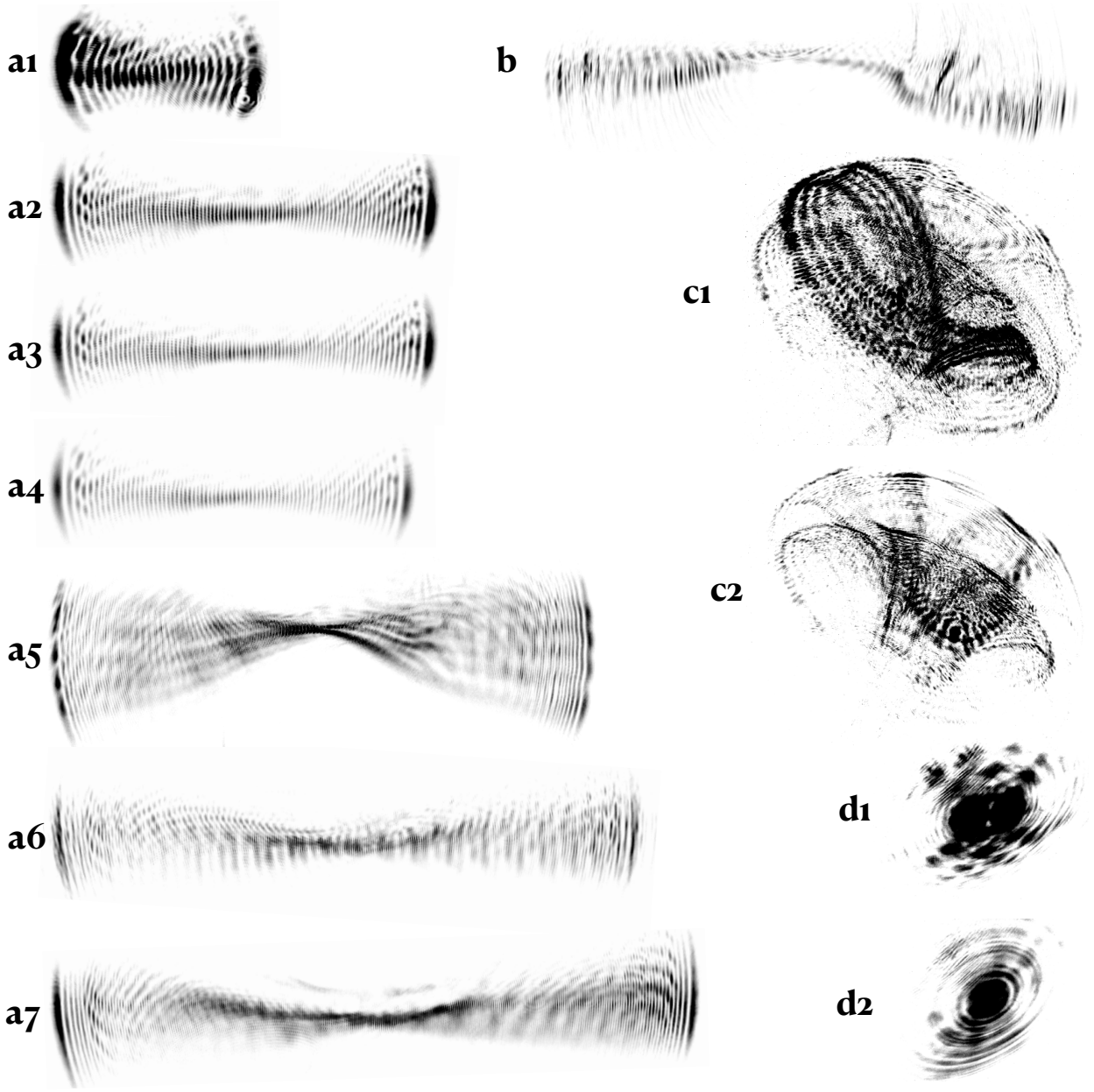

Figure 10.3: High-NA cavity output images. **a1**-**a7**, Evolution of cavity modes as the input beam is progressively offset in one transverse direction. **b**, Degradation in beam quality due to excessive transverse offset, potentially caused by mirror aberrations or losses. **c1**-**c2**, Superposition of various Hermite-Gaussian modes, resulting in distinctive and intriguing patterns. **d1**-**d2**, Cavity tuning to nearly excite the pure 01 and 00 modes, respectively.

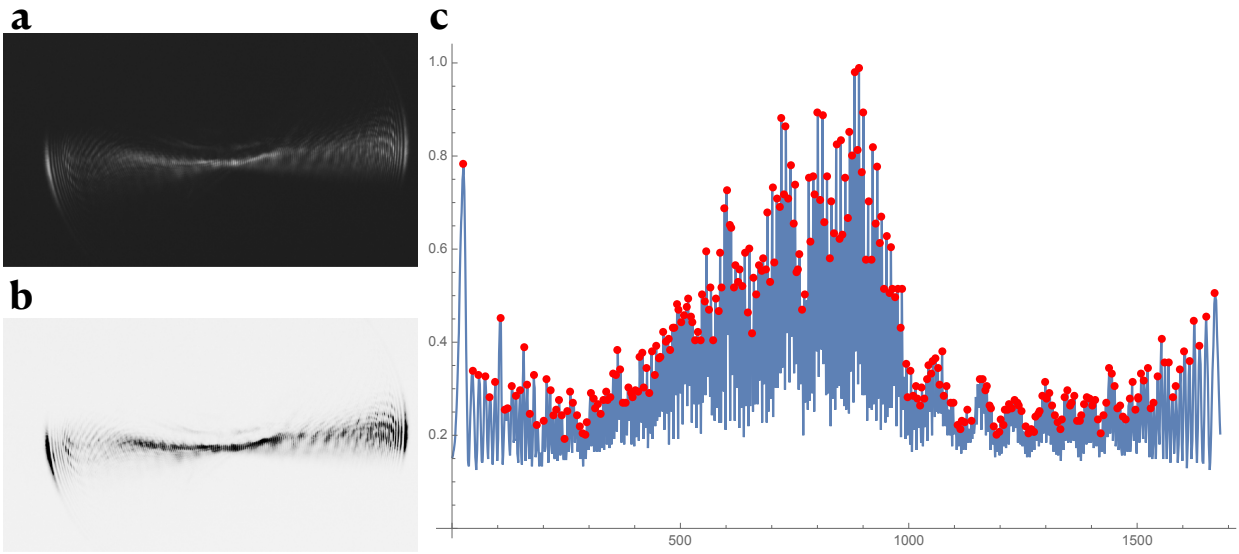

Figure 10.4: Sequence for data analysis of high-NA cavity output images. **a**, The original output image captured by the camera, where white fringes indicate areas of higher intensity. **b**, The inverted image with adjusted contrast to enhance visibility. **c**, The processed image, sliced along a chosen axis, is then analyzed by a mode counter to determine the number of peaks along that axis. In this instance, 287 fringes were identified, corresponding to mode $l = 287$.

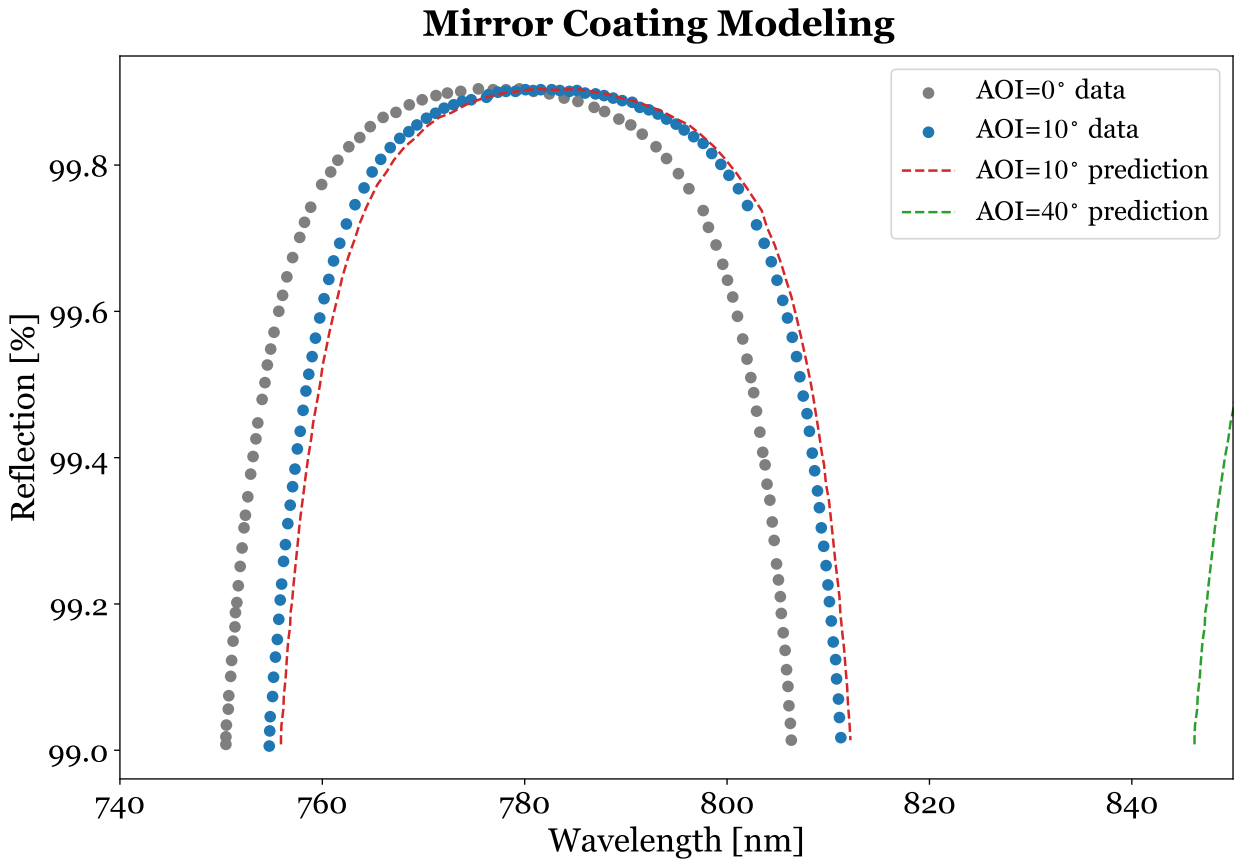

Figure 10.5: Reverse-engineering the mirror coating modeling function provided by the supplier. Reflectivity data was transformed from 0 degrees to 10 degrees and then extrapolated to predict the reflectivity at 40 degrees. The predictions for 10 degrees closely match the provided data, validating our model and indicating that reflectivity at 40 degrees would be significantly low at our wavelength of interest.

10.4 Conclusion

Our design achieved a highest mode number of 278, corresponding to a numerical aperture half-angle of 38 degrees. This setup only managed to suppress 22% of the emission, which is insufficient for significantly enhancing cooperativity. As we moved further in the transverse direction, we noticed a deterioration in mode shape and fainter intensity, likely due to factors such as spherical aberration, mirror imperfections, strain, and issues with high AOI mirror coatings. However, with advancements in mirror coating technology, this project could become viable again in the future.

CHAPTER 11
ENHANCING RYDBERG COUPLING WITH CONFOCAL CAVITY

11.1 Introduction

Rydberg atoms are atoms with one of their electrons excited to a very high principal quantum number, giving them unique properties such as large size, long lifetimes, strong interactions (including blockade effects [19]), and high sensitivity to external fields. These distinctive characteristics make Rydberg atoms crucial in various applications, including quantum information processing [20–22], the simulation of many-body quantum physics [23], and precision metrology.

To maximize the benefits of Rydberg physics, it is often necessary to enhance the coupling between the Rydberg state and other atomic states, typically requiring a blue build-up cavity. Ideally, such a cavity should allow precise alignment with the atom without the need for in-vacuum adjustment knobs, which can complicate the experimental setup. This is where a confocal cavity becomes particularly advantageous. A confocal cavity, where the focal points of the two mirrors overlap at the cavity's center, is less sensitive to misalignment and allows for easier positional adjustments compared to standard cavities.

In a typical cavity, misalignment can significantly diminish the atom-cavity interaction. However, the unique geometry of a confocal cavity ensures that even if one mirror is tilted, the center of curvature remains on the surface of the opposite mirror, only slightly shifting the optical axis. This property makes the confocal cavity highly beneficial for optical designs where some degree of misalignment is inevitable or even desirable.

Confocal optical cavities are essential tools in the study of light-matter interactions, particularly in areas such as quantum optics and laser physics. These cavities, characterized by their equal-radius mirrors spaced at their radius of curvature, offer unique advantages

including a large mode volume and insensitivity to misalignment. The confocal configuration ensures that the optical modes are highly degenerate, simplifying the analysis and utilization of these modes for various applications. This chapter provides an overview of the principles and experimental considerations in the study of confocal cavities, emphasizing the practical techniques employed to achieve and maintain confocal alignment and the significance of these cavities in advancing our understanding of optical phenomena.

11.2 Experimental Methods

In the confocal cavity setup (Fig. 11.1), the cavity laser is collimated, phase-shifted, and directed into the confocal cavity. An optical window is positioned just before the confocal cavity, enabling horizontal or vertical displacement of the beam from the optical axis without altering the angle of incidence. This setup facilitates the excitation of higher-order modes within the confocal cavity. The output from the cavity is divided by a beam splitter, directing part of the beam to a photodiode path and the other part to a camera path.

Key components of the confocal cavity setup are summarized in Tab. 11.1. The confocal cavity is made of two fused silica plano-concave mirrors (Layertec, PN: 144220) each with an ROC of 50 mm, a diameter of 12.7 mm, and 99.86% reflectivity. A 2-inch N-BK7 broadband precision window (Thorlabs, PN: WG12012-B) ensures that the incoming beam be displaced laterally without tilt. Light is focused using a 50.0 mm focal length achromatic doublet lens (Thorlabs, PN: AC254-050-B) and a 3.1 mm aspheric lens for fiber coupling (Thorlabs, PN: C330TMD-B). A 50:50 non-polarizing beamsplitter cube (Thorlabs, PN: BS011) divides the light path. The setup also includes a camera and a photodiode (Thorlabs, PN: PDA100A) for alignment and detection, ensuring optimal performance of the system.

The beam waist parameter w_0, according to Eq. 4.41, is

$$w_0 = \sqrt{\frac{\lambda d}{2\pi}\sqrt{\frac{2R}{d} - 1}} = \sqrt{\frac{780 \text{ nm} \times 50 \text{ mm}}{2\pi} \times 1} = 78.8 \ \mu\text{m} \tag{11.1}$$

For a confocal cavity the spot sizes at the mirrors are $\sqrt{2}$ times the waist size at the cavity center, so

$$w_1, w_2 = \sqrt{2} w_0 = 111\ \mu\text{m} \tag{11.2}$$

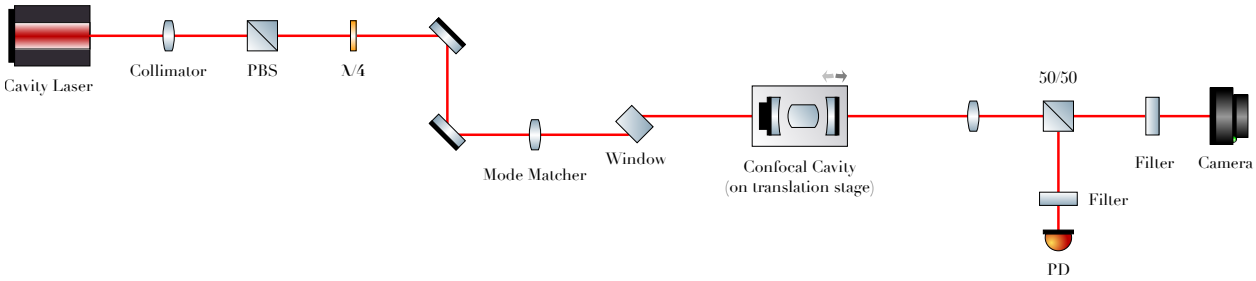

Figure 11.1: Schematic of the confocal cavity setup. An optical window is employed to shift the beam laterally upon entering the confocal cavity without altering the angle of incidence, to excite higher-order modes. The resulting output from the cavity is monitored using a camera and a photodiode.

Confocal Cavity	**Supplier**	**PN**	**Qty**
Cavity Mirror: fused silica pl-concave, diameter Φ=12.7 mm, ROC = 50 mm, AR coated, reflectivity R=99.86%	Layertec	144220	2
Window: Φ=2" N-BK7 Broadband Precision Window, AR Coated: 650 - 1050 nm, t = 12 mm	Thorlabs	WG12012-B	1
Lens: f = 50.0 mm, Φ =1" Achromatic Doublet, ARC: 650 - 1050 nm	Thorlabs	AC254-050-B	1
Asphere: for fiber coupling, f = 3.1 mm	Thorlabs	C330TMD-B	1
Beam Splitter: 50:50 Non-Polarizing Beamsplitter Cube	Thorlabs	BS011	1
Mirror Mount: for Φ=2" optics	Thorlabs	KM200	1
Photodiode	Thorlabs	PDA100A	1

Table 11.1: Breakdown of confocal cavity setup components.

Confocal Cavity	Symbol	Detail
Cavity Length	d	50 mm
Radius of Curvature	ROC	50 mm
Mirror Diameter	Φ	12.7 mm
Free Spectral Range	FSR	3 GHz
Waist Size	w_0	78.8 μm
Rayleigh Range	z_R	25 mm
Finesse	$\mathcal{F}$	620
Odd/Even Purity		1:40
Maximum Transmission	$T_{\max}$	20%

Table 11.2: Summary of the confocal cavity setup.

11.3 Results and Discussion

The beam is laterally displaced without tilt by rotating a thick optical window on a rotational mount. Initially, the position of the incident beam was recorded by correlating the number of knob rotations using a specific formula. As shown in Fig. 11.2, let t represent the thickness of the optical window, θ_1 the incident angle to the window, θ_2 the refractive angle, l the path length inside the window, and d the lateral beam displacement. Then we have the following relationship:

$$d = l\sin(\theta_1 - \theta_2) = \frac{t}{\cos\theta_2}\sin(\theta_1 - \theta_2) \tag{11.3}$$

where $\theta_1 = 0.00505$ rad $\cdot$ rev.

However, the required rotation angles eventually exceeded the limits of the rotational mount. To address this, we developed a method to linearly calibrate the number of rotations to the cavity output position observed on the camera. This allows us to deduce the incident beam position from the camera data. An example of calibration procedure is included in Fig. 11.4.

We have experimentally observed **confocality**. On the camera, when the incident beam goes through the center of the cavity, only one output beam with significant power is observed. However, when the incident beam is offset, both the original beam location and its

parity partner show significant power and move together symmetrically. On the photodiode, when the incident beam goes through the center of the cavity, the transmission is at its highest, with only one peak per free spectral range (FSR), corresponding to the degenerate even modes. When the incident beam is offset, transmission quickly reduces by about half, and odd modes appear in the middle of the FSR between the even modes. All even modes remain degenerate, as do all odd modes.

Cavity transmission is plotted against lateral displacements for both experimental rounds in Figs. 11.5-11.8. A **"pedestal" structure** is observed in which the cavity transmission decreases to a fraction of its initial value as the beam is laterally displaced from the center. The theory for the confocal cavity is described in Sec. 4.6 and illustrated below in Fig. 11.3. When the optical beam is precisely aligned with the center of the cavity, the dominant mode excited is the fundamental TEM_{00} mode, which is degenerate with all even modes. This mode is characterized by a single, well-defined peak at the center of the beam profile, leading to a higher transmission peak due to efficient excitation by the incident beam. As the beam is laterally displaced from the central axis, higher-order modes become more prominently excited. In a confocal cavity, this can be thought of as resonantly exciting a "ring" or "bowtie" mode, which traverses the cavity twice before retracing its path. This mode has two lobes that strike the mirrors at four different locations, two on the input side and two on the output side. In this scenario, the excitation is asymmetric, with only one lobe being effectively excited. This results in an impedance mismatch and a fourfold reduction in the transmission profile, forming the "pedestal" structure.

Cavity transmission can be **optimized** by adjusting the cavity length to restore confocality. As the beam is displaced laterally along an axis, the effective radius of curvature (ROC) decreases in the other transverse direction as the beam moves outward. Unoptimized and optimized transmissions are plotted against the transverse displacement of the incident beam, showing a consistent improvement in transmission when the cavity length is properly

compensated. We have experimentally observed that the transmission remains above 5% for approximately four waist sizes before it begins to deteriorate further.

In principle, transmitted peak intensity could be 100%, but the actual intensity is around 20% at its highest. Considering only the mirror losses inside the cavity, according to Eq. 4.9, we should still expect a finesse of about 2000 or more if the cavity is well-aligned,

$$\mathcal{F} = \frac{\pi\sqrt{r}}{1-r} = \frac{\pi\sqrt{99.86\%}}{1-99.86\%} = 2242 \tag{11.4}$$

The discrepancy between the observed and predicted finesse and transmission height arises from the imperfect degeneracy of higher-order modes, which prevents all the even or odd modes from constructively interfering with one another, ultimately resulting in lower transmission and finesse values.

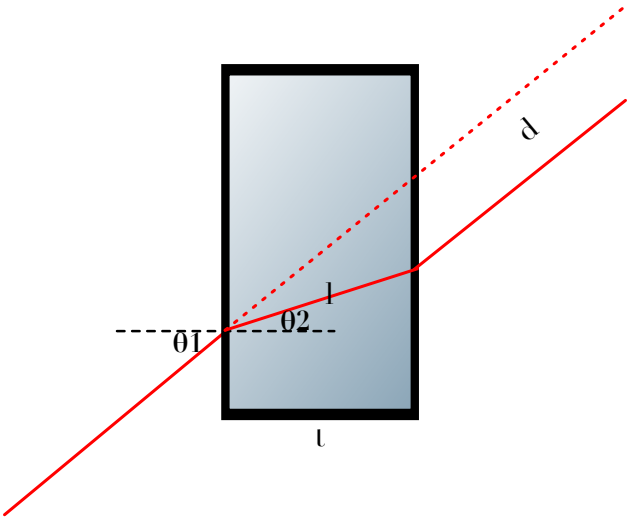

Figure 11.2: Diagram illustrating the relationship between the beam displacement and the incident angle, which corresponds to the rotational angle of the optical window.

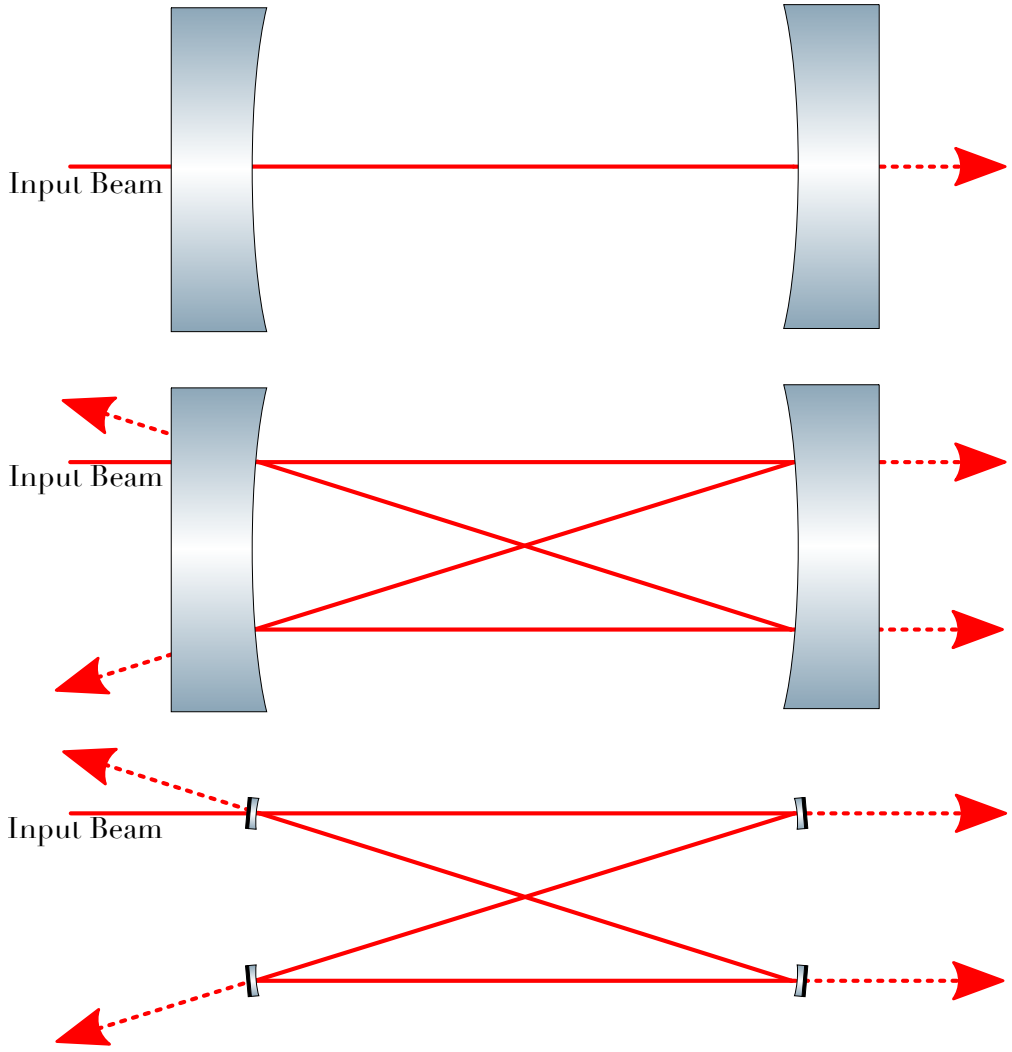

Figure 11.3: Diagram illustrating the origin of the pedestal structure in transmission vs. displacement plots. **Top**, When only the TEM00 mode is excited, the input beam efficiently couples to the confocal cavity mode. **Middle**, When the beam is displaced laterally, the cavity is in a ring or bowtie mode. However, the input beam only effectively excites one of the two input ports, leading to a fourfold reduction in transmission. **Bottom**, the confocal cavity in ring mode can be thought of as a four-mirror bowtie cavity.

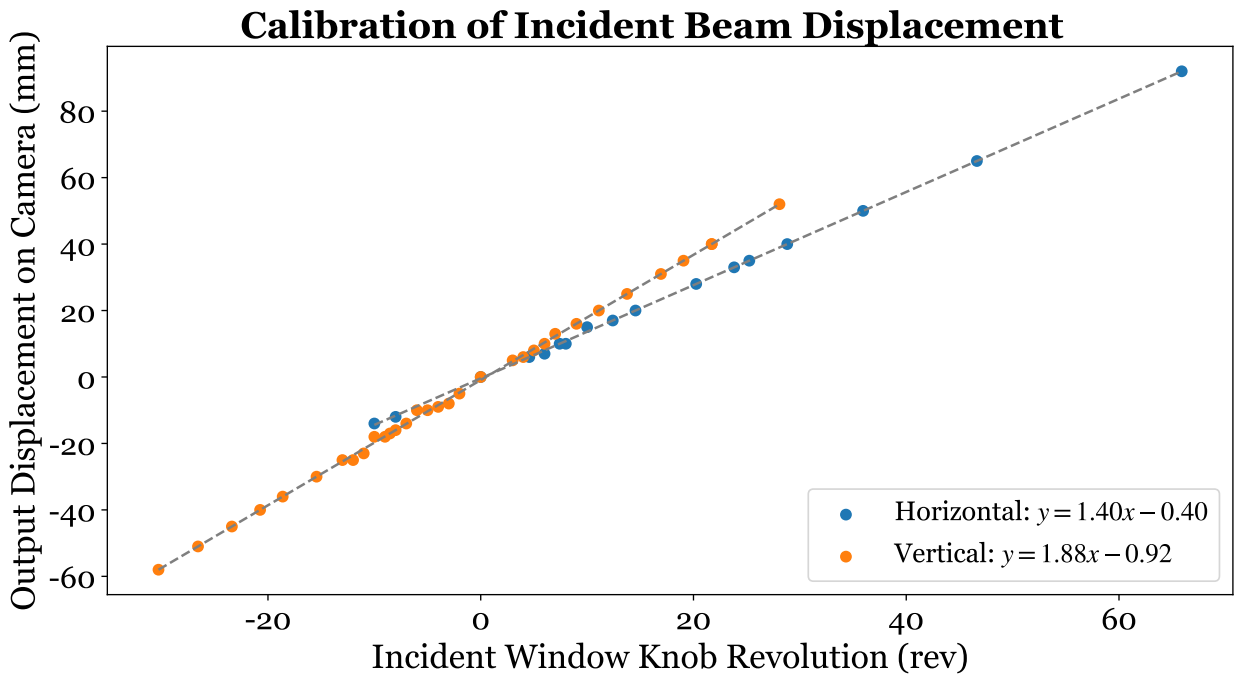

Figure 11.4: Calibration plot of input window rotation versus beam displacement, aiding in precise beam alignment with the confocal cavity.

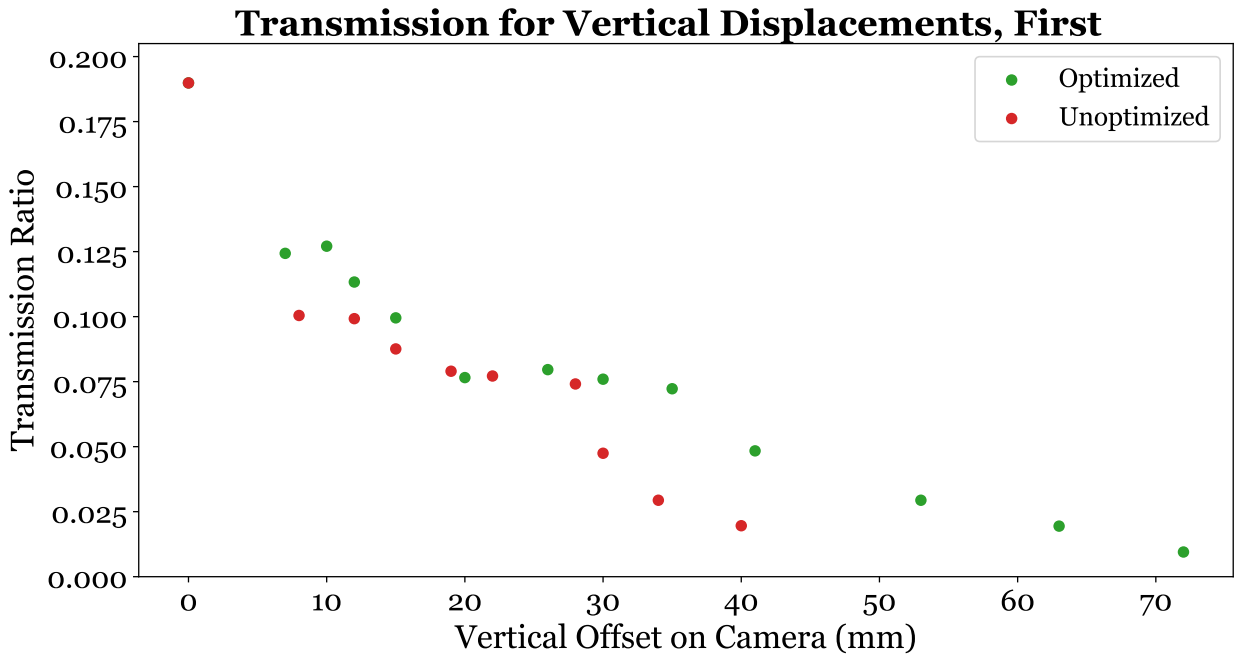

Figure 11.5: Transmission profile of a confocal cavity with vertical beam displacement, showing higher transmission after confocality optimization. The pedestal shape reflects the confocal cavity's expected behavior.

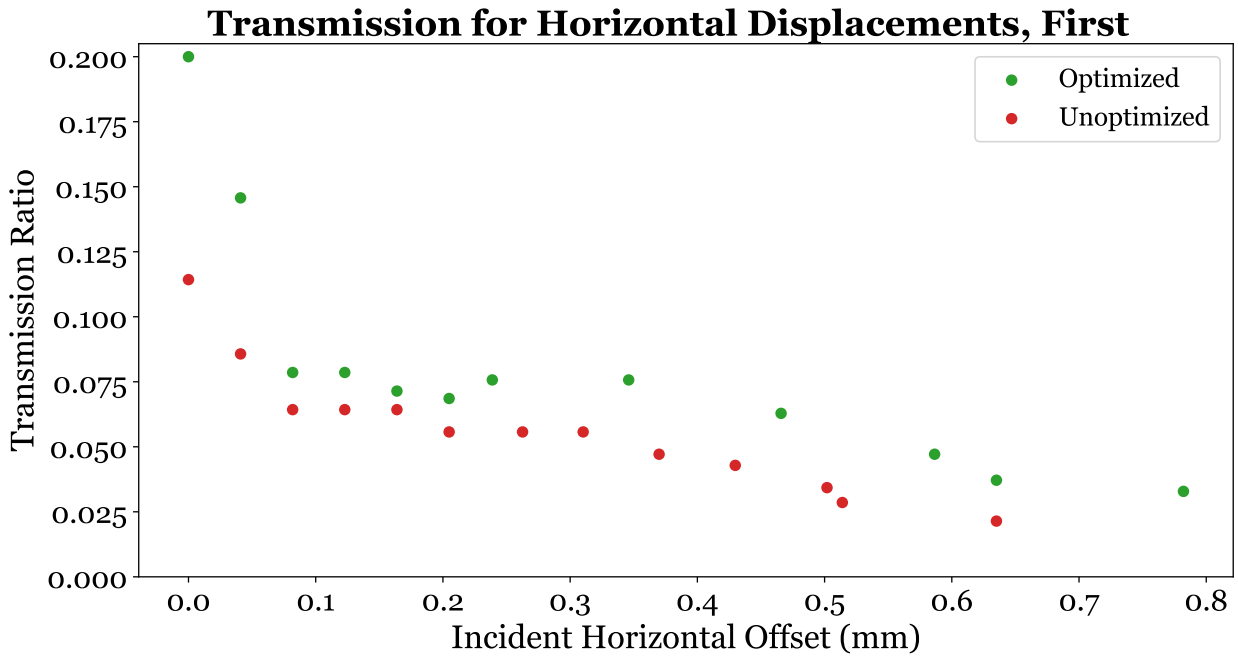

Figure 11.6: Transmission profile of a confocal cavity with horizontal beam displacement, showing higher transmission after confocality optimization. The pedestal shape reflects the confocal cavity's expected behavior.

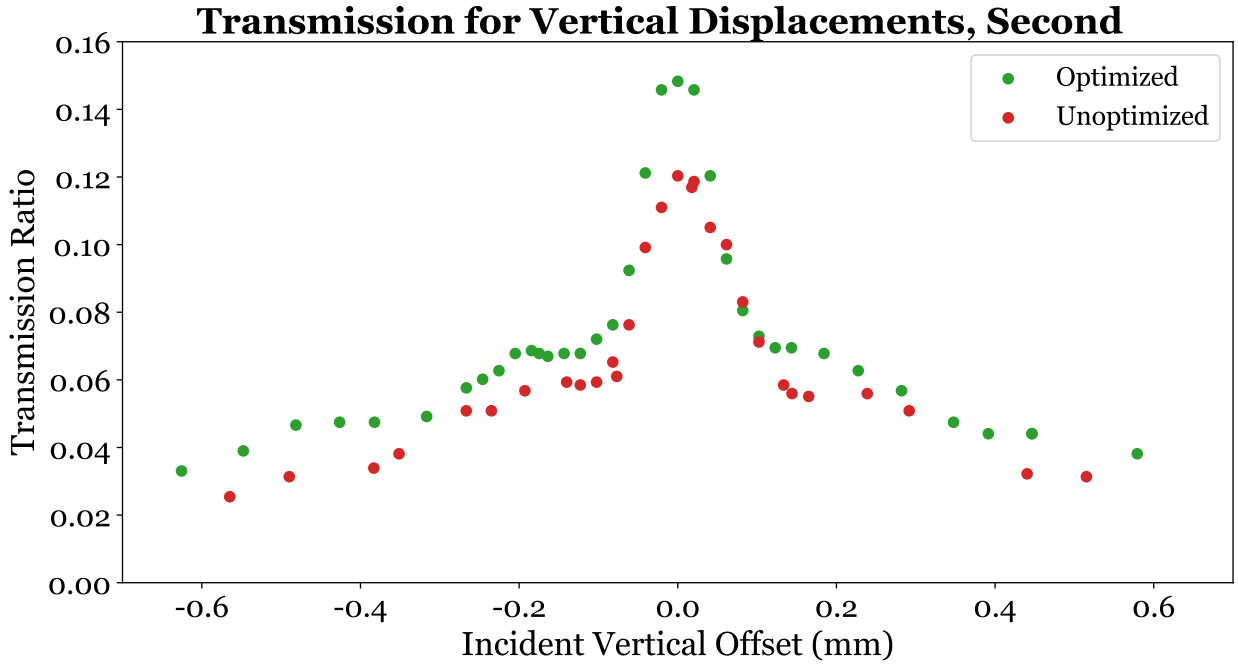

Figure 11.7: Transmission profile of a confocal cavity with vertical beam displacement, showing higher transmission after confocality optimization. The pedestal shape reflects the confocal cavity's expected behavior.

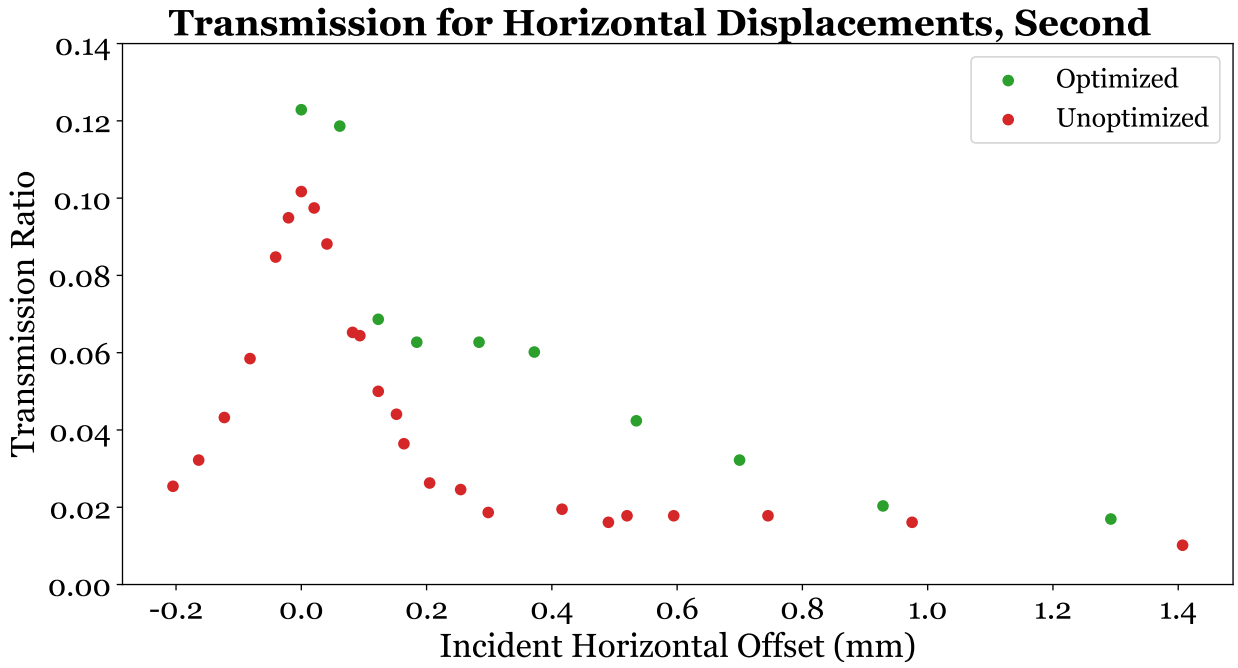

Figure 11.8: Transmission profile of a confocal cavity with horizontal beam displacement, showing higher transmission after confocality optimization. The pedestal shape reflects the confocal cavity's expected behavior.

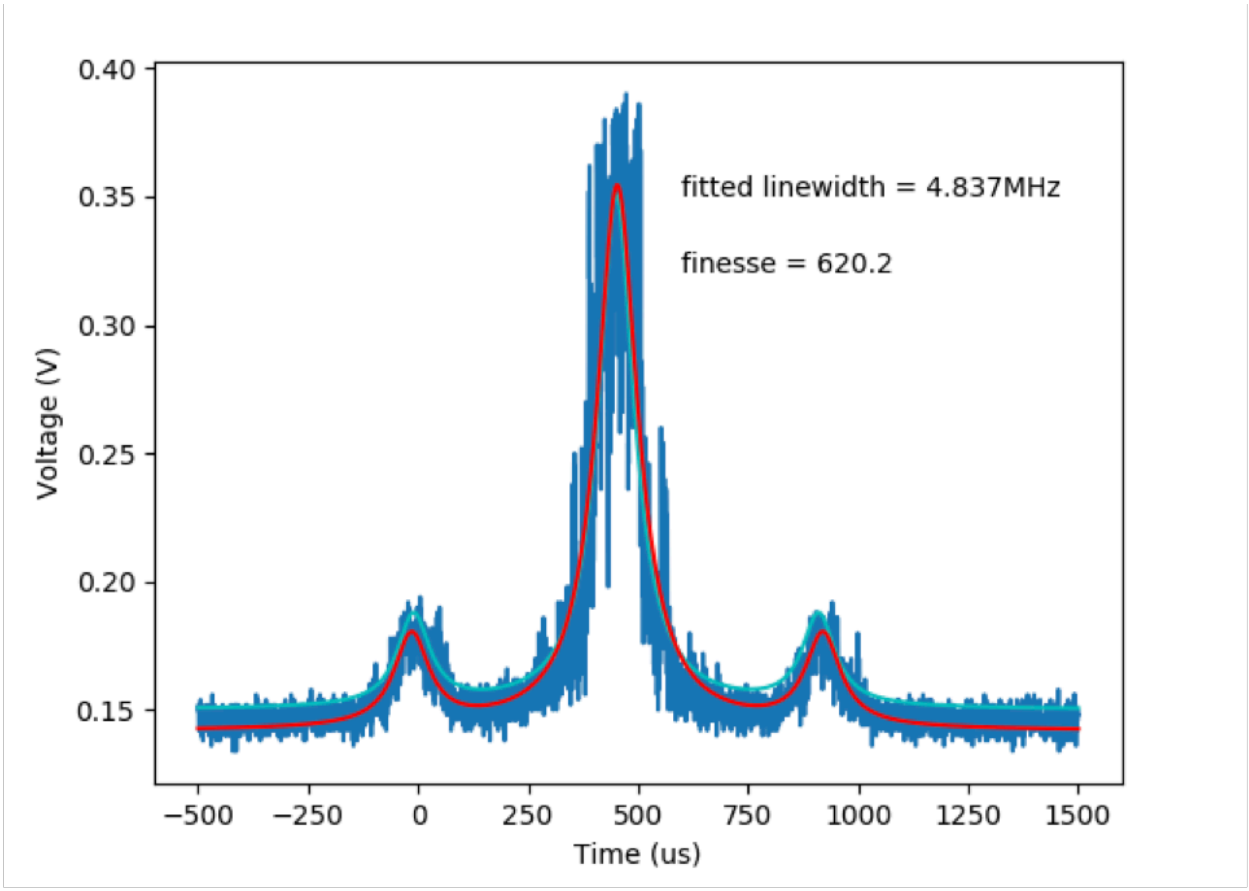

Figure 11.9: A finesse sideband measurement records a finesse of 620.

11.4 Future Directions

A hybrid setup containing both IR and UV optics was designed and built. The UV laser was constructed from scratch by phase-locking a 532 nm green laser. This setup has been preliminarily analyzed, although promising data has not yet been obtained.

In the UV/IR hybrid confocal cavity setup, outlined in Tab. 11.3, both IR and UV lasers are introduced into the beam path via a dichroic beamsplitter and are precisely aligned using irises. Once the cavity is locked to a specific mode, introducing UV power from the backside of the mirror would cause localized heating and deformation of the mirror coating, leading to a change in the effective cavity length and resonant frequencies. This would allow for effective use of UV laser-induced mirror deformation alongside IR optical measurements, providing a versatile and precise setup for advanced optical experiments.

The setup includes a harmonic beamsplitter (Thorlabs, PN: HBSY0534) that reflects UV wavelengths (266 nm, 355 nm) and transmits IR wavelengths (532 nm, 1064 nm). A bandpass filter (Semrock, PN: LL01-785-12.5) is positioned in the beam path at an angle to filter the IR light, ensuring it predominantly contains the 780 nm wavelength. UV optics are used for beam focusing and redirecting.

Second-harmonic generation requires photons to obey conservation of energy and momentum: $\omega_1 + \omega_2 = \omega_3$ and $n_1\omega_1 + n_2\omega_2 = n_3\omega_3$. These conditions can be achieved with a birefringent material, where the refractive indices for the ordinary (n_o) and extraordinary rays (n_e) differ. By conservation of momentum:

$$\frac{\sin^2\theta}{n_e^2(2\omega)} + \frac{\cos^2\theta}{n_o^2(2\omega)} = \frac{1}{n_o^2(\omega)} \tag{11.5}$$

Equivalently,

$$\sin\theta^2 = \left(\frac{1}{n_o^2(\omega)} - \frac{1}{n_o^2(2\omega)}\right) / \left(\frac{1}{n_e^2(2\omega)} - \frac{1}{n_o^2(2\omega)}\right) \tag{11.6}$$

For BBO crystal specifically,

$$\sin\theta^2 = \left(\frac{1}{1.675^2} - \frac{1}{1.7571^2}\right) / \left(\frac{1}{1.6139^2} - \frac{1}{1.7571^2}\right) \tag{11.7}$$

$$\theta = 47.40^\circ \tag{11.8}$$

is our phase-matching angle.

UV/IR Hybrid Confocal Setup	**Supplier**	**PN**	**Qty**
UV Laser: broken	-	DC30H-266	1
BBO Crystal: 5 mm x 5 mm x 5 mm, $\theta = 47.7^\circ$, $\phi = 90^\circ$	Eksma Optics	BBO-0423-07	1
Short Bandpass Filter: 300 nm blocking edge short-pass filter	Semrock	FF01-300	1
Thermal Sensor	Ophir	30A-BB-18	1
Harmonic Beamsplitter: $\Phi = 1/2$", Reflects 266 nm and 355 nm, Transmits 532 nm and 1064 nm	Thorlabs	HBSY0534	1
Filter: bandpass filter, $\Phi = 12.5$ mm	Semrock	LL01-785-12.5	1
UV Mirror: Φ= 1" Nd:YAG Mirror, 262 - 266 nm, 0° to 45° AOI	Thorlabs	NB1-K04	2
UV Lens: f = 50.0 mm, Φ= 1" UV Fused Silica Plano-Convex Lens, AR Coating: 245-400 nm	Thorlabs	LA4148-UV	1
Asphere: for fiber coupling, $f = 3.1$ mm	Thorlabs	C330TMD-B	1
Beam Splitter: 50:50 Non-Polarizing Beamsplitter Cube	Thorlabs	BS011	1
Mirror Mount: for Φ=2" optics	Thorlabs	KM200	1
Photodiode	Thorlabs	PDA100A	1

Table 11.3: Breakdown of hybrid confocal cavity setup's additional components.

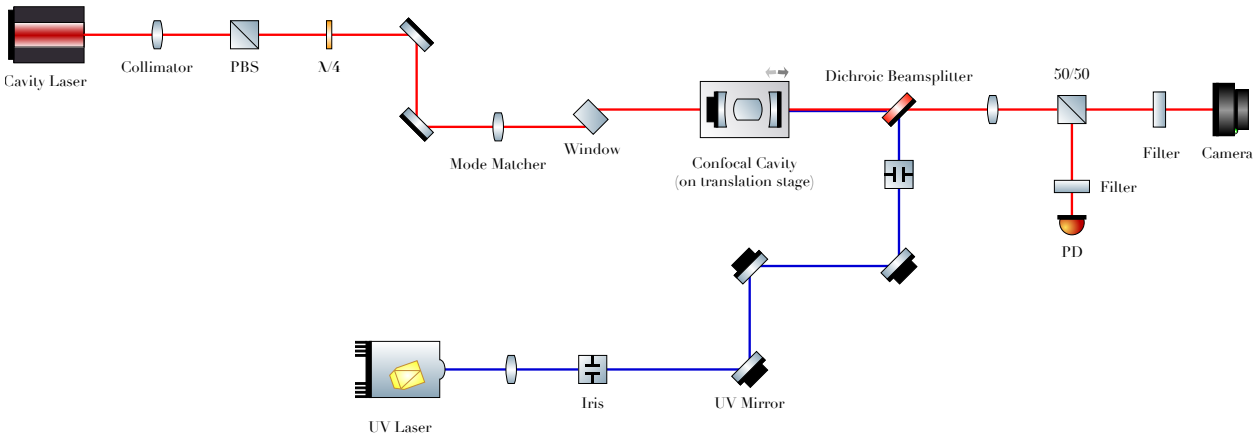

Figure 11.10: Schematic of the confocal cavity setup: Both infrared (IR) and ultraviolet (UV) lasers are introduced into the beam path via a dichroic beamsplitter and are precisely aligned using irises. Once the cavity is locked to a specific mode, introducing UV power from the backside of the mirror would cause localized heating and deformation of the mirror coating, leading to a change in the effective cavity length and resonant frequencies.

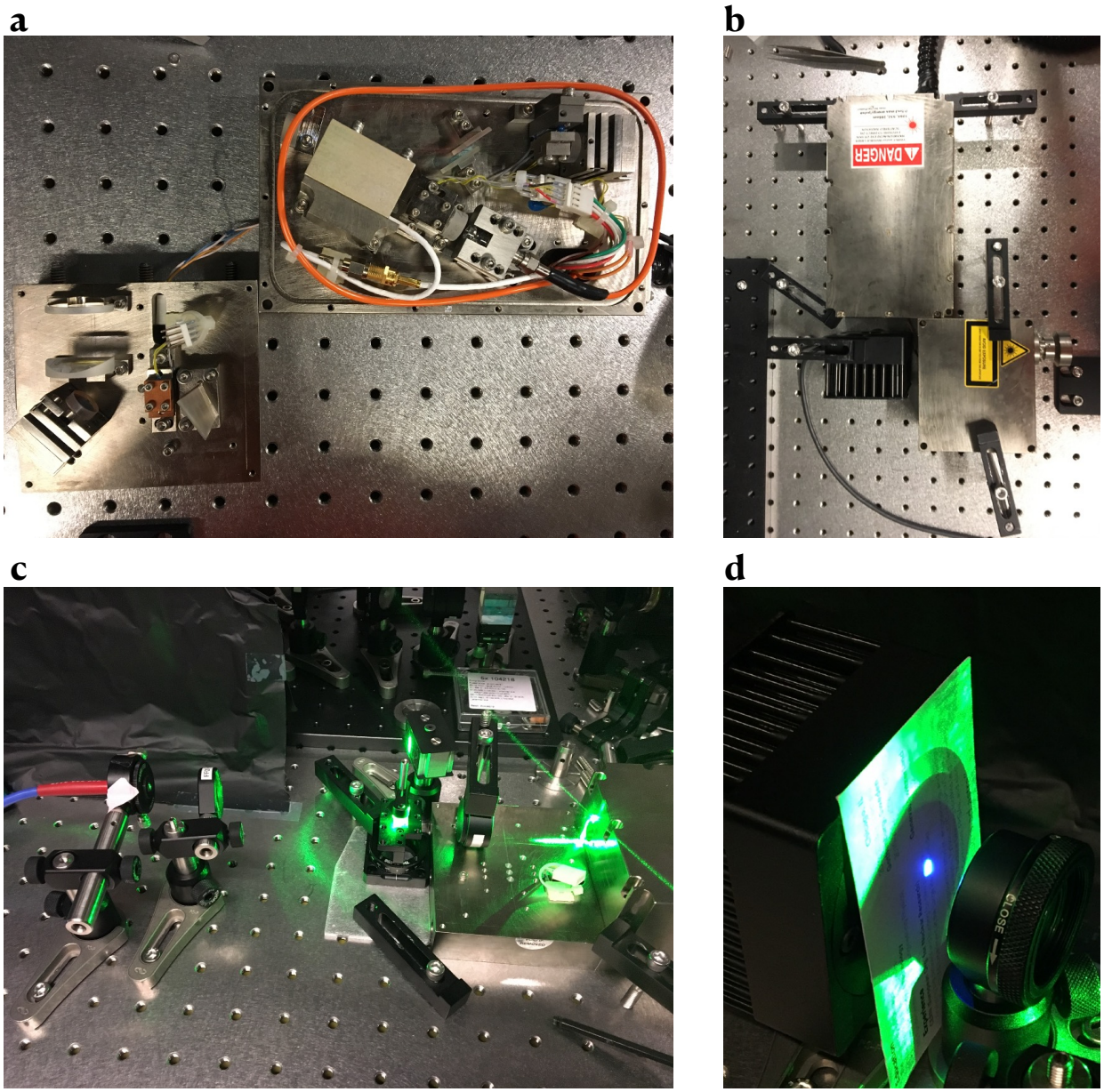

Figure 11.11: The UV laser setup. **a**, Original laser box, with the top right displaying green 532 nm beam generation, and the bottom left showing second harmonic generation to produce the UV 266 nm beam from the 532 nm beam. **b**, Laser box in its enclosure. **c**, Expanded green laser setup for power measurement or beam profiling. **d**, UV beam successfully generated, as seen on the fluorescence business card showing ultraviolet light.

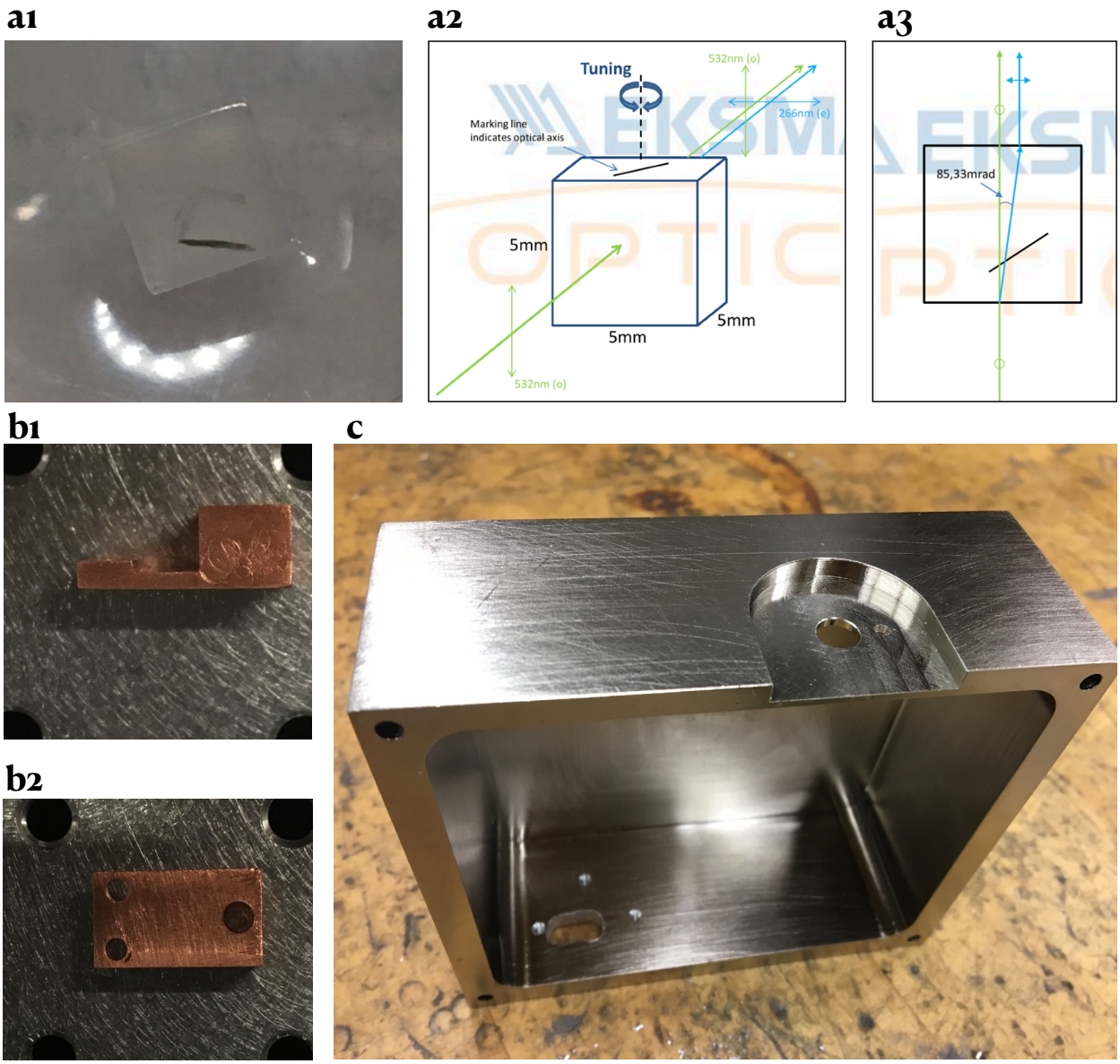

Figure 11.12: New components to fix the UV laser. **a1**, The new BBO crystal. **a2-a3**, Angle diagrams for the BBO crystal, displaying birefringence. **b1-b2**, New copper holders to house the newly introduced BBO crystal. **c**, New housing for the laser module.

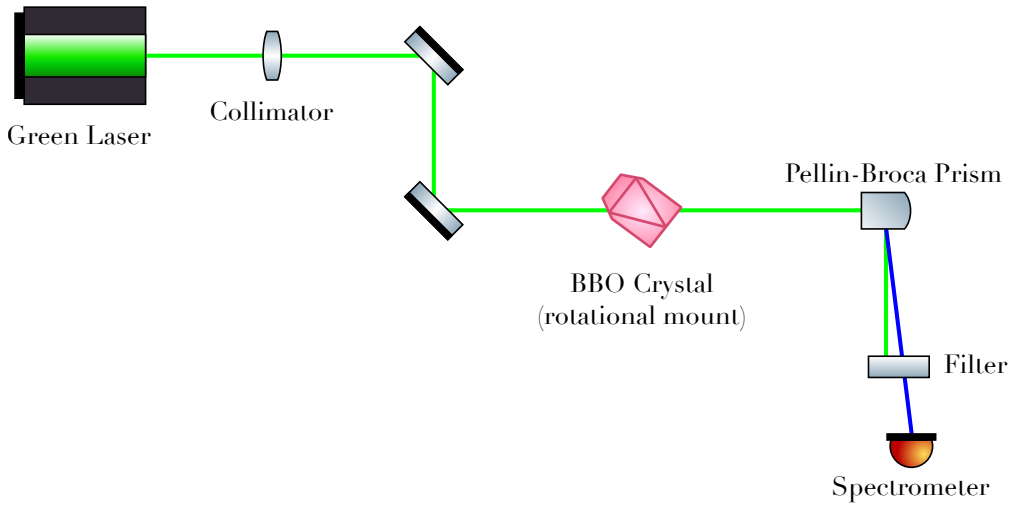

Figure 11.13: Schematic for second-harmonic generation of the UV laser. A new BBO crystal is used to generate the second-harmonic beam. A Pellin-Broca prism spatially separates the residual green beam from the generated UV beam while rotating the entire beam by 90 degrees. A spectrometer is placed after a short-pass filter to measure the UV power.

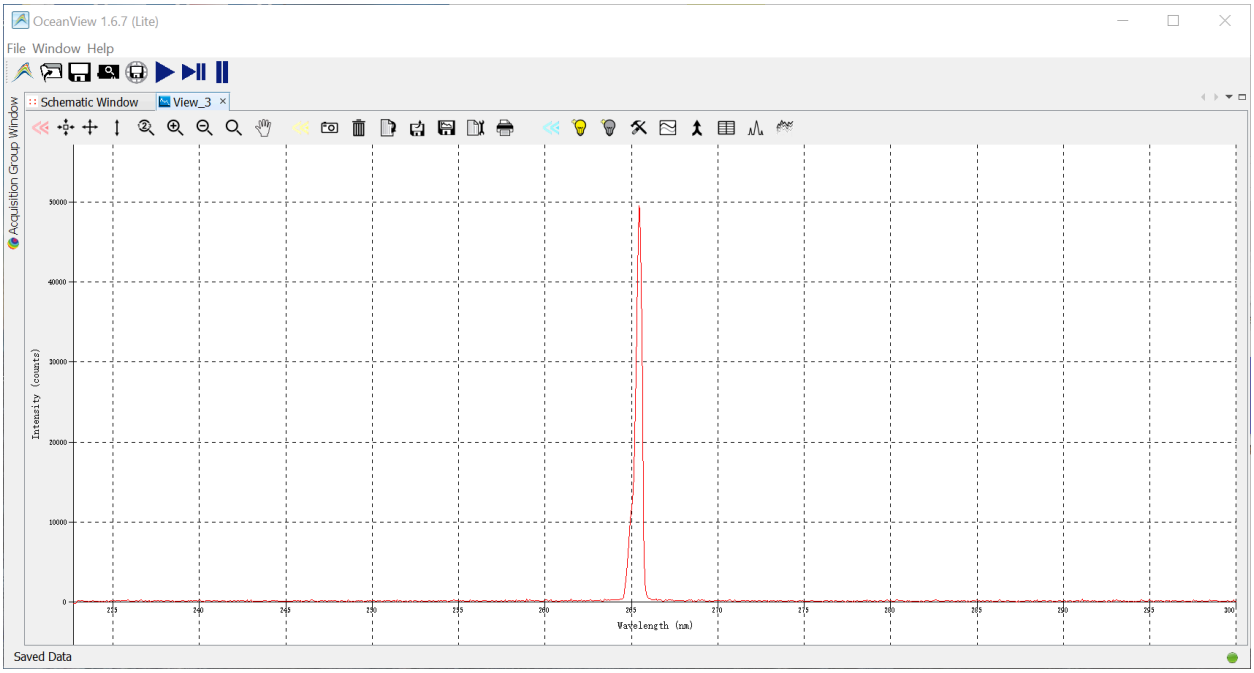

Figure 11.14: Spectrometer measurement of the UV peak, with power plotted against wavelengths.

11.5 Conclusion

Our experiments have successfully demonstrated the confocality of the cavity system. When the incident beam is aligned through the center of the cavity, the camera captures a single output beam with significant power. However, when the incident beam is offset, we observe that both the original beam location and its parity partner exhibit substantial power, moving symmetrically together.

The relationship between cavity transmission and lateral beam displacement has been analyzed, revealing a characteristic pedestal structure. As the beam is laterally displaced from the center, the cavity transmission decreases to a fraction of its initial value. The highest recorded transmission was 20%, and our measurements show that transmission remains above 5% for approximately four waist sizes before deteriorating further. However, this region of high transmission is not sufficiently wide for our purposes. Ideally, the atoms should be displaced far enough from the cavity's center to avoid strong blue power buildup due to interference, which is undesirable for the experiment's goals. This limitation indicates the need for further refinement in the cavity design to achieve optimal performance.

CHAPTER 12
ULTRA-HIGH VACUUM APPARATUS WITH INNOVATIVE LOADLOCK TECHNIQUE

12.1 Introduction

Cavity QED is useful for studying fundamental aspects of quantum mechanics such as decoherence, entanglement, and measurement [24, 25]. Over the past decade, the AMO community has made substantial advances on exerting control over individual trapped atoms [26–28], ensemble of atoms [29–31], ultra-cold atoms in the BEC state [32, 33], and atoms trapped in tweezer arrays [34–36]. This has interesting prospects for quantum information processing [37, 38], secure communication [39], simulation of quantum systems [40–42], and precision sensing [43].

Using cavities in vacuum enriches the scientific efforts of generating entangled states [44], studying decoherence [45], computing with Rydberg arrays [46], and building robust quantum networks [47–49]. Different applications have motivated a great variety of cavity designs, including twisted cavities [50, 51], near concentric cavities [52, 53], fiber cavities [54, 55], off-axis parabolic cavities [56], and lens cavities [57] have been demonstrated, but there remain exciting opportunities to explore new geometries, aberration corrected cavities [57], coupled cavities [58] for atomic physics and quantum information applications.

Integrating and testing exotic cavity geometries with cold atoms is challenging because achieving sufficient vacuum is a months-long process requiring removal of external optics, replacement of in-vacuum optics, baking of the chamber, and re-alignment of external optics. One way around this is cryo-pumping as demonstrated in recent microwave/mmwave to optical transduction experiments [59, 60] and cryogenic cavity optomechanics [61, 62], where all material-constraints are relaxed and bakes are obviated by cryo-pumping. Other methods include putting the cavity *outside* of the vacuum chamber [63, 64] to remove the

need for in-vacuum optics all-together, and using loadlocks [65–68] for rapid cycling. The first option has limitations such as requiring much space for cryogenic technical supplies, needing vibration isolation schemes, differential contraction of materials, and poor piezo performance. The second option limits the cavity geometry to be larger than the vacuum system, increasing the mode waist & reducing the finesse, and thus limiting the achievable single-atom cooperativity [69].

We present a loadlock apparatus designed to optimize the turnaround time for cold atom cavity QED experiments. Our apparatus consists of a science chamber and a loadlock chamber separated by a gate valve, featuring in-vacuum MOT optics, ^{87}Rb dispensers, and a cavity carrier attached to a position manipulator. It supports a sizable cavity structure with maximal optical access to the atoms and exterior laser beams, and rapid cycling when introducing a new cavity.

We characterize its performance by loading and transporting cold ensembles of ^{87}Rb atoms at temperatures below 10 µK, over 4" ($\sim$ 10 cm), in 30 ms. The apparatus offers a 4"×4"×3" ($\sim$ 10 cm×10 cm×8 cm) volume for custom cavity structures, with 40 electrical feedthroughs on plug-and-go connectors for cavity electrodes, MOT quadrupole coils, dispensers, and heating wires.

In this chapter, Sec. 12.2 introduces the innovative loadlock technique. Sec. 12.3 describes the design and components of the UHV System. Sec. 12.4 outlines the assembly and integration procedure of the entire UHV system, and Sec. 12.5 details the assembly of the bare UHV system. Sec. 12.6 describes the operation and maintenance of the UHV system. Sec. 12.7 evaluates the performance of the UHV system.

In the following chapters, we will describe other distinctive elements of the vacuum system, including a cavity carrier platform, an in-vacuum MOT setup, and an atom delivery system.

12.2 Innovative Loadlock Technique

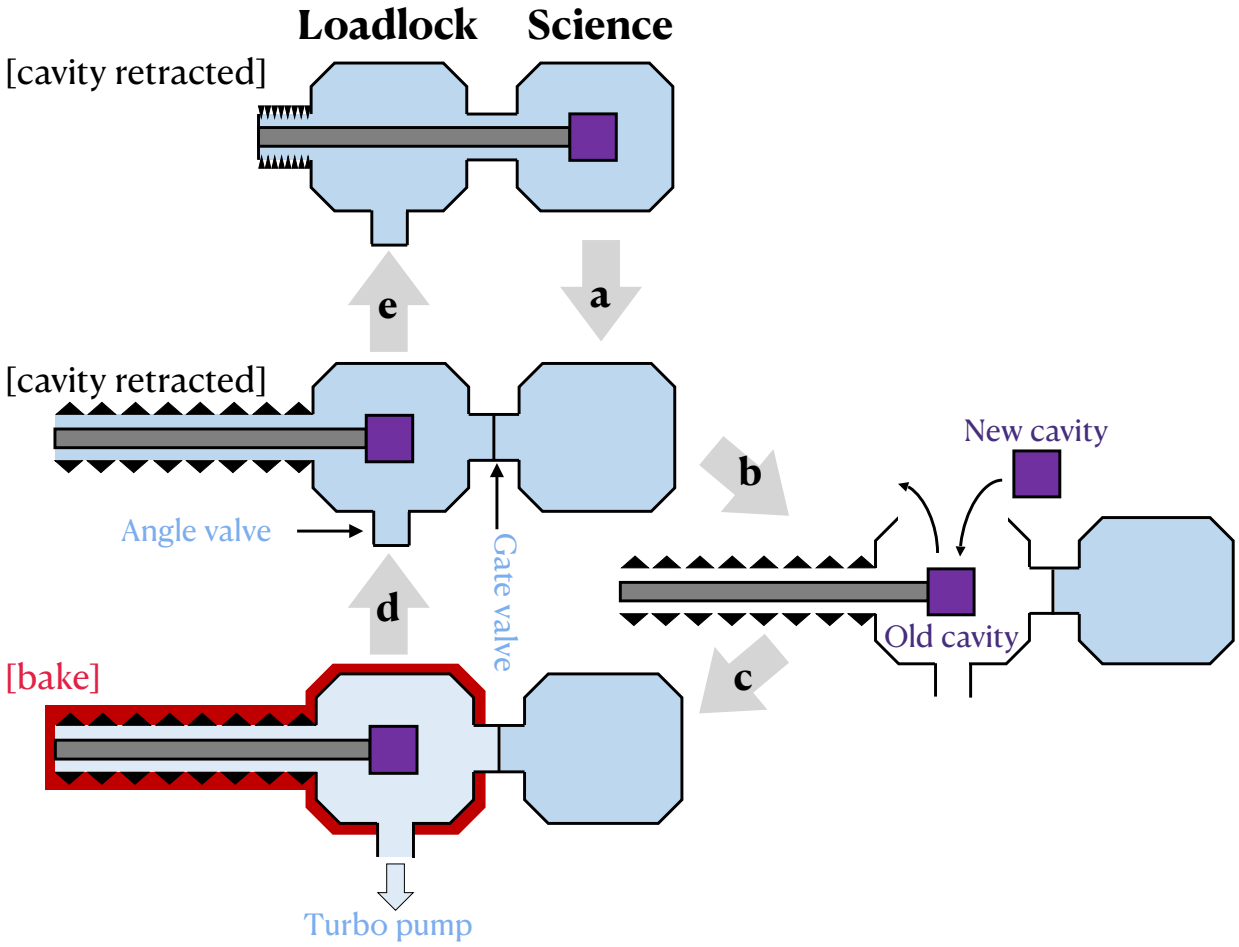

Figure 12.1: The loadlock procedure. A typical cycle of loading a new cavity into an UHV environment requires the following steps: **a**. Manipulate the translator to retract the cavity into the loadlock chamber, close the gate valve. **b**. Vent only the loadlock chamber through the angle valve, open two flanges of the loadlock chamber, install a new cavity. **c.** Close up the loadlock chamber, pump and bake only the loadlock chamber. **d.** Shut the angle valve, cool down the loadlock chamber. **e.** Open the gate valve, manipulate the translator to extend the cavity into the science chamber. The whole process takes about a week.

The loadlock vacuum architecture employs two chambers separated by a gate valve, so venting the auxiliary chamber to air for sample installation need not disrupt the UHV environment of–or optical alignment to–the main chamber. It is a powerful approach used broadly across chemistry such as molecular beam epitaxy [70], scanning electron microscopes, and

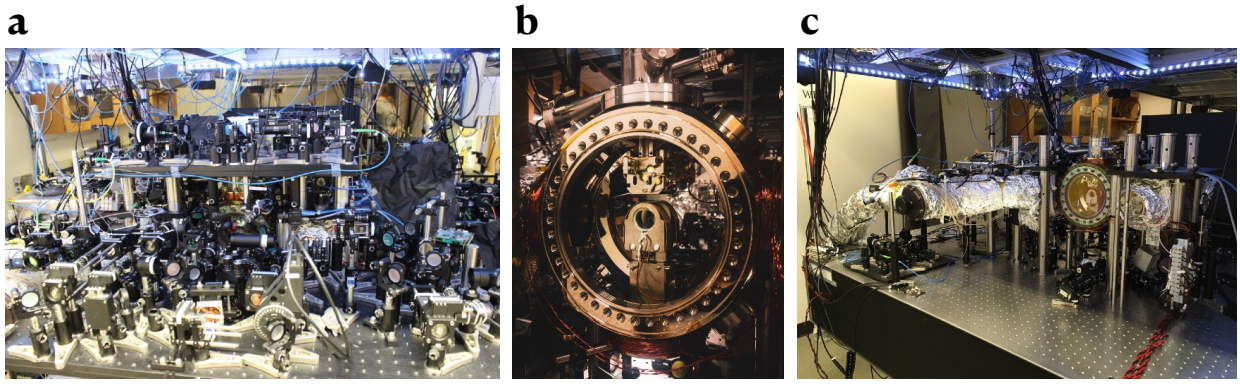

Figure 12.2: Benefits of employing a loadlock technique. Traditionally, the workflow of readying a new cavity for the UHV environment involves the following labor-intensive stages **a**, before switching the cavity. **b**, during normal operation. **c**, after switching the cavity.

Position Manipulation	**Supplier**	**PN**	**Qty**
Translator: Z manipulator, 16" stroke	Nor-cal	Z-B450C-T275T-1.53-16	1
Groove Grabber: 8" CF, split axial clamping	Kimball Physics	MCF800-GrvGrb-C01	1
Support Tube: 2.75" CF	Nor-cal	Custom: appx. A.2	1
Probe Support: vacuum-grease gliding mechanism	Nor-cal	Custom: appx. A.2	1

Table 12.1: Breakdown of position manipulation components.

cold atom experiments [71], for getting a sample from atmosphere into UHV quickly. While the system in [71] supports a quantum gas experiment setup for BEC applications, our system emphasizes a higher repetition rate by putting the MOT quadrupole coils in the vacuum chamber. The loadlock architecture introduces substantial added complexity in the form of additional space taken by the loadlock chamber and a translator used for moving samples around, and trickier wire management, but provides otherwise seamless integration with standard cold atom technologies.

The workflow for readying a new cavity having been exposed to air into the UHV-clean science chamber to interface with cold trapped atoms follows the steps shown in Fig. 12.1. We first manipulate the translator to retract the old cavity into the loadlock chamber, and close the gate valve to isolate the two chambers. We then vent only the loadlock chamber

through the angle valve, open two flanges of the loadlock chamber, switch in a new cavity. We then close up the loadlock chamber, pump only the loadlock chamber with the turbo pump and an ion pump, while baking it to 110 ° C limited by in-vacuum Torr Seal epoxy. Torr Seal epoxy is employed to allow rapid, room-temperature attachment of in-vacuum mirrors, lenses, and piezos to their mounts, as well as securement of Kapton-insulated wires to the quadrupole coils in the science chamber. The cavity structure is radiatively heated by the vacuum chamber walls, which are themselves directly heated by externally wrapped heater-tapes. While we do not directly measure the cavity system's temperature, we have verified that a week-long bake is sufficient to achieve our requisite pressure of 4×10^{-10} Torr at room temperature. Once the loadlock pressure at high temperature is satisfactory, we then shut the angle valve, cool down the loadlock chamber to room temperature. If the loadlock pressure at room temperature is satisfactory, we open the gate valve, and manipulate the translator to extend the cavity into the science chamber. To achieve a room temperature pressure of 4×10^{-10} Torr, we rely upon the heuristic of associating a 40 ° C decrease in the baking temperature with a decade of drop in the vacuum pressure, indicating that we will need a pressure of $\sim 1 \times 10^{-8}$ Torr at 110 ° C—this has been born out by our experimental results. Finally, we fire the titanium sublimation pump inside the ion pump attached to the science chamber, once the system has cooled down to the room temperature and reaches below 1×10^{-9} Torr vacuum pressure.

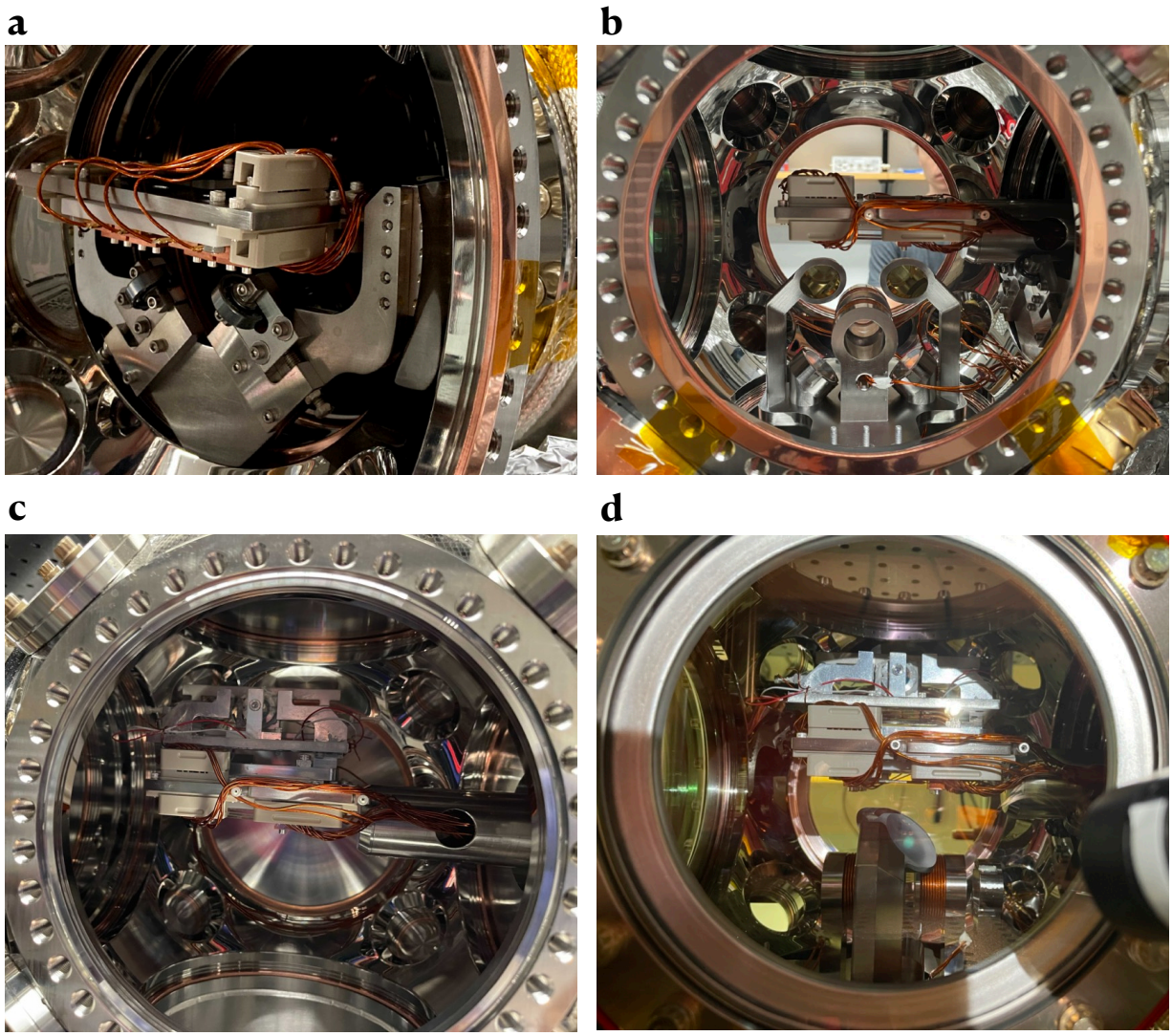

Figure 12.3: Photos depicting the transportation of the cavity carrier, with or without a cavity. **a**, the cavity carrier platform being transported from the loadlock chamber to the science chamber. **b**, the cavity carrier platform transported to the center of the science chamber. **c**, a cavity on the carrier platform being transported from the loadlock chamber to the science chamber. **d**, the cavity on the carrier platform transported to the center of the science chamber. Note that the orientation of the in-vacuum MOT setup was corrected before the cavity was installed.

12.3 Design and Components of the UHV System

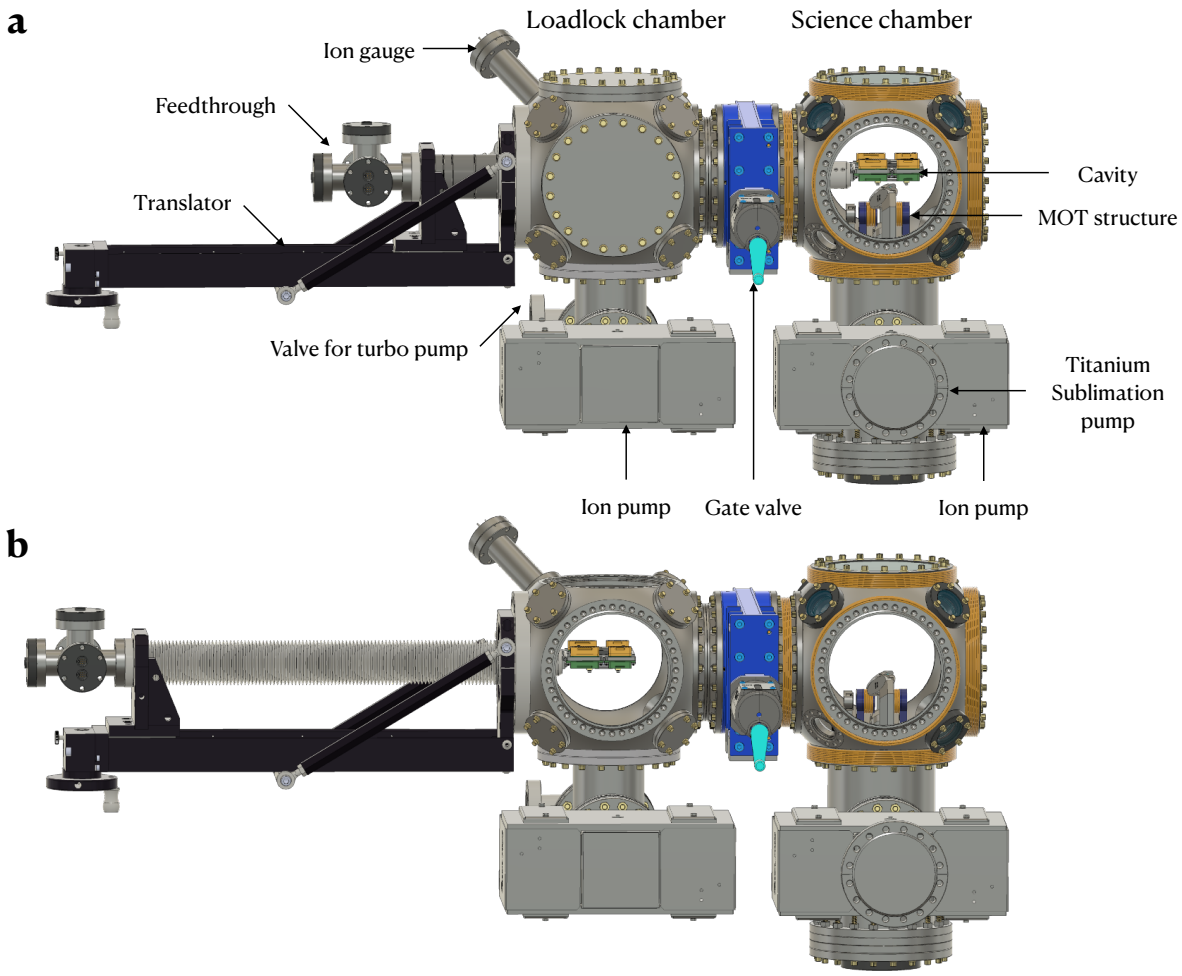

Figure 12.4: Schematic of the loadlock vacuum apparatus. The system consists of two vacuum chambers: a loadlock chamber separated from a science chamber by a gate valve. The science chamber is kept at UHV by an ion pump, and is designed to have maximal optical access. An in-vacuum MOT setup stays in the science chamber. A translator moves the carrier structure supporting an optical cavity and atomic dispensers across the two chambers. The apparatus is depicted in two configurations: **a**, science mode, where the cavity is extended into the science chamber, and **b**, installation mode, where the cavity is retracted back in the loadlock chamber.

To minimize disruptions caused by cavity replacement during experiments, we utilize a two-chamber architecture separated by a gate valve: a primary “science" chamber housing the

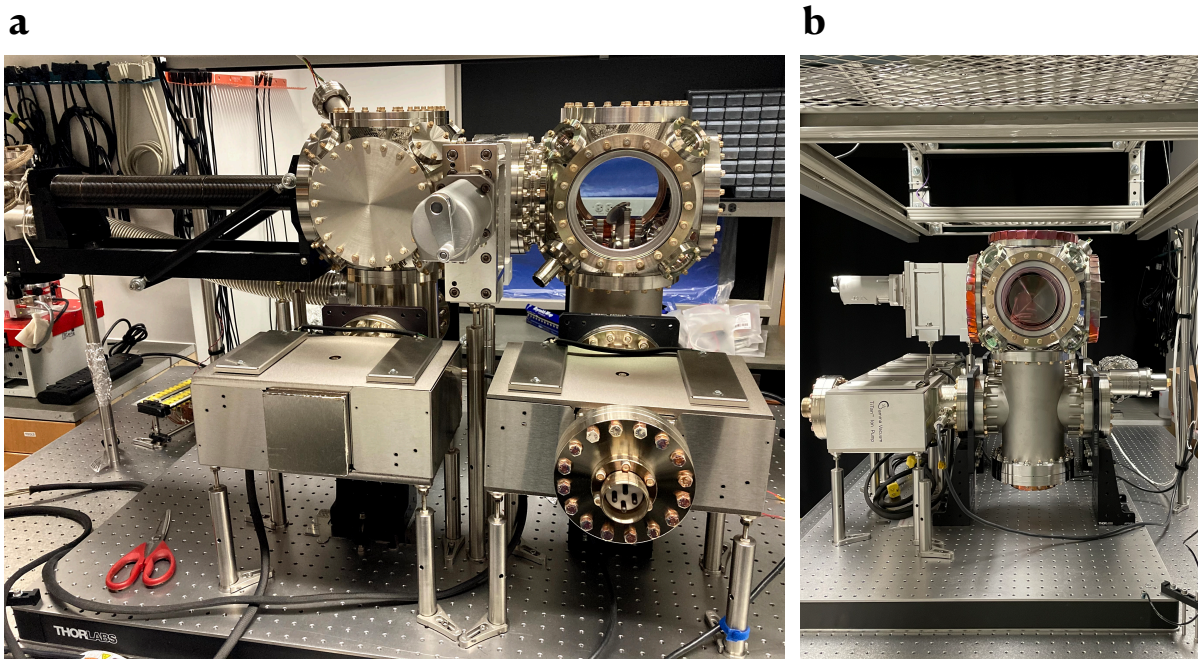

Figure 12.5: Photographs of the loadlock vacuum apparatus. The apparatus has dimensions 3.5'×4'×2.5' (107 cm×122 cm×76 cm), and comfortably fits atop a standard 4'×8' (122 cm×244 cm) vibration isolated optical table. Space is available under and around the vacuum chamber to conveniently set up optical breadboards. The viewports of the main chamber are AR coated to transmit multiple wavelengths of interest. The gate valve is manually actuated.

UHV-clean setup for cold trapped atoms, and an auxiliary “loadlock" chamber where an initially unbaked cavity is installed and independently cleaned by baking. Schematics and photos illustrating this setup are provided in Fig. 12.4 and Fig. 12.5 respectively. A z-manipulator with a 60” (152 cm) throw moves the cleaned cavity-under-test between the loadlock chamber (refer to Fig. 12.4b) and the science chamber (refer to Fig. 12.4a).

To maintain a continuous UHV-clean environment in the science chamber, an ion pump is attached through a vacuum cross at the bottom. For the loadlock chamber, which undergoes frequent pumping and baking cycles from atmospheric pressure to UHV, a turbo pump and an ion pump are attached via a vacuum tee at the bottom, with an ion gauge positioned at the top to monitor pressure.

Fig. 12.6 graphically displays components of the loadlock vacuum apparatus. Tab. 12.2 outlines permanently installed vacuum hardware components, Tab. 12.3 outlines consumable vacuum hardware components, and Tab. 12.5 outlines the optical viewport components. In the upcoming section, we will introduce the innovative loadlock technique.

Our vacuum is limited in two ways by the Torr Seal in-vacuum epoxy. Firstly because it outgasses, and secondly because it limits the maximum permissible temperature during the bakeout to $\sim 110\,^\circ$ C. While the achieved pressure of 4×10^{-10} Torr is more than sufficient for our science goals, moving to glue-less mounting technologies (Appendix A3 of [60]) would resolve this limitation. The remaining unanswered question is the extent to which the large surface area of the in-vacuum coils would limit the achievable pressure.

Thanks to the loadlock architecture and the gate valve in particular, the entire process above does not expose the UHV-clean science chamber to air, and therefore there is no need to remove the optics surrounding the science chamber. The downtime required to ready the first cavity after the initial bake establishing a baseline pressure measurement, and any new cavity in general, is drastically reduced to about a week, since the cavity carrier, not the cavity itself, was pre-baked once before during the initial bake.

The thermal gradient across the gate valve between the load lock chamber and the science chamber does not present an issue; it is, however, critical that the valve not be operated in the presence of this thermal gradient. This iterative process is further simplified and expedited by our decisions to: 1) use metal flanges without viewports on the loadlock chamber to tolerate large thermal gradients, 2) apply more aggressive temperature ramps during bakeouts, 3) attach heating tapes and aluminum foil to the bottom of the loadlock chamber permanently, 4) route electrical feedthrough wires inside the tube of the translator in an organized manner, and 5) design the cavity-carrying platform to be plug-and-go style.

Fig. 12.2 graphically displays the potential benefits of employing a loadlock technique. Fig. 12.3 illustrates the transportation of the cavity carrier, both in the absence and presence

of an optical cavity. Tab. 12.1 outlines position manipulation components. In the upcoming section, we will describe the assembly and integration of the UHV system with loadlock.

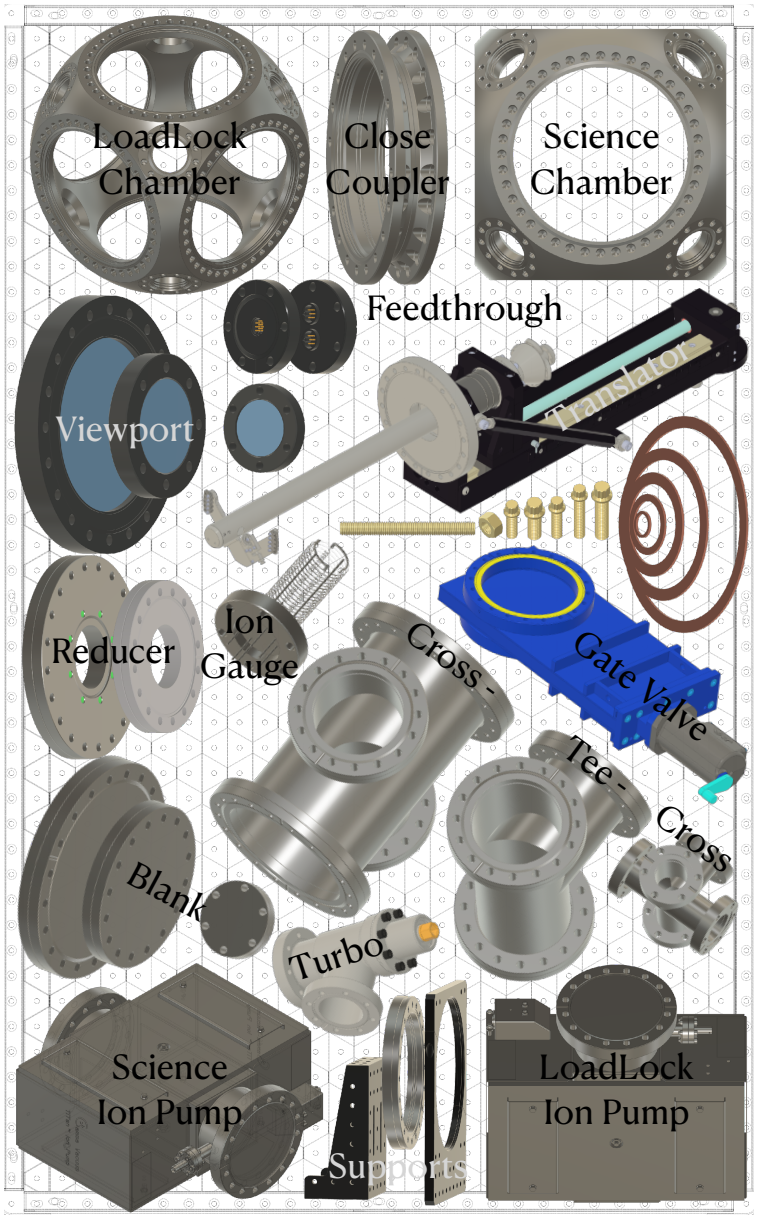

Figure 12.6: A graphical display of components of the loadlock vacuum apparatus.

Vacuum Hardware: permanent	**Supplier**	**PN**	**Qty**
Spherical Cube: loadlock chamber, six 8" CF, eight 2.75" CF	Kimball Physics	MCF800-SphCube-G6C8	1
Spherical Cube: science chamber, six 8" CF, eight 2.75" CF	Kimball Physics	MCF800-SphCube-G6C8	1
Cross: 4-way, reducing, 8" CF × 6" CF	MDC Vacuum	405050	1
Tee: anti-reducing, 8" CF on two 6" CF	Lesker	Custom: appx. A.3	1
Close Coupler: rotatable, two 6" CF	Kimball Physics	MCF800-ClsCplr-G1r1	2
Reducing Flange: zero-length, 8" CF to 4.5" CF	Lesker	RF800X450	1
Reducing Flange: zero-length, 6" CF to 4.5" CF	Lesker	RF600X450	1
Blank Flange: 8" CF	Lesker	F0800X000N	4
Blank Flange: 6" CF	Lesker	F0600X000N	1
Blank Flange: 2.75" CF	Lesker	F0275X000N	8
Nipple: 2.75" CF, for ion gauge	MDC	402002	1
External Bracket: 6" CF	Kimball Physics	MCF600-ExtBrkt-LS	4
Mounting Flange: double-sided, two 6" CF	Kimball Physics	MCF600-MtgFlg-F2	4
Angle Bracket	Thorlabs	AP90RL	4
Pillar Post: 1/4"-20 thread, 6" long, for pump support	McMaster-Carr	93322A446	8
Swivel Mount: 1/4"-20 threaded stud, 1-1/4" long, for pump support	McMaster-Carr	6111K46	8
Optical Breadboard: imperial 30"×48"×2.4" breadboard	Thorlabs	B3048F	1

Table 12.2: Breakdown of vacuum hardware components, permanently installed.

Vacuum Hardware: consumable	**Supplier**	**PN**	**Qty**
Copper Gasket: 8" CF, 10-pack	Lesker	GA-0800	4
Copper Gasket: 6" CF, 10-pack	Lesker	GA-0600	3
Copper Gasket: 4.5" CF, 10-pack	Lesker	GA-0450	1
Copper Gasket: 2.75" CF, 10-pack	Lesker	GA-0275	3
Copper Gasket: 8" CF, fully annealed, 10-pack	Lesker	VZCUA150	6
Copper Gasket: 6" CF, fully annealed, 10-pack	Lesker	VZCUA100	4
Copper Gasket: 4.5" CF, fully annealed, 10-pack	Lesker	VZCUA64	2
Copper Gasket: 2.75" CF, fully annealed, 10-pack	Lesker	VZCUA38	6
Silver-Plated Bolt: for 6" CF or 8" CF through-hole flanges, 25-pack	Kimball Physics	MCF 5/16-24 x 1 1/4	10
Silver-Plated Bolt: for 6" CF or 8" CF tapped flanges, 25-pack	Kimball Physics	MCF 5/16-24 x 3/4	4
Silver-Plated Bolt: for 2.75" CF tapped flanges, 25-pack	Kimball Physics	MCF 1/4-28 x 7/8	5
Silver-Plated Bolt: for 6" CF or 8" CF through-hole flanges, 25-pack	Duniway Stockroom Corp	SFBN-24-225	1
Silver-Plated Bolt: for 4.5" CF or 6" CF tapped flanges, 25-pack	Duniway Stockroom Corp	SBX-24-125	2
Silver-Plated Bolt: 5/16-24 × 1", for triple flange	U-C Components	TWP-3116-NA	25
Stainless Threaded Rod: 5/16"-24 × 4", for triple flanges	McMaster-Carr	98750A455	~ 50
Stainless Nut: hex, 1/4"-20 × 1.25"	McMaster-Carr	95505A601	~ 50
Stainless Screw: hex, 1/4"-20 × 1.25"	McMaster-Carr	92196A544	~ 50
Silver-Plated Nut: for 6" CF or 8" CF through-hole flanges, through hole, 25-pack	Duniway Stockroom Corp	SN-5/16	6

Table 12.3: Breakdown of vacuum hardware components, consumable.

Pressure Manipulation	**Supplier**	**PN**	**Qty**
Roughing Pump: in Turbo Pump station	Pfeiffer Vacuum	PM 025 016 AT	1
Turbo Pump station: HiCube 80 Eco	Pfeiffer Vacuum	PM 025 016 AT	1
Ion Pump: DI element, for loadlock	Gamma Vacuum	100LDI6SSC1N	1
Ion Pump: CV element, for science	Gamma Vacuum	100LDI6DSC1T	1
Titanium Sublimation Pump (TSP): inside the science Ion Pump	Gamma Vacuum	100LDI6DSC1T	1
Ion Pump & TSP Controller	Gamma Vacuum	DIGITEL QPC	1
Ion Gauge: nude, dual filament, closed cage grid	Stanford Research Systems	NR-F-UHV	1
Ion Gauge Controller	Stanford Research Systems	IGC100	1
Gate Valve: all-metal, 6" CF, hand-wheel manual drive	VAT	10844-UE01-0004	1
Angle Valve: all-metal, hand-wheel manual drive	Pfeiffer Vacuum	420VEC063.A	1
Leak Detector	Adixen	ASM 142	1

Table 12.4: Breakdown of pressure manipulation components.

Viewport	**Supplier**	**PN**	**Qty**
Viewport: UV Fused Silica, 8" CF	Lesker	VPZL-800Q	4
Viewport: UV Fused Silica, 2.75" CF	Lesker	VPZL-275Q	7
Viewport: UV Fused Silica, 4.5" CF	Lesker	VPZL-450Q	1
Coating: both sides R<0.5% @ 480nm, 780nm, 1010nm, 1560nm	Spectrum Thin Films	Custom	1

Table 12.5: Breakdown of viewport components.

12.4 Assembly and Integration of UHV System with Loadlock

The UHV system was assembled in stages in for simplicity and isolation during troubleshooting.

During Stage I, the vacuum chamber was constructed from scratch on an optical breadboard atop a mobile cart, with the translator temporarily replaced by a blank metal flange. It was subsequently pumped and baked to achieve UHV level.

During Stage II, the translator system was separately assembled, where the feedthrough wires were routed through the translator tube, and the feedthrough connectors were made in contacts with the cavity carrier and the feedthrough flange, then attached to the vacuum system. Unfortunately, through the process, we discovered that the geometry of the original feedthrough flanges that came with the translator's utility hat assembly was too tight for the contact pins, and would cause dangerous electrical shorts between the high voltage to the nearby conducting chamber walls. Therefore, the original smaller utility hat (1.33" CF) was replaced with a larger five-way cross (2.75" CF). This procedure is detailed in Ch. 13.

During Stage III, the in-vacuum MOT setup was separately assembled, then installed into the science chamber. This procedure is detailed in Ch. 14.

During Stage IV, a small waist cavity was separately assembled, then inserted into the loadlock chamber.

Fig. 12.7 depicts Stage I assembly process, Fig. 12.8 and Fig. 12.9 depict Stage II assembly process with a focus on the feedthrough and cavity carrier respectively, and Fig. 12.10 depicts Stage III assembly process. In the upcoming section, we will describe the operation and maintenance of the UHV system.

Figure 12.7: Snapshots for Stage I, assembly of the vacuum chamber with the translator temporarily replaced by a blank flange. **a**, delivery of vacuum system components. **b**, **c**, and **d**, progress during Stage I. **e**, and **f**, near-completion of Stage I, lacking one 'leg' of the vacuum chamber. **g** and **h**, completion of Stage I.

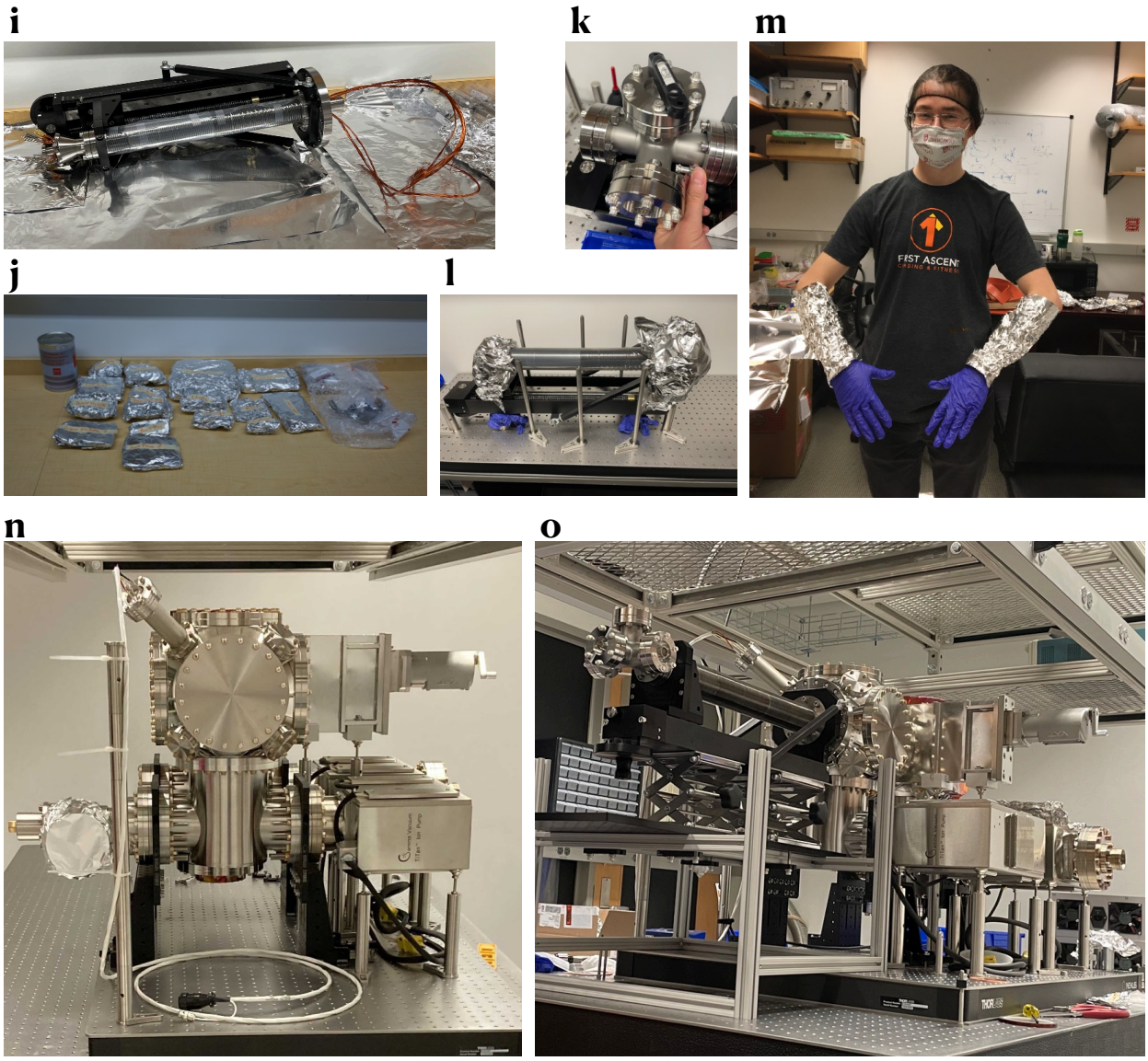

Figure 12.8: Snapshots for Stage II, integration of the translator and the feedthrough system to the vacuum chamber. Vacuum tasks on the translator were initially conducted on a desk covered in aluminum foil before the neighboring office became a lab space. **i**, original, now obsolete, translator setup with bad utility hat assembly. **j**, foil packets containing cleaned vacuum components. **k** and **l**, replaced translator setup. **m**, arms wrapped in aluminum foil to prevent contamination. **n**, vacuum system relocated to the lab space. **o**, completion of translator installation in Stage II.

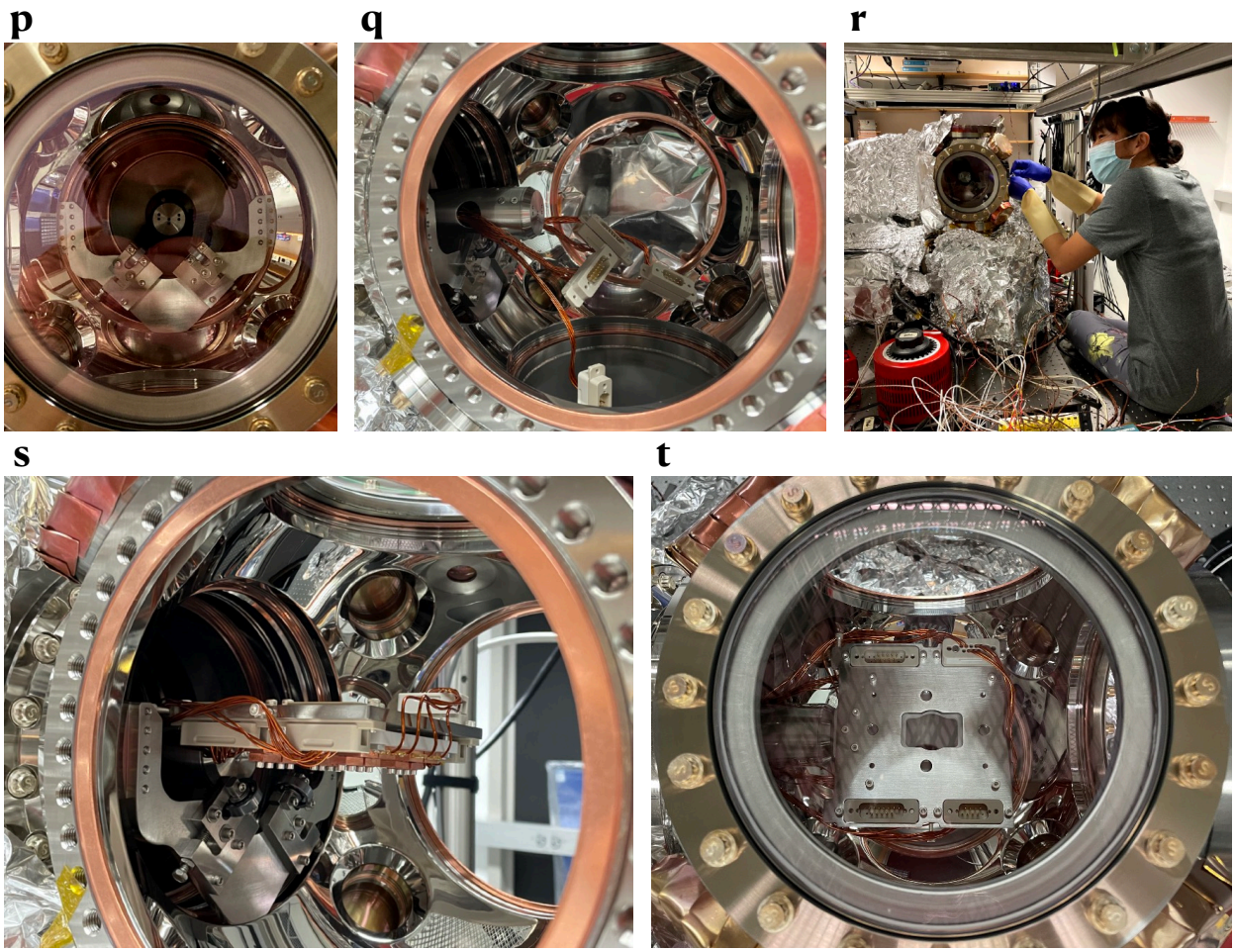

Figure 12.9: Snapshots for Stage II, integration of the translator and the feedthrough system to the vacuum chamber (cont'ed). **p**, V-stand installation. **q**, routing of feedthrough connectors. **r**, cavity carrier installation. **s**, integration of the cavity carrier with the feedthrough connectors. **t**, completion of Stage II.

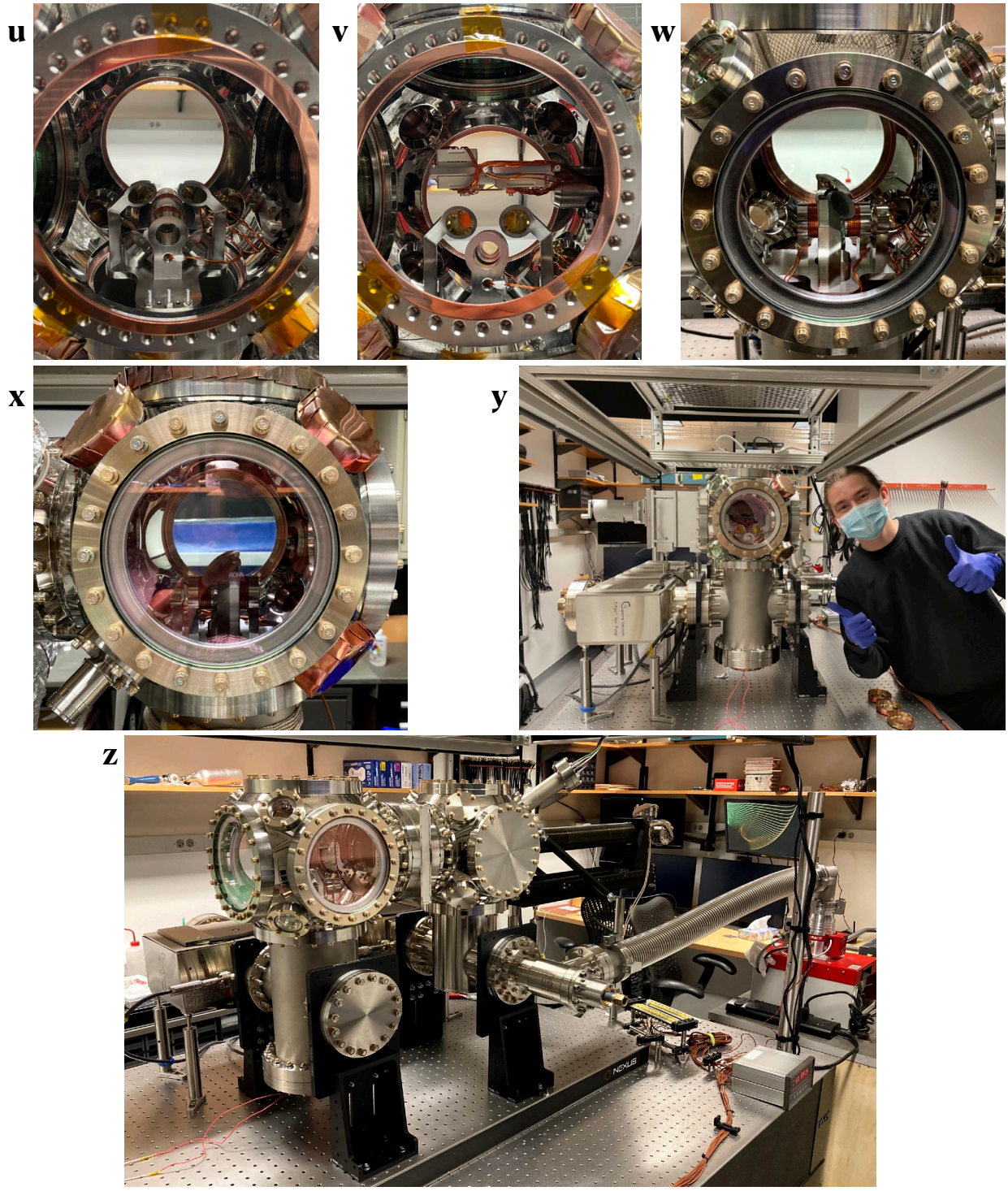

Figure 12.10: Snapshots for Stage III, installation of the in-vacuum MOT setup. **u** and **v**, initial attempt at setup installation with incorrect orientation. **w**, corrected orientation of the in-vacuum MOT setup. **x**, attachment of the feedthrough flange. **y** and **z**, completion of Stage III–construction of the entire vacuum chamber without a cavity.

12.5 Assembly of the Bare UHV System (Stage I)

During Stage I, the vacuum chamber assembly took place, temporarily replacing the translator with a blank flange. Fig. 12.11 and Fig. 12.12 depict the Stage I assembly procedure. Tab. 12.6 documents tools used during the process. Concurrently, the conversion of a neighboring office into a lab space significantly impacted the vacuum workflow. Fig. 12.13 illustrates vacuum workflow before lab renovation, Fig. 12.14 documents the ongoing lab renovation process, and Fig. 12.15 captures the state post-renovation.

Here are a few considerations for maintaining cleanliness and efficiency during the vacuum assembly process. Always protect the knife edge from damage. Use good copper gaskets between flanges to ensure a proper seal. Tighten bolts with a torque wrench as recommended, but avoid tightening them flush metal-to-metal, as flanges may need further tightening during the helium leak checking process. Use silver-plated bolts/nuts to prevent seizing during bakeouts. Wear powderless gloves when handling in-vacuum components, including copper gaskets, and keep track of their usage to avoid contamination. For holding a copper gasket vertically in place, consider using gasket clips if the flange has a convenient leak-checking slot. Otherwise, carefully tape kapton tapes outside the knife edge. When leaving a clean vacuum part in the air, cover it with aluminum foil to prevent contamination. Utilize the leveling laser for aligning vacuum components, as it has proven to be very useful in ensuring proper alignment.

Prepare the setup. Prepare a clean and leveled optical breadboard.

Attach the bottom viewport. Keep the cross protected in its plastic covering to safeguard the knife edge. Connect the reducing flange to the cross. Attach the bottom viewport to the reducing flange. Position the assembly with the viewport facing down and resting on bolts, supported by a lab jack for adjustable height.

Construct and integrate the first 'leg' of the vacuum chamber opposite to the science ion pump. Connect a mounting flange to a mounting bracket and fasten them to

an angle bracket. Secure the 'leg' in a suitable position on the breadboard. Place a copper gasket between the mounting flange and the cross. Align the cross to the 'leg', and close the gap between them to recess the copper gasket appropriately. Insert stainless studs through the assembly and add silver-plated nuts from the cross' side. Prepare a blank flange. Place a copper gasket between the mounting flange and the blank flange. Attach the blank flange. Add silver-plated nuts from the blank flange's side. Begin by hand-tightening the nuts, then use a torque wrench and a tight-clearance wrench to tighten each pair of nuts against each other in a star pattern overall.

Construct and integrate the second 'leg' of the vacuum chamber adjacent to the science ion pump. Connect a mounting flange to a mounting bracket and fasten them to an angle bracket. Place a copper gasket between the mounting flange and the cross. Align the 'leg' to the cross, and close the gap between them to recess the copper gasket appropriately. Insert stainless studs through the assembly and add silver-plated nuts from the cross' side. Support the science ion pump on a lab jack and align it vertically to the cross. Place a copper gasket between the mounting flange and the science ion pump. Align the science ion pump atop the lab jack to the 'leg', and close the gap between them to recess the copper gasket appropriately. Add silver-plated nuts from the science ion pump' side. Begin by hand-tightening the nuts, then use a torque wrench and a tight-clearance wrench to tighten each pair of nuts against each other in a star pattern overall. Add swivel mounts to support the science ion pump, raise them to the appropriate level, and remove the lab jack. Fully tighten the nuts of the triple flanges on both the first and second 'leg' of the vacuum chamber.

Assemble and attach the science chamber. Keep a spherical cube protected in its plastic covering to safeguard the knife edge. Attach seven small viewports and a small blank flange (to be replaced later by a feedthrough flange) to the spherical cube. Attach four large viewports to the spherical cube. Attach the assembled spherical cube, i.e. the

science chamber, to the cross from the top. For all sealing tasks mentioned in this step, ensure proper positioning of copper gaskets, and fully tighten the silver-plated bolts to the threaded holes on the spherical cube.

Attach the gate valve. Attach a close coupler to the science chamber, ensuring good rotational orientation. Support the gate valve on two custom-made blocks on top of two pillar posts. Place a copper gasket between the gate valve and the close coupler. Align and attach the gate valve to the close coupler. Place another copper gasket on other side of the gate valve. Attach another close coupler to the gate valve.

Assemble and attach the loadlock chamber and tee. Keep a spherical cube protected in its plastic covering to safeguard the knife edge. Attach eight small blank flanges to the spherical cube. Attach four large blank flanges to the spherical cube. Attach the tee to the assembled spherical cube, i.e. the loadlock chamber. Support the loadlock assembly on a lab jack from the bottom of the tee. Place a copper gasket between the close coupler and the loadlock chamber. Align the loadlock chamber to the close coupler with a leveling laser, and close the gap between them to recess the copper gasket appropriately. Fully tighten bolts of the close couplers.

Construct and integrate the third 'leg' of the vacuum chamber adjacent to the turbo pump. Connect a mounting flange to a mounting bracket and fasten them to an angle bracket. Place a copper gasket between the mounting flange and the tee. Align the 'leg' to the tee, and close the gap between them to recess the copper gasket appropriately. Insert stainless studs through the assembly and add silver-plated nuts from the tee' side. Prepare a reducing flange for the turbo pump. Place a copper gasket between the mounting flange and the reducing flange. Attach the reducing flange. Add silver-plated nuts from the reducing flange's side. Begin by hand-tightening the nuts, then use a torque wrench and a tight-clearance wrench to tighten each pair of nuts against each other in a star pattern overall. For the alignment tasks mentioned in this step, use the leveling laser and the lab

jack to finely adjust for the mechanical deflection of the chamber built so far.

Attach the ion gauge. Prepare the ion gauge. Attach the ion gauge to the loadlock chamber.

Attach the feedthrough flange. Prepare the feedthrough flange for in-vacuum MOT setup. Attach the feedthrough flange to the science chamber.

Attach the turbo pump. Prepare the turbo pump. Place a copper gasket between the turbo pump and the mounting flange. Attach the turbo pump to the mounting flange.

Construct and integrate the fourth 'leg' of the vacuum chamber adjacent to the loadlock ion pump. Connect a mounting flange to a mounting bracket and fasten them to an angle bracket. Place a copper gasket between the mounting flange and the tee. Align the 'leg' to the tee, and close the gap between them to recess the copper gasket appropriately. Insert stainless studs through the assembly and add silver-plated nuts from the tee' side. Support the loadlock ion pump on a lab jack and align it vertically to the tee. Place a copper gasket between the mounting flange and the loadlock ion pump. Align the loadlock ion pump atop the lab jack to the 'leg', and close the gap between them to recess the copper gasket appropriately. Add silver-plated nuts from the loadlock ion pump' side. Begin by hand-tightening the nuts, then use a torque wrench and a tight-clearance wrench to tighten each pair of nuts against each other in a star pattern overall. Add swivel mounts to support the loadlock ion pump, raise them to the appropriate level, and remove the lab jack. For the alignment tasks mentioned in this step, use the leveling laser and the lab jack to finely adjust for the mechanical deflection of the chamber built so far. Fully tighten the nuts of the triple flanges on both the third and fourth 'leg' of the vacuum chamber.

Attach the bellow. Attach the CF-KF adaptor to the turbo pump. Attach the bellow to the KF adaptor. This completes the first stage of the vacuum chamber assembly.

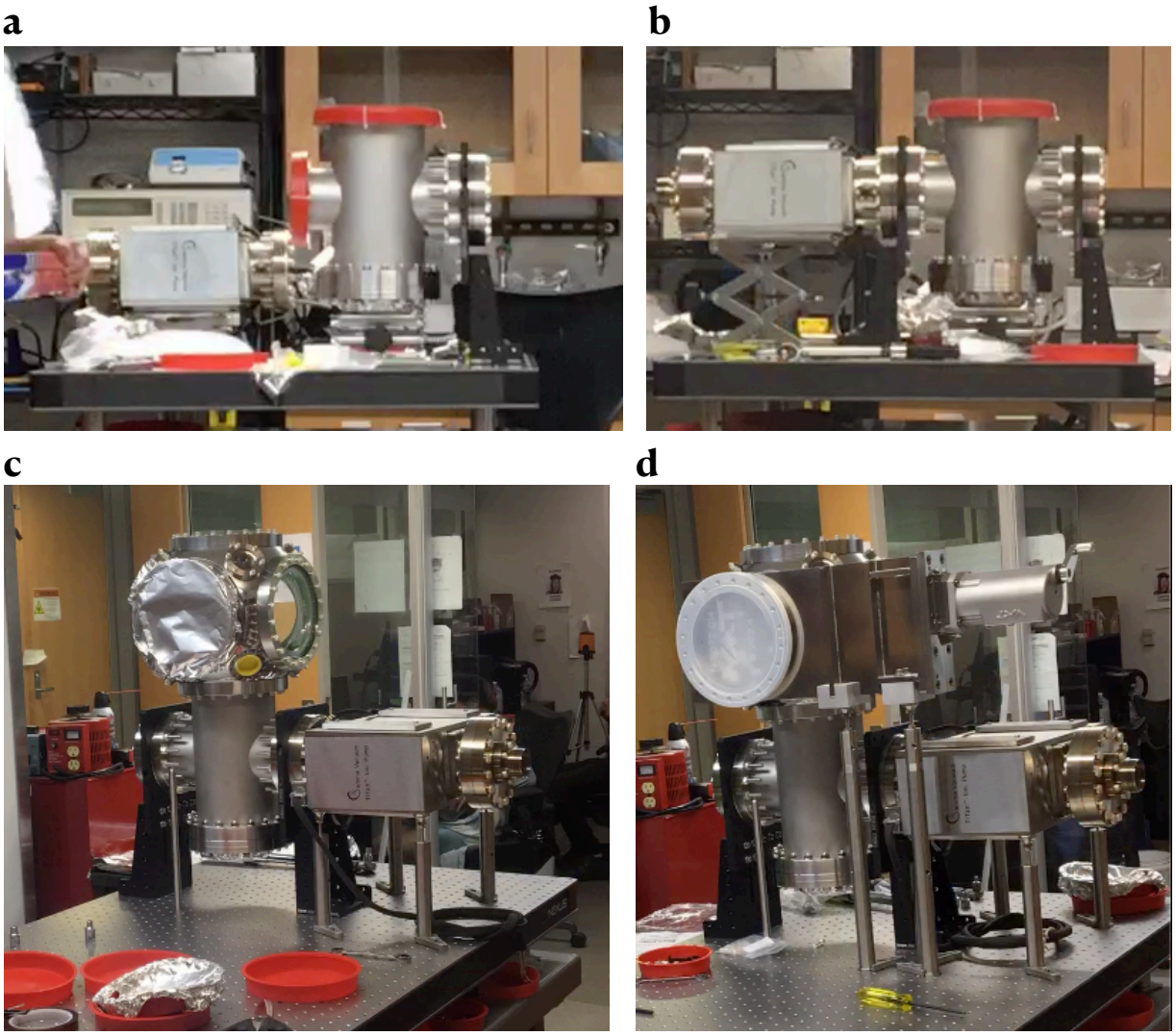

Figure 12.11: Assembly procedure for Stage I. **a**, the cross and the 4.5" CF viewport were assembled. **b**, the science ion pump was attached to the Cross assembly, supported on two angle brackets. **c**, the science chamber was attached to the top of the half-assembly. **d**, the gate valve was attached to the half-assembly (continued on next page).

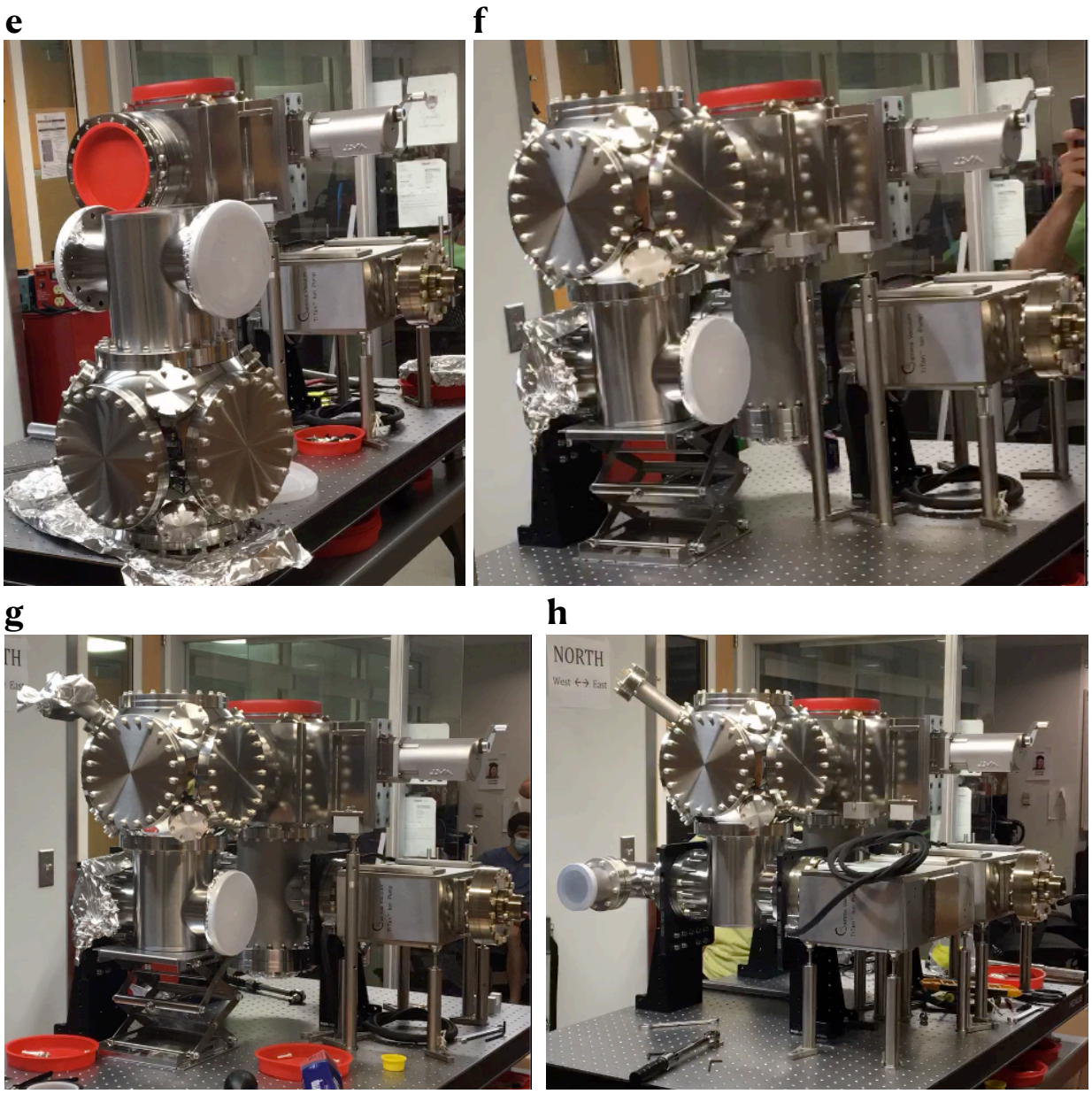

Figure 12.12: Assembly procedure for Stage I (cont'd). **e**, the loadlock chamber and the tee were assembled together, inversely assembled due to weight distribution. **f**, the loadlock half was connected to the gate valve, supported by a lab jack. **g**, the ion gauge was attached to the loadlock chamber. **h**, the loadlock half was supported from below by two angle brackets, attached to the loadlock ion pump, and the turbo pump.

Vacuum Assembly: tooling	**Supplier**	**PN**	**Qty**
Heavy Duty Table: 34"×48"×30" rolling table	McMaster-Carr	5206T42	1
Leveling Laser: red cross-hair line	McMaster-Carr	4098T26	1
Tubular Level: surface mount	McMaster-Carr	2160A4	1
Thread Die: stainless, 5-40 UHC thread, for machining brass dowel pins	McMaster-Carr	2576A135	1
Hex Nut: stainless, 5-40 UHC thread, for machining the brass dowel pins	McMaster-Carr	91841A006	4
Lab Jack: 10" × 10", height-adjustable	McMaster-Carr	9967T55	2
Lab Jack: 8" × 8", height-adjustable	McMaster-Carr	9967T44	1
Lab Jack: 6" × 6", height-adjustable	McMaster-Carr	9967T43	1
Torque Wrench: adjustable, ratcheting	McMaster-Carr	85555A311	1
12-Point Socket: 1/4" size	McMaster-Carr	5544A26	2
12-Point Socket: 5/16" size	McMaster-Carr	5544A27	2
6-Point Socket: 1/2" size, 1-1/8" long	McMaster-Carr	5544A16	2
6-Point Socket: 1/2" size, 7/8" long	McMaster-Carr	5544A106	2
Hex Bit Socket: 9/64" size, 1-5/8" long	McMaster-Carr	5570A65	1
Hex Bit Socket: 6 mm size, 2-3/4" long	McMaster-Carr	8367A24	1
Offset Socket: for tight-clearance, 1/2" size, 1-1/2" long	McMaster-Carr	5844A13	1
Gasket Clip	Lesker	VGC0275S	~ 10
Wire Stripper: for 20-30 AWG Kapton-insulated wire	Accu-Glass Products	100192	1
Crimp Tool: for 20-32 AWG wire, used with a positioner	DMC	AFM8	1
Positioner: for type-1 contacts	DMC	K155	1
Positioner: for type-2 contacts	DMC	K13-1	1
Nitrile Gloves: powder-free, non-sterile	N/A	N/A	~ 100
Torr Seal Epoxy: low outgassing characteristics, flash point 175° C	Lesker	N/A	2
Pillar Post: male-female, 12"	McMaster-Carr	94033A460	20
Pillar Post: male-female, 10"	McMaster-Carr	94033A455	8
Pillar Post: male-female, 8"	McMaster-Carr	94033A453	8
Pillar Post: female, 12"	McMaster-Carr	93322A460	3
Pillar Post: female, 4"	McMaster-Carr	93322A430	2
Pillar Post: female, 1-1/2"	McMaster-Carr	93322A416	1
Wedge: 5" × 1", for moving	McMaster-Carr	5081A2	1
Wedge: 6" × 1-1/4", for moving	McMaster-Carr	5081A3	1
Wedge: 8" × 1-5/8", for moving	McMaster-Carr	5081A4	1

Table 12.6: Breakdown of vacuum assembly components.

Figure 12.13: The vacuum chamber setup before the neighboring office was renovated to be a lab space. **a**, the vacuum chamber, lacking the translator, assembled, pumped, and baked on a mobile steel cart situated in the preparation room. Meanwhile, the neighboring office space was transferred into a temporary clean area for meticulous vacuum tasks, such as routing the feedthrough setup through the translator. **b** and **c**, to maintain stringent cleanliness standards, the office carpet was shielded with fabric and aluminum foil to prevent any carpet debris from contaminating the air in contact with the vacuum environment. Additionally, layers of aluminum foil were applied to the office tables to ensure cleanliness for direct contact with vacuum components.

Figure 12.14: The conversion of the neighboring office into a lab space, overseen by our building manager, Bentley. **a**, the removal of previous furnishings and the installation of a ceiling rack positioned above the optical table area. **b**, a contractor's tool cart used for drilling electrical holes into the wall. **c1** and **c2**, markup locations for drilled holes in the wall for routing cooling water pipes and Ethernet wires. **d1** and **d2**, previous office desks were dismantled and replaced by lab countertops. **e**, the transportation of the vacuum chamber atop an optical breadboard using a crane.

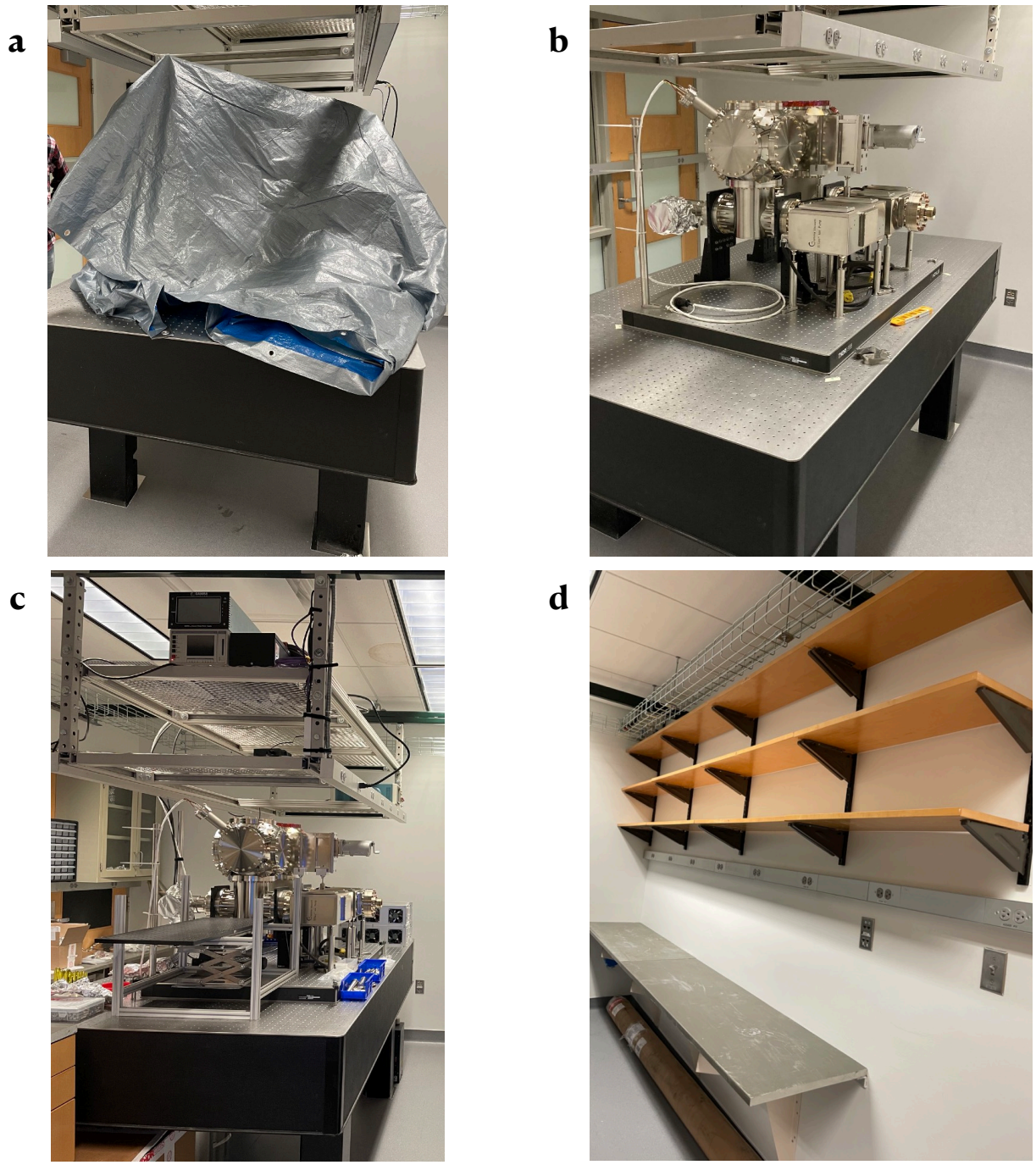

Figure 12.15: The transformation of the newly renovated lab space. **a**, the vacuum chamber shielded for dust protection while being transported from the preparation room to the lab space. **b**, the vacuum chamber subsequently unveiled in its new location. **c**, the optical table accommodating the vacuum chamber, prepared for the installation of vacuum equipment and the attachment of the translator. **d**, the side optical table designated for vacuum and optical setups.

12.6 Operation and Maintenance of the UHV System

The operation and maintenance of the UHV system are crucial for maintaining its functionality and ensuring optimal experimental conditions. This section discusses key practices and equipment used in the operation and maintenance processes.

Bakeout procedures are crucial for preparing the vacuum chamber by eliminating adsorbed gases and contaminants. Copper hats (Fig. 12.16) are used to distribute heat evenly across viewport flanges, reducing the risk of damaging thermal gradients during bakeouts. Heating tapes and pads (Fig. 12.17 and Fig. 12.18) are strategically applied throughout the vacuum chamber to regulate temperatures. These fiberglass heating tapes and flexible heating pads are carefully wrapped around or affixed to critical components such as the turbo pump, ion pumps, translator, gate valve, and flanges to ensure uniform heating. Power control during heating is managed using Variacs. Tab. 12.7 provides a detailed breakdown of components used for vacuum bakeout.

Effective temperature monitoring is critical during bakeouts and normal operation to ensure stability and safety. Fig. 12.19 illustrates thermocouple wires strategically placed at various locations within the vacuum chamber. These thermocouples provide real-time feedback to regulate heating elements and achieve uniform temperature distribution. Tab. 12.8 details the designation of temperature delivery components across the bakeout areas. Tab. 12.9 details the designation of temperature measurement components across the bakeout areas.

Maintaining stable temperatures within the vacuum chamber is enhanced by heat retention techniques. Aluminum foil is wrapped around the vacuum chamber to improve heat retention during bakeouts, minimize heat loss and maintain consistent temperatures, as shown in Fig. 12.20 and Fig. 12.20, before and after the translator was introduced, respectively.

After the initial construction & bakeout the pressure of the science chamber was found to be 3×10^{-10} Torr. After we exposed the loadlock to air, re-baked it, and transported the cavity carrier into the science chamber, the pressure of the science chamber was 4×10^{-10}

Torr, and the final loadlock pressure was 4×10^{-10}.

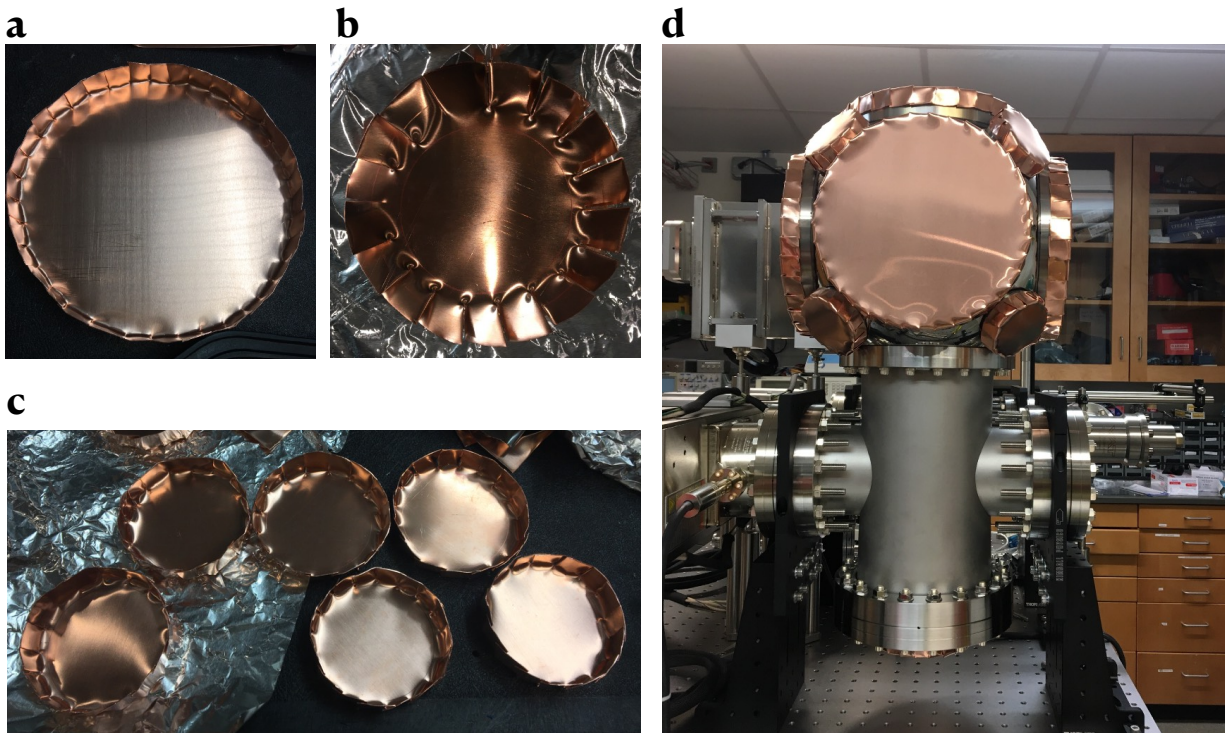

Figure 12.16: The copper hats served to evenly distribute heat across viewport flanges, mitigating the risk of damaging thermal gradients during vacuum bakeouts. **a**, a small copper hat being crafted by cutting copper sheet metal with scissors. **b**, a finished large copper hat. **c**, an array of finished small copper hats. **c**, the copper hats covering the viewports on the main chamber.

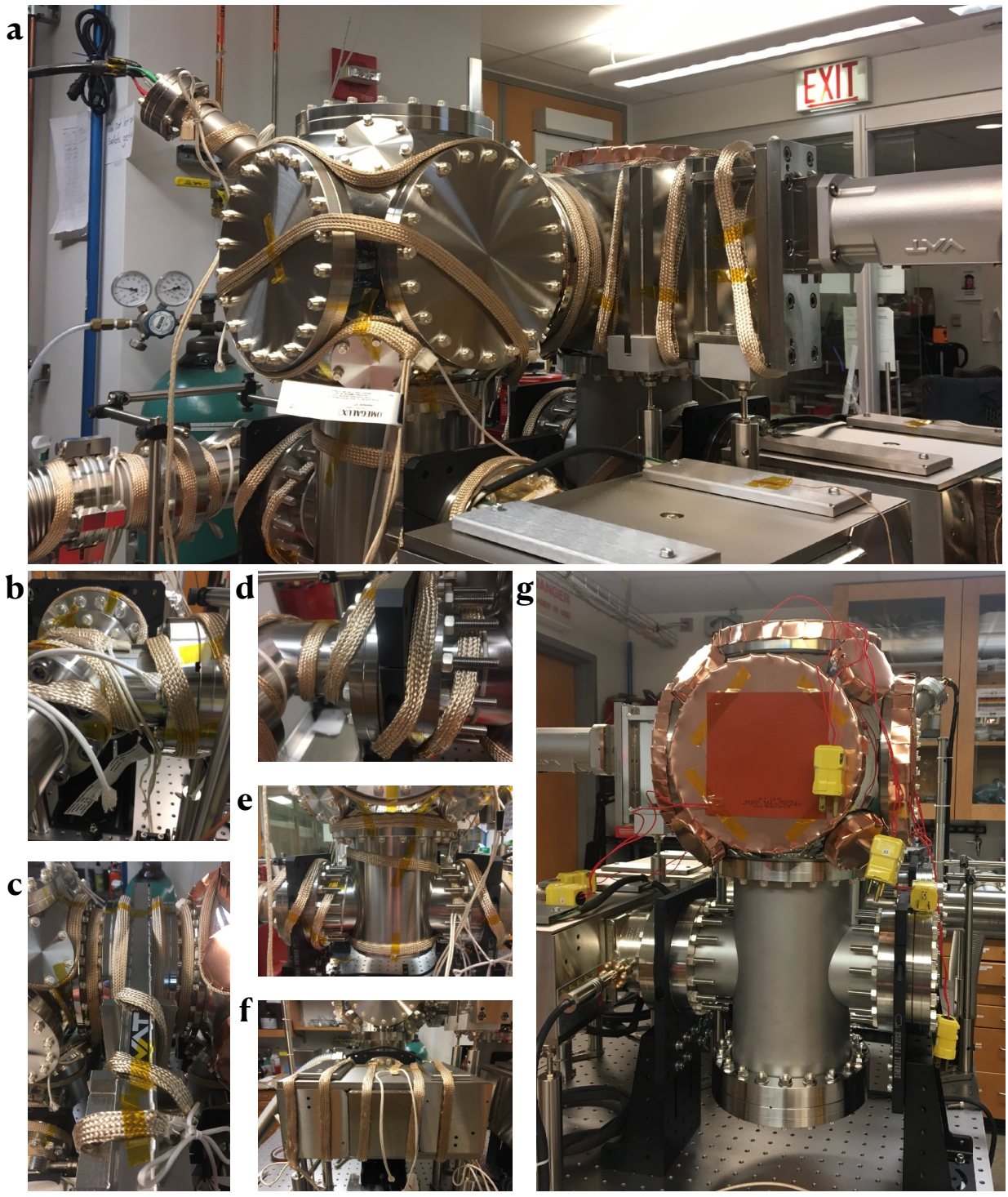

Figure 12.17: Heating tapes and heating pads applied strategically around the vacuum chamber, lacking the translator. Heat tapes wrapped around the loadlock chamber in **a**, the turbo pump in **b**, the gate valve in **c**, the triple flange in **d**, the vacuum tee in **e**, the ion pump in **f**. Heating tapes attached to the viewports of the science chamber in **g**.

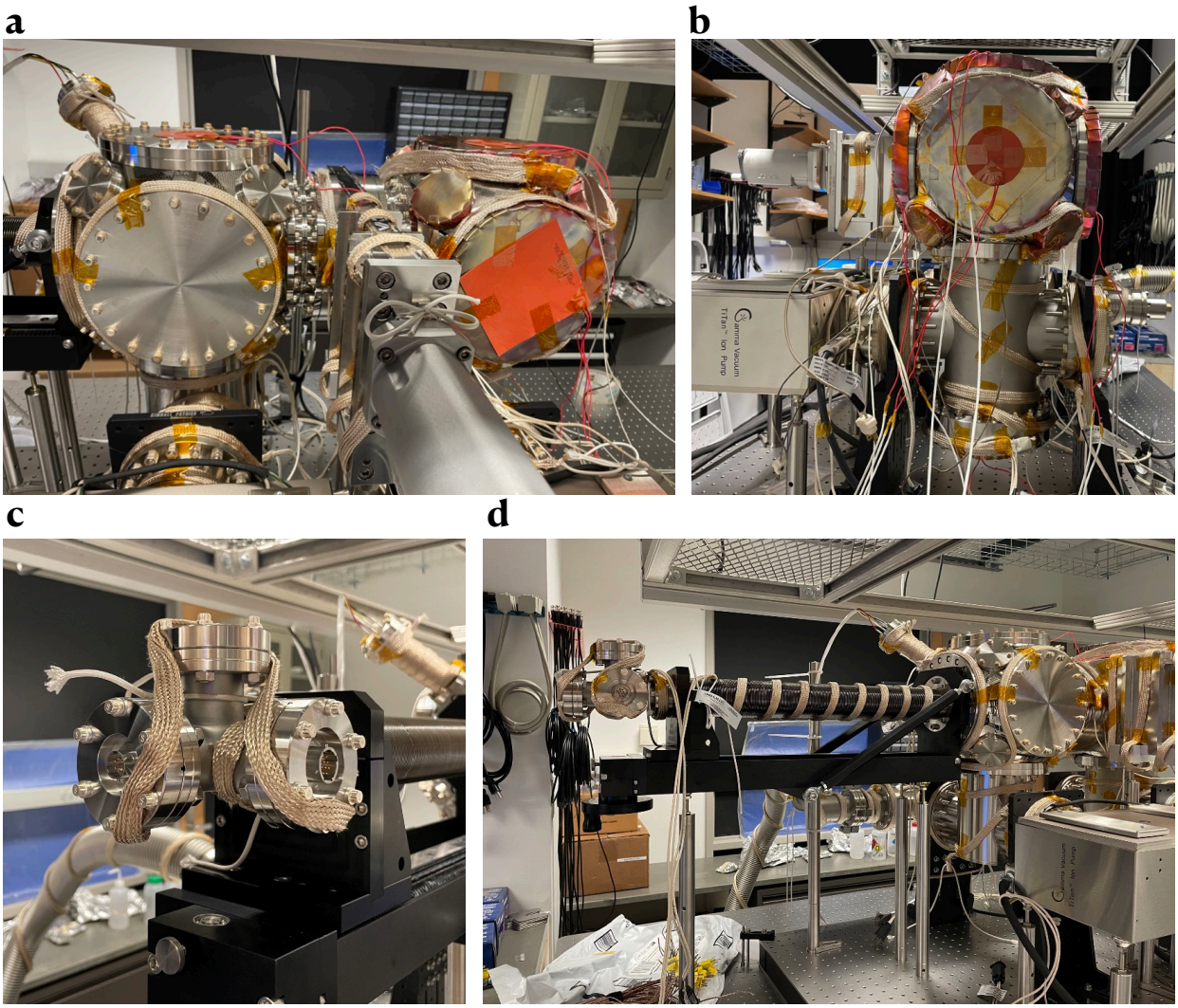

Figure 12.18: Heat tapes and heat pads applied strategically around the vacuum chamber, with the translator, for temperature control. **a**, the loadlock chamber and the science chamber observed from the perspective of the gate valve. **b**, a view of the science chamber. **c**, the wrapping of the five-way cross. **d**, the wrapping of the translator arm.

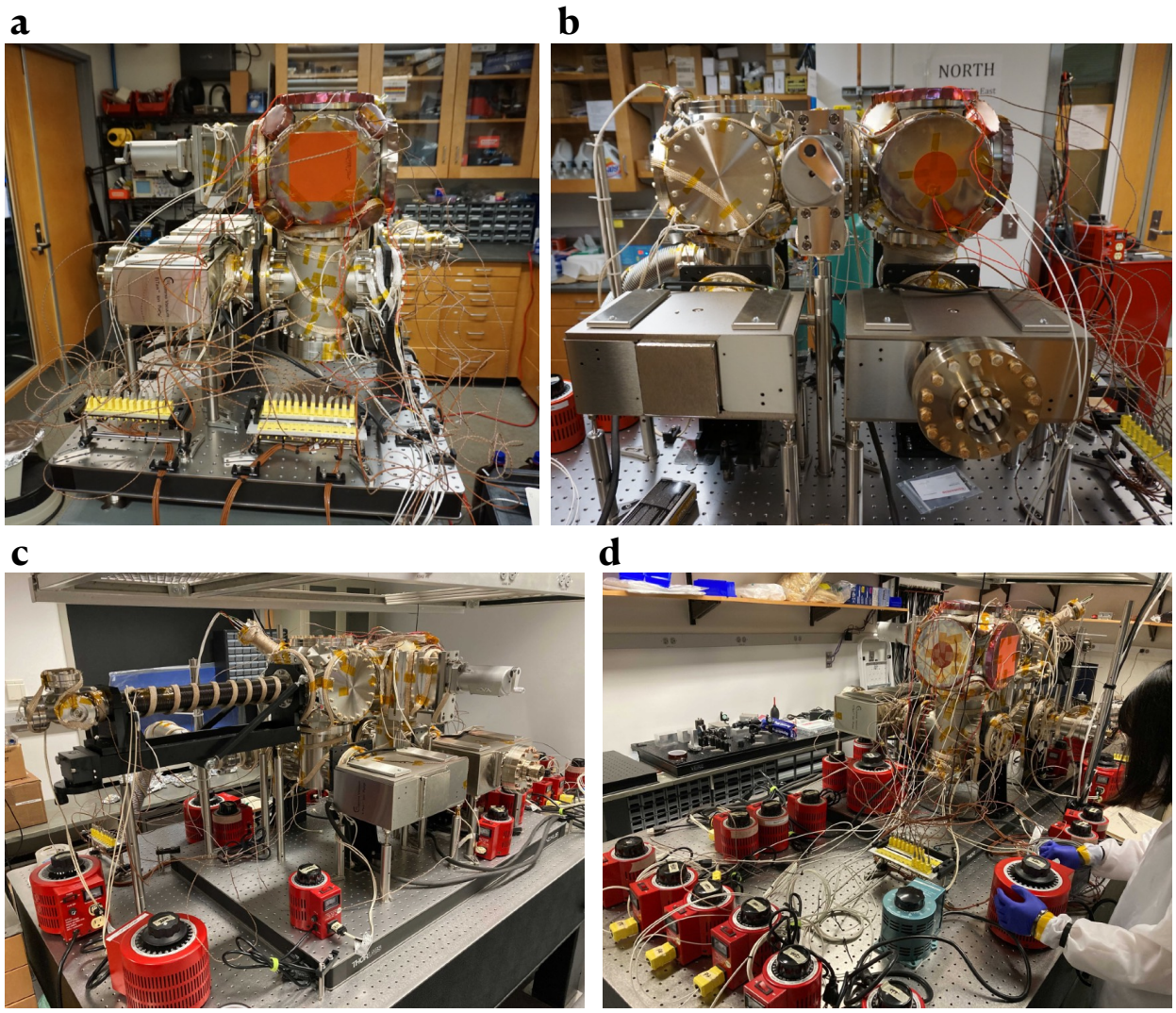

Figure 12.19: Thermocouple wires attached to various spots on the vacuum chamber for temperature control. The bakeout before the lab renovation: **a**, from the science chamber's perspective, and **b**, from the gate valve's perspective. The bakeout after the lab renovation: **c**, from the translator's perspective, and **d**, from the science chamber's perspective.

Figure 12.20: Aluminum foil wrapped around the vacuum chamber, lacking the translator, for improved heat retention during bakeout. **a**, a single from the loadlock chamber's perspective. **b**, multiple layers from the science chamber's perspective. **c**, the turbo pump station. **d**, the ion gauge with exposed pins. **e**, the ion gauge carefully foiled to prevent electrical shorts.

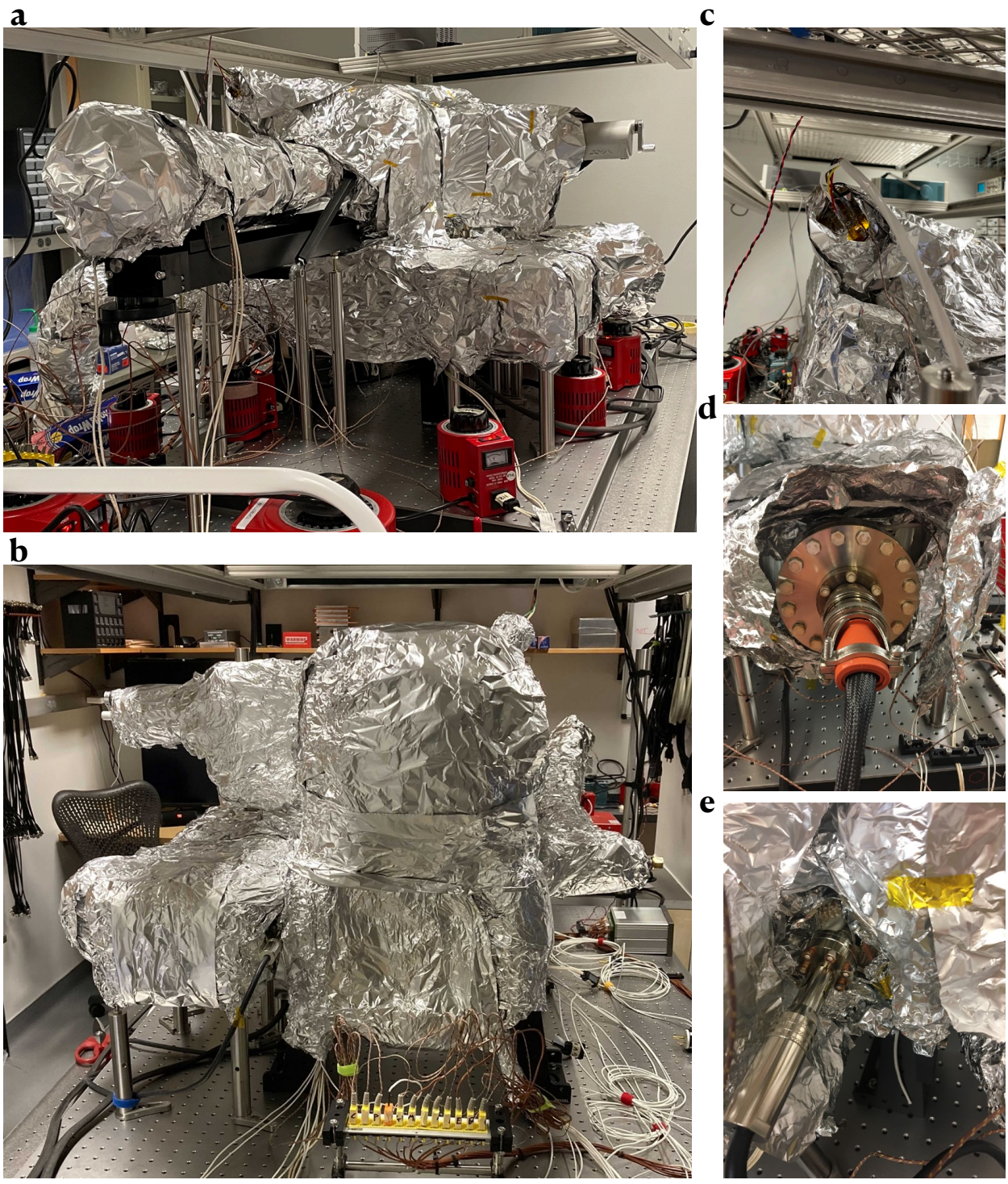

Figure 12.21: Aluminum foil wrapped around the vacuum chamber, with the translator. **a**, from the translator and the loadlock chamber's perspective. **b**, from the science chamber's perspective. **c**, the ion gauge. **d**, the Ti-sub pump connection. **e**, the ion pump connection.

Vacuum Bakeout: components	**Supplier**	**PN**	**Qty**
Variac: for power control	N/A	N/A	~ 30
Thermal Couple: ready-made, glass braid insulated, 72”	Omega	5SRTC-TT-K-20-72	~ 10
Thermal Couple: ready-made, glass braid insulated, 36”	Omega	5SRTC-GG-K-20-36	~ 10
Thermal Couple: ready-made, glass braid insulated, 72”	Omega	5SRTC-GG-K-20-72	~ 10
Silicon Heater: flexible heating pad, rectangular 3” $\times$ 3”	Omega	SRFGA-303/10-P	8
Silicon Heater: flexible heating pad, round 3” diameter	Omega	SRFGA-3/10	2
Silicon Heater: flexible heating pad, rectangular 2” $\times$ 5”	Omega	SRFGA-205/2-P	2
Heating Tape: high-temp, 4’ long	Omega	DHT051040LD	3
Heating Tape: high-temp, 6’ long	Omega	DHT051060LD	3
Heating Tape: high-temp, 8’ long	Omega	DHT051080LD	3
High-Temperature Wire: Mica, 450°C rated, 10’ long, AWG 16	Bryne	N/A	4
High-Temperature Wire: Mica, 450°C rated, 10’ long, AWG 18	Bryne	N/A	8
Aluminum Foil: 200 square-foot	Reynolds Wrap	N/A	~ 10
Copper Sheet: to spread heat across viewports, 12” $\times$ 12” $\times$ 0.02”	McMaster-Carr	2545T11	5
Copper Sheet: to spread heat across viewports, 4” $\times$ 24” $\times$ 0.02”	McMaster-Carr	8963K203	3
Copper Sheet: to spread heat across viewports, 6” $\times$ 6” $\times$ 0.02”	McMaster-Carr	8963K204	2
Sheet Metal Cutter	McMaster-Carr	38805A74	1

Table 12.7: Breakdown of vacuum bakeout components.

Vacuum Bakeout: control	**Label**	**Bakeout Area**
Heating Tape	HT1	Loadlock chamber
Heating Tape	HT2	Loadlock tee
Heating Tape	HT3	Loadlock ion pump
Heating Tape	HT4	Loadlock triple flange, ion pump side
Heating Tape	HT5	Loadlock triple flange, turbo pump side
Heating Tape	HT6	Gate valve and close couplers
Heating Tape	HT7	Science chamber
Heating Tape	HT8	Science cross
Heating Tape	HT9	Science ion pump
Heating Tape	HT10	Science triple flange, ion pump side
Heating Tape	HT11	Science triple flange, blank flange side
Heating Tape	HT12	Ion gauge
Heating Tape	HT13	Turbo pump angle valve
Heating Tape	HT14	Turbo pump bellow
Heating Pad	HP1	Science chamber viewport, top
Heating Pad	HP2	Science chamber viewport, bottom
Heating Pad	HP3	Science chamber viewport, front
Heating Pad	HP4	Science chamber viewport, ion pump side
Heating Pad	HP5	Science chamber viewport, blank flange side
Heating Pad	HP6	Loadlock chamber blank flange, top

Table 12.8: Temperature control for vacuum bakeout, temperature delivery. A combination of heating tapes and heating pads, controlled by variacs, were utilized for precise temperature delivery while maintaining independence among different bakeout areas.

Vacuum Bakeout: control	**Label**	**Bakeout Area**
Thermal Couple	TC1	Loadlock chamber flange, top
Thermal Couple	TC2	Loadlock chamber flange, ion pump side
Thermal Couple	TC3	Loadlock chamber flange, turbo pump side
Thermal Couple	TC4	Loadlock chamber flange, translator side
Thermal Couple	TC5	Loadlock tee
Thermal Couple	TC6	Loadlock ion pump
Thermal Couple	TC7	Loadlock triple flange, ion pump side
Thermal Couple	TC8	Loadlock triple flange, turbo pump side
Thermal Couple	TC9	Science chamber viewport, top
Thermal Couple	TC10	Science chamber viewport, ion pump side
Thermal Couple	TC11	Science chamber viewport, blank flange side
Thermal Couple	TC12	Science chamber viewport, MOT side
Thermal Couple	TC13	Science chamber viewport, bottom
Thermal Couple	TC14	Science chamber viewport, small diagonal 1
Thermal Couple	TC15	Science chamber viewport, small diagonal 2
Thermal Couple	TC16	Science chamber viewport, small diagonal 3
Thermal Couple	TC17	Science chamber viewport, small diagonal 4
Thermal Couple	TC18	Science chamber viewport, small diagonal 5
Thermal Couple	TC19	Science chamber viewport, small diagonal 6
Thermal Couple	TC20	Science chamber viewport, small diagonal 7
Thermal Couple	TC21	Science chamber viewport, small diagonal 8
Thermal Couple	TC22	Science cross
Thermal Couple	TC23	Science ion pump
Thermal Couple	TC24	Science triple flange, ion pump side
Thermal Couple	TC25	Science triple flange, blank flange pump side
Thermal Couple	TC26	Ion gauge
Thermal Couple	TC27	Turbo pump angle valve
Thermal Couple	TC28	Turbo pump bellow

Table 12.9: Temperature control for vacuum bakeout, temperature measurement. Thermal couples, with readings displayed by a homemade breakout panel, were utilized for precise temperature measurements of various bakeout areas.

12.7 Performance of the UHV System

The ultra-high vacuum (UHV) system's performance was evaluated through a series of bake-outs and pressure measurements, both in the absence and presence of a cavity. The purpose of these experiments was to establish a baseline for temperature and pressure behavior and to ensure the system's integrity and performance for subsequent experimental procedures.

12.7.1 Initial Bakeout in the Absence of a Cavity

During the initial vacuum bakeout, temperature measurements were recorded by thermal couples, and the results are shown in Figure 12.22. The corresponding pressure measurements, recorded by the ion pumps, are presented in Figure 12.23. These measurements indicate the outgassing rate and the efficiency of the ion pumps in maintaining the desired vacuum level. Additionally, the relationship between pressure and temperature during this bakeout was analyzed, as shown in Figure 12.24. This relationship is crucial for understanding the dynamics of the vacuum system and ensuring that the bakeout process effectively reduces the pressure to UHV levels, thus serves as a reference for future bakeouts.

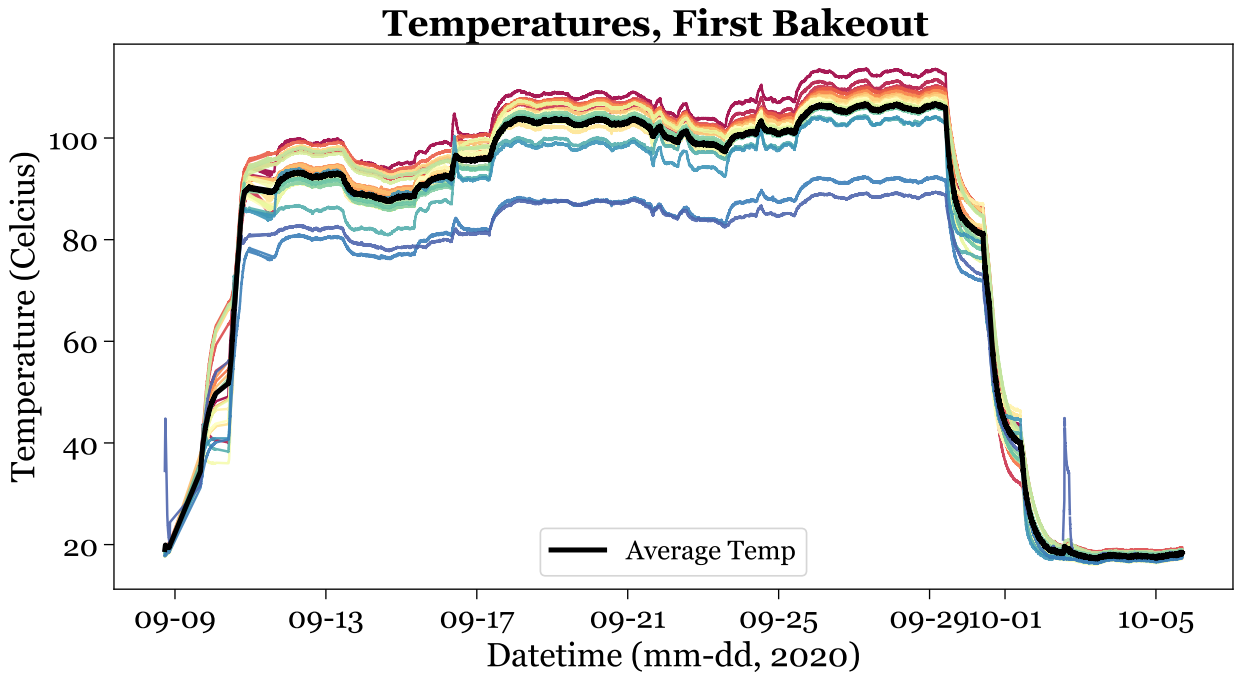

Figure 12.22: Temperature measurements during the initial vacuum bakeout, in the absence of a cavity, recorded by the thermal couples.

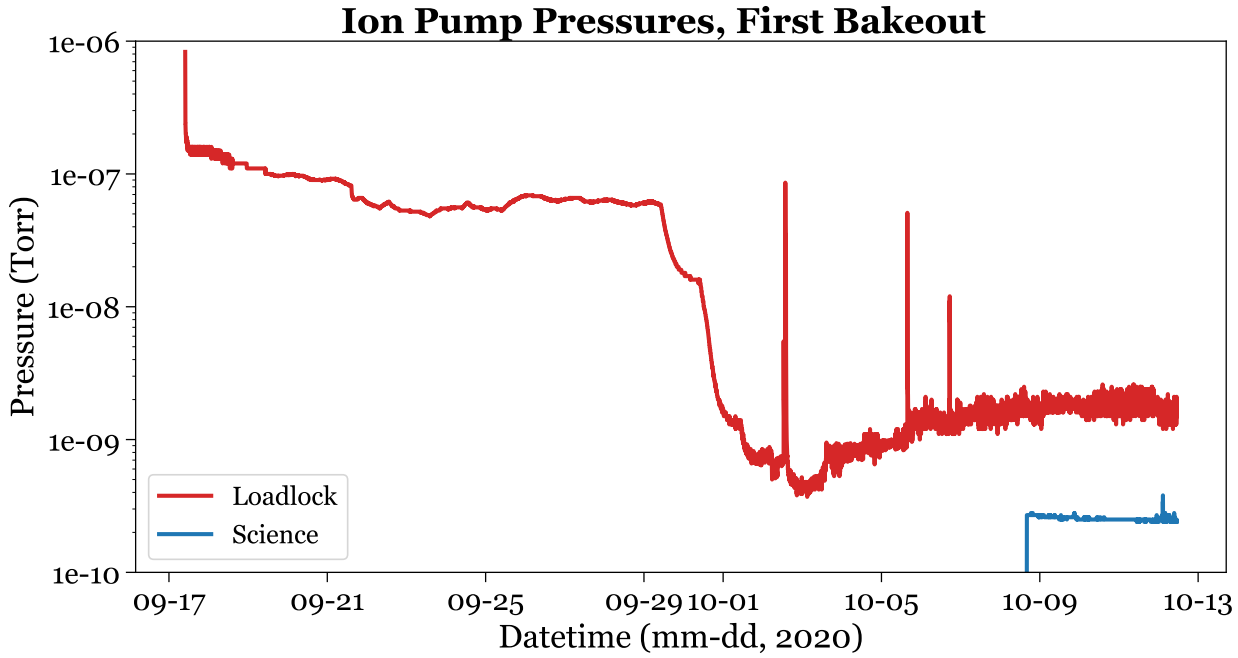

Figure 12.23: Pressure measurements during the initial vacuum bakeout, in the absence of a cavity, recorded by the ion pumps.

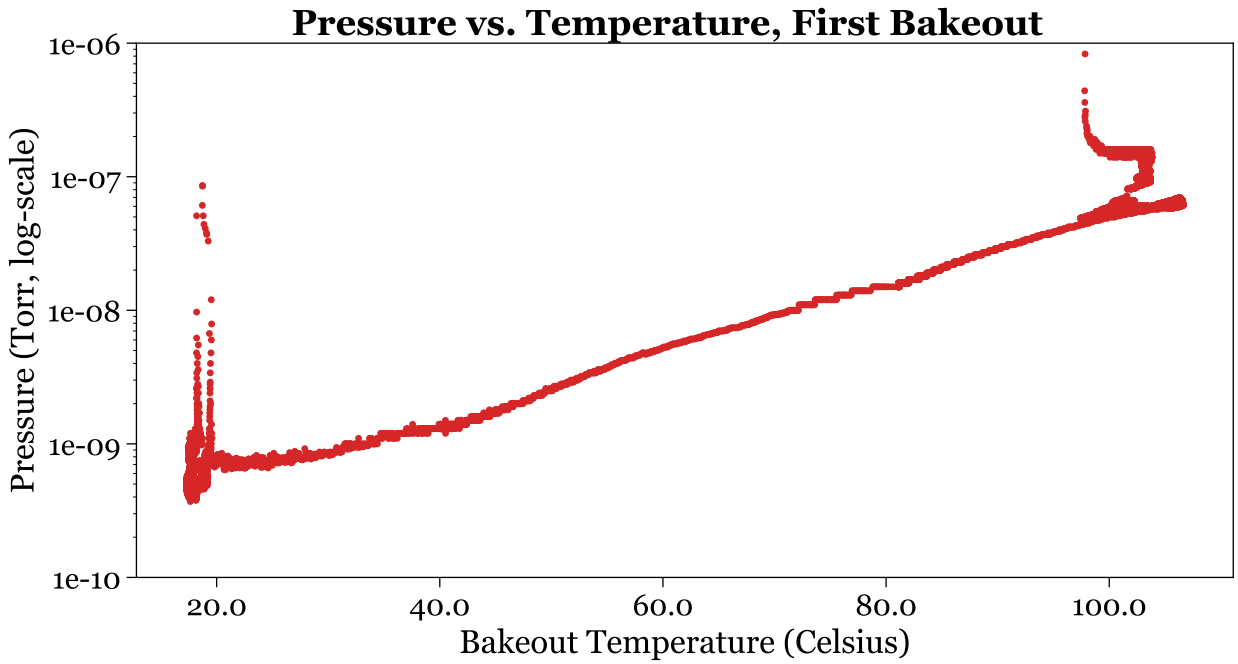

Figure 12.24: Pressure vs temperature measurements during the initial vacuum bakeout, to establish a baseline relationship between the two.

12.7.2 Second Bakeout in the Absence of a Cavity

A second vacuum bakeout was performed to further refine the vacuum conditions. During this bakeout, a leak was detected and subsequently fixed. The temperature and pressure measurements, recorded by the thermal couples and ion pumps respectively, are shown in Figures 12.25 and 12.26. The relationship between pressure and temperature during this bakeout was analyzed, as shown in Figure 12.27.

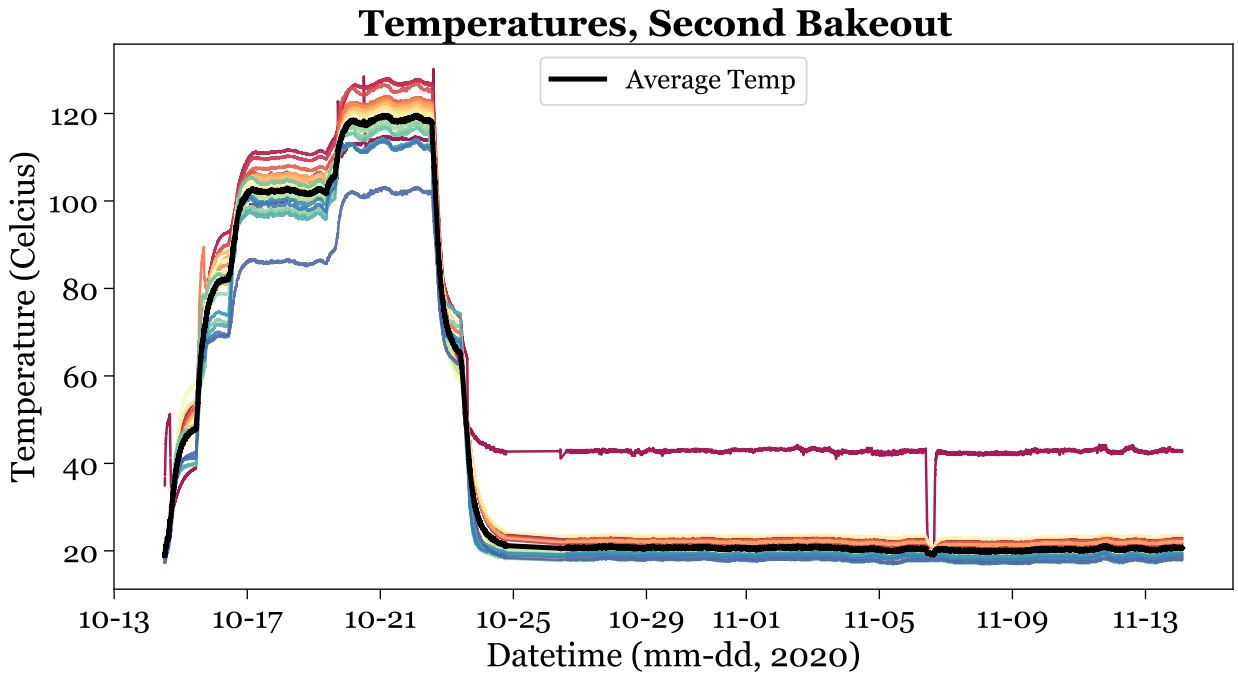

Figure 12.25: Temperature measurements during the second vacuum bakeout, in the absence of a cavity, recorded by the thermal couples. A leak was detected and subsequently fixed.

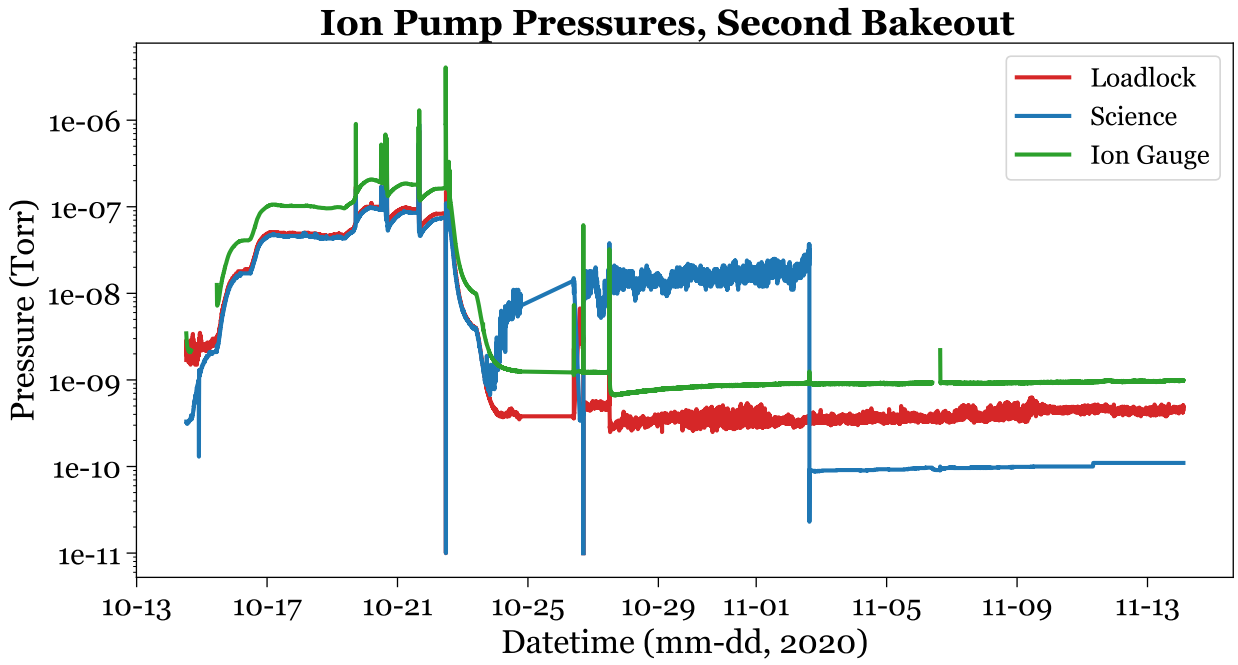

Figure 12.26: Pressure measurements during the second vacuum bakeout, in the absence of a cavity, recorded by the ion pumps and the ion gauge. A leak was detected and subsequently fixed.

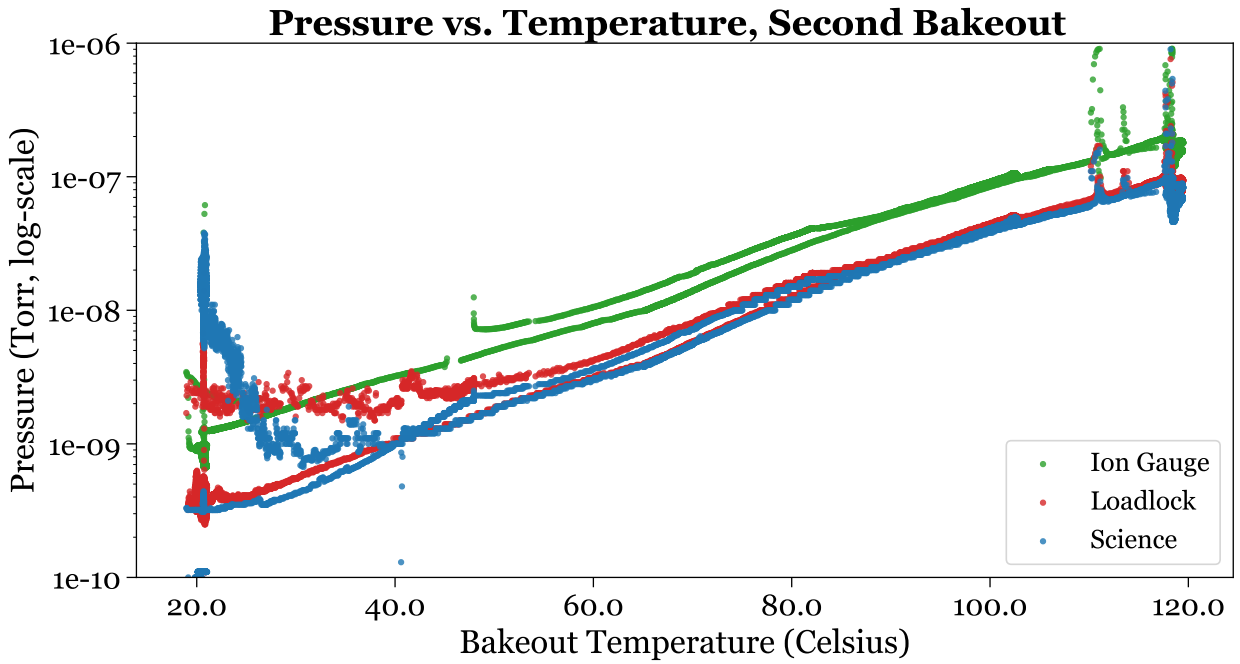

Figure 12.27: Pressure vs temperature measurements during the second vacuum bakeout.

12.7.3 First Bakeout in the Presence of a Cavity

Subsequent bakeouts were performed with the cavity installed in the vacuum chamber. The temperature measurements recorded during the first bakeout with the cavity are shown in Figure 12.28, and the corresponding pressure measurements are presented in Figure 12.29.

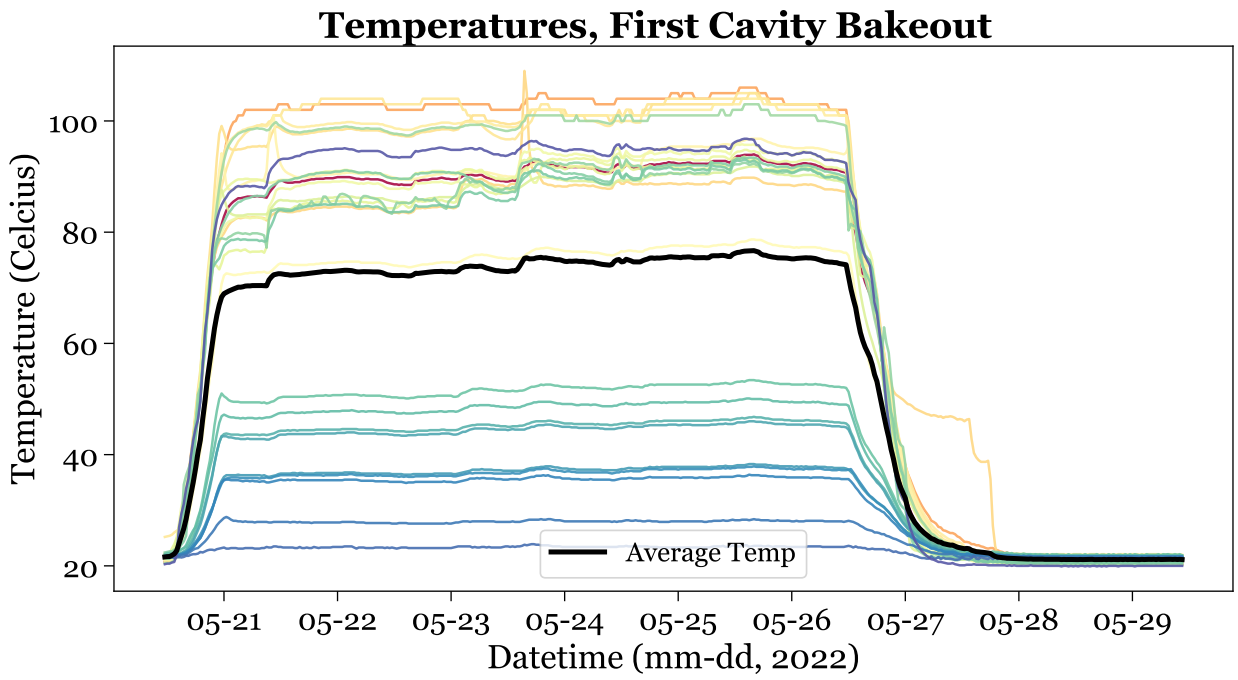

Figure 12.28: Temperature measurements during the first vacuum bakeout, in the presence of a cavity, recorded by the thermal couples.

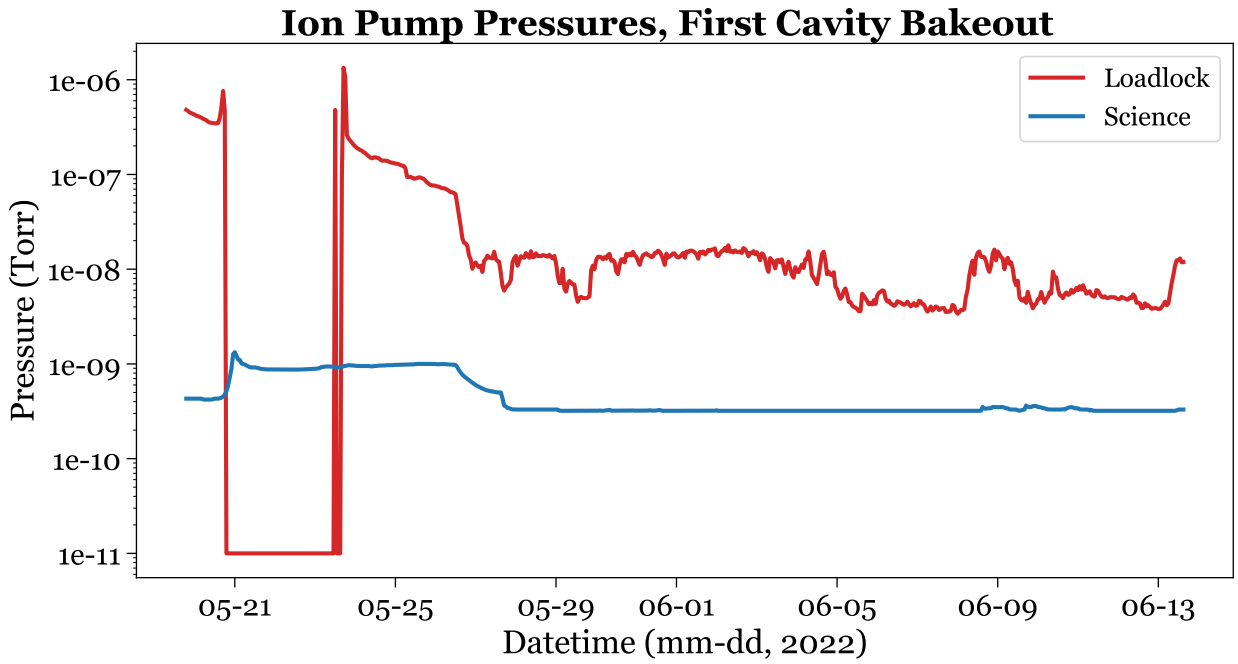

Figure 12.29: Pressure measurements during the first vacuum bakeout, in the presence of a cavity, recorded by the ion pumps.

12.7.4 Second Bakeout in the Presence of a Cavity

Similarly, the second bakeout with the cavity in place was performed, with temperature and pressure measurements shown in Figures 12.30 and 12.31. These measurements are critical for ensuring that the cavity does not introduce additional outgassing or vacuum degradation, thereby confirming the system's readiness for high-precision experimental work.

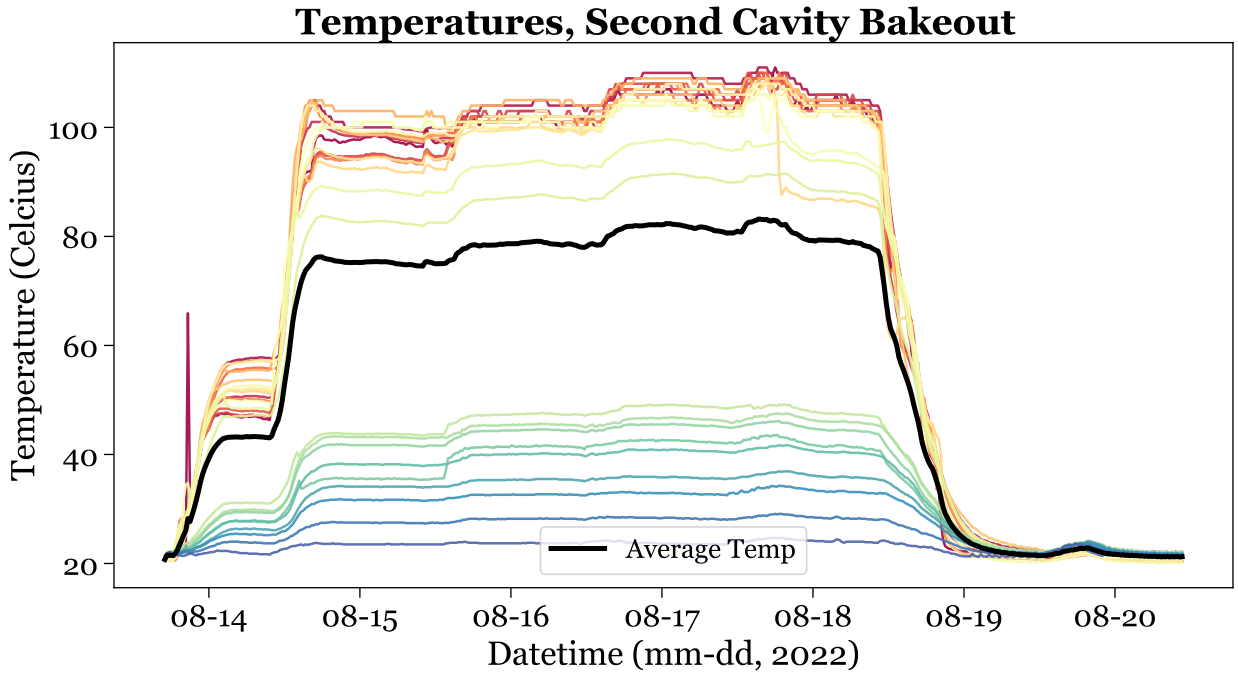

Figure 12.30: Temperature measurements during the second vacuum bakeout, in the presence of a cavity, recorded by the thermal couples.

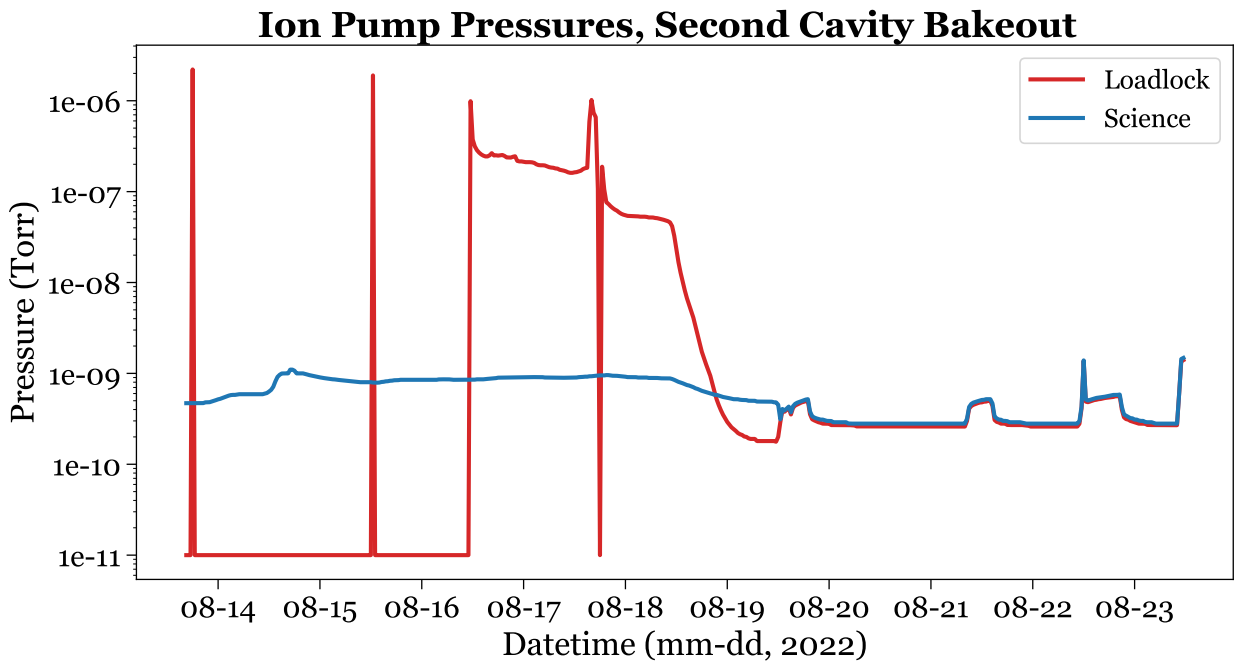

Figure 12.31: Pressure measurements during the second vacuum bakeout, in the presence of a cavity, recorded by the ion pumps.

CHAPTER 13

CAVITY CARRIER, FEEDTHROUGH, AND TRANSLATOR

13.1 Introduction

The atom source consists of four Rb dispensers held below the central cavity plate facing downwards, as shown in Fig. 13.1, so the ejected atomic vapor has line-of-sight access to the center of the MOT assembly, but no line-of-sight access to the optical cavity above the plate; this minimizes deposition of Rb atoms on the cavity mirrors. The dispensers are part of the transportable setup for easy replacement, and can be individually controlled. Structurally, the dispensers are sandwiched between copper blocks which are tensioned by silver-plated, vented screws and spring washers[1], and electrically isolated by a macor plate suspended below the central stainless plate.

1. The spring washers are important because we have, in the past, observed that the time-varying thermal load associated with turning the dispensers on and off can eventually loosen the screws and break electrical contact

13.2 Design and Components of the Cavity Carrier

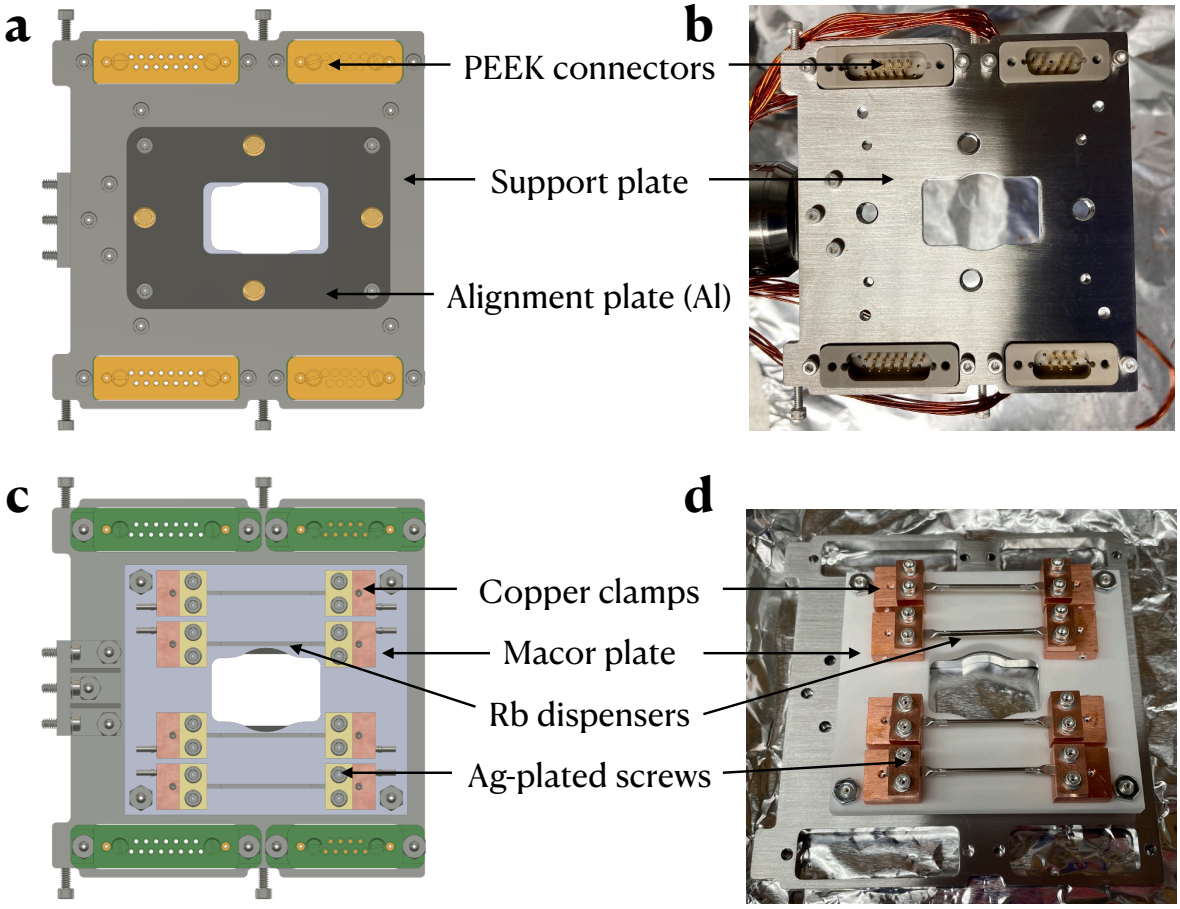

Figure 13.1: Cavity carrier. **a**, **b**, Looking from above, this structure carries an optical cavity above, and is secured to the end of the translator. Four dowel pins and four silver-plated screws are used to precisely align and secure the optical cavity with the carrier plate. Four pairs of PEEK connectors deliver electrical connections to the optical cavity through Kapton-coated feedthrough wires bundled inside the translator tube. **c**, **d**, Below the cavity carrier reside four Rb dispensers which are independently controlled and easily replaceable, and each has line-of-sight access to the position of the MOT, but no line-of-sight access to the optical cavity above that can cause atom deposition on the optical surfaces. A Macor plate is used as an electrical insulator to set a voltage difference across the dispensers. Silver-plated vented screws and spring washers are used to sandwich the dispensers between two layers of copper blocks, and gold pins are pressed from the side of the copper block to make secure electrical connections, in a way that the electrical connections can withstand thermal cycles of the vacuum bakeouts.

In-Vacuum Cavity Carrier: cavity	**Supplier**	**PN**	**Qty**
Cavity Base Plate, stainless	3ERP	Custom: appx. A.9	1
Alignment Plate: aluminum	3ERP	Custom: appx. A.11	1
Dowel Pin: machined from brass rod with a die, 1/8" diameter x 3'	McMaster-Carr	8953K101	4
L-Bracket, stainless	3ERP	Custom: appx. A.13	1
sub-D PEEK Connector: male, with mounting ears, 9-pin	Accu-Glass Products	112125	2
sub-D PEEK Connector: female, 9-socket	Accu-Glass Products	100440	2
sub-D PEEK Connector: male, with mounting ears, 15-pin	Accu-Glass Products	100423	2
sub-D PEEK Connector: female, 15-socket	Accu-Glass Products	100450	2
Contact: gold-plated pins, male, for 20-24 AWG, 10 pack	Accu-Glass Products	100170	16
Contact: gold sockets, female, for 20-24 AWG, 10 pack	Accu-Glass Products	100180	16
Wire: Kapton-insulated, silver-plated, 22 AWG, 30 Ft.	Accu-Glass Products	100680	3
Wire: Kapton-insulated, silver-plated, 20 AWG, 30 Ft.	Accu-Glass Products	100675	3

Table 13.1: Breakdown of in-vacuum cavity carrier components, with an emphasis on cavity support.

To simplify the process of moving the cavity-under-test between the two chambers, a cavity carrier structure connected to the end plate of the translator tube is designed to support a cavity on top with maximal flexibility (Fig. 13.1). The cavity carrier assembly consists of a central stainless steel plate which connects to the translator and structural support. On top of the cavity carrier, another smaller plate is mounted to mechanically support a cavity with four screws and four dowel pins for positional accuracy. On two sides of the central stainless plate, four female PEEK connectors are fastened below to hold a total of 40 gold pins each individually connected to a Kapton-insulated wire, which are then bundled and fed inside

In-Vacuum Cavity Carrier: dispenser	**Supplier**	**PN**	**Qty**
Rb Dispenser	SAES Getters	5G0130	4
Macor Plate: macor	3ERP	Custom: appx. A.10	1
Spacer, stainless	McMaster-Carr	-	4
Dispenser Clamp: copper, bottom	3ERP	Custom: appx. A.12	8
Dispenser Clamp: copper, top	3ERP	Custom: appx. A.12	8
Vented Screw: hex, 4-40 × 3/8"	U-C Components	C-406-A	4
Vented Screw: hex, 4-40 × 5/8"	U-C Components	C-410-A	4
Vented Screw: hex, 4-40 × 1/2"	U-C Components	C-408-A	15
Vented Screw: hex, 2-56 × 1/4"	U-C Components	C-204-A	16
Vented Screw: flathead, 2-56 × 3/8"	U-C Components	FA-206-A	16
Vented Screw: set screw, 2-56 × 3/32"	U-C Components	T-202-SVA	8
Spring Washer: for 2-56 thread	McMaster-Carr	9712K52	16
Nut: hex, 4-40 thread	McMaster-Carr	91841A005	15
Nut: hex, 2-56 thread	McMaster-Carr	91841A003	16

Table 13.2: Breakdown of in-vacuum cavity carrier components, with an emphasis on dispenser support.

the translator tube to the feedthrough flange. The cavity-under-test is intended to connect via PEEK connectors to electrodes, piezo control, heating, and other electrical components.

13.3 Assembly and Integration of Translator with Cavity Carrier (Stage IIa)

To resolve the geometrical conflict with the original utility hat feedthrough setup (Fig. 13.2), a new five-way cross was installed. This five-way cross is attached to the base flange with a 2.75" CF triple flange, providing four 2.75" CF flanges for feedthroughs. Two flanges house 6-pin MPC feedthrough connectors, one houses a 10-pin MPC feedthrough connector, and the remaining one houses an 18-pin MPCT feedthrough connector.

Assemble the five-way cross. Clean all in-vacuum parts and tools: parts (Fig. 13.7) as well as metal-tipped tools (e.g., tweezers, razor blades, and wire cutters) are sonicated,

while tools with plastic parts (e.g., the Kapton wire stripper) are wiped down with IPA (Fig. 13.8). Cut the wires to the appropriate lengths and organize them into four bundles of 10 wires and one bundle of 6 wires. Crimp the wires to gold pins and seat the pins inside the respective feedthrough connectors, securing them with retaining rings before closing the connectors as per the instructions. This process is shown in Fig. 13.3.

Attach the five-way cross to the base of the translator. Remove the copper gasket from the triple flange and slide the translator tube out. Since the copper gasket has a non-standard inner diameter, lathe a new gasket to ensure compatibility with the translator tube setup. Hold the assembled five-way cross, place the new copper gasket, organize the wires, and attach it to the translator. Insert screws through the rotational base flange and tighten them with a torque wrench. This process is shown in Fig. 13.4.

Attach the cavity plate to the translator tube. Connect the cavity plate to the translator tube using the L-bracket and organize the bundles of wires. Strip and crimp the wires to gold pins, seat the pins inside half of the PEEK connectors, secure them with retaining rings, and close the PEEK connectors. Fasten the PEEK connectors to the cavity plate, ensuring all components are securely connected and properly organized. This process is shown in Fig. 13.5 and Fig. 13.6.

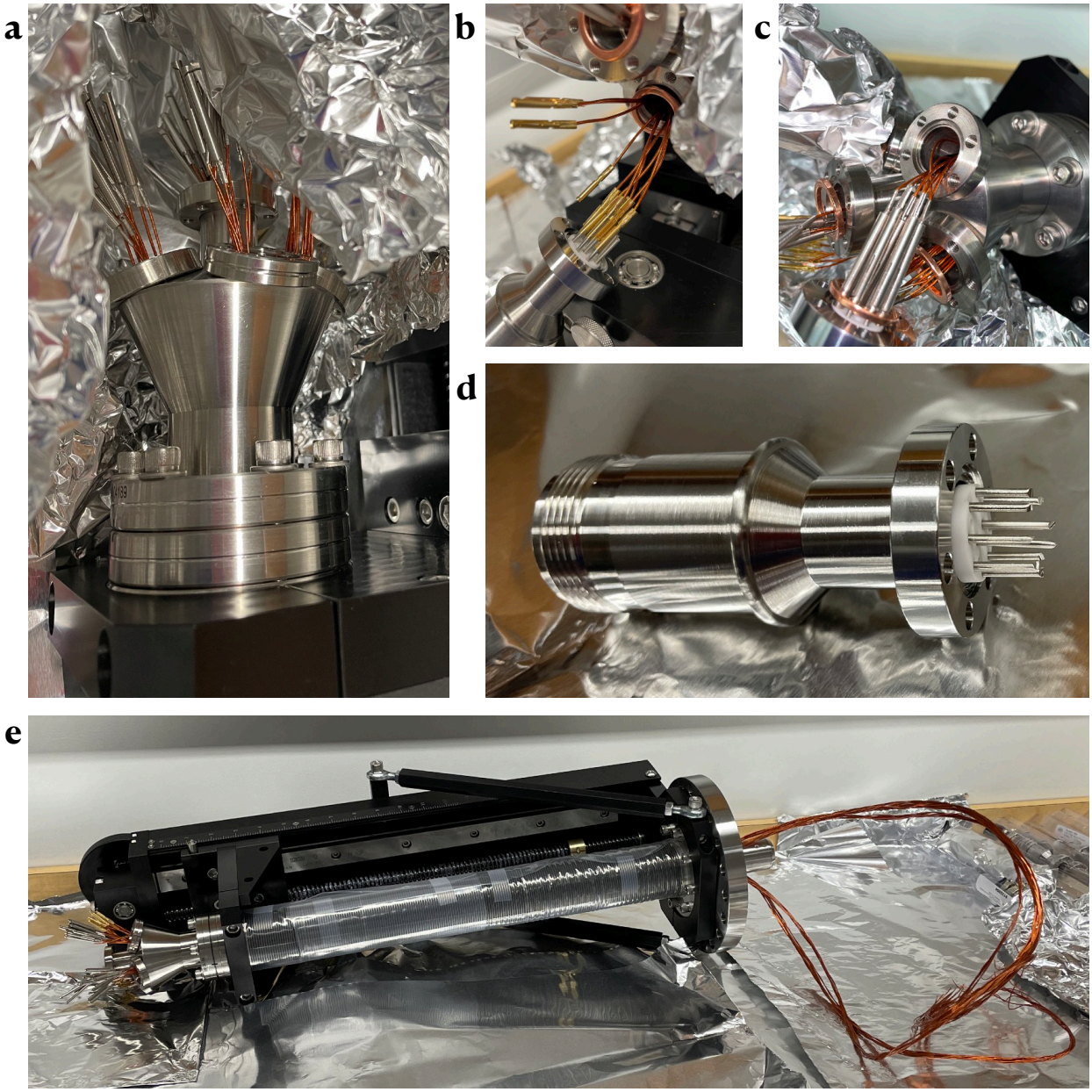

Figure 13.2: Obsolete feedthrough assembly. This feedthrough assembly is now obsolete due to its default setup with the translator, which led to potential electrical shorts between the voltage-carrying pins and the chamber walls, thus consequently replaced. **a**, the utility feedthrough hat assembly. Failed examples feedthrough connectors with short and long pins in **b** and **c**, respectively. **d**, a feedthrough connector with shortened pins. **e**, the obsolete feedthrough assembly.

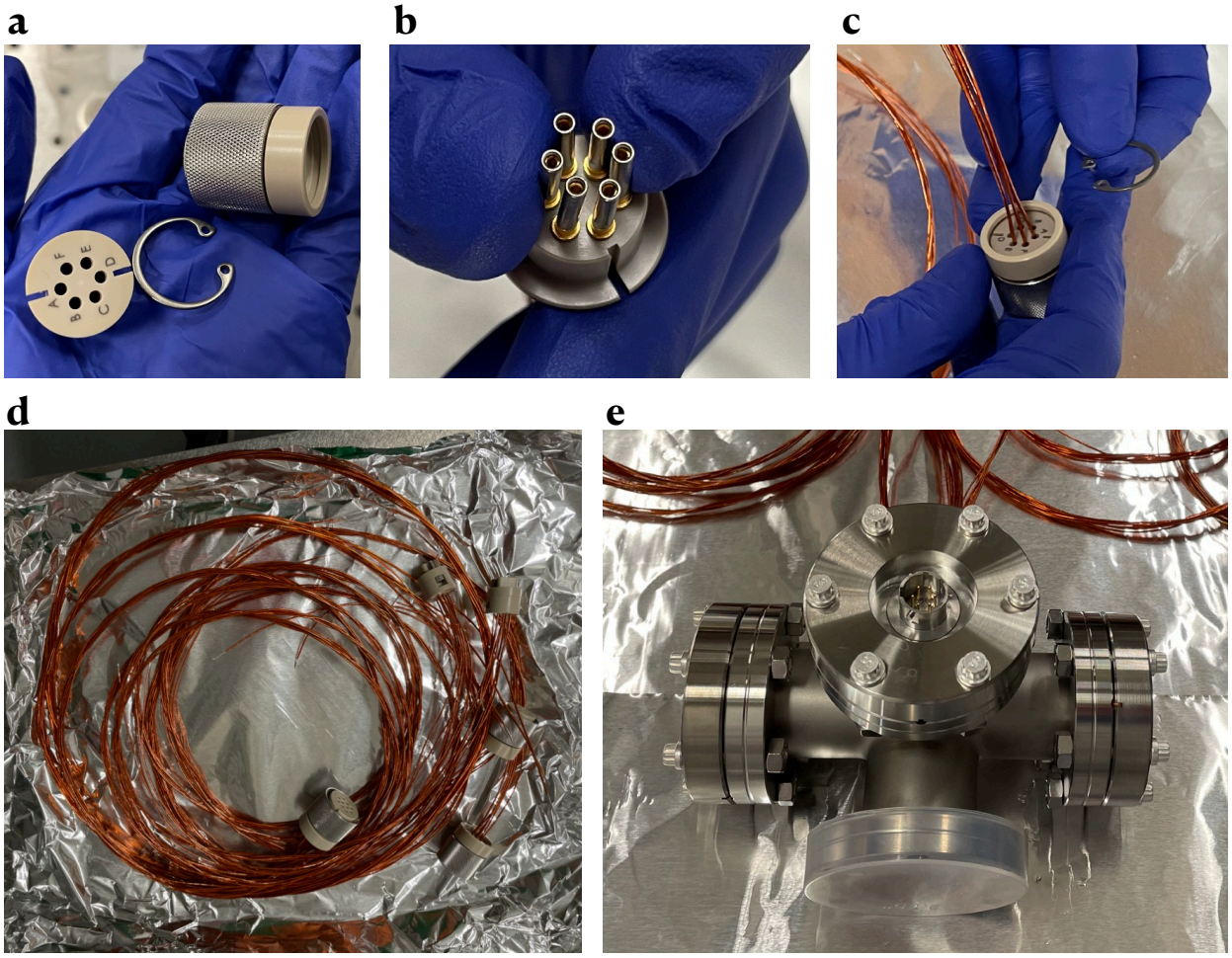

Figure 13.3: Assembly of the five-way cross. **a**, components of a feedthrough connector barrel, including an insulating spacer, a retaining ring, and contacts. **b**, properly seated contacts inside the connector barrel. **c**, Kapton-coated copper wires crimped onto the contacts, with the contacts positioned between the connector barrel and a retaining ring inserted for tensioning. **d**, completed feedthrough connector with attached Kapton-coated copper wires. **e**, top view of the five-way cross.

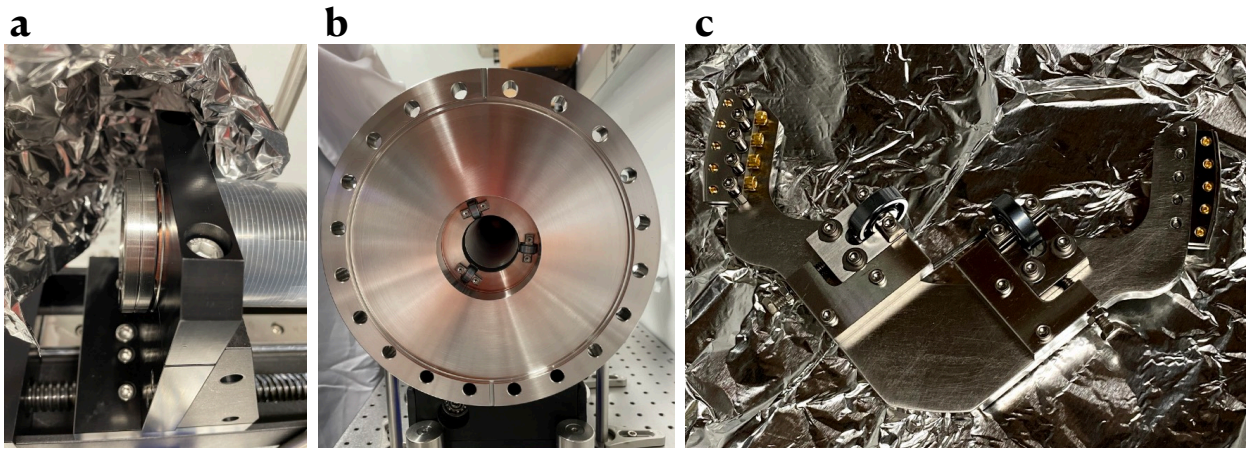

Figure 13.4: Components of the translator. **a**, triple flange used for attaching the five-way cross, replacing the original utility hat. **b**, base flange of the translator, equipped with three gliding wheels with vacuum-grade grease applied to support the translator tube. **c**, the V-stand with two sliding wheels, designed to guide and support the translator tube at the close coupler between the loadlock and the science chamber, preventing sagging.

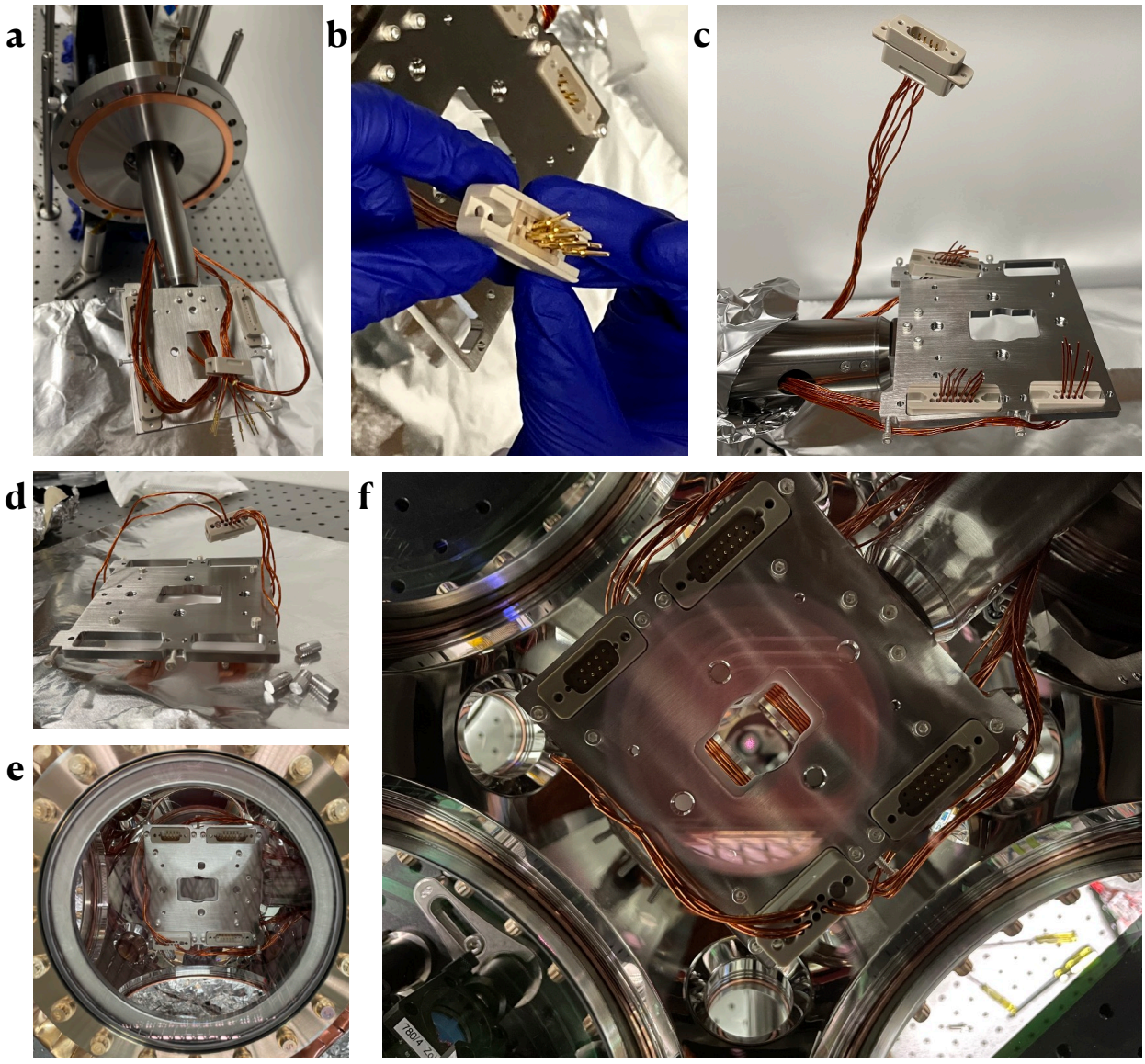

Figure 13.5: Assembly of the cavity plate, top view. **a**, feedthrough wires routed through the translator tube and the female PEEK connectors, organized and crimped onto contacts. **b**, three opened bottom female PEEK connectors fastened to the steel cavity plate, alongside a closed female PEEK connector. **c**, gold-plated contacts being seated between two halves of a female PEEK connector. **d**, a male PEEK connector for the dispenser setup. **e**, the cavity carrier installed inside the vacuum chamber. **f**, the cavity carrier plate inside the vacuum chamber during operation mode.

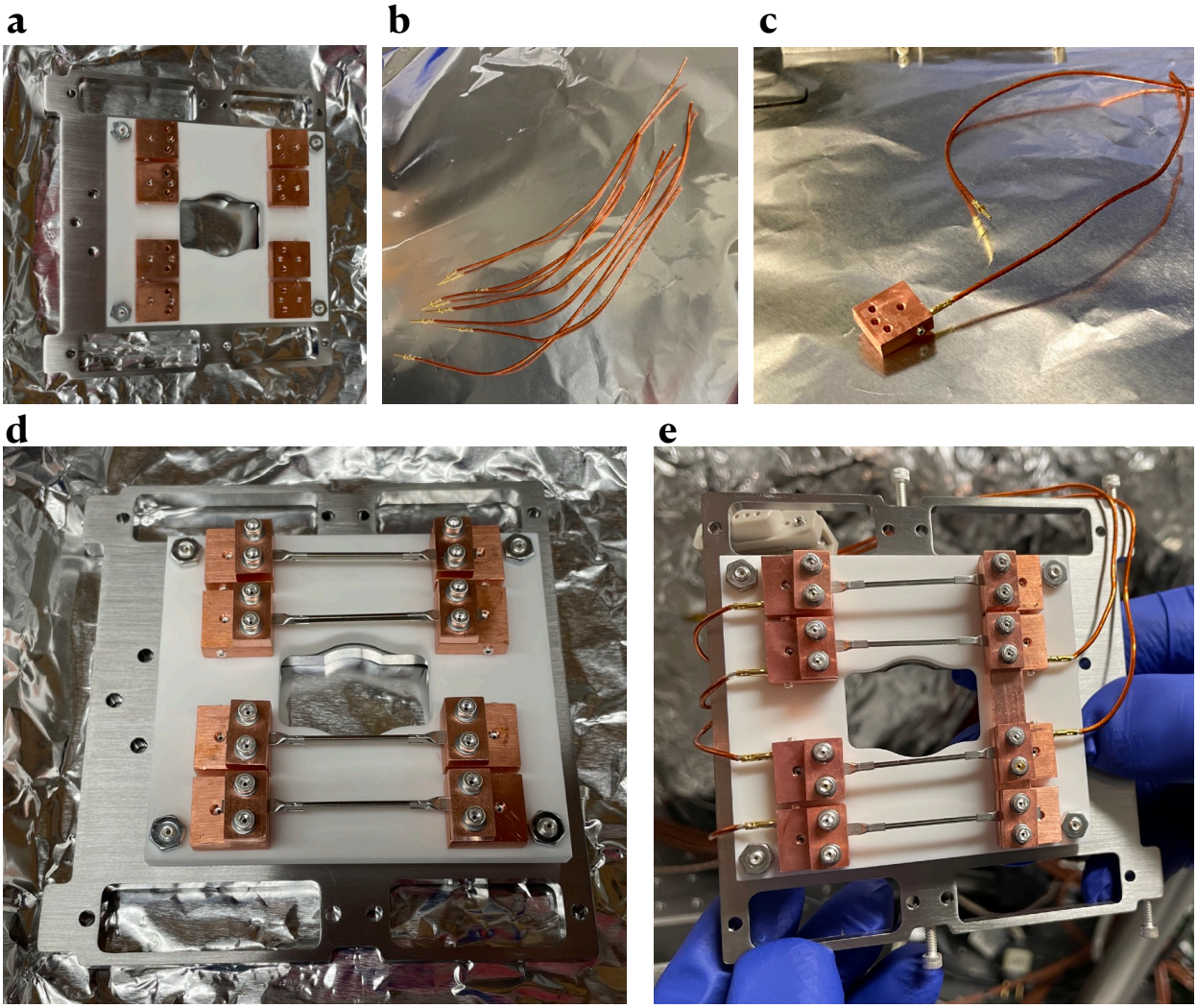

Figure 13.6: Assembly of the cavity plate, bottom view. **a**, the bottom copper blocks, Macor plate, spacers (hidden), and steel cavity plate assembled together. **b**, Kapton-coated wires stripped and crimped to contacts. **c**, the stripped side of a Kapton-coated wire crimped to a contact, then electrically connected to a copper block by the tension of a silver-plated vented set screw. **d**, four dispensers electrically connected to the copper blocks by spring washers and silver-plated vented screws tensioning the top and bottom copper blocks. **e**, finished bottom view of the cavity plate.

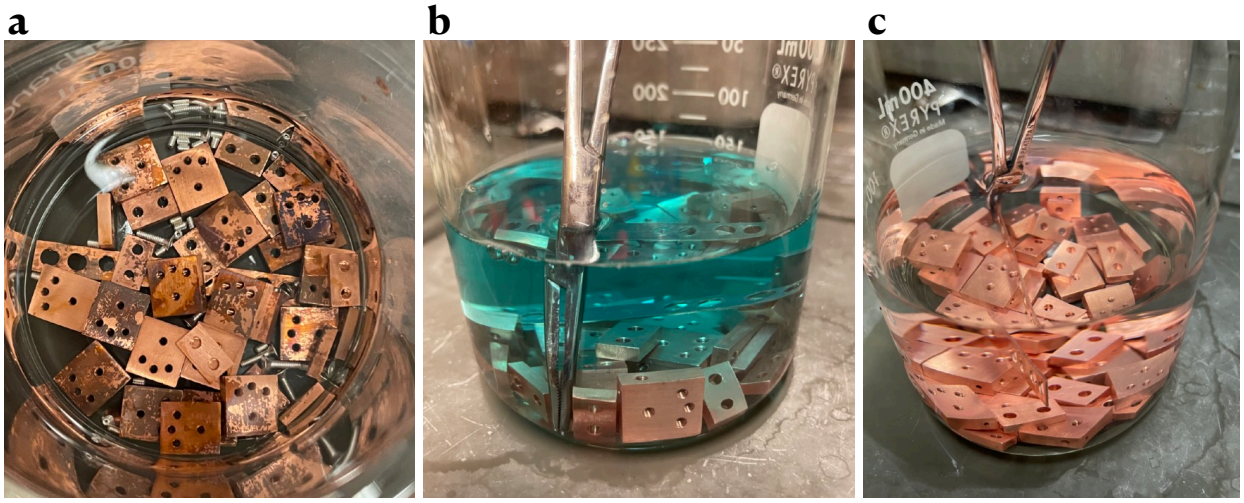

Figure 13.7: Cleaning of copper blocks. **a**, oxidized copper. **b**, the copper blocks being sonicated in hydrofluoric acid. **c**, the copper blocks with restored salmon color after chemical cleaning.

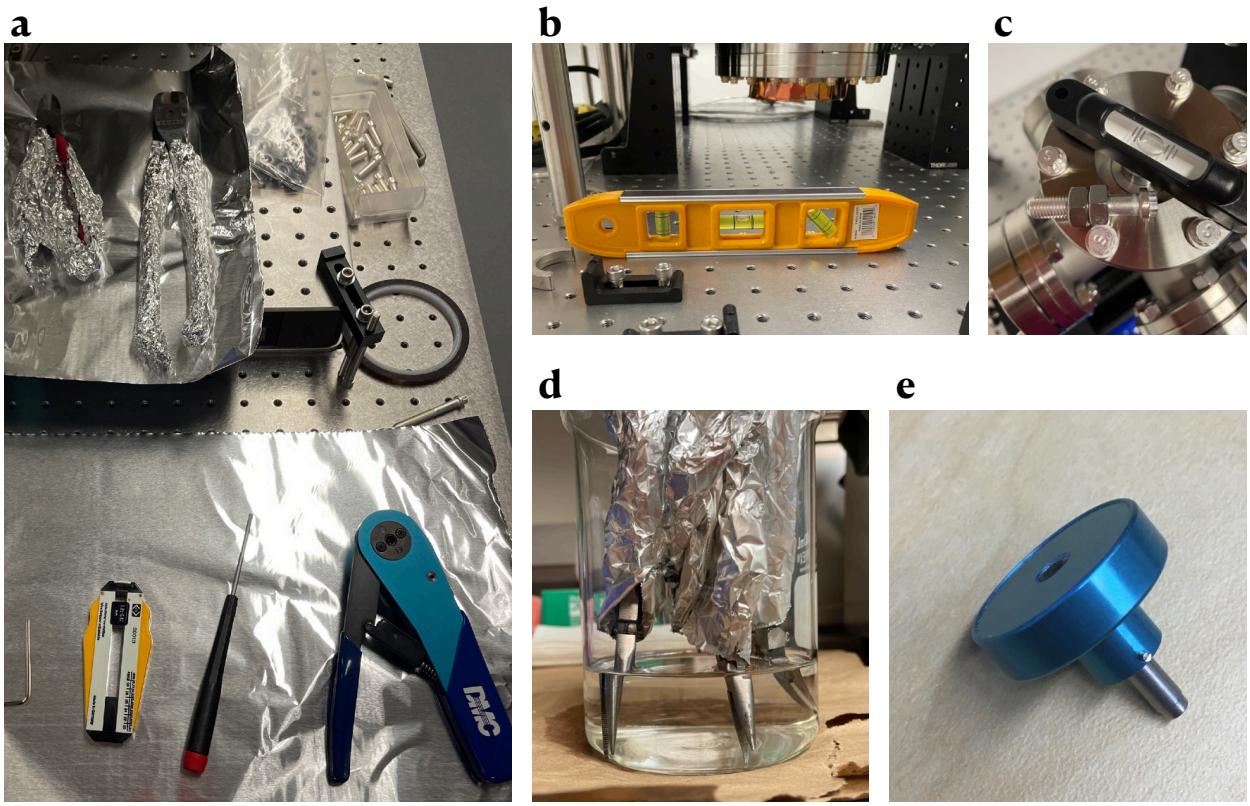

Figure 13.8: Tools used for vacuum assembly Stage II. **a**, tools undergoing partial sonication (top) or chemical wiping (bottom). **b** and **c**, levels for ensuring precise leveling of optical table and chamber components, respectively. **d**, tool tips subjected to sonication.**e**, a positioner utilized for crimping feedthrough contacts.

13.4 Design and Components of the Feedthrough System

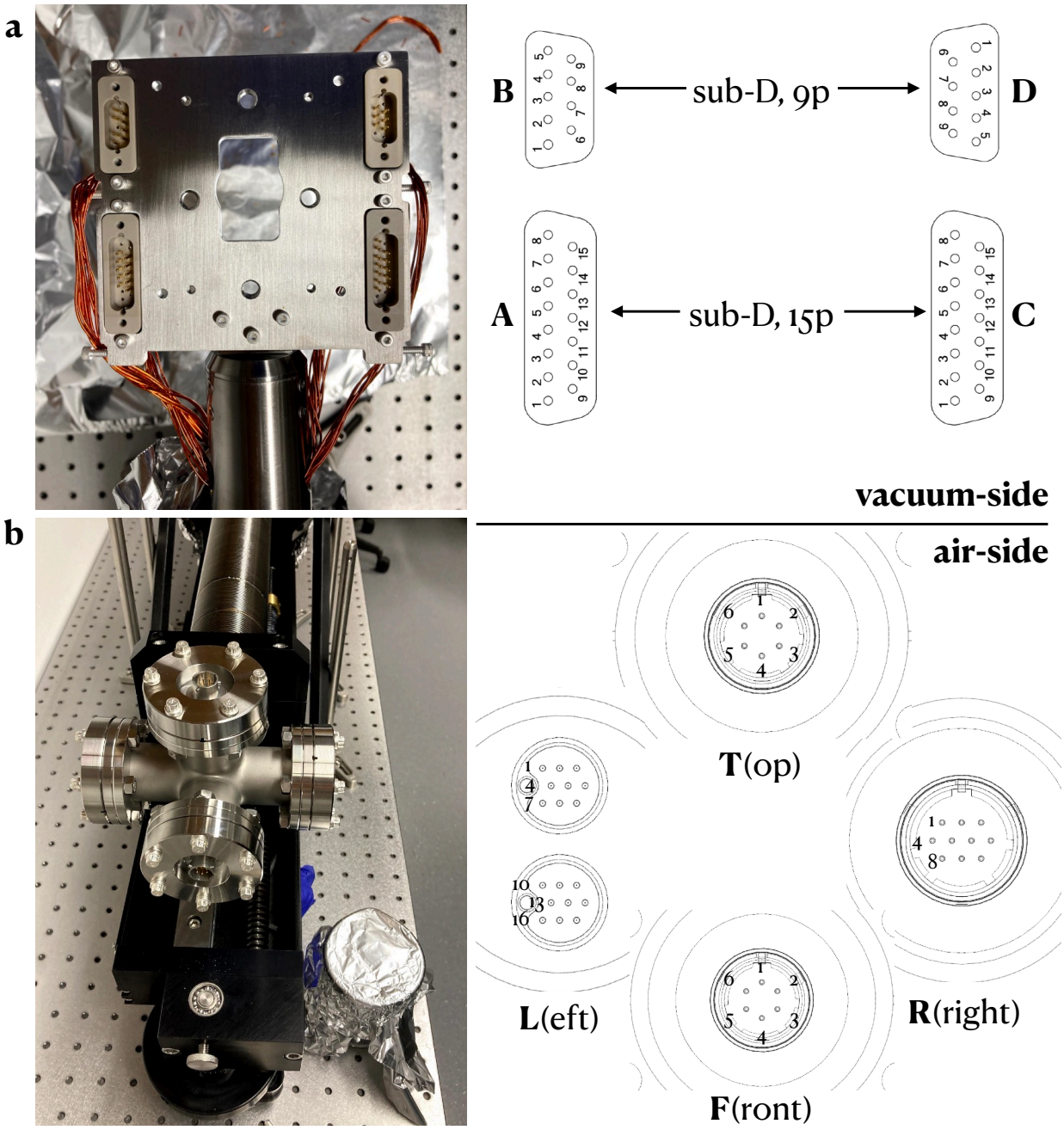

Figure 13.9: Feedthrough pinout. **a**, in-vacuum PEEK connectors, as seen from the perspective of the cavity plate. Note the asymmetry of the connectors. **b**, air-side feedthrough flanges on the five-way cross.

Feedthrough Pinout: purpose	**Vacuum-side Pin**	**Air-side Pin**
Magnetic Coil: sensitive to noise	PEEK C3	LEFT 1
Magnetic Coil: sensitive to noise	PEEK C14	LEFT 2
Magnetic Coil: sensitive to noise	PEEK C7	LEFT 3
Magnetic Coil: sensitive to noise	PEEK C5	LEFT 4
Magnetic Coil: sensitive to noise	PEEK C2	LEFT 5
Magnetic Coil: sensitive to noise	PEEK C11	LEFT 6
Cavity Electrode: sensitive to noise	PEEK A13	LEFT 8
Cavity Electrode: sensitive to noise	PEEK A4	LEFT 9
Cavity Electrode: sensitive to noise	PEEK A12	LEFT 10
Cavity Electrode: sensitive to noise	PEEK A11	LEFT 11
Cavity Electrode: sensitive to noise	PEEK A5	LEFT 12
Cavity Electrode: sensitive to noise	PEEK A6	LEFT 14
Cavity Electrode: sensitive to noise	PEEK A3	LEFT 15
Cavity Electrode: sensitive to noise	PEEK A7	LEFT 16
Cavity Electrode: sensitive to noise	PEEK A14	LEFT 17
Cavity Electrode: sensitive to noise	PEEK A10	LEFT 18
Dispenser: rated for 5A	PEEK B4	RIGHT 1
Heating Wire: rated for 5A	PEEK D1	RIGHT 2
Dispenser: rated for 5A	PEEK B8	RIGHT 3
Dispenser Ground: rated for 5A	PEEK B1	RIGHT 4
Dispenser: rated for 5A	PEEK B7	RIGHT 7
Dispenser: rated for 5A	PEEK B5	RIGHT 8
Dispenser Ground: rated for 5A	PEEK B2	RIGHT 9
Heating Wire: rated for 5A	PEEK D5	RIGHT 10
Piezo: noisy, rated for 1kV	PEEK D8	FRONT 1
Piezo: noisy, rated for 1kV	PEEK D4	FRONT 2
Piezo: noisy, rated for 1kV	PEEK D2	FRONT 3
Piezo: noisy, rated for 1kV	PEEK D3	FRONT 4
Piezo: noisy, rated for 1kV	PEEK D6	FRONT 5
Piezo: noisy, rated for 1kV	PEEK D7	FRONT 6
Piezo Actuator: noisy, rated for 100V	PEEK C6	TOP 1
Piezo Actuator: noisy, rated for 100V	PEEK C10	TOP 2
Piezo Actuator: noisy, rated for 100V	PEEK C12	TOP 3
Piezo Actuator: noisy, rated for 100V	PEEK C3	TOP 4
Piezo Actuator: noisy, rated for 100V	PEEK C8	TOP 5
Piezo Actuator: noisy, rated for 100V	PEEK C13	TOP 6

Table 13.3: Breakdown of UHV-air interface feedthrough pinouts. Ensure isolation.

UHV-Air Interface Feedthrough	**Supplier**	**PN**	**Qty**
Cross: 5-way, 2.75" CF, for feedthrough flange attachments	Lesker	C5-0275	1
Feedthrough Flange: double-ended Mil-C-26482 style connector, 2.75" CF, 1 kV & 5 A rating, 6 pins	Lesker	IFDRG067013	2
Feedthrough Flange: double-ended Mil-C-26482 style connector, 2.75" CF, 1 kV & 5 A rating, 10 pins	Lesker	IFDRG107013	1
Feedthrough Flange: double-ended sub-C style connector, 2.75" CF, 500 V & 5 A rating, 2 × 9 pins	Lesker	IFDJG181053	1
Feedthrough Connector: Mil-C-26482 style connector, 6 pin, vacuum-side	Lesker	FTACIR6V	2
Feedthrough Connector: Mil-C-26482 style connector, 6 pin, atmosphere-side	Lesker	FTACIR6AC	2
Feedthrough Connector: Mil-C-26482 style connector, 10 pin, vacuum-side	Lesker	FTACIR10V	1
Feedthrough Connector: Mil-C-26482 style connector, 10 pin, atmosphere-side	Lesker	FTACIR10AC	1
Feedthrough Connector: sub-C style PEEK connector, 9 pin, vacuum-side	Lesker	FTACIR10V	2
Feedthrough Connector: sub-C style PEEK connector, 9 pin, atmosphere-side	Lesker	FTAC09FA	2
Contact: for sub-C connectors, 20-24 AWG wire, 10 pack	Lesker	FTACCONTF	4

Table 13.4: Breakdown of UHV-air interface feedthrough components.

13.5 Assembly and Integration of UHV System with Translator (Stage IIb)

Prepare the Components. Remove the reducer flange from the translator. Remove the blank 8" flange from the loadlock chamber. Support its weight, wrap exposed knife edges with foil, and protect the blank with a sacrificial gasket.

Attach the Translator. Clip a copper gasket in place. Ensure the translator flange is correctly oriented (screw at 12 o'clock). Tilt the translator flange to attach it to the chamber, seat the gasket, and run the screws in. Tighten screws finger-tight, then to 180 in-lbs with a torque wrench. Align the translator to the loadlock chamber by adjusting the height and positioning of two lab jacks. Tighten all screws to 150 in-lbs in two rounds. This process is shown in Fig. 13.10.

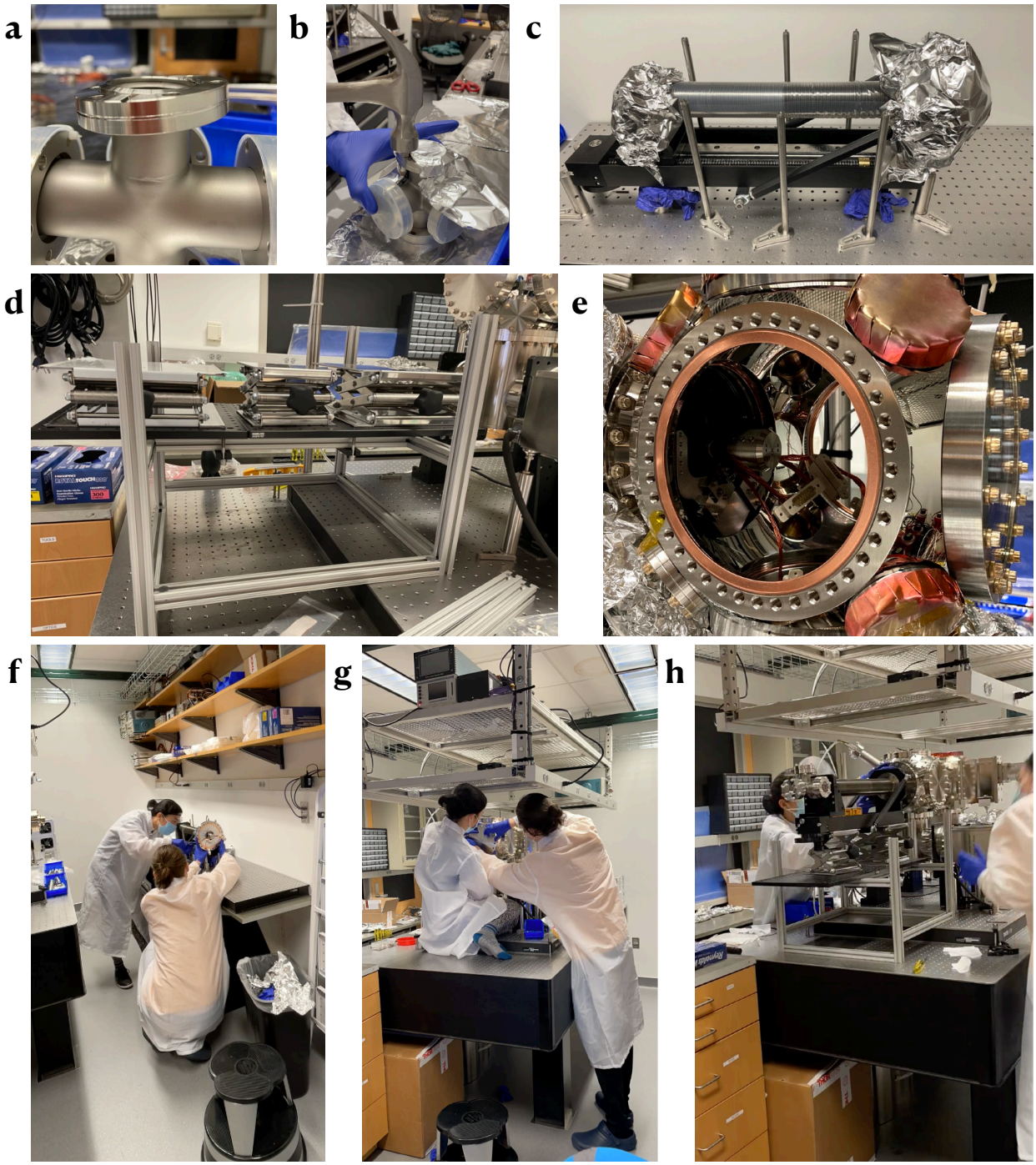

Figure 13.10: Assembly and integration of the translator to the vacuum system. A stuck flange on the five way cross in **a** was made unstuck by a hammer in **b**. **c**, the translator to be integrated with the cavity carrier and the feedthrough system. **d**, lab jacks for supporting the translator during assembly. **e**, V-stand, translator and feedthrough connectors installed in the vacuum chamber. **f**, the translator being serviced. **g**, blank replacement flange removed from the vacuum chamber. **h**, the translator installed to the vacuum chamber.

13.6 Stability of UHV System with Translator

The cavity-under-test supported by the cavity carrier is not fixed to the MOT structure, in the science position. The relative motion of the two should not prevent a stable delivery as far as vibrations are maintained below the order of 100 µm. To provide a sense of scale, the size of our atomic cloud is on the order of $\sim$ 100 µm in each dimension, and the size of the resonator waist is $\sim$ 10-30 µm, we anticipate that atom transport to the cavity will be insensitive to vibrations smaller than 100 µm rms. Indeed, even for cavity mode of 1 µm or smaller, the transport sensitivity would be set by the larger 100 µm sample size. To estimate the extent to which the relative motion between the loadlock and the science chamber prevents a stable delivery of atoms, we include in Fig. 13.11 results of a modal frequency analysis indicate that the dominant modes that couple to the cavity length and position should be below 500 Hz, and thus easily suppressed by a combination of passive vibration isolation and active feedback [72]. The study was performed in Fusion 360 and uses a slightly simplified model of our vacuum system. The first 10 modes are pictured, and the color bar indicates local displacement amplitudes. This study shows that the dominant vibration modes that couple to the cavity position are below 500 Hz.

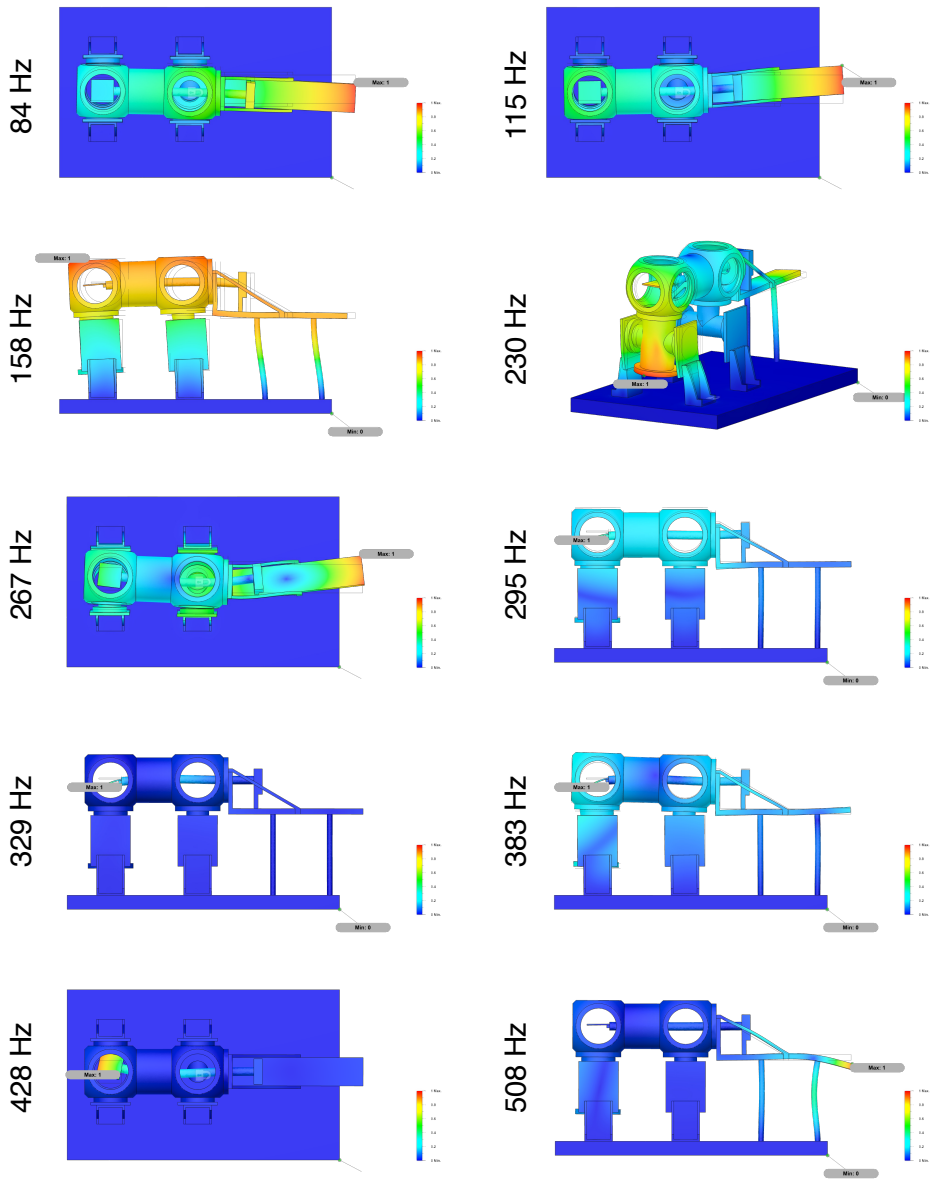

Figure 13.11: Vibration simulation of the vacuum loadlock apparatus. The results of a modal frequency analysis indicate that the dominant modes that couple to the cavity length and position should be below 500 Hz.

CHAPTER 14

MAGNETO-OPTICAL TRAP (MOT)

14.1 Introduction

To maximize optical access, the science chamber is covered with four 8" (20 cm) viewports orthographically, one 4.5" (11 cm) viewport below through a vacuum cross, and seven 2.75" (7 cm) viewports diagonally, all of which are broadband coated (Fig. 12.4). At the bottom of the science chamber is located an in-vacuum MOT setup, as shown in Fig. 14.1, comprising a structure for supporting directional optics for atom cooling (MOT optics), and a structure for supporting quadrupole coils for atom trapping (MOT coils).

14.2 In-Vacuum MOT Setup

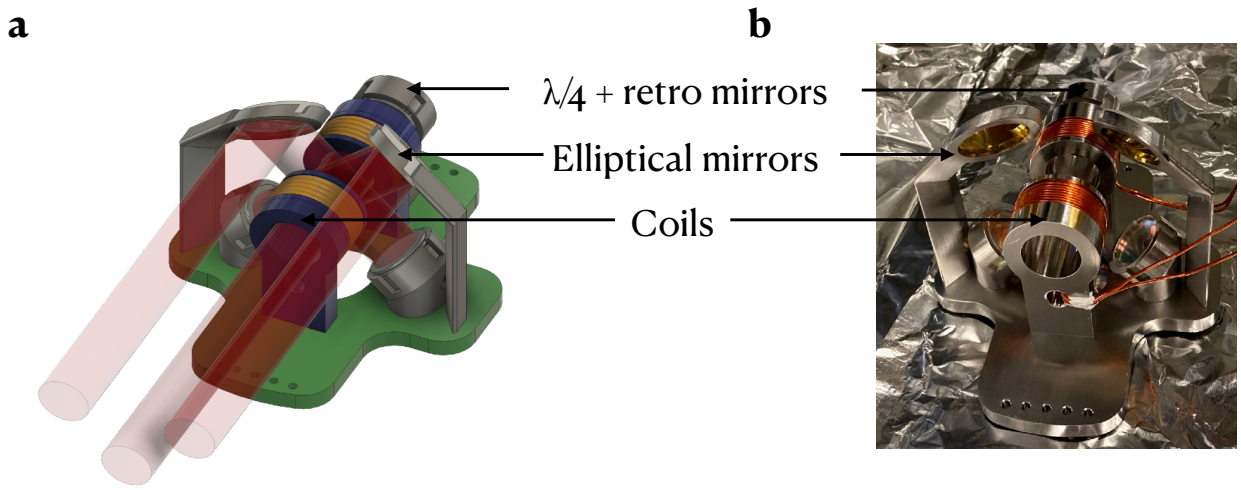

Figure 14.1: In-vacuum MOT setup. The setup, depicted schematically in **a,** and by photograph in **b,** consists of a pair of **MOT coils** for trapping atoms, and **MOT optics** for cooling atoms. The in-vacuum MOT coils are made of several layers of Kapton-insulated copper wires tightly wrapped around two steel holders spaced 1" (2.54 cm) apart. The in-vacuum geometry allows the coils to generate a large magnetic field gradient (about 20 G/cm) with only 3 A of current. The in-vacuum design speeds up the experimental sequence by preventing eddy currents from being generated in the copper gaskets. The in-vacuum MOT optics are an assembly of steel structures holding directional mirrors and quarter waveplates necessary to achieve a MOT. All three parallel beams entering through a single viewport intersect orthogonally at the MOT location, which is below the center of the science chamber to maximize available space for the cavity structure.

The in-vacuum MOT optics (Fig. 14.1) are mounted to a steel structure supporting circular and elliptical mirrors and quarter waveplates to direct three parallel incoming beams entering through a single viewport to orthogonally intersect at the MOT location. The MOT is formed 2" (5 cm) below the geometric center of the vacuum chamber to maximize the available volume for the cavity structure, which is ultimately limited to aforementioned 4"×4"×3" (∼ 10 cm×10 cm×8 cm).

The in-vacuum MOT coils (Fig. 14.1) are made of 4 layers of 9 turns of Kapton-insulated wires tightly wrapped around two steel holders spaced by 1" (2.5 cm). Placing coils inside vacuum minimizes eddy currents induced by coil turn on/off, increasing the experimental

repetition rate. Additionally, since the geometry of the coils is not constrained by the (substantial) size of the vacuum chamber, a large magnetic field gradient (20 G/cm) can be generated with low electrical current (3 A) and minimal heat dissipation. The MOT coils exhibit a room temperature resistance of approximately 100 mΩ. When the coils are heated to 100°C, their resistance, including the cables on the atmosphere side, increases to around 205 mΩ. Magnetic field and magnetic field gradient simulations of the in-vacuum MOT coil setup are included in Fig. 14.2.

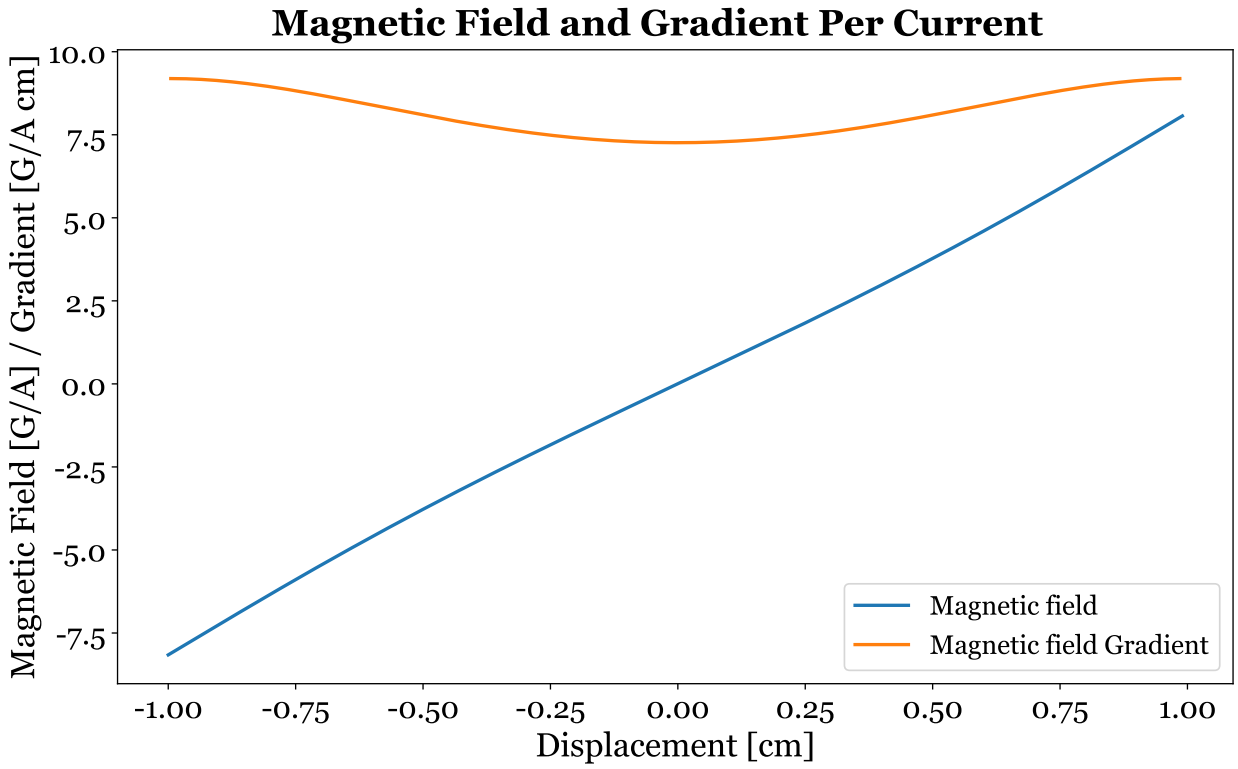

Figure 14.2: Simulation of the in-vacuum MOT coil setup. Each coil has 9 turns per layer, with 4 layers in total, and an outer radius minus inner radius of approximately 5mm. The top layer lies slightly inward of the outer radius. The coils are wound with 18 AWG Kapton-coated wires.

In-Vacuum MOT: optics and coils	**Supplier**	**PN**	**Qty**
MOT Base Plate: stainless	3ERP	Custom: appx. A.4	1
Groove Grabber: for holding the Base Plate inside 8" CF chamber	Kimball Physics	MCF800-GrvGrb-C01	2
Coil: Kapton-insulated, silver-plated, 18 AWG, 15 Ft.	Accu-Glass Products	112697	6
Coil Mount: stainless	3ERP	Custom: appx. A.5	2
Retaining Ring: stainless	3ERP	Custom: appx. A.6	2
Circular Mirror Mount: stainless, back	3ERP	Custom: appx. A.6	1
Circular Mirror Mount: stainless, bottom	3ERP	Custom: appx. A.7	2
Elliptical Mirror Mount: stainless, left	3ERP	Custom: appx. A.8	1
Elliptical Mirror Mount: stainless, right	3ERP	Custom: appx. A.8	1
Circular Mirror	Thorlabs		3
Elliptical Mirror	Thorlabs		2
Quarter Waveplate	Thorlabs		3
Hex Nut: 4-40 thread	McMaster-Carr	91841A005	~ 20

Table 14.1: Breakdown of in-vacuum MOT components

14.3 Assembly and Integration of Science Chamber with In-Vacuum MOT Setup (Stage III)

During Stage III, the in-vacuum MOT setup was separately assembled, then installed into the science chamber. Fig. 14.3 depicts the Stage III assembly procedure.

Start by cleaning the elliptical mirror mounts and ensuring the elliptical mirrors are properly seated. Once in place, glue and cure them. Repeat this process for the circular mirror mounts: clean them, seat the circular mirrors along with the retaining rings, and then glue and cure them. Attach the two elliptical mounts and the three circular mirror mounts to the base plate. This completes the **in-vacuum MOT optics setup**.

Meanwhile, measure the resistance of the cleaned copper wires using the four-terminal sensing setup. Strip the ends of the wires and temporarily crimp them onto gold pins for accurate measurement. Once measured, tightly wind the coils around the MOT coil mounts, ensuring that there are 9 wires per layer and that each layer lays flat. Be cautious to avoid scraping the kapton wire against the walls of the MOT coil mount, which are chamfered to prevent accidental shorts. Strain-relieve the wires to the mount with glue, leaving enough extra length to connect to the chamber feedthrough port later. This completes the **in-vacuum MOT coil setup**.

Once the in-vacuum MOT optics and in-vacuum MOT coil setups are securely fastened onto the base plate, open the science chamber. Position the base plate inside the science chamber by connecting two groove grabbers to the inside grooves of the bottom flange. Finally, crimp gold pins onto the four ends of the MOT coils and connect them to the feedthrough flange on the science chamber.

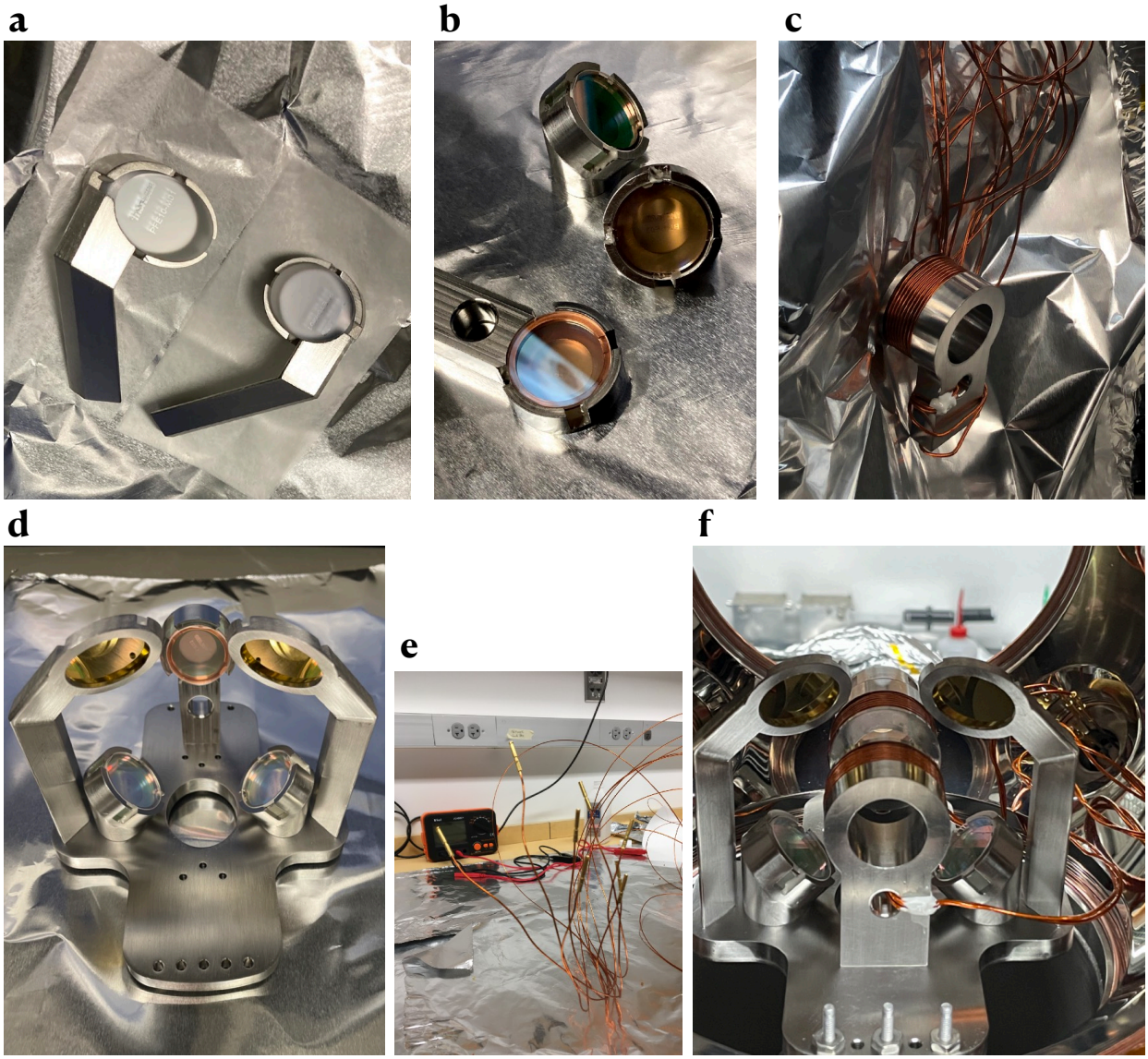

Figure 14.3: Assembly of the in-vacuum MOT setup. **a**, cleaned elliptical mirror mounts with properly seated elliptical mirrors. **b**, cleaned circular mirror mounts with properly seated circular mirrors and retaining rings. **c**, a finished MOT coil with Kapton-coated copper wires wound around and glued to the coil mount. **d**, completed in-vacuum MOT optics setup. **e**, four-terminal sensing setup for resistance measurement of the in-vacuum MOT coils. **f**, completed in-vacuum MOT optics and MOT coils setup installed in the science chamber.

14.4 Outside-Vacuum Optics for Cooling Beams Generation

The outside-vacuum MOT optics system (Fig. 14.4 and Fig. 14.5) is designed to establish a stable and efficient environment for atom cooling and trapping (theory in Chp. 7.2). It consists of three essential branches: the **reference laser**, which stabilizes the frequencies of the MOT and repumper lasers according to the atomic transition of the trapped species; the **MOT laser**, responsible for primary atom cooling and trapping within the MOT by lowering temperatures to microkelvin levels and spatially confining atoms using laser cooling and magnetic field gradients; and the **repumper laser**, which prevents atoms from entering dark states not addressed by the primary cooling transition, thus averting potential atom loss from the cooling cycle. Each component plays a critical role in ensuring the stability, accuracy, and effectiveness required for the precise trapping and cooling of a significant number of atoms, as described below.

In the reference laser setup (Fig. 14.4), the frequency of the reference laser (Fig. 14.6) is stabilized using a laser locking technique. It is locked to the $3 \rightarrow 4'$ transition of ^{85}Rb atoms (Tab. 14.2) by utilizing the saturated absorption spectroscopy technique (detailed in Chp. 7.3). This stabilization is crucial for ensuring that both the MOT and repumper lasers are precisely tuned to the necessary atomic transitions. An isolator is placed immediately after the laser diode to prevent back reflections from destabilizing the laser. A polarizing beam splitter (PBS) and a half-wave plate are employed to distribute the majority of the beam power into the MOT and repumper branches while directing a smaller portion of the beam power into the vapor cell. A quarter-wave plate is used to redirect the back-reflected beam from the vapor cell into a photodiode. The fast photodiode monitors the laser output and provides feedback to the laser locking mechanisms, ensuring that the laser remains stable and locked to the desired frequency. Finally, the reference laser beam is split into multiple paths using fiber splitters, directing portions of the beam to the MOT laser and repumper laser branches.

The MOT laser setup involves a two-stage process. During the first stage (schematic in Fig. 14.4, photos in Fig. 14.8a-c), the MOT laser frequency is stabilized, the beam power is amplified, and the beam is mixed with the repumper light to generate two output signals. During the second stage (schematic in Fig. 14.5, photo in Fig. 14.8d), these two output signals are fiber-coupled, the beams are expanded to approximately 1 inch in diameter, and then launched into the science chamber through a viewport. This results in three pairs of counter-propagating, red-detuned laser beams intersecting at the cooling region inside the vacuum chamber. These beams create a three-dimensional optical molasses, which, in conjunction with a quadrupole magnetic field, traps and cools the atoms.

In the first stage of the MOT laser setup, a seed laser (Fig. 14.6) provides the initial light for the MOT. An isolator is placed immediately after the laser diode to prevent back reflections from destabilizing the laser. The frequency of the seed laser is stabilized relative to the reference laser using a frequency offset lock. In this scheme, a fiber splitter combines a portion of the stabilized reference laser beam with the sampled seed laser beam, which are GHz apart in frequency. The combined light is directed to a photodiode, which converts the optical signal to a microwave signal. This microwave signal is then mixed with a target offset frequency precisely generated by a direct digital synthesizer (DDS). The output of the mixer, filtered by a low pass filter and a helical filter to improve signal clarity, provides feedback to stabilize the seed laser frequency.

The stabilized seed laser light is then fiber-coupled and amplified to the necessary power levels using a tapered amplifier (TA, Fig. 14.7) to ensure sufficient laser power for effectively cooling and trapping the atoms in the MOT. An isolator is placed immediately after the TA to prevent back reflections from destabilizing it. An acousto-optic modulator (AOM) provides the necessary control over the frequency and the amplitude of the MOT laser beam. In addition, the intensity of the MOT beams can also be controlled by the PBS and the half-wave plate. Beam intensity is crucial: excessive intensity can cause overheating,

while insufficient intensity may not provide sufficient cooling. Thanks to the laser control techniques, the MOT laser is typically red-detuned by a few linewidths from the 2→ 3' transition of ^{87}Rb atoms (Tab. 14.2). This detuning ensures that atoms moving towards the laser light experience a Doppler shift that brings them into resonance, ultimately allowing for effective cooling.

The repumper laser setup similarly involves a two-stage process. In the first stage, the repumper laser frequency is stabilized, and the beam is mixed with the amplified MOT light to generate two output signals (Fig. 14.4). In the second stage, these two output signals are fiber-coupled, the beams are expanded to approximately 1 inch in diameter, and then launched into the science chamber through a viewport.

In the first stage of the repumper laser setup, the frequency of the laser is stabilized relative to the reference laser using a frequency offset lock. An isolator is placed immediately after the laser diode to prevent back reflections from destabilizing the laser. Similar to the MOT setup, a fiber splitter combines a portion of the stabilized reference laser beam with the sampled repumper laser beam, which are several GHz apart in frequency. The combined light is directed to a photodiode, which converts the optical signal to a microwave signal. This microwave signal is then mixed with a target offset frequency precisely generated by a DDS. The output of the mixer, filtered by a low pass filter and a helical filter to improve signal clarity, provides feedback to stabilize the seed laser frequency.

The stabilized repumper laser light is directed to an AOM, which provides the necessary control over the frequency and the amplitude of the repumper laser beam. In addition, the intensity of the repumper beams can also be controlled by a PBS and a half-wave plate. Beam intensity is crucial: excessive intensity can cause overheating, while insufficient intensity may not effectively counteract atom loss. Thanks to the laser control techniques, the repumper laser is typically at the 1→ 2' transition of ^{87}Rb atoms (Tab. 14.2). This tuning ensures that atoms in dark states are excited back to a state where they can interact with the MOT

laser, preventing atom loss from the cooling cycle and increasing the MOT's efficiency.

In the second stage of the MOT and repumper setup (Fig. 14.5), light from the two fiber-coupled ports is expanded to approximately 1 inch in diameter using a 25x telescope. The more powerful beam is split into two beams by a beam splitter, resulting in three beams in total. These beams are redirected to enter the science chamber horizontally through the front viewport. Each beam passes through a quarter-wave plate to achieve the circular polarization required for the MOT setup.

Inside the science chamber, the three horizontal beams are redirected by mirrors fixed to the in-vacuum MOT structure into the trapped atom region. They are then phase-shifted and back-reflected by quarter-wave plates to form the counter-propagating beams necessary for the MOT.

Reference Laser	**Setting**
Transition	^{85}Rb 3 $\rightarrow$ 4'
Laser Frequency	384229243 MHz
TC setting	13.348 kΩ
Current setting	127.13 mA
MOT Laser	**Setting**
Transition	^{87}Rb 2 $\rightarrow$ 3'
Laser Frequency	384228115 MHz
TC setting	11.991 kΩ
Current setting	117.6 mA
DDS frequency	1289 MHz
Beatnote frequency	1127 MHz (on resonance) 1217 MHz (10 MHz detuned + 80 MHz AOM)
AOM	Blueshifts 80 MHz
Repumper Laser	**Setting**
Transition	^{87}Rb 1 $\rightarrow$ 2'
Laser Frequency	384234683 MHz
TC setting	14.812 kΩ
Current setting	103.47 mA
DDS frequency	5436 MHz (labbrick=6500, RFSoC=1064)
Beatnote frequency	5440 MHz (on resonance) 5520 MHz (80 MHz AOM)
AOM	Redshifts 80 MHz

Table 14.2: Settings for the MOT lasers.

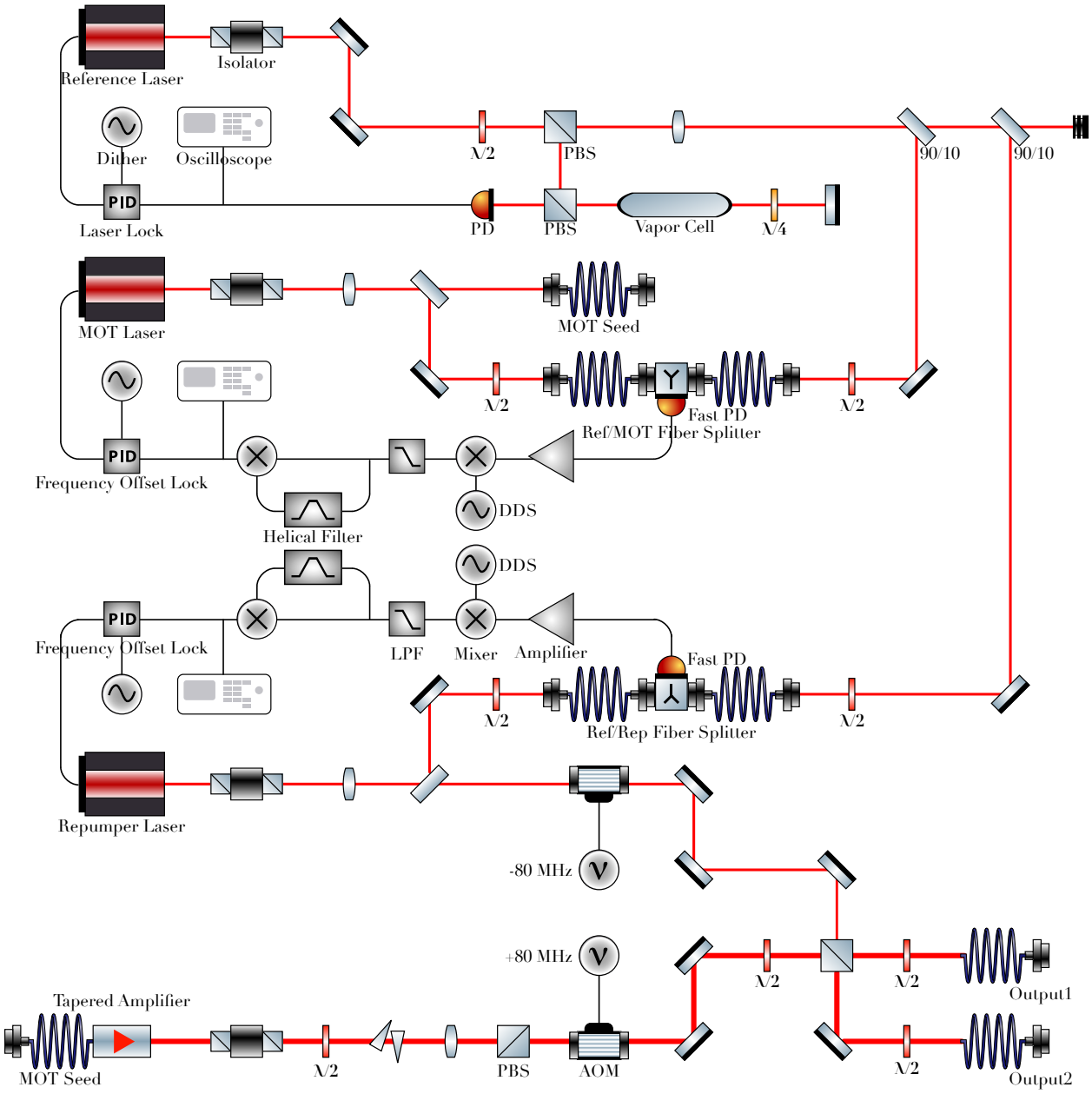

Figure 14.4: Schematic of the outside-vacuum MOT setup. A reference laser is locked to the atomic transition line of the Rb vapor cell via Saturation Absorption spectroscopy (SAS). The MOT and repumper lasers are frequency-locked to this reference laser, amplified, and mixed to generate cooling beams.

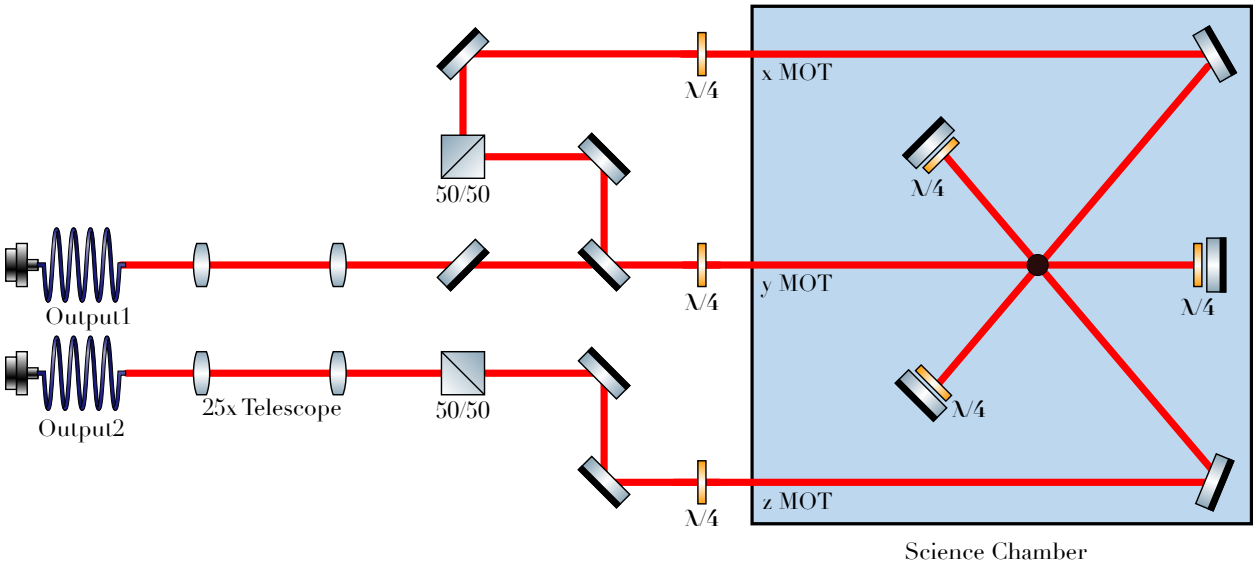

Figure 14.5: Schematic of launching optics for interfacing the outside-vacuum and in-vacuum MOT setup. The combined MOT and repumper beams were expanded to approximately 1 cm, split, aligned, redirected into the vacuum chamber, intercepted, and back-reflected.

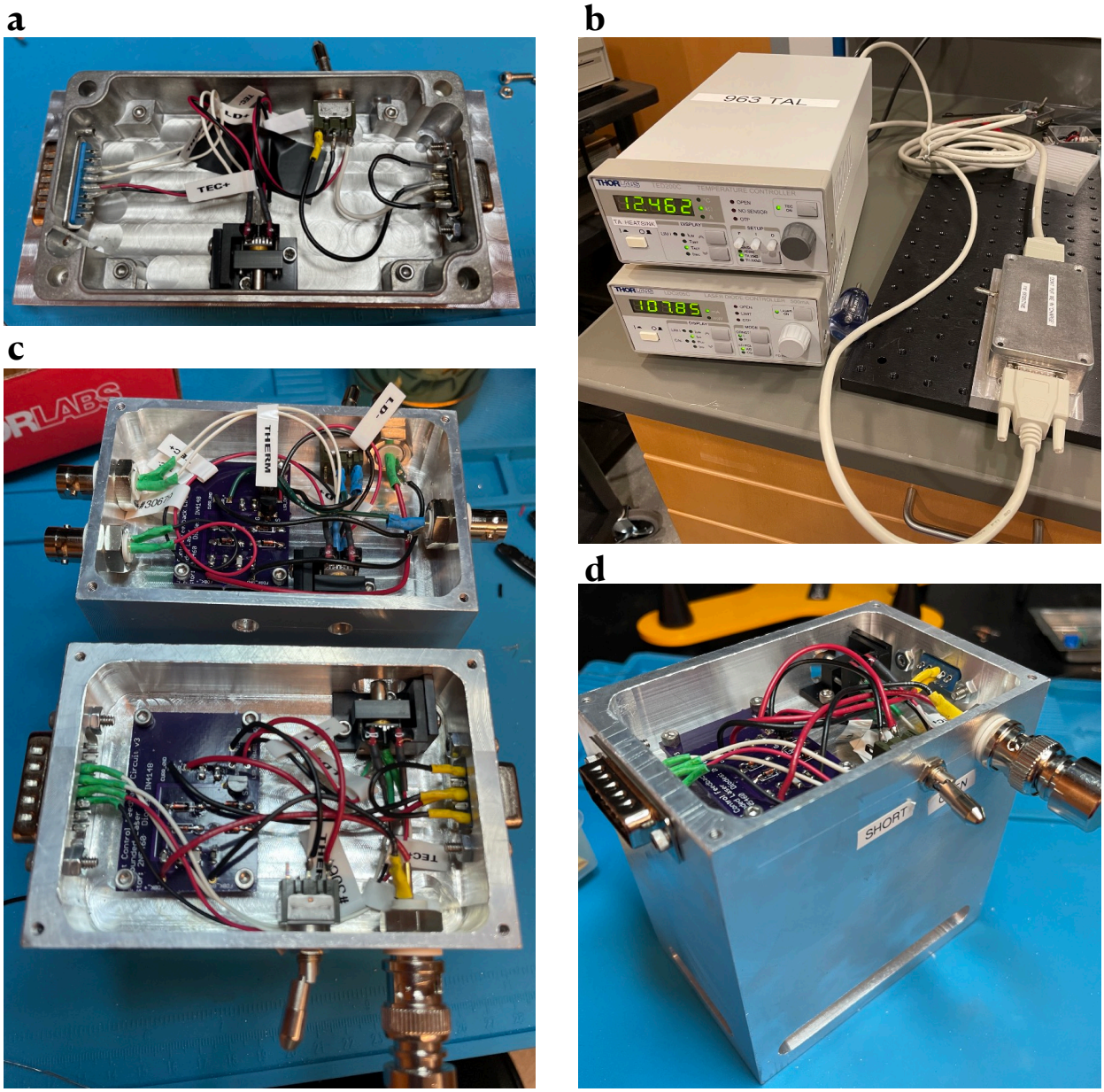

Figure 14.6: Lasers utilized in the MOT setup. **a**, reference laser diode housed within a control box. **b**, reference laser connected with current and temperature controllers. **c**, MOT and repumper lasers, fast current feedback circuit boards, and a metal block for heatsink and positional stability. **d**, side-view of the MOT laser.

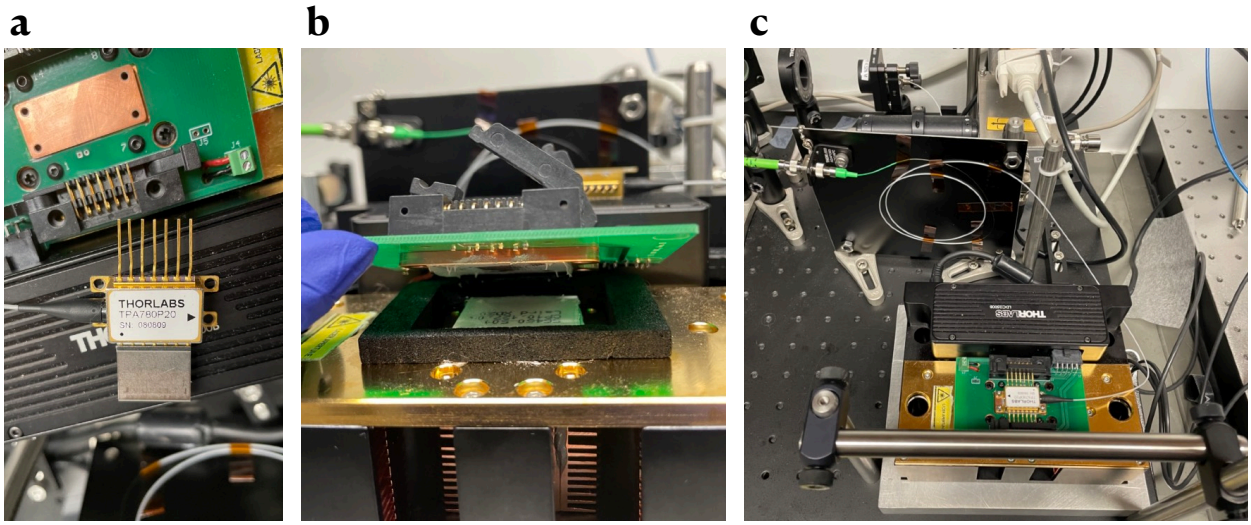

Figure 14.7: Tapered amplifier utilized in the MOT setup. **a**, fiber-coupled tapered amplifier housed in a butterfly mount. **b**, housing of the tapered amplifier with space for applying heat paste. **c**, tapered amplifier setup in operation, with the incoming fiber strain relieved.

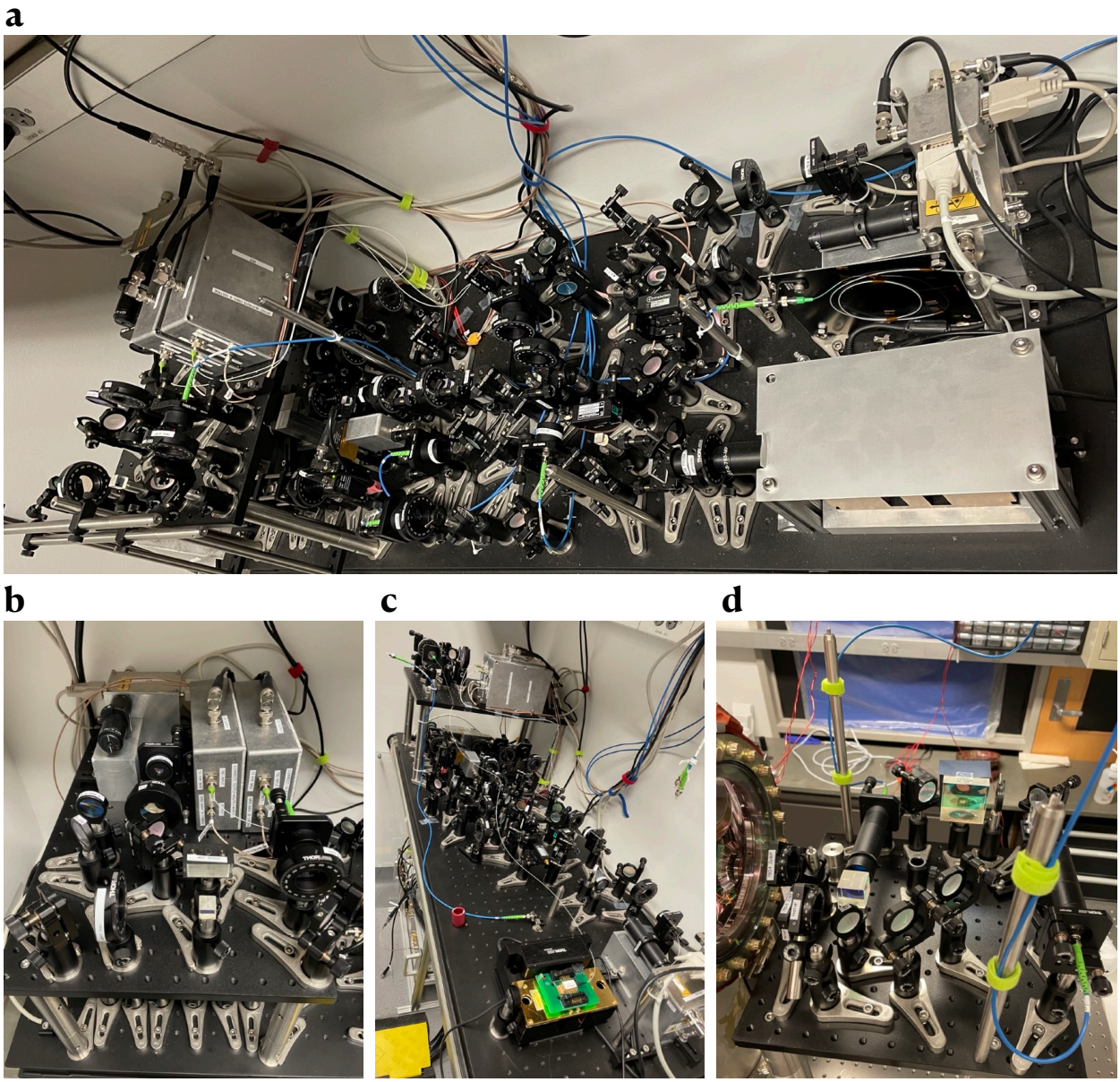

Figure 14.8: Outside-vacuum optics for the MOT setup. **a**, optical breadboard for generating reference beam, amplified MOT beam, and repumper beam. **b**, area designated for MOT seed laser and beatnote locking electronics. **c**, area designated for the repumper laser and the tapered amplifier for the MOT beam. **d**, entrance optics for directing the amplified MOT beam and the repumper beam into the vacuum chamber.

14.5 Outside-Vacuum Bias Magnetic Coils for Field Correction

The geometry of the bias coils consists of 100 windings per window, with 1.5 A of current running through each coil. This configuration was expected to yield a resistance resulting in a 2 V drop per coil, and 4 V when the coils are connected in series, generating a magnetic field of 2.5 Gauss at the center (Fig. 14.9). The coils were wound with approximately 500 meters of 20 AWG enameled magnet wire from Remington.

To securely attach the wires to the chamber, brackets were fabricated to prevent the wires from sliding off the windows. During the winding process, the spool was kept in the plane of the flange to minimize twisting, and Kapton tape was applied after each layer to hold it in place.

After completing all the coils, we found that 3 out of 6 coils had shorted to the chamber, specifically in the North, Bottom, and Top windows. The suspected cause was the bottom layer of coils rubbing against the brackets. To address this issue, we unwrapped the coils, covered the brackets with tape, and then rewrapped them. The finished setup is shown in Fig. 14.10.

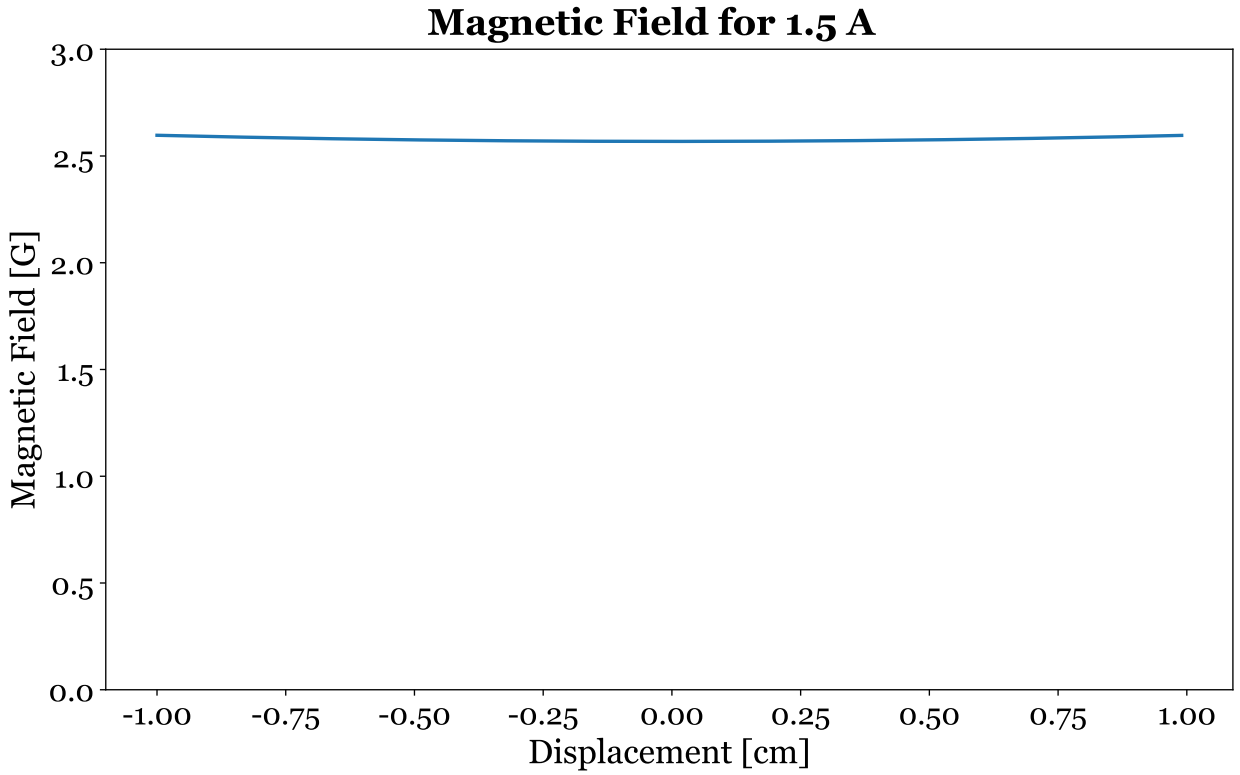

Figure 14.9: Simulation of the magnetic field generated with a pair of bias coils. The two coils are spaced 9 inches apart, each wrapped around an 8-inch diameter window with 100 windings. Each coil carries 1.5 A, causing a 2 V drop per coil, totaling 4 V in series, generating a 2.5 Gauss field at the center. The coils use 20 AWG enameled magnet wire.

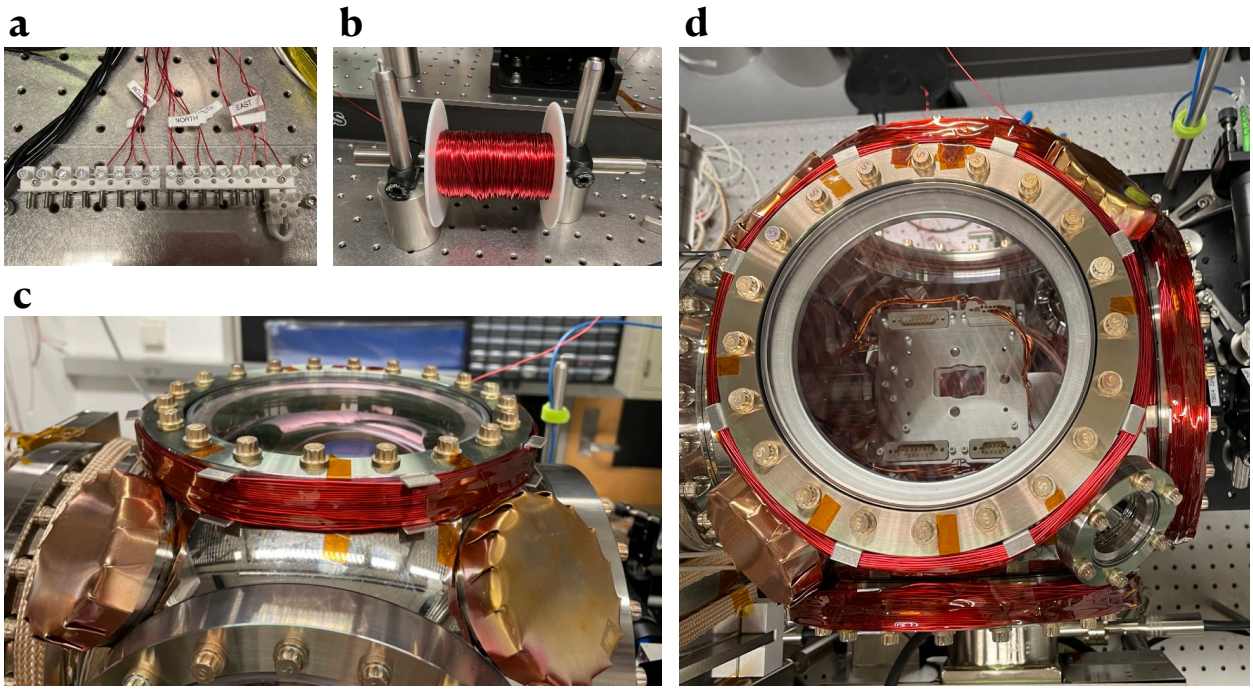

Figure 14.10: Outside-vacuum magnetic coils for zeroing the Earth field. **a**, breakout board for controlling three independent coil currents in the six spools of wires. **b**, tool used for winding the bias coils. **c**, zoomed in view of a bias coil wrapped around the top science chamber viewport. **d**, top view of three pairs of bias coils wrapped around the science chamber.

14.6 Optimization and Control

14.6.1 Laser Lockbox

The laser lockbox circuit (Fig. 14.11) is designed to precisely stabilize the laser frequency either to an atomic transition or an offset frequency of another laser. It begins by processing the photodiode signal to generate an error signal, which is essential for its operation within a proportional-integral (PI) feedback loop. The circuit's port configuration is detailed in Tab. 14.3, where the PROP_GAIN potentiometer controls proportional gain, while the TOTAL_GAIN potentiometer predominantly manages integral gain.

The circuit first processes the photodiode input. The photodiode detects laser intensity, converting it to an electrical signal. This signal (PHOTODIODE) passes through an op-amp IC2A configured as a buffer to ensure low enough output impedance, and IC2B configured as an inverting amplifier with gain controlled by ERR_GAIN.

The error signal is then processed through feedback loops: IC5B buffers the signal, TOTAL_GAIN adjusts overall gain, and IC5A applies proportional gain (PROP_GAIN).

Finally, the circuit produces the output signal. The OUTPUT_OFFSET potentiometer adjusts the baseline level of the output signal, while IC5D integrates the error signal for integral control, thereby yielding the precise output signal (OUTPUT).

Voltage regulators (IC3, IC4) are used to provide stable ±15V for op-amps and other components, critical for consistent circuit performance. Bypass capacitors are used to reduce noise in the circuit.

14.6.2 Fast Laser Feedback

The fast current control feedback circuit (Fig. 14.12) is originally part of an optical phase-locked loop (OPLL) used for stabilizing the frequency of diode lasers [73]. However, we have repurposed this circuit for fast feedback response to correct high-frequency noise and protect

Port Name	Type	Function
PHOTODIODE	Input	Receives the signal from the photodetector
DITHER_IN	Input	Modulates the laser frequency
ERR_MOD	Input	Additional modulation of the error signal
ERROR_OUT	Output	Provides the processed error signal
OUTPUT	Output	Final control signal output
POWER_IN	Input	DC power
UNLOCK	Control	Switch
DITHER_AMP	Control	Sets the amplitude of modulation of the laser frequency
TOTAL_GAIN	Control	Manages integral control of PID
PROP_GAIN	Control	Manages proportional control of PID
OUTPUT_OFFSET	Control	Adjusts the output signal baseline
ERR_GAIN	Control	Adjusts the gain of the error signal
ERR_OFFSET	Control	Adjusts the baseline level of the error signal

Table 14.3: Breakdown of laser lockbox components

the laser diode.

The circuit is primarily designed to address high-frequency noise and fluctuations. The N-junction FET, the main component used for modulating the current, is placed in parallel with the laser diode. The FET receives a voltage signal from the feedback circuit, and if this signal exceeds a certain threshold, the injection current for the laser diode is diverted to flow between the drain and source of the FET, effectively bypassing the laser diode. This setup provides a fast response to changes in the input signal, helping to stabilize the laser diode's current and maintain consistent laser output.

Additionally, the circuit serves a protective function by ensuring that the laser diode is not subjected to overcurrent conditions that could cause damage. The gate of the FET is clamped by protection diodes, which prevent the gate voltage from exceeding safe levels and protect the FET from potential damage.

14.6.3 Coil Driver

The coil driver circuit (schematic in Fig. 14.13, photos in Fig. 14.14a-e) is designed to drive magnetic coils by precisely regulating the current through them. It employs an instrumentation amplifier, an operational amplifier, and various passive components to achieve this control. Specifically, two circuit boards are used to independently control the in-vacuum MOT quadrupole coils, while three boards manage the outside-vacuum bias coils—one for each of the x-, y-, and z-axes, with each pair of coils connected in series.

Control input processing. The control signals from the lab server are applied to the input terminals (X1-1 and X1-2) via a BNC cable. Initially, these signals are conditioned by a voltage divider network. The conditioned differential signal is then amplified and buffered by an instrumentation amplifier (INA114P), with its gain set by an associated resistor network.

Current feedback loop. Current amplification is performed through a feedback loop utilizing an LM3886 operational amplifier configured as a current amplifier. The gain of the output stage is determined by resistors R9 and R10. The non-inverting input of the LM3886 receives the amplified signal from the instrumentation amplifier, while its inverting input is connected to the voltage across the magnetic coil, sensed by a 0.5 Ohm sense resistor (R5) in series with the gain resistor R10. This sense resistor provides a feedback voltage proportional to the current flowing through the magnetic coils, enabling precise current measurement and control.

Signal filtering. To minimize noise in the current output, the power supplies are regulated using voltage regulators (IC2, IC3), providing a stable $\pm$15V supply essential for the op-amps and other components. The output signals are further filtered by high-voltage capacitors and, if necessary, an optional low-pass filter network to mitigate high-frequency oscillations due to coil inductance.

Thermal management. Given the high-current nature of the signals, the controller box is designed with water cooling. The sense resistors are thermally adhered to a copper

Port Name	**Type**	**Function**
±18V	Input	DC power
X1_1, X1_2 (CTRL IN)	Control	Control signal from the lab server
X4_1, X4_2 (OUTPUT)	Output	Output current

Table 14.4: Breakdown of coil driver components

plate, which is attached to a cooled aluminum backplane (Fig. 14.14b-d). During initial testing, cooling water was supplied by a standalone chiller (Fig. 14.14e) to ensure effective thermal management.

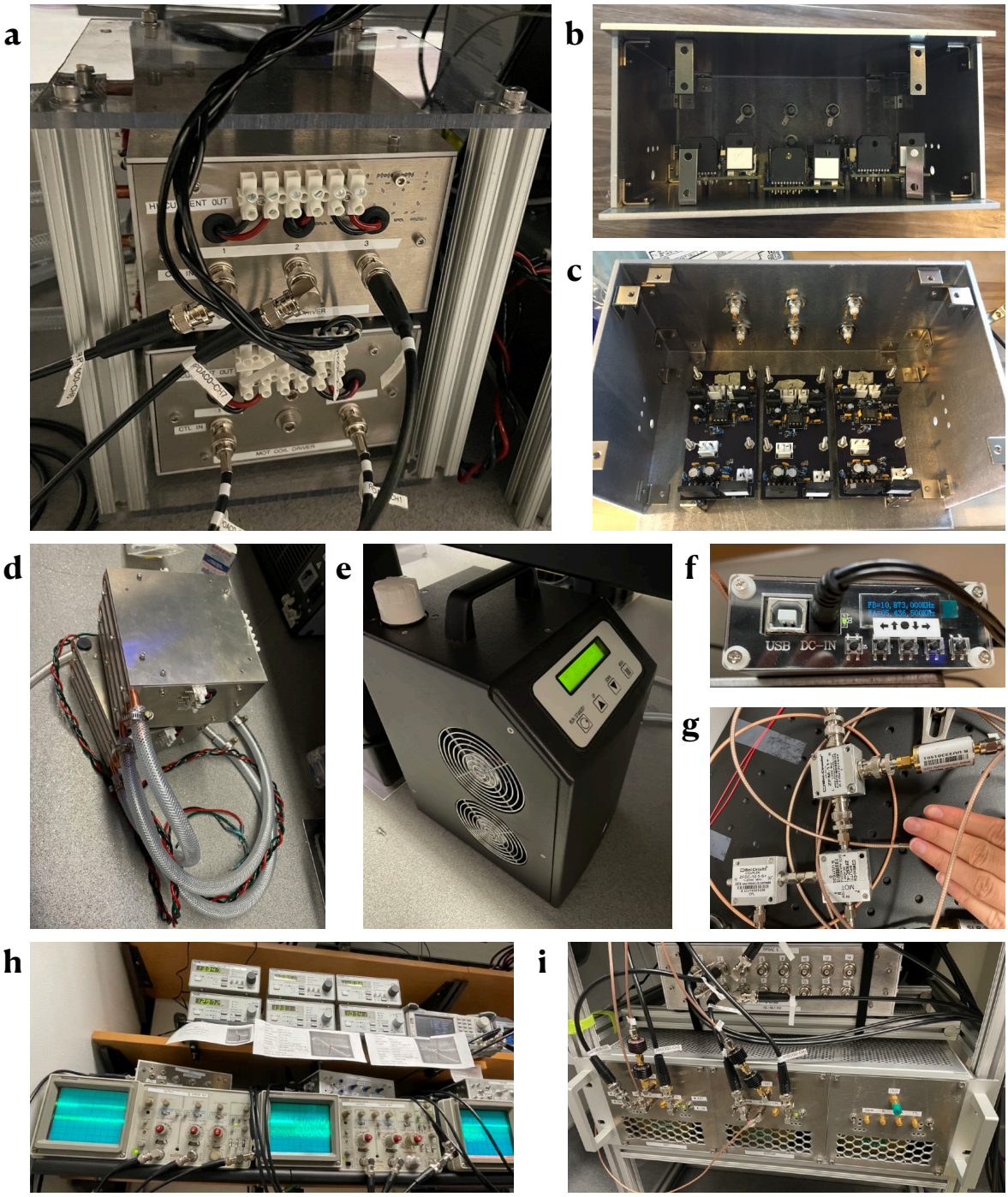

Figure 14.14: Electronics for the MOT setup. The high-current controllers housed in **a** for the in-vacuum MOT coils and outside-vacuum bias coils, with internal views in **b** and **c**, and an external view in **d**, water-cooled by a chiller in **e**. **f**, frequency offset generation for beatnote locking. **g**, electronics for beatnote locking. **h**, frequency-locked lasers. **i**, AOM drivers.

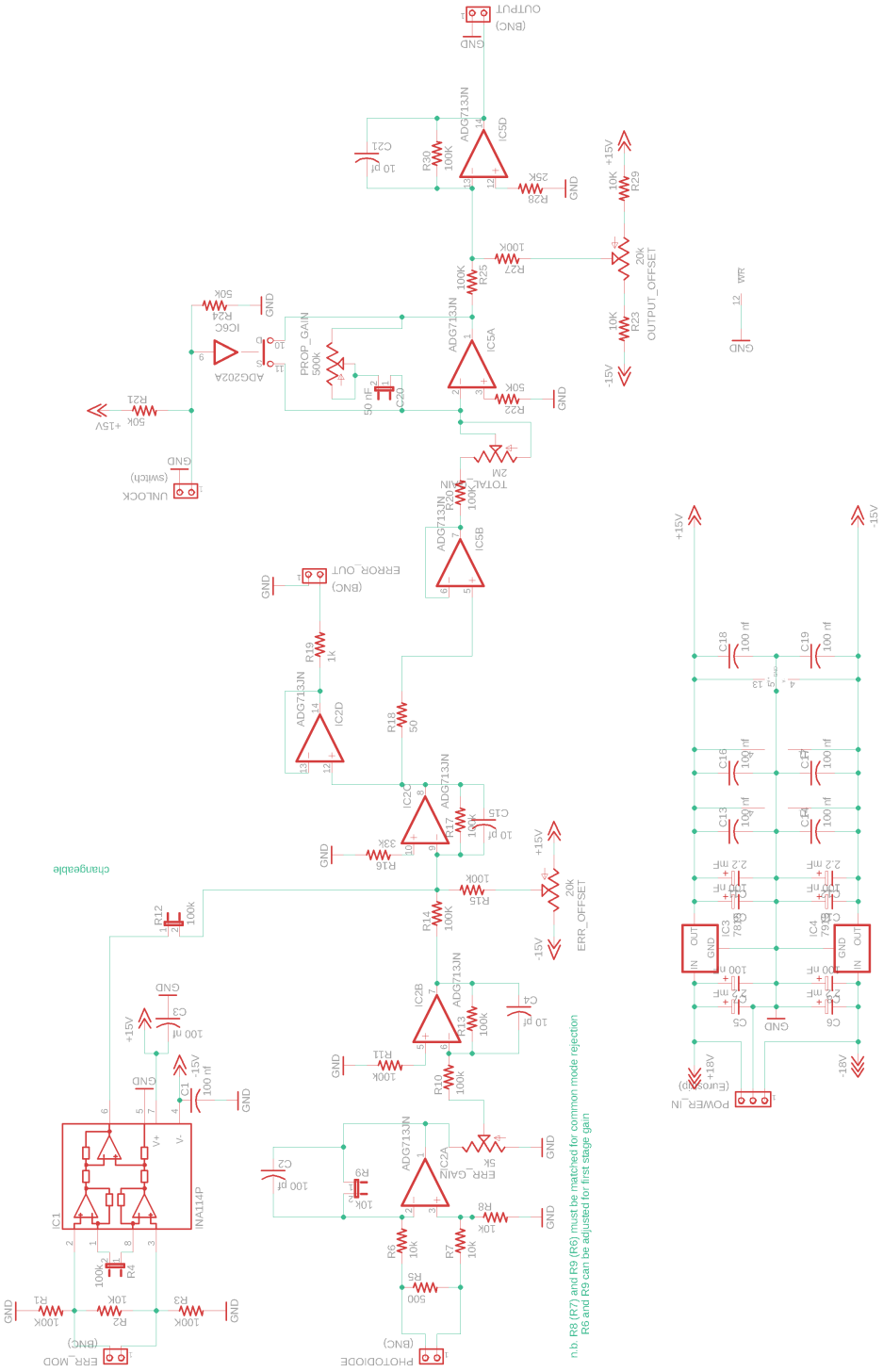

Figure 14.11: Schematics of the laser frequency stabilization circuit. The circuit processes the photodiode signal, generate an error signal, and use this error signal in a proportional-integral (PI) feedback loop to stabilize the laser frequency.

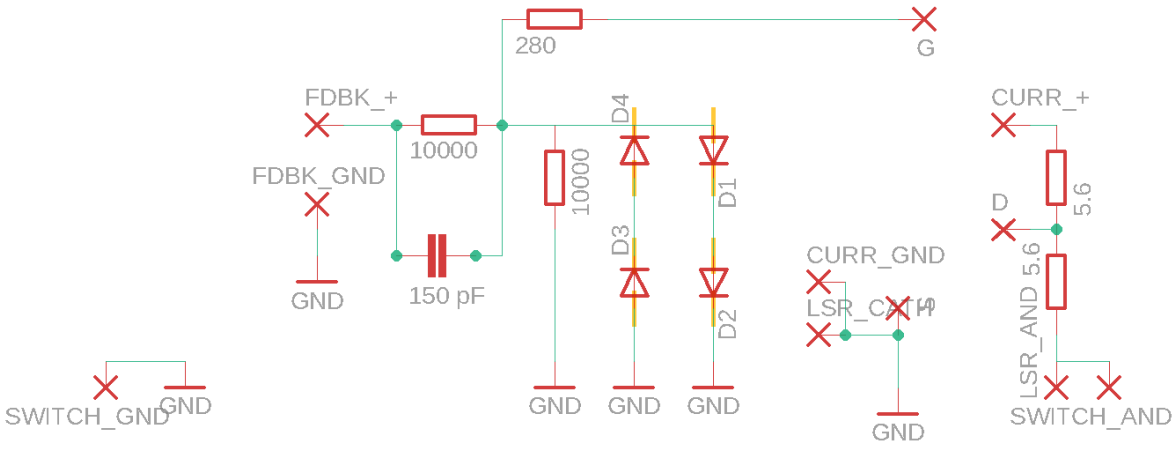

Figure 14.12: Schematics of the fast current control circuit for each laser diode.

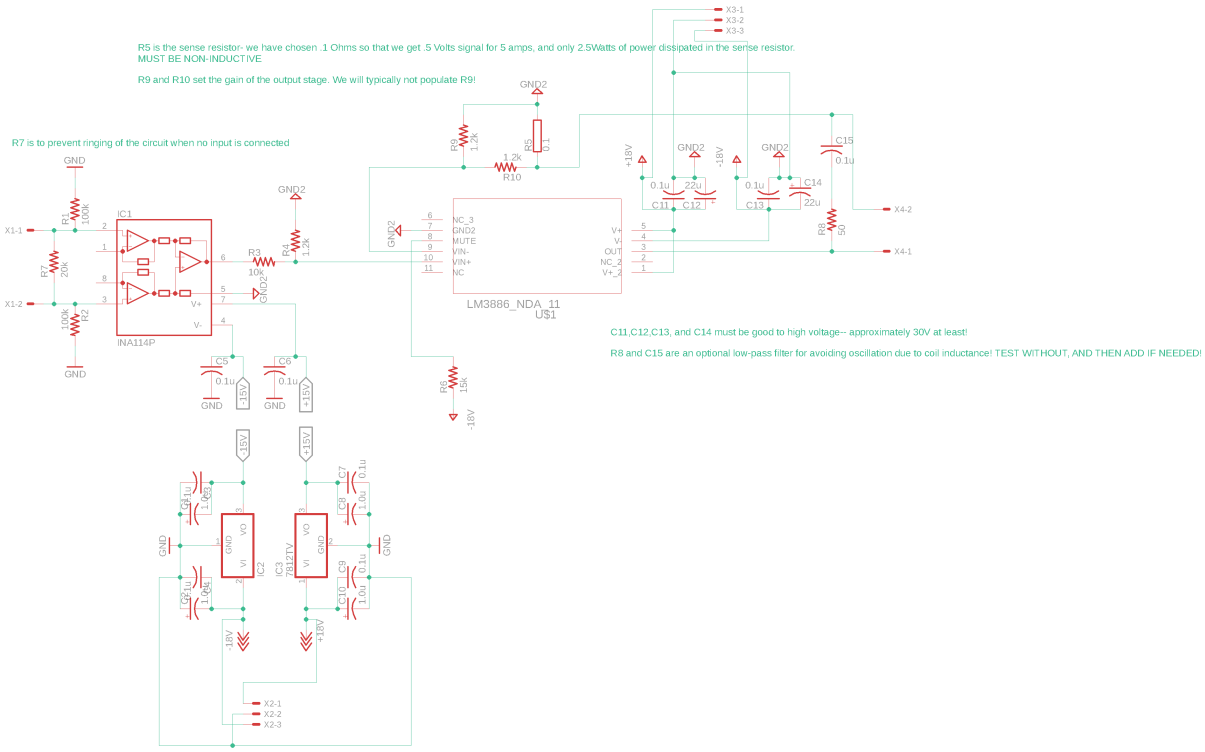

Figure 14.13: Schematics of the coil driver circuit. The circuit drive one spool of magnetic coil by regulating the current through it. It is used for both in-vacuum MOT quadrupole coils, and outside-vacuum bias coils.

14.7 Characterization of Atom Source

As shown in Fig. 14.16, we have cooled and trapped a ^{87}Rb MOT with post-PGC temperature of under $\sim$10 µK. Panel (a) shows fluorescence images of the atomic cloud in time of flight, while panel (b) shows the extracted rms cloud sizes along the two imaging axes and corresponding fits with extracted temperatures.

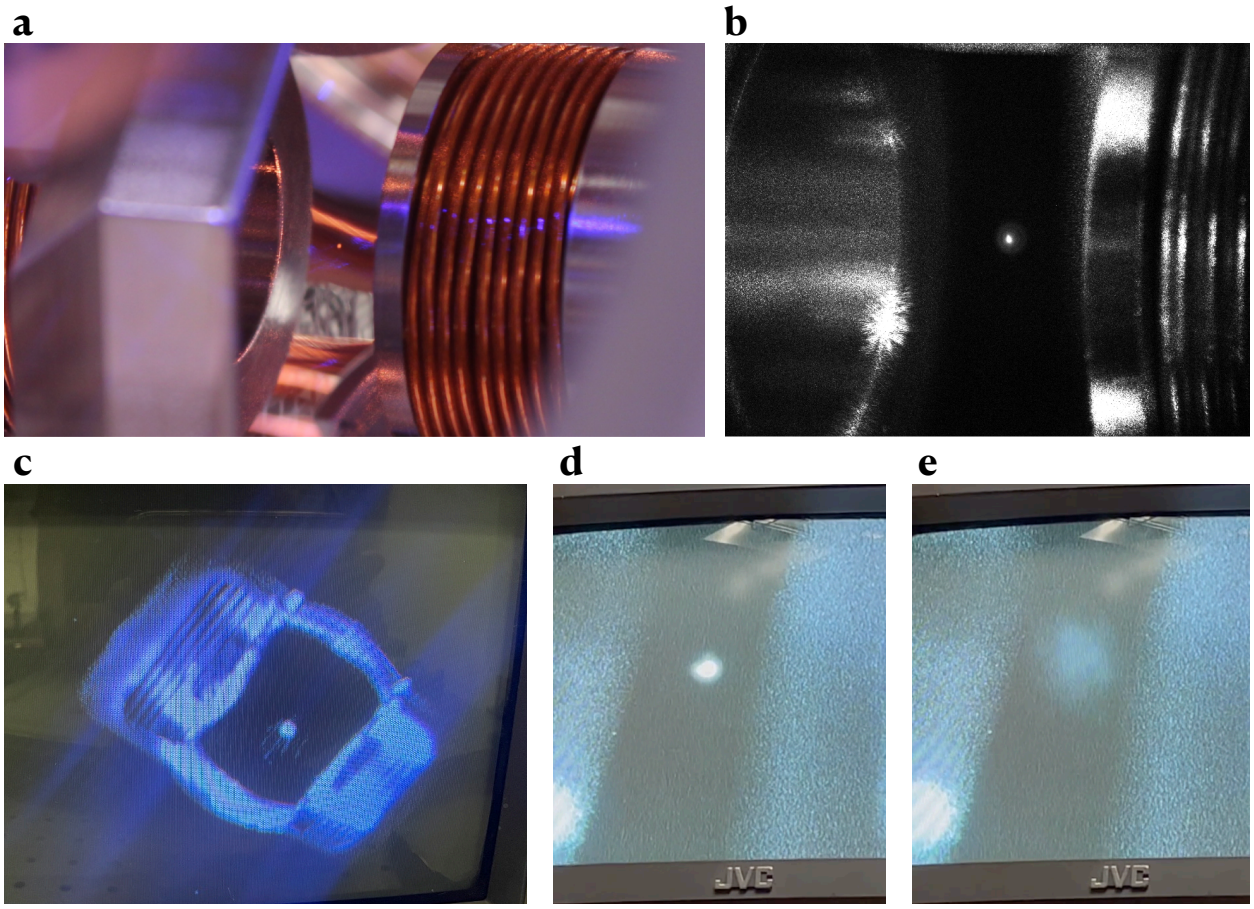

Figure 14.15: Fluorescent imaging of the atomic cloud. Fluorescence imaging of the atomic cloud, side views in **a** and **b**, and a top view in **c**. Expansion of the atomic cloud, with weak magnetic field gradient in **d** and strong magnetic field gradient in **e**.

14.7.1 Atomic Temperature

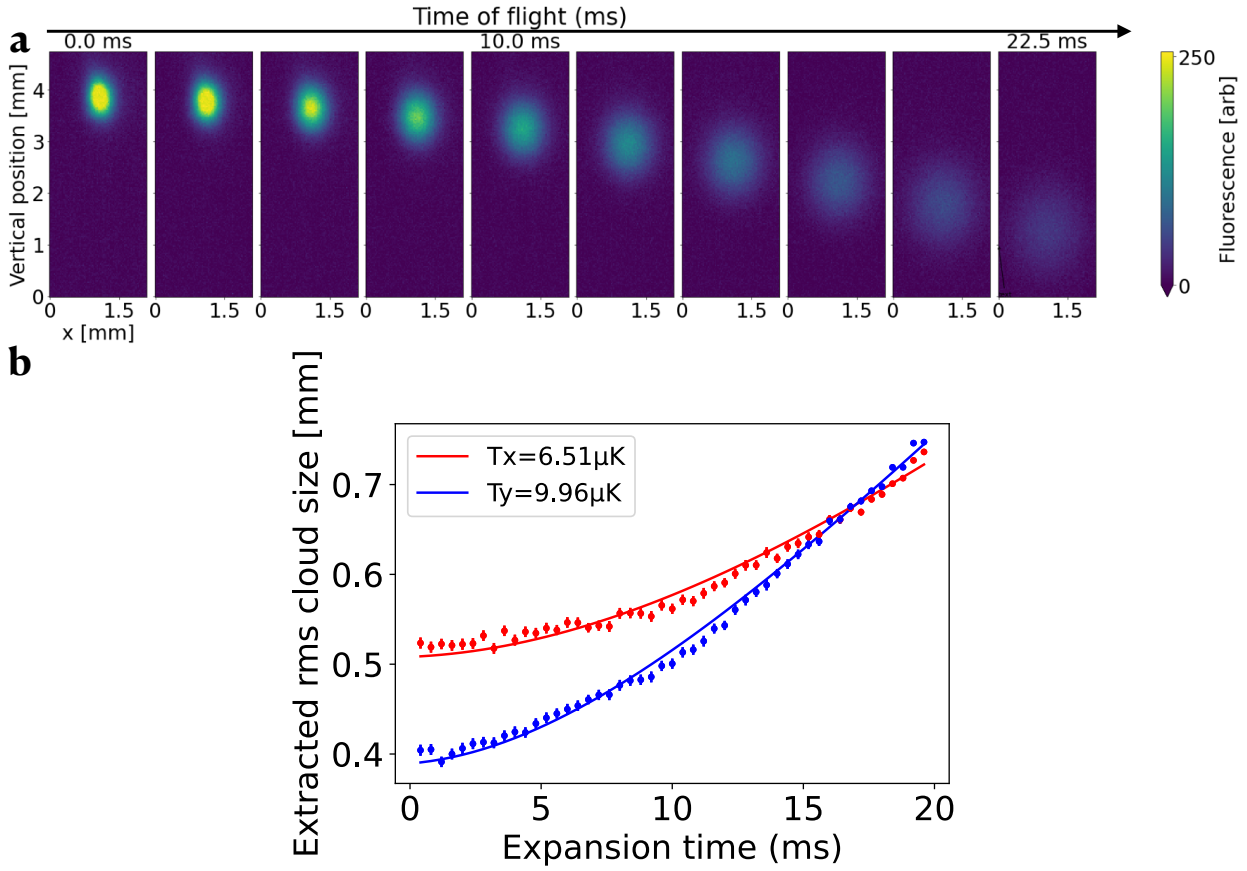

Figure 14.16: Characterization of the atom source. **a**, Upon achieving a good vacuum quality, we have cooled and trapped a ^{87}Rb MOT using polarization gradient cooling, and performed a time-of-flight expansion measurement based on atom florescence. These images are captured by a camera situated on an optical breadboard to the opposite side of the ion pump attached to the science chamber, angled horizontally such that it has direct line-of-sight access to the atomic cloud, without being blocked by the MOT structures. **b**, The spot size of the MOT vs. expansion time was plotted to extract the post-PGC temperature of the atomic cloud to be less than 10 μK in both axes of the imaging plane. The different temperatures measured along the two axes likely result from a combination of imperfect MOT beam wavefronts, imbalanced MOT beam powers, and imperfect magnetic field gradients during PGC.

CHAPTER 15

ATOMIC CONVEYOR BELT

15.1 Introduction

Once an atomic cloud is formed by the Rb dispensers (Fig. 15.1), cooled by the MOT lasers (Fig. 14.1), and trapped by the magnetic field gradient (Fig. 14.1) at near the bottom of the science chamber, we transport the atomic cloud upwards by 4" (10 cm) to the cavity-under-test via an optical conveyor belt.

15.2 Design and Construction of the Atomic Conveyor Belt

The optical conveyor belt is made of two counter-propagating 120 mW, 785 nm beams optically amplified from an Innovative Photonics Solutions laser with 100 kHz linewidth, and with the differential optical path length balanced to minimize atom heating due to laser phase noise [74].

The lattice is translated by inducing an adjustable frequency offset up to 2 MHz between the beams with two double-pass acousto-optic modulators, typically reaching a maximum atomic acceleration of 1500 m/s^2. Each beam is focused at the center of the transport path to a waist of 120 µm, resulting in an axial trap frequency of $2\pi \times 110$ kHz and a trap depth of $2\pi \times 6$ MHz. A quick calculation of the dipole trap is included in Sec. 7.1.

In the atomic conveyor belt setup (Fig. 15.2), a seed laser provides the initial light for the red-detuned lattice beam. An isolator is installed immediately after the laser diode to prevent back reflections from destabilizing the laser. The seed laser light is then amplified to the required power levels using a tapered amplifier. An interlock circuit is situated just upstream of the tapered amplifier to protect it from operating at high current without any seed power. Another isolator, placed immediately after the tapered amplifier, prevents back reflections from affecting its stability. The amplified light is subsequently divided into two

branches by a 50:50 beam splitter. Each branch undergoes an identical double-pass AOM setup, where it first passes through a polarizing beam splitter, experiences a frequency shift by a variable amount from the AOM, is phase-shifted by a quarter-wave plate, reflected by an end mirror, and then undergoes a frequency shift during its second pass through the AOM. The double-passed beams are reflected by the polarizing beam splitters and are fiber-coupled to form the top and bottom lattice beams directed towards the science chamber.

In the lattice launch setup, each beam is filtered through an angled 780 nm filter, its polarization is cleaned up, and the beams are focused at the midpoint between the MOT and the cavity region.

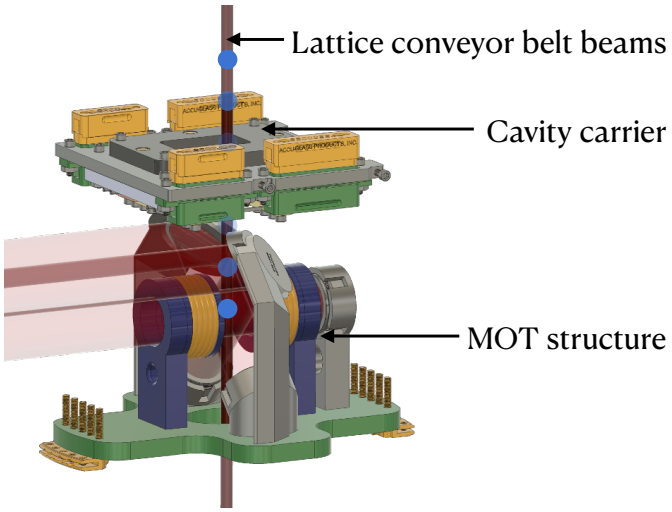

Figure 15.1: Atomic transport system. This system transports cold trapped Rb atoms from the position of the MOT upwards into the center of the optical cavity, for a total distance of about 4" (10.2 cm). It consists of two counter-propagating 785 nm beams, each delivering 120 mW from above or below the science chamber. The beams are frequency-shifted via two AOMs to have a relative offset up to 2 MHz (corresponding to $\sim$ 0.8 m/s maximum transport speed). They are focused at the center of the transport path to create a 120 µm waist (lattice depth about 38 µK), and path-length balanced to minimize phase-noise induced atom heating.

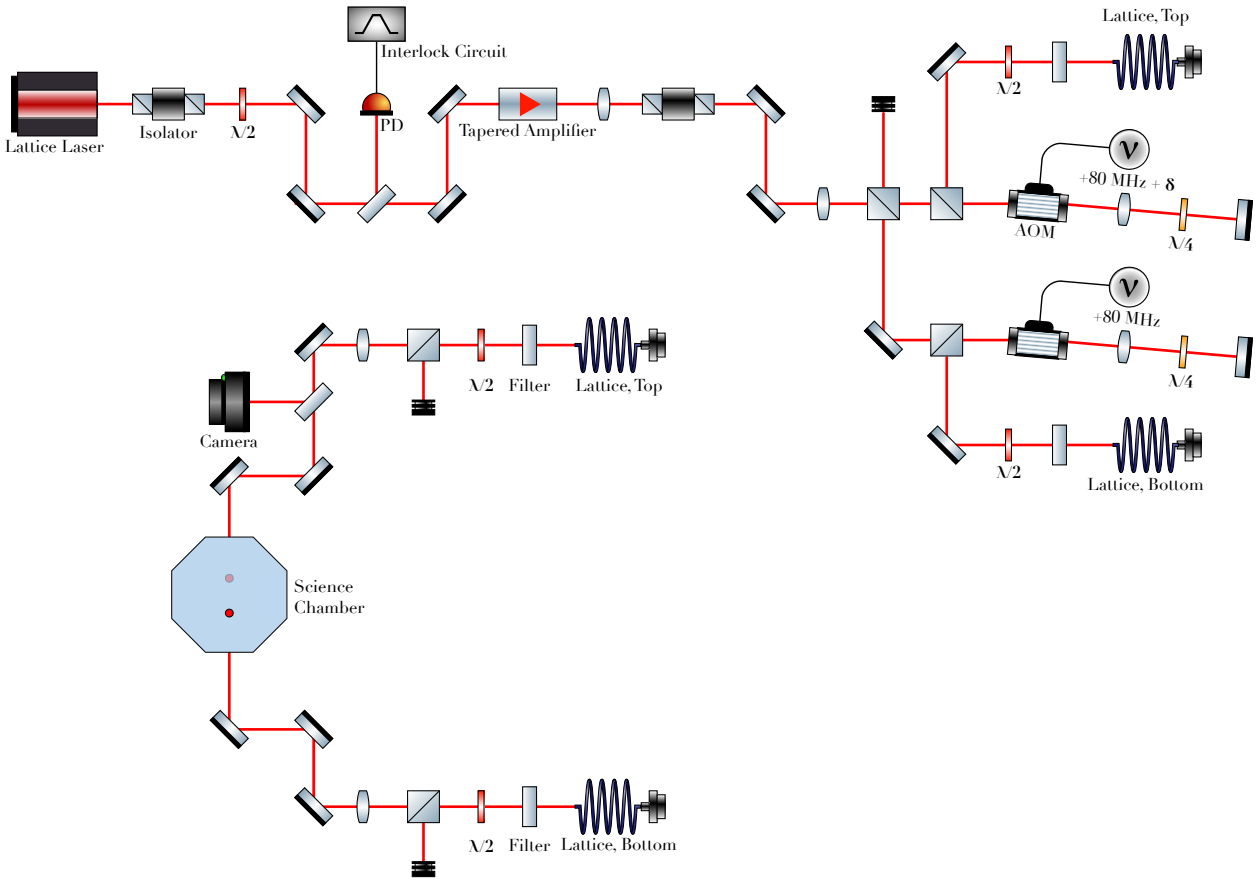

Figure 15.2: Schematics of the lattice conveyor belt. The lattice laser was interlocked, amplified, split into top and bottom beams, and frequency-shifted by two AOMs in a double-pass configuration to generate a 2δ (several MHz) frequency offset for transporting the atoms. Beam launching optics in the bottom panel were path-length balanced to minimize phase-noise induced atom heating.

Dipole Trap	**Symbol**	**Detail**
Laser Wavelength	λ	785 nm
Beam Power	P	120 mW
Beam Waist	w_0	120 μm
Trap Depth	U	$2\pi\times$ 6 MHz
Trap Temperature	T	38 μK

Table 15.1: Summary of the dipole trap setup.

15.3 Implementation of the Atomic Conveyor Belt

The physical implementation of the atomic conveyor belt is illustrated in the following images. Fig. 15.3 details the construction, characterization, and protection of the tapered amplifier, including its housing, beam shape after amplification, and safety interlock circuit. The optics involved in the generation, amplification, and launching of the lattice beam are shown in Fig. 15.4, highlighting the setup for beam amplification, the double-pass AOM for frequency shifting, and the top and bottom arm beam launches.

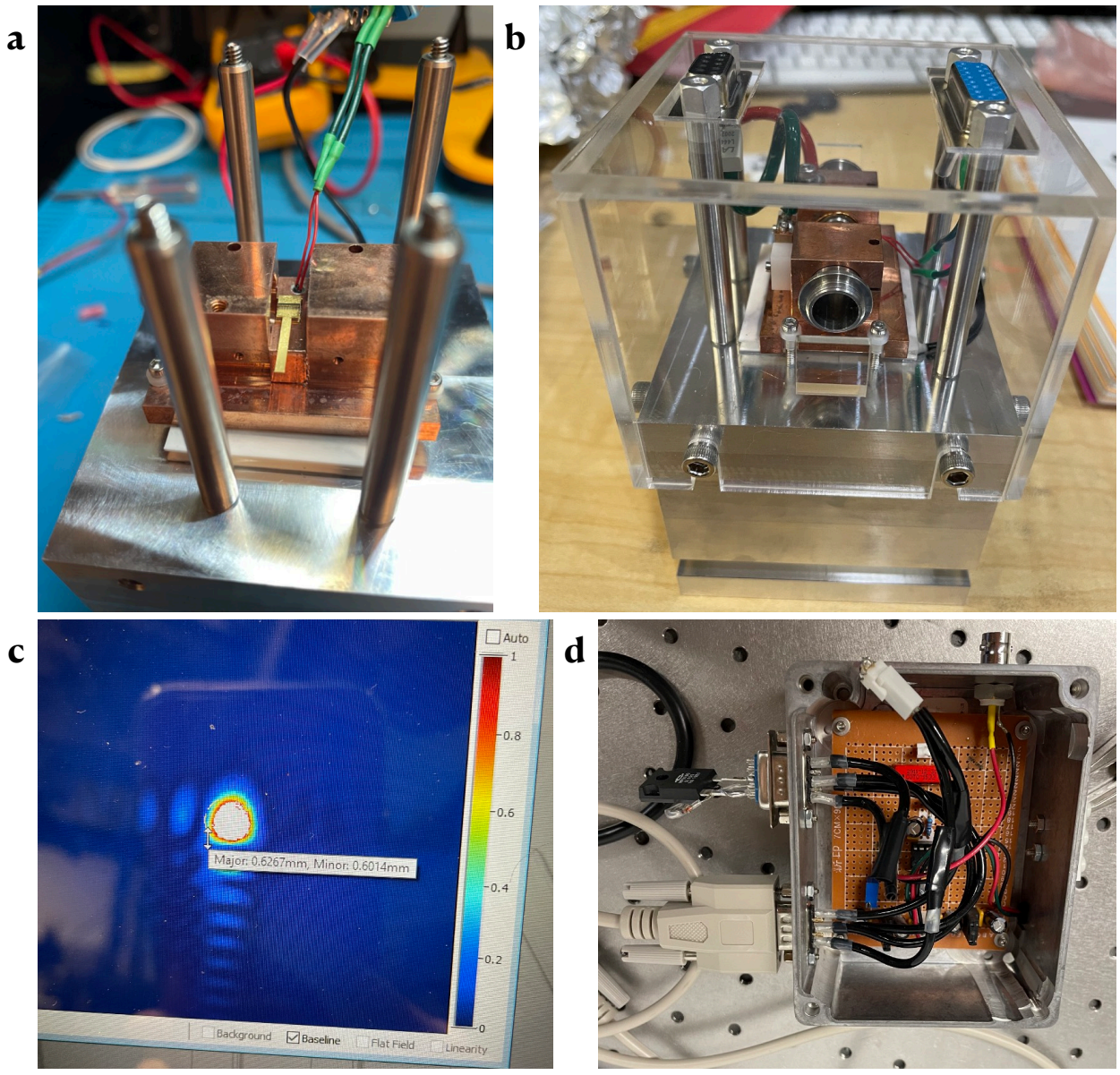

Figure 15.3: Laser and tapered amplifier used in the optical conveyor belt setup. **a**, tapered amplifier for the lattice beam. **b**, tapered amplifier housed in its heatsink. **c**, characterization of beam shape after amplification. **d**, interlock circuit implemented for safety measures.

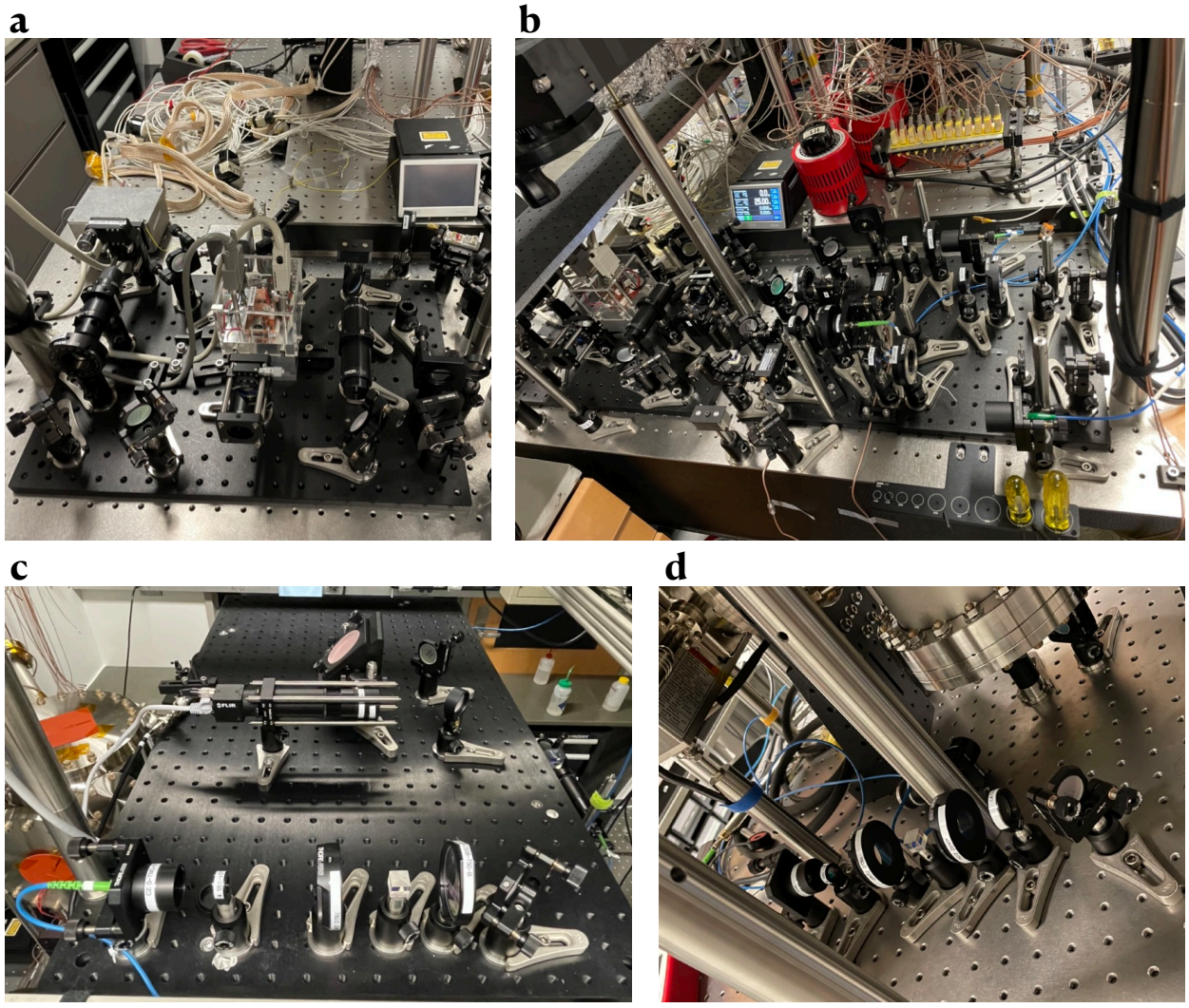

Figure 15.4: Optics of the optical conveyor belt setup. **a**, generation and amplification of the lattice beam. **b**, double-pass AOM setup for shifting the beam frequency. **c**, top-arm beam launch. **d**, bottom-arm beam launch.

15.4 Characterization of Atomic Conveyor Belt

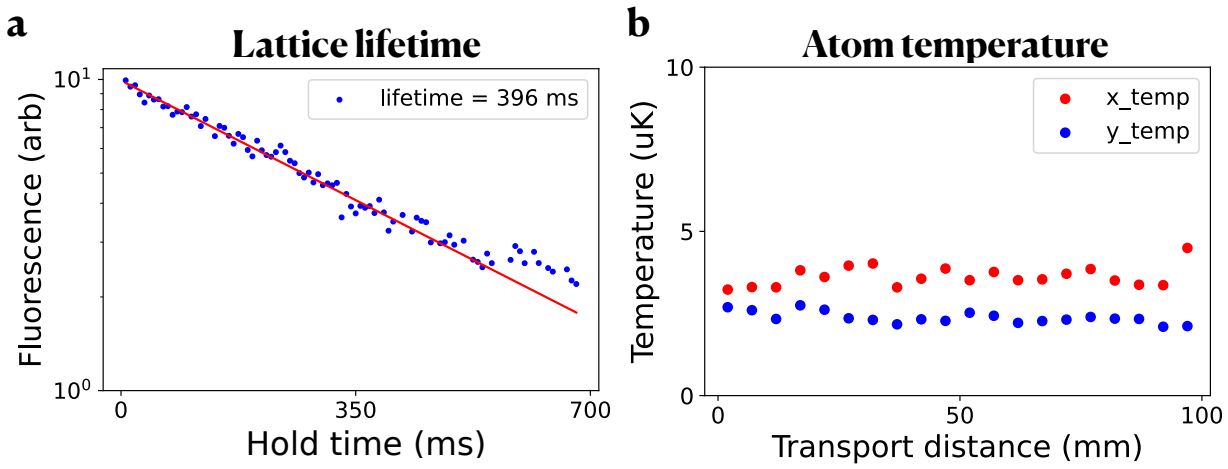

Figure 15.5: Characterization of the atomic transport system. The following data are taken by transporting cold Rb atoms towards the cavity center and then back by a certain transport distance, and measuring their fluorescence after varying hold times. We then fit the trend to an exponential curve to extract the lifetime parameter. **a,** 10.0 cm transport, showing a lattice lifetime of 396 ms. **b,** We have measured the temperature of the cold atoms being transported, by performing an expansion measurement in both transverse directions as summarized in each point on the graph, and repeat this process for various transport distances ranging from 0 mm to 100 mm. We have observed no effect of the transport distance on the lattice temperature.

We have demonstrated the ability to reproducibly transport atoms from the MOT position to the designated resonator position over a transport distance of 114 mm and a single-trip duration of 16 ms. We load ∼80% of the atoms into the lattice, limited by imperfect MOT/lattice overlap. Round-trip transport experiments indicate a one-way transport efficiency of ∼63%, for a total MOT to cavity transfer efficiency of ∼50%. The atomic temperature remained below 10 µK, independent of transport distance.

This is borne out by a fluorescence imaging experiment where we transferred the atoms from the MOT up to a variable distance, ultimately reaching the designated resonator center, and then back down (see Figure 15.5). The transport efficiency was extracted by comparing the level of fluorescence before and after the transport. The temperature in the lattice was

measured through time-of-flight expansion measurements of the atoms after transport. We do not expect the sample to thermalize during the course of the experiment due to the relatively low atomic density of the sample.

CHAPTER 16

OUTLOOK

We have installed the first cavity into the loadlock chamber, pumped and baked and transferred to the science chamber. At the time of the transfer, the loadlock chamber's ion pump read 4.5×10^{-10} Torr, and the science chamber's ion pump read 4×10^{-10} Torr, which established a UHV status successfully. One open question is the extent to which the long lever-arm of the translator will couple mechanical vibrations into the resonator. While such vibrations should be common mode across the resonator, residual coupling can be suppressed via FPGA-based pole/zero cancellation & feedback [72]. We anticipate numerous upcoming opportunities to harness this technology to benchmark novel resonators coupled to atoms [50, 57, 75] for many-body physics [76].

APPENDIX A

MECHANICAL DRAWINGS

A.1 UHV components

This chapter presents a comprehensive list of mechanical drawings of custom-made UHV components, the in-vacuum MOT setup, the in-vacuum cavity carrier, and the small waist cavity. For the custom-made UHV components, I am including drawings for the all-metal-valve, the translator, and the ConFlat Tee. For the in-vacuum MOT setup, I am including drawings for the support plane, the MOT coil mount, the back mirror mount, the bottom mirror mount, and the elliptical mirror mount. For the cavity carrier setup, I am including drawings for the baseplate, the Macor plate, the top cavity mating plate, the dispenser clamps, and the L-bracket. For the small waist cavity setup, I am including drawings for the entire setup, the horizontal flexure, the vertical flexure, the lens mount, the curved mirror mount, and the prism mirror mount for molasses beams.

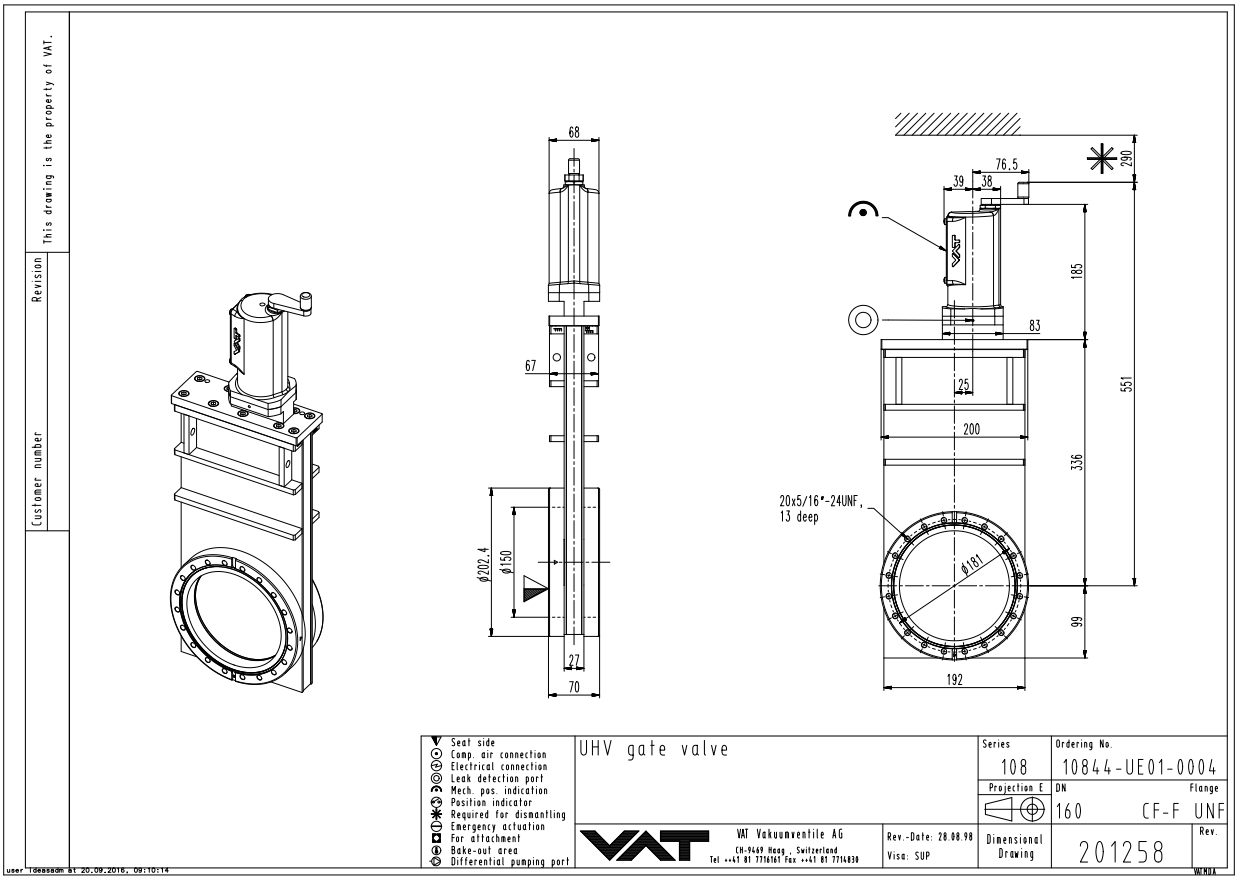

Figure A.1: All-metal gate valve for separating the science chamber and the loadlock chamber. It was designed by VAT, and we selected the manual actuation option to avoid any electromagnetic interference to the atoms. It can be baked to 200 C if the valve is closed.

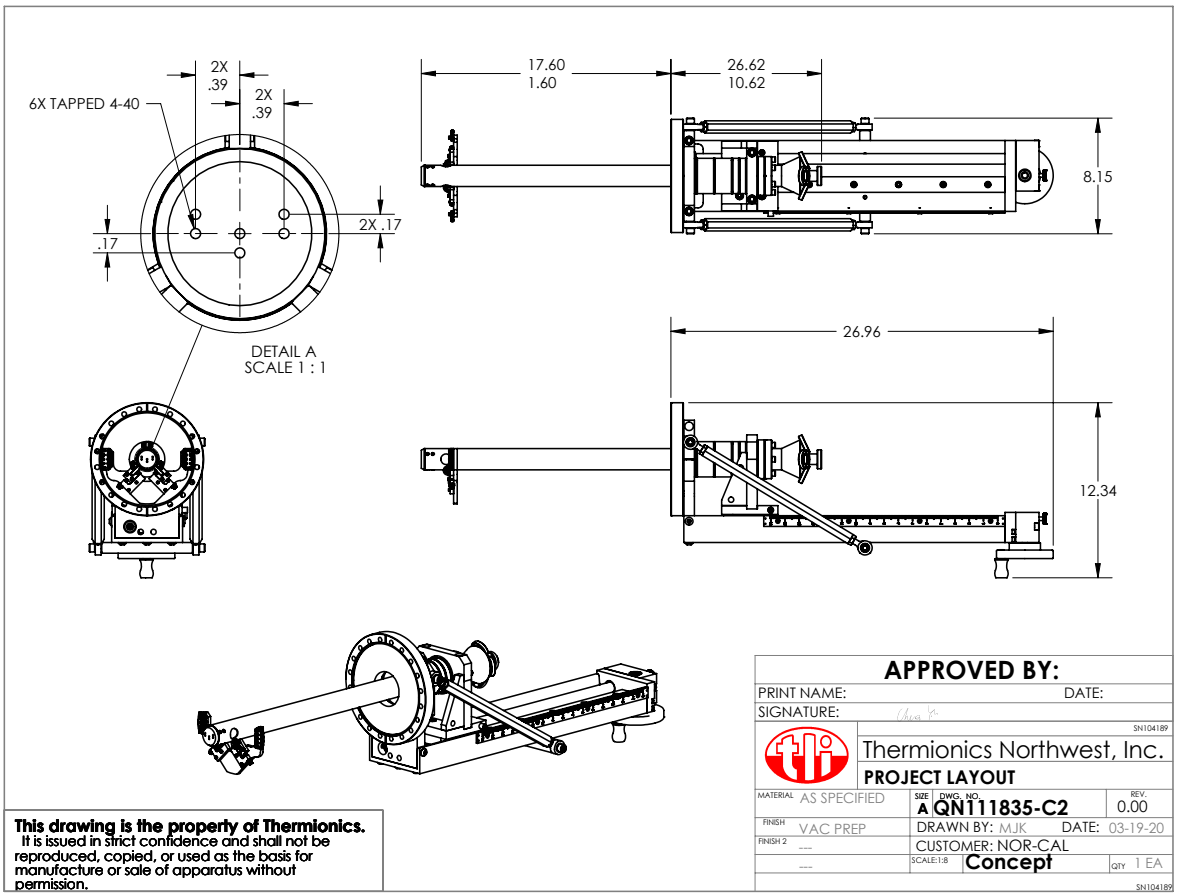

Figure A.2: The translator for moving the cavity horizontally between the science chamber and the loadlock chamber. It was designed by Thermionics Northwest, and we again selected the manual actuation option. The base flange was mounted to a flange on the loadlock chamber. The cavity was attached to the end of the tube. The V-stand with two wheels was used to support and guide the tube across two chambers, and was attached to a close coupler of the chamber through two groove grabbers. During the installation process, we have found that the feedthrough connectors on the utility hat were inappropriately sized, so we have replaced it with a larger 5-way cross with feedthrough flanges.

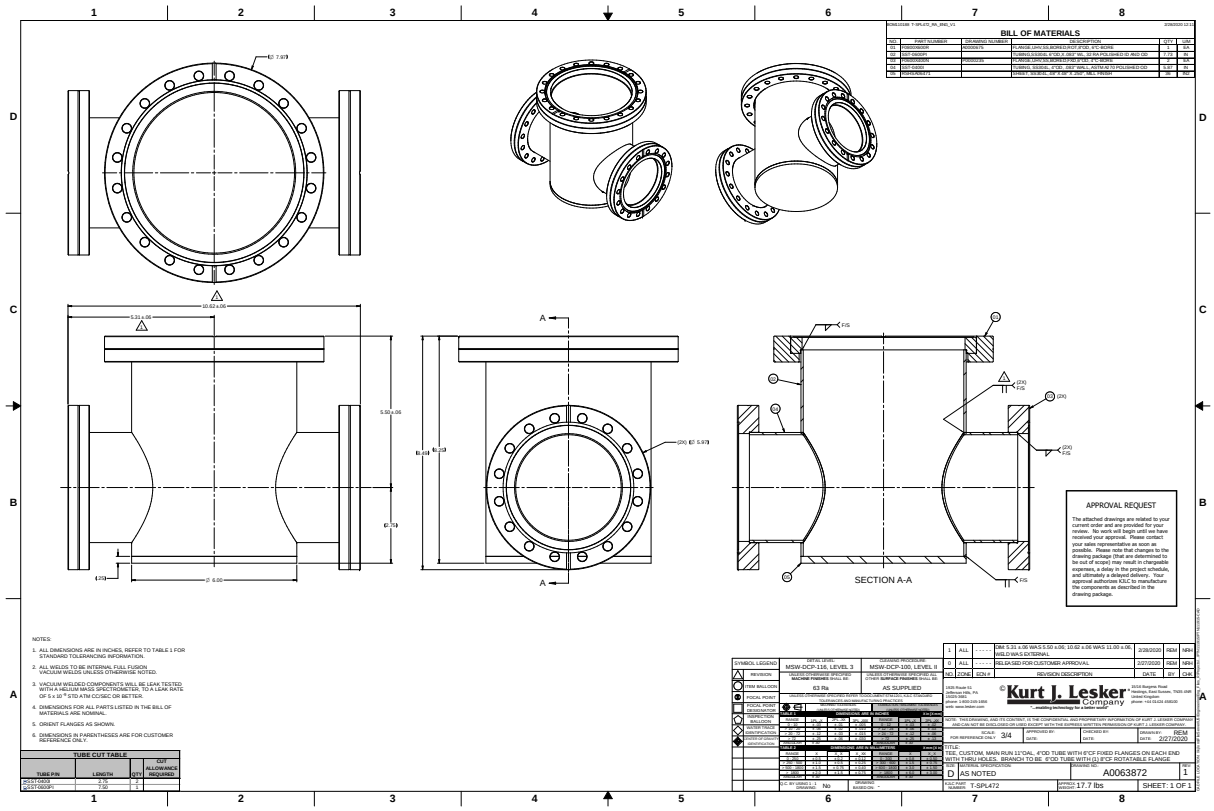

Figure A.3: An anti-reducing tee for attaching the loadlock chamber to two mechanical support flanges below. This needed to be custom-made because our side flanges (6”) are smaller than the base flange (8”), which is not a typical configuration.

A.2 In-vacuum MOT setup

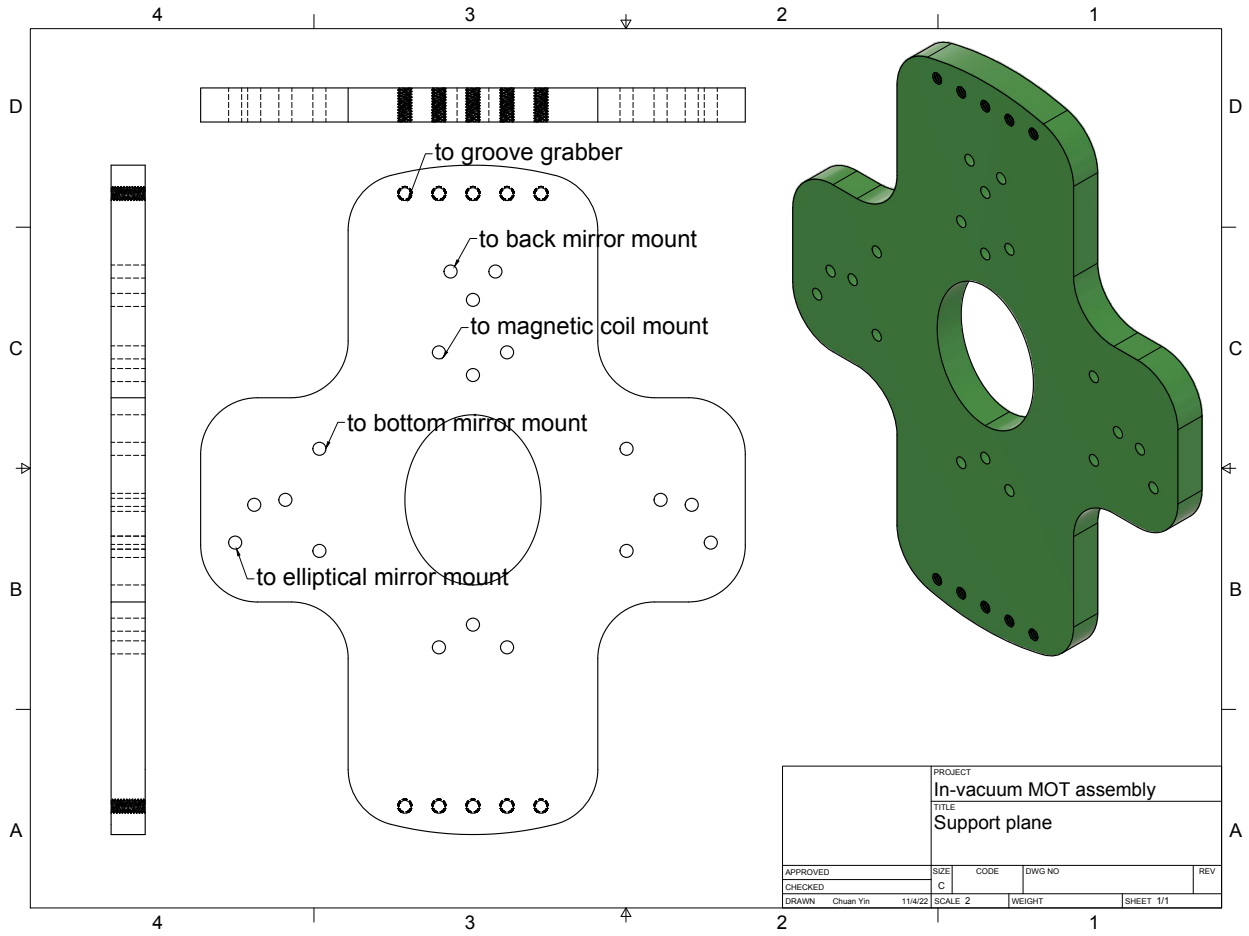

Figure A.4: Stainless steel base plate for holding in-vacuum MOT components, including two magnetic coil mounts, a back mirror mount, two bottom mirror mounts, and two elliptical mirror mounts. It is attached to the chamber through two groove grabbers.

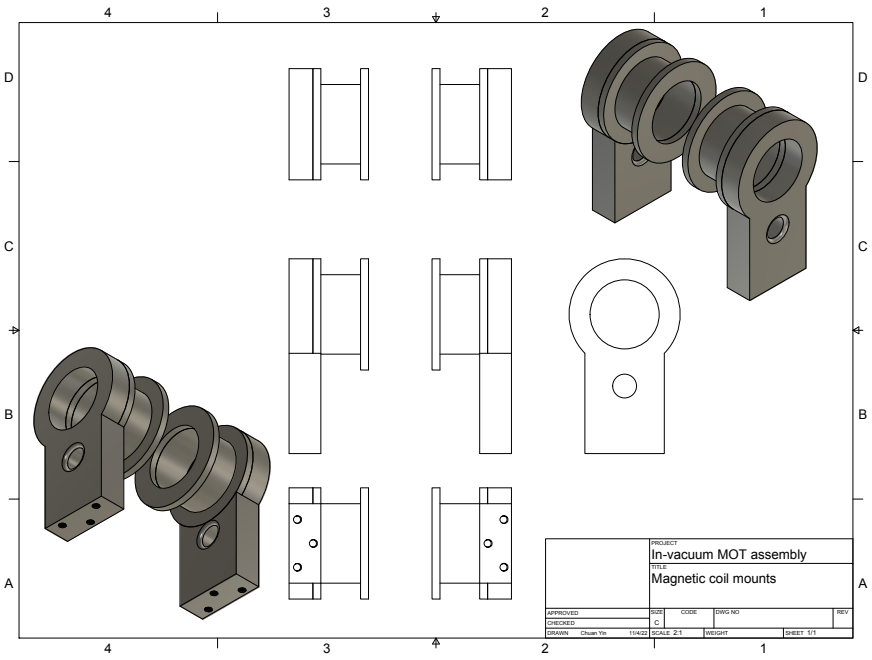

Figure A.5: Stainless steel mounts for winding the MOT quadrupole coils around. A venting hole was later drilled to the base of each of the coil mount, so any trapped air pocket could be outgassed, preventing virtual leaks. Two holes for guiding the outgoing Kapton wires were chamfered to avoid stripping and shorting the wires.

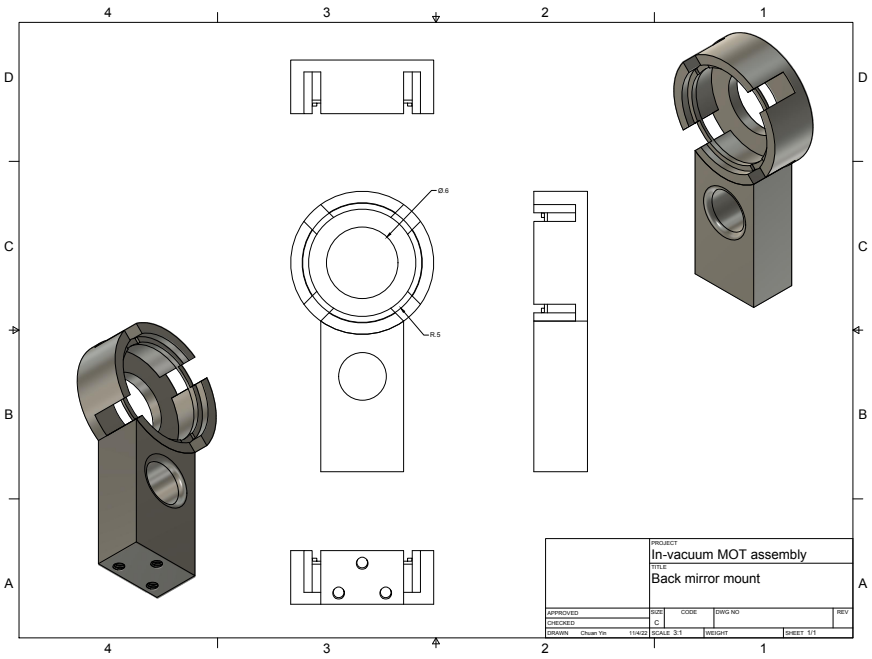

Figure A.6: Stainless steel mount for the back reflecting mirror and the quarter waveplate, separated by a vented ring spacer.

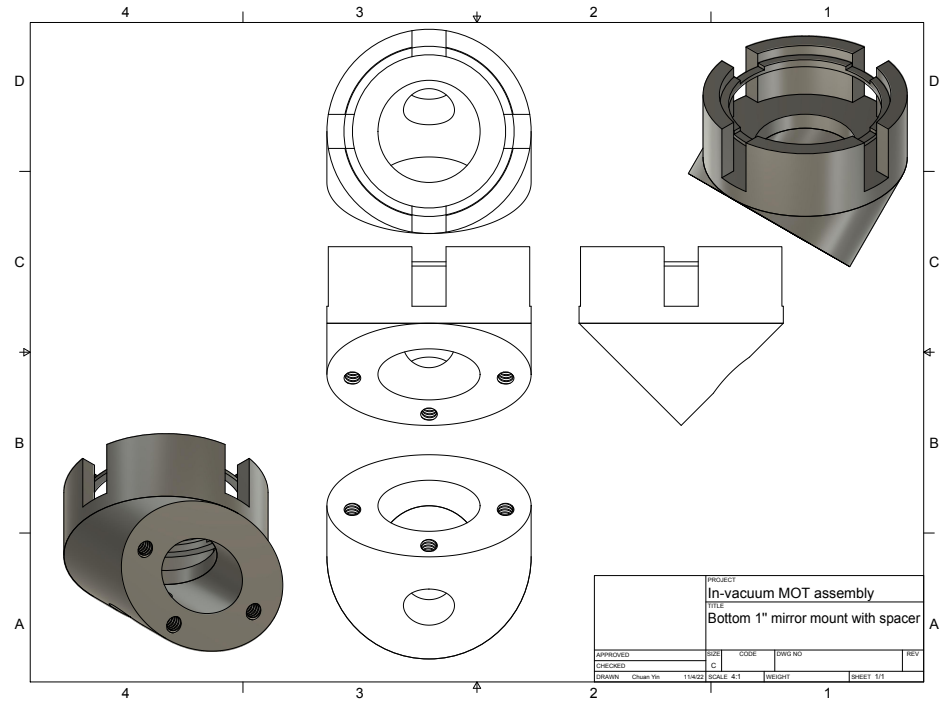

Figure A.7: Stainless steel mount for the bottom redirecting mirror and the quarter waveplate, separated by a vented ring spacer.

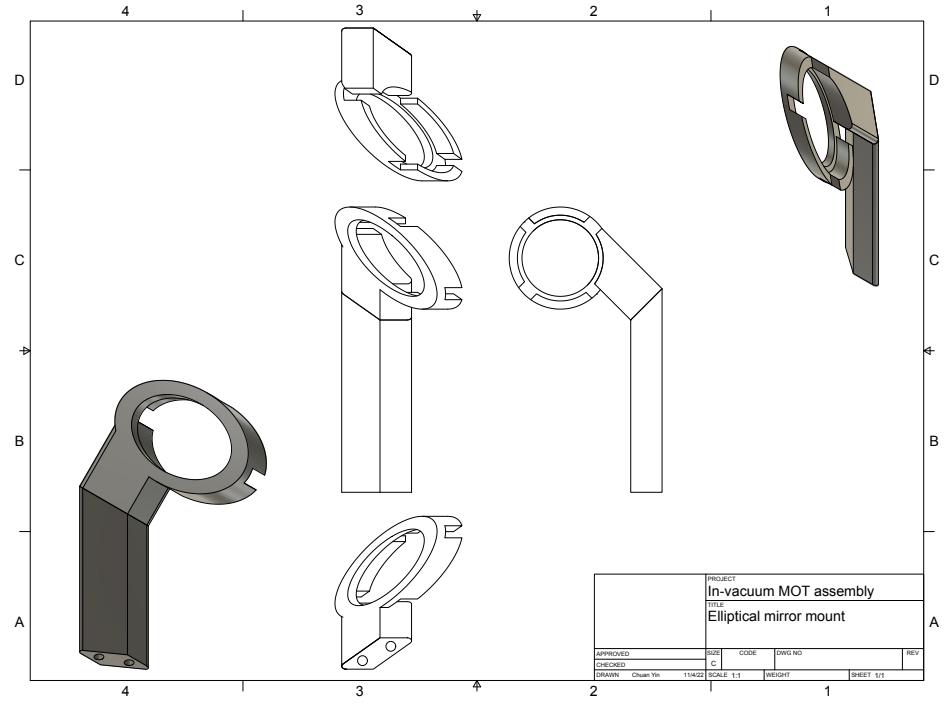

Figure A.8: Stainless steel mount for the redirecting elliptical mirror.

A.3 Cavity carrier setup

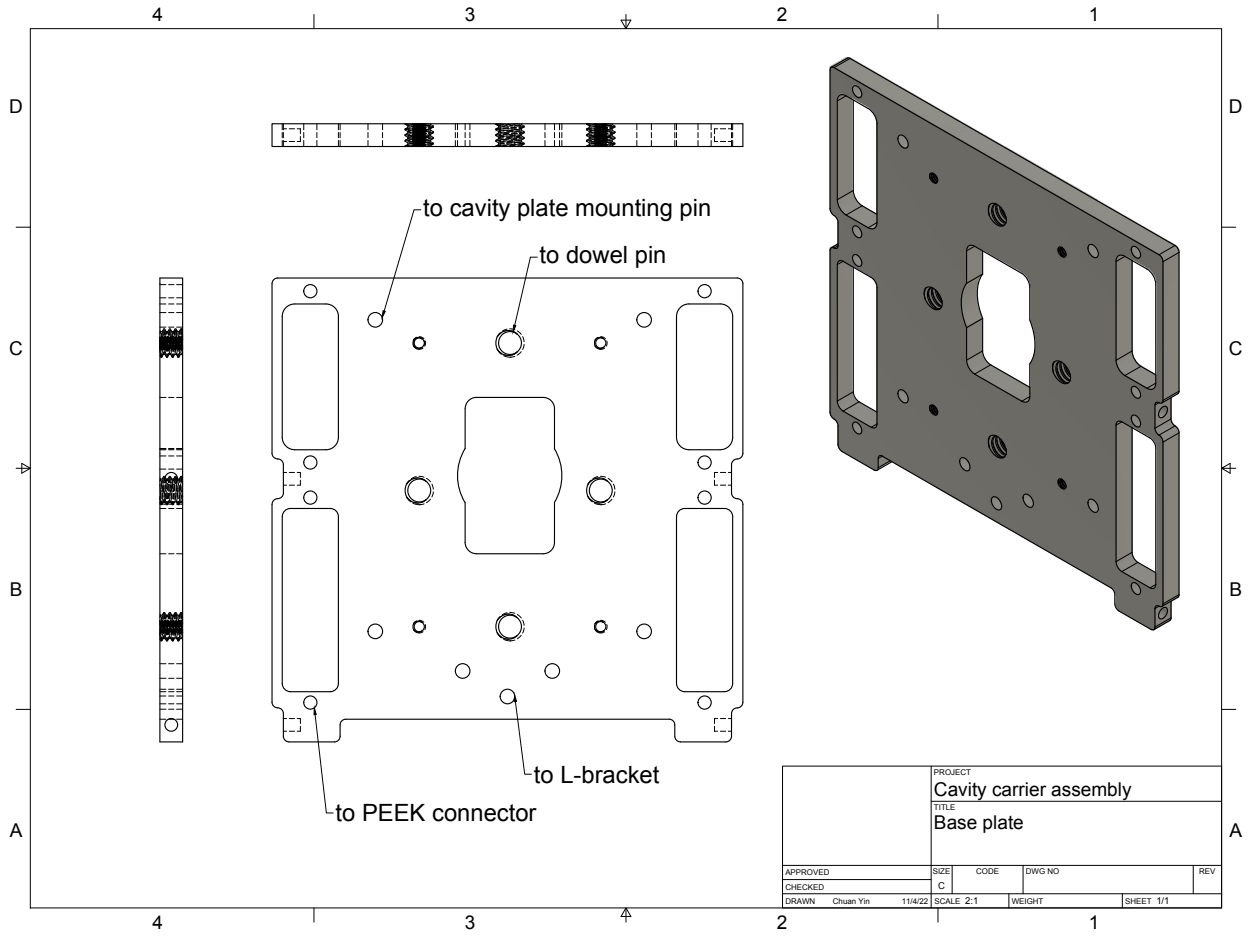

Figure A.9: Stainless steel baseplate for mounting the cavity, four PEEK connectors, and four dispensers. It is connected to the end of the translator tube through an L-bracket.

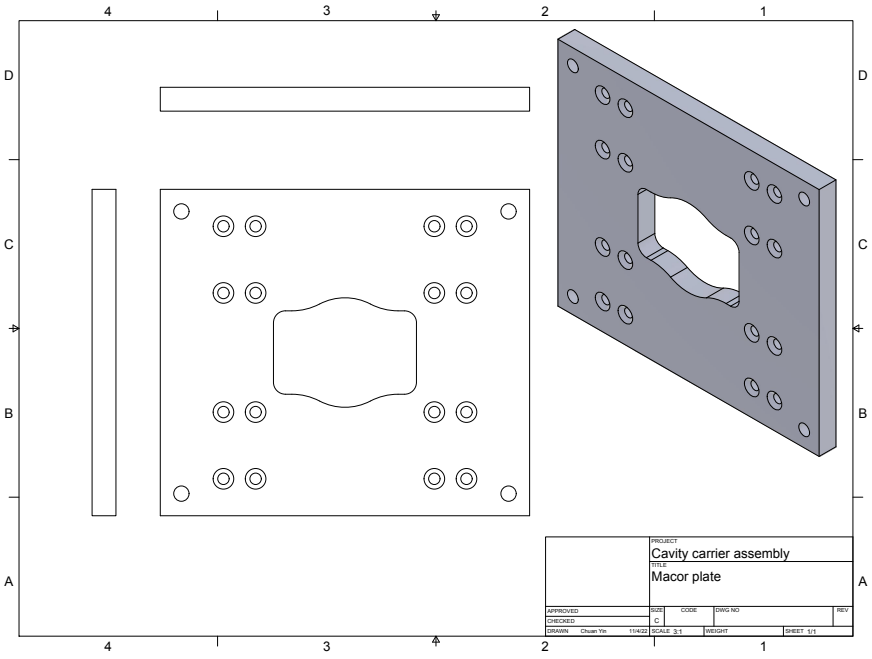

Figure A.10: Macor plate for mounting four dispensers below via the copper clamps, and providing electrical insulation across the positive and ground terminals. The 2-56 screw holes are recessed to reduce the vertical space the structure takes up.

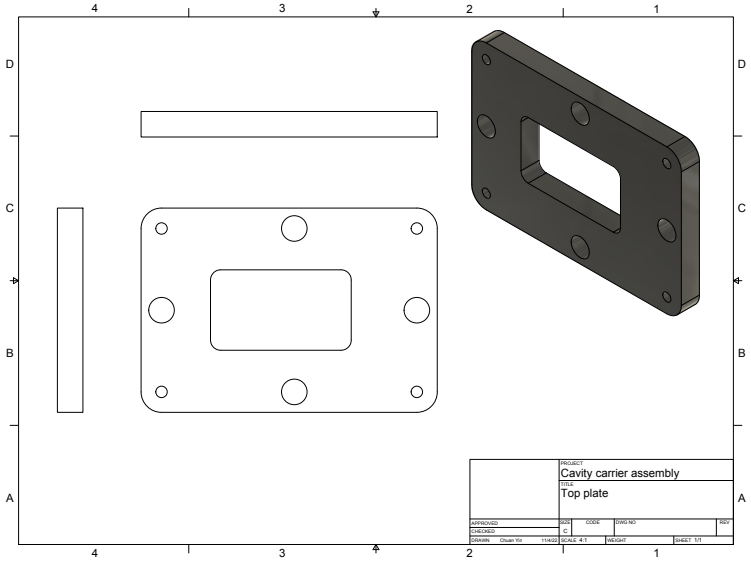

Figure A.11: Aluminum top plate for mating and aligning the cavity to the stainless baseplate. The four smaller holes are for 4-40 screws, and the four bigger holes are for dowel alignment pins.

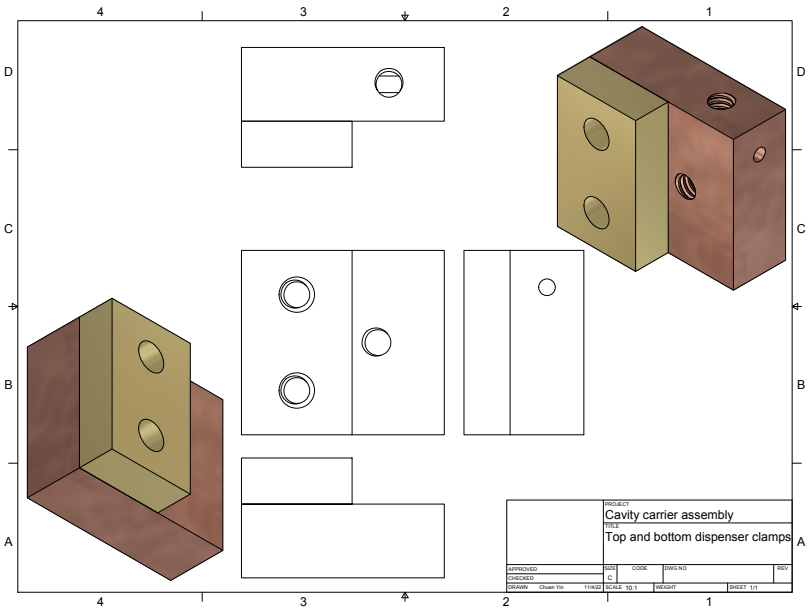

Figure A.12: Copper blocks for clamping a Rb dispenser in between. The bottom piece is screwed to the Macor plate from below via 2-56 countersunk screws, and the top piece is screwed to the bottom piece with a dispenser in the middle via 2-56 hex head screws. Spring washers are used to add a clamping force so that vacuum bakeouts do not cause faulty electrical connections. A small hole on the side is designated for inserting the current-carrying gold pin into, and a set screw comes in from another side to make good electrical contact between the copper block and the gold pin.

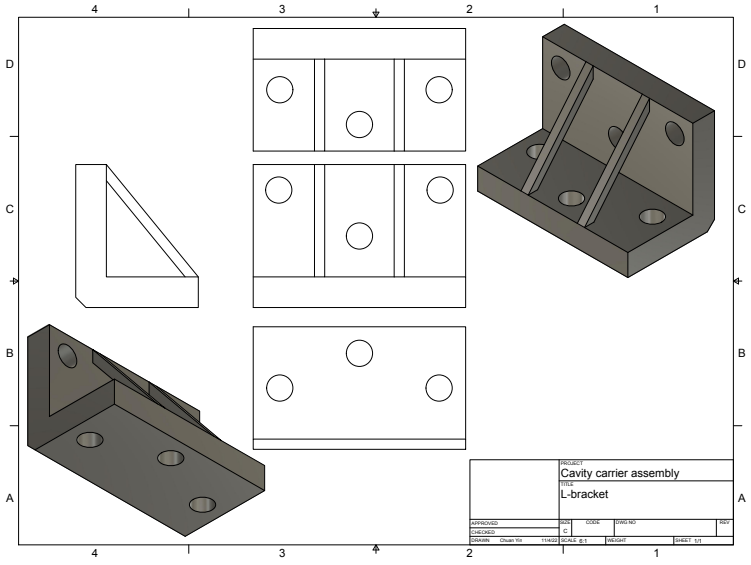

Figure A.13: Stainless steel L-bracket for attaching the cavity baseplate to the end of the translator tube. It is reinforced with two diagonal bars.

REFERENCES

[1] Daniel A Steck. Classical and modern optics. *Oregon University*, 2006.

[2] Daniel A Steck. Quantum and atom optics. *Oregon University*, 2007.

[3] Steven Chu, JE Bjorkholm, A Ashkin, and Alex Cable. Experimental observation of optically trapped atoms. *Physical review letters*, 57(3):314, 1986.

[4] Steven L Rolston, Christoph Gerz, Kristian Helmerson, PS Jessen, Paul D Lett, William D Phillips, RJ Spreeuw, and CI Westbrook. Trapping atoms with optical potentials. In *1992 Shanghai International Symposium on Quantum Optics*, volume 1726, pages 205–211. SPIE, 1992.

[5] Eric L Raab, Mara Prentiss, Alex Cable, Steven Chu, and David E Pritchard. Trapping of neutral sodium atoms with radiation pressure. *Physical review letters*, 59(23):2631, 1987.

[6] Paul D Lett, William D Phillips, SL Rolston, Carol E Tanner, RN Watts, and CI Westbrook. Optical molasses. *JOSA B*, 6(11):2084–2107, 1989.

[7] Ch Salomon, J Dalibard, WD Phillips, A Clairon, and S Guellati. Laser cooling of cesium atoms below 3 μk. *Europhysics Letters*, 12(8):683, 1990.

[8] Jean Dalibard and Claude Cohen-Tannoudji. Laser cooling below the doppler limit by polarization gradients: simple theoretical models. *JOSA B*, 6(11):2023–2045, 1989.

[9] Edwin T Jaynes and Frederick W Cummings. Comparison of quantum and semiclassical radiation theories with application to the beam maser. *Proceedings of the IEEE*, 51(1):89–109, 1963.

[10] Edward Mills Purcell. Spontaneous emission probabilities at radio frequencies. In *Confined Electrons and Photons: New Physics and Applications*, pages 839–839. Springer, 1995.

[11] Ph Goy, JM Raimond, M Gross, and S Haroche. Observation of cavity-enhanced single-atom spontaneous emission. *Physical review letters*, 50(24):1903, 1983.

[12] Christina J Hood, TW Lynn, AC Doherty, AS Parkins, and HJ Kimble. The atom-cavity microscope: Single atoms bound in orbit by single photons. *Science*, 287(5457):1447–1453, 2000.

[13] Michel Brune, F Schmidt-Kaler, Abdelhamid Maali, J Dreyer, E Hagley, JM Raimond, and S Haroche. Quantum rabi oscillation: A direct test of field quantization in a cavity. *Physical review letters*, 76(11):1800, 1996.

[14] Susumu Noda, Masayuki Fujita, and Takashi Asano. Spontaneous-emission control by photonic crystals and nanocavities. *Nature photonics*, 1(8):449–458, 2007.

[15] Peter Lodahl, A Floris van Driel, Ivan S Nikolaev, Arie Irman, Karin Overgaag, Daniël Vanmaekelbergh, and Willem L Vos. Controlling the dynamics of spontaneous emission from quantum dots by photonic crystals. *Nature*, 430(7000):654–657, 2004.

[16] Wonho Jhe, A Anderson, Edwards A Hinds, D Meschede, Luigi Moi, and Serge Haroche. Suppression of spontaneous decay at optical frequencies: Test of vacuum-field anisotropy in confined space. *Physical review letters*, 58(7):666, 1987.

[17] Thijs Klaassen, Arthur Hoogeboom, Martin P van Exter, and JP Woerdman. Gouy phase of nonparaxial eigenmodes in a folded resonator. *JOSA A*, 21(9):1689–1693, 2004.

[18] Daniel B Higginbottom, Geoff T Campbell, Gabriel Araneda, Fengzhou Fang, Yves

Colombe, Ben C Buchler, and Ping Koy Lam. Fabrication of ultrahigh-precision hemispherical mirrors for quantum-optics applications. *Scientific Reports*, 8(1):221, 2018.

[19] Kevin M Birnbaum, Andreea Boca, Russell Miller, Allen D Boozer, Tracy E Northup, and H Jeff Kimble. Photon blockade in an optical cavity with one trapped atom. *Nature*, 436(7047):87–90, 2005.

[20] Dieter Jaksch, Juan Ignacio Cirac, Peter Zoller, Steve L Rolston, Robin Côté, and Mikhail D Lukin. Fast quantum gates for neutral atoms. *Physical Review Letters*, 85(10):2208, 2000.

[21] Mark Saffman, Thad G Walker, and Klaus Mølmer. Quantum information with rydberg atoms. *Reviews of modern physics*, 82(3):2313–2363, 2010.

[22] Klemens Hammerer, Anders S Sørensen, and Eugene S Polzik. Quantum interface between light and atomic ensembles. *Reviews of Modern Physics*, 82(2):1041–1093, 2010.

[23] Antoine Browaeys and Thierry Lahaye. Many-body physics with individually controlled rydberg atoms. *Nature Physics*, 16(2):132–142, 2020.

[24] Thomas Pellizzari, Simon A Gardiner, Juan Ignacio Cirac, and Peter Zoller. Decoherence, continuous observation, and quantum computing: A cavity qed model. *Physical Review Letters*, 75(21):3788, 1995.

[25] H Mabuchi and AC Doherty. Cavity quantum electrodynamics: coherence in context. *Science*, 298(5597):1372–1377, 2002.

[26] Tatjana Wilk, A Gaëtan, C Evellin, J Wolters, Y Miroshnychenko, P Grangier, and Antoine Browaeys. Entanglement of two individual neutral atoms using rydberg blockade. *Physical review letters*, 104(1):010502, 2010.

[27] Nicolas Schlosser, Georges Reymond, Igor Protsenko, and Philippe Grangier. Sub-poissonian loading of single atoms in a microscopic dipole trap. *Nature*, 411(6841):1024–1027, 2001.

[28] L Isenhower, E Urban, XL Zhang, AT Gill, T Henage, Todd A Johnson, TG Walker, and M Saffman. Demonstration of a neutral atom controlled-not quantum gate. *Physical review letters*, 104(1):010503, 2010.

[29] MD Lukin. Colloquium: Trapping and manipulating photon states in atomic ensembles. *Reviews of Modern Physics*, 75(2):457, 2003.

[30] M Ebert, M Kwon, TG Walker, and M Saffman. Coherence and rydberg blockade of atomic ensemble qubits. *Physical Review Letters*, 115(9):093601, 2015.

[31] Shanchao Zhang, Chang Liu, Shuyu Zhou, Chih-Sung Chuu, Michael MT Loy, and Shengwang Du. Coherent control of single-photon absorption and reemission in a two-level atomic ensemble. *Physical review letters*, 109(26):263601, 2012.

[32] Oliver Morsch and Markus Oberthaler. Dynamics of bose-einstein condensates in optical lattices. *Reviews of modern physics*, 78(1):179, 2006.

[33] Alexander L Fetter. Rotating trapped bose-einstein condensates. *Reviews of Modern Physics*, 81(2):647, 2009.

[34] Adam M Kaufman and Kang-Kuen Ni. Quantum science with optical tweezer arrays of ultracold atoms and molecules. *Nature Physics*, 17(12):1324–1333, 2021.

[35] Hannes Bernien, Sylvain Schwartz, Alexander Keesling, Harry Levine, Ahmed Omran, Hannes Pichler, Soonwon Choi, Alexander S Zibrov, Manuel Endres, Markus Greiner, et al. Probing many-body dynamics on a 51-atom quantum simulator. *Nature*, 551(7682):579–584, 2017.

[36] AM Kaufman, BJ Lester, CM Reynolds, ML Wall, M Foss-Feig, KRA Hazzard, AM Rey, and CA Regal. Two-particle quantum interference in tunnel-coupled optical tweezers. *Science*, 345(6194):306–309, 2014.

[37] Harry Levine, Alexander Keesling, Ahmed Omran, Hannes Bernien, Sylvain Schwartz, Alexander S Zibrov, Manuel Endres, Markus Greiner, Vladan Vuletić, and Mikhail D Lukin. High-fidelity control and entanglement of rydberg-atom qubits. *Physical review letters*, 121(12):123603, 2018.

[38] T Xia, M Lichtman, K Maller, AW Carr, MJ Piotrowicz, L Isenhower, and M Saffman. Randomized benchmarking of single-qubit gates in a 2d array of neutral-atom qubits. *Physical review letters*, 114(10):100503, 2015.

[39] Lu-Ming Duan, JI Cirac, P Zoller, and ES Polzik. Quantum communication between atomic ensembles using coherent light. *Physical review letters*, 85(26):5643, 2000.

[40] Iulia Buluta and Franco Nori. Quantum simulators. *Science*, 326(5949):108–111, 2009.

[41] Maciej Lewenstein, Anna Sanpera, Veronica Ahufinger, Bogdan Damski, Aditi Sen, and Ujjwal Sen. Ultracold atomic gases in optical lattices: mimicking condensed matter physics and beyond. *Advances in Physics*, 56(2):243–379, 2007.

[42] Dieter Jaksch and Peter Zoller. The cold atom hubbard toolbox. *Annals of physics*, 315(1):52–79, 2005.

[43] Gershon Kurizki, Patrice Bertet, Yuimaru Kubo, Klaus Mølmer, David Petrosyan, Peter Rabl, and Jörg Schmiedmayer. Quantum technologies with hybrid systems. *Proceedings of the National Academy of Sciences*, 112(13):3866–3873, 2015.

[44] Wenlan Chen, Jiazhong Hu, Yiheng Duan, Boris Braverman, Hao Zhang, and Vladan Vuletić. Carving complex many-atom entangled states by single-photon detection. *Physical review letters*, 115(25):250502, 2015.

[45] Julien Vaneecloo, Sébastien Garcia, and Alexei Ourjoumtsev. Intracavity rydberg superatom for optical quantum engineering: Coherent control, single-shot detection, and optical π phase shift. *Physical Review X*, 12(2):021034, 2022.

[46] Joshua Ramette, Josiah Sinclair, Zachary Vendeiro, Alyssa Rudelis, Marko Cetina, and Vladan Vuletić. Any-to-any connected cavity-mediated architecture for quantum computing with trapped ions or rydberg arrays. *PRX Quantum*, 3(1):010344, 2022.

[47] Hideo Mabuchi, M Armen, B Lev, Marko Loncar, Jelena Vuckovic, H Jeff Kimble, John Preskill, Michael L Roukes, Axel Scherer, and Steven J van Enk. Quantum networks based on cavity qed. *Quantum Inf. Comput.*, 1(4):7–12, 2001.

[48] H Jeff Kimble. The quantum internet. *Nature*, 453(7198):1023–1030, 2008.

[49] Stephan Ritter, Christian Nölleke, Carolin Hahn, Andreas Reiserer, Andreas Neuzner, Manuel Uphoff, Martin Mücke, Eden Figueroa, Joerg Bochmann, and Gerhard Rempe. An elementary quantum network of single atoms in optical cavities. *Nature*, 484(7393):195–200, 2012.

[50] Nathan Schine, Albert Ryou, Andrey Gromov, Ariel Sommer, and Jonathan Simon. Synthetic landau levels for photons. *Nature*, 534(7609):671–675, 2016.

[51] Logan W Clark, Nathan Schine, Claire Baum, Ningyuan Jia, and Jonathan Simon. Observation of laughlin states made of light. *Nature*, 582(7810):41–45, 2020.

[52] Yu-Ting Chen, Michal Szurek, Beili Hu, Julius de Hond, Boris Braverman, and Vladan Vuletic. High finesse bow-tie cavity for strong atom-photon coupling in rydberg arrays. *Optics Express*, 30(21):37426–37435, 2022.

[53] Adrian Nugraha Utama, Chang Hoong Chow, Chi Huan Nguyen, and Christian Kurtsiefer. Coupling light to higher order transverse modes of a near-concentric optical cavity. *Optics Express*, 29(6):8130–8141, 2021.

[54] David Hunger, Tilo Steinmetz, Yves Colombe, Christian Deutsch, Theodor W Hänsch, and Jakob Reichel. A fiber fabry–perot cavity with high finesse. *New Journal of Physics*, 12(6):065038, 2010.

[55] Manuel Brekenfeld, Dominik Niemietz, Joseph Dale Christesen, and Gerhard Rempe. A quantum network node with crossed optical fibre cavities. *Nature Physics*, 16(6):647–651, 2020.

[56] Yaoting Wang, Ruihong Zhang, Wujun Li, Boyang Li, Wenjia Shi, and Yanchao Zhang. Experimental investigation on the eliminating astigmatism in off-axis parabolic mirror ring cavity. *Optics & Laser Technology*, 109:348–351, 2019.

[57] Matt Jaffe, Lukas Palm, Claire Baum, Lavanya Taneja, and Jonathan Simon. Aberrated optical cavities. *Physical Review A*, 104(1):013524, 2021.

[58] Mark Stone, Aziza Suleymanzade, Lavanya Taneja, David I Schuster, and Jonathan Simon. Optical mode conversion in coupled fabry–perot resonators. *Optics Letters*, 46(1):21–24, 2021.

[59] Timothy P McKenna, Jeremy D Witmer, Rishi N Patel, Wentao Jiang, Raphaël Van Laer, Patricio Arrangoiz-Arriola, E Alex Wollack, Jason F Herrmann, and Amir H Safavi-Naeini. Cryogenic microwave-to-optical conversion using a triply resonant lithium-niobate-on-sapphire transducer. *Optica*, 7(12):1737–1745, 2020.

[60] Aishwarya Kumar, Aziza Suleymanzade, Mark Stone, Lavanya Taneja, Alexander Anferov, David I Schuster, and Jonathan Simon. Quantum-enabled millimetre wave to optical transduction using neutral atoms. *Nature*, 615(7953):614–619, 2023.

[61] Simon Gröblacher, Jared B Hertzberg, Michael R Vanner, Garrett D Cole, Sylvain Gigan, KC Schwab, and Markus Aspelmeyer. Demonstration of an ultracold micro-optomechanical oscillator in a cryogenic cavity. *Nature Physics*, 5(7):485–488, 2009.

[62] Stephan Falke, Nathan Lemke, Christian Grebing, Burghard Lipphardt, Stefan Weyers, Vladislav Gerginov, Nils Huntemann, Christian Hagemann, Ali Al-Masoudi, Sebastian Häfner, et al. A strontium lattice clock with inaccuracy and its frequency. *New Journal of Physics*, 16(7):073023, 2014.

[63] Sheng-Jun Yang, Xu-Jie Wang, Xiao-Hui Bao, and Jian-Wei Pan. An efficient quantum light–matter interface with sub-second lifetime. *Nature Photonics*, 10(6):381–384, 2016.

[64] Chao-Wei Yang, Jun Li, Ming-Ti Zhou, Xiao Jiang, Xiao-Hui Bao, and Jian-Wei Pan. Single-shot measurement of a rydberg superatom via collective photon burst. *arXiv preprint arXiv:2106.10858*, 2021.

[65] RE Kirby, GJ Collet, and K Skarpaas. An in-situ photocathode loading system for the slc polarized electron gun. In *Proceedings of International Conference on Particle Accelerators*, pages 3030–3032. IEEE, 1993.

[66] E Springate, CA Froud, ICE Turcu, S Spurdle, DS Wolff, S Hook, B Landowski, JG Underwood, A Cavalleri, SS Dhesi, et al. Artemis: synchronised xuv and laser sources for ultrafast time-resolved science. *CLF Ann Report*, 9:221–4, 2008.

[67] Pau Mestres, Johann Berthelot, Marko Spasenović, Jan Gieseler, Lukas Novotny, and Romain Quidant. Long distance manipulation of a levitated nanoparticle in high vacuum. *arXiv preprint arXiv:1505.02012*, 2015.

[68] Hai Zhong, Gotthold Fläschner, Alexander Schwarz, Roland Wiesendanger, Philipp Christoph, Tobias Wagner, Andreas Bick, Christina Staarmann, Benjamin Abeln, Klaus Sengstock, et al. A millikelvin all-fiber cavity optomechanical apparatus for merging with ultra-cold atoms in a hybrid quantum system. *Review of Scientific Instruments*, 88(2):023115, 2017.

[69] Haruka Tanji-Suzuki, Ian D Leroux, Monika H Schleier-Smith, Marko Cetina, Andrew T Grier, Jonathan Simon, and Vladan Vuletić. Interaction between atomic ensembles and optical resonators: Classical description. In *Advances in atomic, molecular, and optical physics*, volume 60, pages 201–237. Elsevier, 2011.

[70] Z Celinski. Molecular beam epitaxy system at an undergraduate institution. *Journal of Vacuum Science & Technology A: Vacuum, Surfaces, and Films*, 19(1):383–385, 2001.

[71] Julian Léonard. *A supersolid of matter and light*. PhD thesis, ETH Zurich, 2017.

[72] Albert Ryou and Jonathan Simon. Active cancellation of acoustical resonances with an fpga fir filter. *Review of Scientific Instruments*, 88(1):013101, 2017.

[73] Jürgen Appel, Andrew MacRae, and Alexander I Lvovsky. A versatile digital ghz phase lock for external cavity diode lasers. *Measurement Science and Technology*, 20(5):055302, 2009.

[74] ME Gehm, KM O'hara, TA Savard, and JE Thomas. Dynamics of noise-induced heating in atom traps. *Physical Review A*, 58(5):3914, 1998.

[75] Matt Jaffe, Lukas Palm, Claire Baum, Lavanya Taneja, Aishwarya Kumar, and Jonathan Simon. Understanding and suppressing backscatter in optical resonators. *Optica*, 9(8):878–885, Aug 2022.

[76] Alexandros Georgakopoulos, Ariel Sommer, and Jonathan Simon. Theory of interacting cavity rydberg polaritons. *Quantum Science and Technology*, 4(1):014005, 2018.

[77] DE Chang, JS Douglas, Alejandro González-Tudela, C-L Hung, and HJ Kimble. Colloquium: Quantum matter built from nanoscopic lattices of atoms and photons. *Reviews of Modern Physics*, 90(3):031002, 2018.

[78] Benjamin Gänger, Jan Phieler, Benjamin Nagler, and Artur Widera. A versatile apparatus for fermionic lithium quantum gases based on an interference-filter laser system. *Review of Scientific Instruments*, 89(9):093105, 2018.

[79] Robert Löw, Ulrich Raitzsch, Rolf Heidemann, Vera Bendkowsky, Björn Butscher, Axel Grabowski, and Tilman Pfau. Apparatus for excitation and detection of rydberg atoms in quantum gases. *arXiv preprint arXiv:0706.2639*, 2007.

[80] Anton Öttl, Stephan Ritter, Michael Köhl, and Tilman Esslinger. Hybrid apparatus for bose-einstein condensation and cavity quantum electrodynamics: Single atom detection in quantum degenerate gases. *Review of Scientific Instruments*, 77(6):063118, 2006.

[81] MS Smith. Editorial: hybridizing quantum physics and engineering. *Phys. Rev. Lett*, 117:100001, 2016.

[82] Atac Imamoğlu. Cavity qed based on collective magnetic dipole coupling: spin ensembles as hybrid two-level systems. *Physical review letters*, 102(8):083602, 2009.

[83] Jean-Michel Raimond, M Brune, and Serge Haroche. Manipulating quantum entanglement with atoms and photons in a cavity. *Reviews of Modern Physics*, 73(3):565, 2001.

[84] RA Hamm, D Ritter, and H Temkin. Compact metalorganic molecular-beam epitaxy growth system. *Journal of Vacuum Science & Technology A: Vacuum, Surfaces, and Films*, 12(5):2790–2794, 1994.

[85] Kater W Murch, Kevin L Moore, Subhadeep Gupta, and Dan M Stamper-Kurn. Observation of quantum-measurement backaction with an ultracold atomic gas. *Nature Physics*, 4(7):561–564, 2008.

[86] Dan M Stamper-Kurn. Cavity optomechanics with cold atoms. In *Cavity optomechanics*, pages 283–325. Springer, 2014.

[87] Ferdinand Brennecke, Stephan Ritter, Tobias Donner, and Tilman Esslinger. Cavity optomechanics with a bose-einstein condensate. *Science*, 322(5899):235–238, 2008.

[88] Monika H Schleier-Smith, Ian D Leroux, Hao Zhang, Mackenzie A Van Camp, and Vladan Vuletić. Optomechanical cavity cooling of an atomic ensemble. *Physical review letters*, 107(14):143005, 2011.

[89] Jeffrey Douglas Thompson, TG Tiecke, Nathalie P de Leon, J Feist, AV Akimov, M Gullans, Alexander S Zibrov, V Vuletić, and Mikhail D Lukin. Coupling a single trapped atom to a nanoscale optical cavity. *Science*, 340(6137):1202–1205, 2013.

[90] Avikar Periwal, Eric S Cooper, Philipp Kunkel, Julian F Wienand, Emily J Davis, and Monika Schleier-Smith. Programmable interactions and emergent geometry in an array of atom clouds. *Nature*, 600(7890):630–635, 2021.

[91] André Heinz, Jan Trautmann, Neven Šantić, Annie Jihyun Park, Immanuel Bloch, and Sebastian Blatt. Crossed optical cavities with large mode diameters. *Optics Letters*, 46(2):250–253, 2021.

[92] Gilles Nogues, Arno Rauschenbeutel, Stefano Osnaghi, Michel Brune, Jean-Michel Raimond, and Sergi Haroche. Seeing a single photon without destroying it. *Nature*, 400(6741):239–242, 1999.

[93] QA Turchette, RJ Thompson, and HJ Kimble. One-dimensional atoms. *Applied physics B-lasers and optics*, 60(2-3):S1–S10, 1995.

[94] H Mabuchi, QA Turchette, MS Chapman, and HJ Kimble. Real-time detection of individual atoms falling through a high-finesse optical cavity. *Optics letters*, 21(17):1393–1395, 1996.

[95] X Maitre, E Hagley, G Nogues, C Wunderlich, P Goy, M Brune, JM Raimond, and

S Haroche. Quantum memory with a single photon in a cavity. *Physical review letters*, 79(4):769, 1997.

[96] Aishwarya Kumar, Aziza Suleymanzade, Mark Stone, Lavanya Taneja, Alexander Anferov, David I. Schuster, and Jonathan Simon. Quantum-limited millimeter wave to optical transduction, 2022.

[97] Autodesk, Inc. Autodesk Fusion 360, 2023.

[98] Jürgen Eschner, Ch Raab, F Schmidt-Kaler, and R Blatt. Light interference from single atoms and their mirror images. *Nature*, 413(6855):495–498, 2001.